Numerical phase-field modelling and experimental validation of sintered steel fracture and fatigue behaviour

Tomić, Zoran

University of Zagreb
Faculty of Mechanical Engineering and Naval Architecture

Zoran Tomić

NUMERICAL PHASE-FIELD MODELLING AND EXPERIMENTAL VALIDATION OF SINTERED STEEL FRACTURE AND FATIGUE BEHAVIOUR

DOCTORAL DISSERTATION

Zagreb, 2023

University of Zagreb
Faculty of Mechanical Engineering and Naval Architecture

Zoran Tomić

NUMERICAL PHASE-FIELD MODELLING AND EXPERIMENTAL VALIDATION OF SINTERED STEEL FRACTURE AND FATIGUE BEHAVIOUR

DOCTORAL DISSERTATION

Supervisors:

Full Prof. Zdenko Tonković, PhD

Full Prof. Nenad Gubeljak, PhD

Zagreb, 2023

Sveučilište u Zagrebu
Fakultet strojarstva i brodogradnje

Zoran Tomić

NUMERIČKO MODELIRANJE I EKSPERIMENTALNA VALIDACIJA LOMNOGA I ZAMORNOGA PONAŠANJA SINTERIRANOGA ČELIKA PRIMJENOM TEORIJE FAZNIH POLJA

DOKTORSKI RAD

Mentori:
prof. dr. sc. Zdenko Tonković
prof. dr. sc. Nenad Gubeljak

Zagreb, 2023.

BIBLIOGRAPHY DATA

UDC	
Keywords:	fracture, fatigue, Phase-field modelling, sintered stell, microscale, macroscale, instrumented indentation
Scientific area:	Technical sciences
Scientific field:	Mechanical engineering
Institution:	Faculty of Mechanical Engineering and Naval Architecture
Thesis supervisors:	Full Prof. Zdenko Tonković, PhD Full Prof. Nenad Gubeljak, PhD
Number of pages:	37
Number of pages (in total):	137
Number of figures:	24
Number of tables:	7
Number of references:	91
Date of examination:	
Thesis defence committee:	Assist. Prof. Tomislav Lesičar, PhD – Chairman of the defence commission Assoc. Prof. Tomislav Jarak, PhD – member Assist. Prof. Eduard Marenić, PhD – member
Archive:	Faculty of Mechanical Engineering and Naval Architecture

ACKNOWLEDGEMENT

In the beginning, I would like to express my sincere gratitude to my mentor Full Prof. Zdenko Tonković, PhD who introduced me to the world of science and research. With his best will, among other obligations, in a very short time period we got a lot of experimental and numerical results. Thank you for the freedom during the entire research and thank you for the great financial support with which we were able to do a lot of multiscale experimental tests. I wish to express my sincere thanks. Also, thanks to the second mentor, Full Prof. Nenad Gubeljak, PhD from Faklulteta za strojništvo, Univerza v Maribor who helped with macroscopic test and result analysis. With many years of experience with experimental tests, we managed to extract interesting results from uniaxial tests.

I wish to express my gratitude to other colleagues from the Chair of Mechanics and Strength of Materials, especially to Assist. Prof. Tomislav Lesičar, PhD and other colleagues from the Faculty. Special sincere gratitude goes to Assoc. Prof. Tomislav Jarak, PhD who read a huge number of drafts and manuscripts, and gave countless advices, suggestions and comments through numerous mails, online meetings and calls. In those difficult times he was one of those who were always available and moody.

Thanks to my special colleagues from the office, Tomislav Polančec, mag. ing. mech. and Tihana Damić, mag. iur. with which daily work was much easier.

My most sincere thanks go to my friends, relatives, and people who were always by my side. In particular, thanks to the Fegareto group, for their unselfish love and unconditional support.

To my sister Ilijana, son-in-law Ivan, mom Ljubica and dad Mirko, to whom I owe everything.

Zoran Tomić, October 2023.

SPECIAL ACKNOWLEDGEMENT

I wish to express a gratitude to the **Croatian Science Foundation**, which financed the research conducted in this thesis under the project "Multiscale Numerical Modelling and Experimental Investigation of Aging Processes in Sintered Structural Components" (MultiSintAge, PZS-1 2019-02-4177)" led by Prof. Zdenko Tonković, PhD.

Zoran Tomić

Zagreb, 2023

Omnia ad maiorem Dei Gloriam.

ABSTRACT

In order to achieve reliable behaviour assessment of heterogeneous materials on macroscale it is necessary to numerically and experimentally model material behaviour on the microscale. The porosity and heterogeneity in fracture mechanics are often considered as defects which decrease the mechanical properties. Usually, such defects are micro-, or even nanoscopic, but significantly decrease material properties, depending on their amount and location.

In recent decade, the powder metallurgy gained attention with the appearance of additive technology or metallic 3D print. Similar to the additive technology is sintering technology, where porous components are used in automotive industry as gears, spurs as other power-transmission components. The residual porosity after sintering is not often regarded as negative feature, rather positive since such microscopic porosity decreases vibration and noise in power transmission chain. Even though porosity in such cases is positive feature, the microporosity influence on macroscopic fracture and fatigue properties remains significant.

To investigate the influence of porosity on mechanical behaviour, in this thesis experimental and numerical investigation is conducted in multiscale manner. For this study, sample batches of three different densities were compacted and sintered from identical metallic powder. The microscopic and macroscopic experimental analysis is conducted. Using high-resolution metallographic imaging detailed heterogeneous microstructure is obtained across whole cross-section, following identification of constituents and porosity amount. Moreover, to determine properties of individual microstructural constituents the instrumented indentation is applied. After that, on macroscale, by uniaxial tension tests elasto-plastic material properties are determined.

Parallel with the experimental investigation, numerical approach is proposed based on the popular phase-field modelling. The existing phase-field model used in this research is based on the generalised formulation for both fracture and fatigue analysis. Before the heterogeneous

modelling, the validation of the formulation is obtained through microindentation modelling on a certified fused silica glass specimen.

To extract elastoplastic behaviour of the micro-constituents, different reconstruction methods are applied on indentation curves. Such data are then fed into porous, heterogenous models. The obtained detailed heterogeneous metallography is converted to precise different size and porosity 2D models. The results are then compared with experimental macroscopic elasto-plastic stress-strain curves.

Using such approach, it is possible to investigate fracture and fatigue behaviour of porous, heterogeneous sintered specimens and determine macroscopic elasto-plastic behaviour based on microscopic parameters of individual constituents. In this way, it is possible to estimate fatigue life in high cyclic regime, observe fracture mechanisms on microscale, as well as construction of advanced materials based on microproperties. The numerical results presented in this thesis agree well with the experimental observations and offer insight into complex behaviour of fracture and fatigue features which can be found in porous sintered specimens.

Keywords: fracture, fatigue, Phase-field modelling, sintered stell, microscale, macroscale, instrumented indentation

GRAPHICAL ABSTRACT

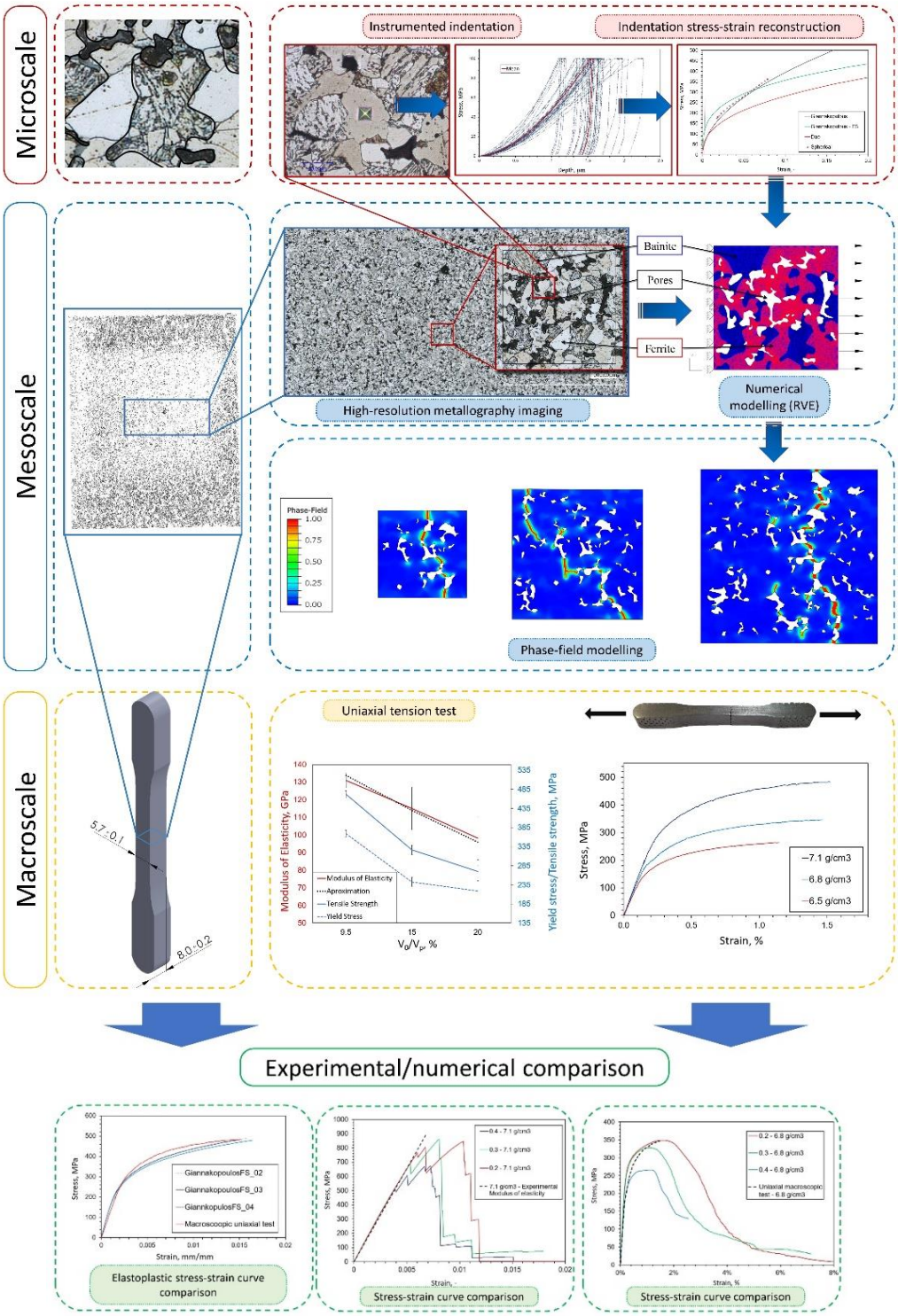

PROŠIRENI SAŽETAK (EXTENDED ABSTRACT IN CROATIAN)

Upotreba naprednih materijala u novije vrijeme, zajedno s prihvatljivim troškovima izrade, igra veliku ulogu u projektiranju strojnih komponenti. Iako konvencionalni procesi izrade (glodanje, tokarenje, različiti računalni CNC višeosni obradni centri...) nisu u potpunosti zanemareni te daju značajan doprinos u proizvodnim procesima, u posljednjem desetljeću novije i učinkovitije tehnike izrade dolaze do izražaja. U tom smislu, metalurgija praha (eng. *powder metallurgy* - PM) doživljava veliku popularnost. Velika iskoristivost sirovine (u nekim slučajevima preko 95% [1]), niski troškovi izrade, što rezultira osviještenošću prema okolišu, kao i dobra svojstva prigušenja buke [2] čini metalurgiju praha privlačnom za mnoge industrije, osobito automobilsku. Kod velike serijske proizvodnje, navedene prednosti dolaze još više do izražaja. Tako su zupčanici, lančanici i slične komponente za prijenos snage i gibanja savršeni kandidati za ovakvu vrstu tehnologije [3].

Sve većim uvođenjem električnih automobila, gdje više buka od motora s unutrašnjim izgaranjem ne dolazi do izražaja, buka od prijenosa snage kod različitih prijenosnika snage i gibanja poprima značajniju ulogu [3]. Porozni sinterirani zupčanici u tom smislu mogu smanjiti buku i vibracije, budući da upravo poroznost materijala djeluje kao prigušivač buke i vibracija [4,5]. U tom smislu poroznost nije negativna značajka, no njen utjecaj na mehaničko ponašanje mora se uzeti u obzir prilikom konstruiranja komponenti. No iako takve sinterirane komponente posjeduju zadovoljavajuća svojstva, kod strojnih dijelova do izražaja dolazi utjecaj poroznosti u materijalu. U mehanici loma i oštećenja dobro je poznato kako takve nepravilnosti u materijalu djeluju kao koncentratori naprezanja i inicijatori pukotine kod statičkog, a pogotovo kod cikličkog opterećivanja strojne komponente.

Danas metalurgija praha dolazi u dvije glavne forme: kao aditivna tehnologija (poznata kao 3D ispis) i kao tehnologija sinteriranja. Obje tehnologije kao osnovni materijal koriste metalni prah, ali proces solidifikacije materijala je značajno različit. Kod aditivne tehnologije prah se zagrijava do točke tališta, te se u slojevima nanosi izgrađujući komponentu. S druge

strane, kod tehnologije sinteriranja prah se kompaktira u alatu, željenih dimenzija i oblika konačne komponente, nakon čega se zagrijava, a potom i hladi, kako bi proces solidifikacije završio [6]. Tijekom postupka sinteriranja (zagrijavanja), koji je najčešće iznad temperature rekristalizacije metalne legure, povezivanje metalnih čestica praha ostvaruje se putem mostova (vratova) između čestica [7,8]. Pod pojmom sinteriranje misli se na u širem smislu na cijeli postupak koji se sastoji od kompaktiranja, zagrijavanja te hlađenja a u užem smislu samo na postupak zagrijavanja do točke tališa. Kroz ovaj rad pod pojmom sinteriranje misli se samo na postupak zagrijavanja otpreska. Rezultirajuća mikrostruktura komponente razlikuje se od inicijalne kompaktirane mikrostrukture. Hlađenje nakon postupka sinteriranja, kao važan čimbenik, definira konačnu mikrostrukturu. Kao što će biti pokazano kroz iduća poglavlja, nastanak mostova i mikrostruktura postat će najvažnije značajke u procesu iniciranja i rasta mikropukotine.

Primarni cilj ovog rada je istražiti utjecaj poroznosti i heterogenosti mikrostrukture na mehaničko ponašanje materijala na makrorazini. Također, cilj je rada pokazati utjecaj poroznosti na proces iniciranja i rasta pukotine na mikrorazini. Nadalje, prikazana je mogućnost naprednog numeričkog modeliranja makroskopskog odziva koji su u direktnoj vezi s mikroskopskim svojstvima materijala. Danas, da bi se što ispravnije modeliralo mehaničko ponašanje materijala koriste se višerazinski pristupi. Pri tome, potrebno je karakterizirati materijal na više razina, od nano do makro razine. U nastavku, dan je kratki pregled literature i postojećih numeričkih postupaka vezanih za modeliranje materijala na mikrorazini.

Pregled literature i postojećih numeričkih modela

Istraživanja različitih autora pokazuju kako je makroskopski mehanički odziv ponajviše definiran udjelom poroznosti na mikrorazini [9–11]. Povećanje poroznosti, odnosno, smanjenje gustoće značajno smanjuje mehanička svojstva materijala, za slučaj statičkog, a pogotovo za slučaj dinamičkog opterećenja. Kao što je uočeno u pojedinim istraživanjima [9,12–14] modul elastičnosti opada linearno s porastom poroznosti, dok granica tečenja i vlačna čvrstoća opadaju nelinearno. S druge strane, mikrostrukturna karakterizacija u radu Chawla i ostalih [12,15] pokazuje kako uzorci s više od 5% poroznosti posjeduju nepravilne pore koje su međusobno povezane. Također, kako navode Kabatova i Dudrova [16–18] iniciranje mikropukotina je upravo na mjestu većih pora, a osobito kod njihovih aglomeracija. Nadalje, mostovi (kohezivne zone koje nastaju spajanjem čestica praha), djeluju kao kritični mikrovolumeni na kojima se lokalizira plastično tečenje materijala tijekom opterećivanja, a

njihov promjer ovisi o pritisku kompaktiranja. Ako je pritisak prilikom kompaktiranja manji, dolazi do formiranja vratova manjih promjera između čestica, a posljedično i manje gustoće otpreska i obrnuto. Zbog navedenih mikroskopskih značajki, makroskopsko ponašanje materijala rezultira s malom plastičnom deformacijom (u iznosu od 1-4%, ovisno o gustoći) i naglim krhkim lomom, pa se u literaturi takvo ponašanje naziva kvazi-krhki lom.

Da bi se istražilo ponašanje spomenutih i sličnih materijala, sve više se primjenjuje numeričko modeliranje procesa deformiranja materijala, kako bi se smanjili troškovi eksperimentalnog istraživanja. Analize utjecaja različitih parametara mogu se provesti relativno jednostavno i jeftino, budući da računalna snaga osobnih, a osobito serverskih računala s godinama raste. Da bi se provela takva složena analiza, gdje su uključene mikrostrukturne značajke, kao što je heterogenost, poroznost i slično, potrebno je poznavati svojstva mikrokonstituenata. Za određivanje potrebnih svojstva, koristi se instrumentirana indentacija na nano- ili mikrorazini. Temeljem rezultata indentacije, krajem devedesetih godina Oliver i Pharr [19] predložili su metodu u kojoj nagib prilikom rasterećenja indentora odgovara modulu elastičnosti materijala. No određivanje parametara u konstitutivnim modelima elasto-plastičnog ponašanja materijala nije moguće dobiti direktno iz krivulje indentacije, nego je na temelju krivulja indentacije, potrebno različitim inverznim metodama odrediti ove parametre. Neke od tih metoda predložili su Giannakopoulos [20] i Dao i ostali [21], preko kojih je moguće odrediti granicu tečenja ispitivanog uzorka pomoću oštrog indentora, kao što su Vickersov ili Berkovichev indentor. Također, na temelju podataka iz indentacije i primjenom inverznih metoda, moguće je definirati konstitutivni zakon kojeg definira sam korisnik, ovisno o potrebama istraživanja, budući da još uvijek ne postoji eksperimentalna ili numerička metoda preko koje bi se na relativno jednostavan način mogao odrediti konstitutivni zakon pojedinih mikrokonstituenata matrice materijala. Također, predložene su različite metode za određivanje elastoplastičnog ponašanja materijala primjenom sfernih indentora [22–26].

S druge strane, za potrebe numeričkog modeliranja procesa deformiranja heterogenih materijala korišteni su različiti numerički alati i metode. Kao najznačajnija numerička metoda posebno se ističe metoda konačnih elemenata (MKE). Različiti autori koristili su MKE za nelinearnu (elastoplastičnu) numeričku analizu ponašanja heterogenih mikrostrukturnih materijala [27–30], duplex [31] ili višefaznih čelika [32]. Osim standardnih MKE formulacija za analizu elastoplastičnog ponašanja materijala, za potrebe analize procesa iniciranja i rasta pukotine kod spomenutih heterogenih materijala u literaturi se primjenjuje proširena metoda konačnih elemenata (eng. *eXtended Finite Element Method* – XFEM) [33,34] i

model kohezivne zone (eng. Cohesive Zone Model – CZM) [35–37]. Zbog velikih nedostataka spomenutih metoda (računalno skupo modeliranje, ograničenost na geometrijski jednostavne modele, definiranje *a priori* pukotine…) metoda faznih polja (eng. *Phase-Field Method*, P-F metoda) u zadnjem desetljeću doživljava snažan i kontinuiran porast iako i PF metoda zahtjeva značajnije računalne resurse kad su u pitanju komplicirani heterogeni modeli. Metodu faznog polja koriste različiti autori kako bi istražili razvoj pukotine na mikrorazini. U autorovom prethodnom radu analiziran je utjecaj grafitnih nodula u nodularnom čeličnom lijevu [38]. Abdollahi i Arias [39] koristili su P-F formulaciju za krhki lom kod feroelektričnog materijala dok su Emdadi i Zaeem [40] analizirali razvoj mikropukotine i anizotropije kod polikristalnog idealiziranog materijala. Kako bi istražio utjecaj granice zrna i anizotropnost istih, Nguyen i ostali [41–43] analizirali su rast pukotine kod idealiziranog heterogenog anizotropnog materijala, gdje je formulacija faznog polja obogaćena spomenutim modelom kohezivne zone. Kasnije, ta formulacija je proširena na kompleksnu 3D analizu betona [44,45]. Granice zrna u nekim radovima modelirane su kao razmazani slojevi između pojedinih zrna koji imaju lomnu žilavost ovisnu o okolnom materijalu [46], ili kao dodatna materijalna faza kao tanki sloj između pojedinih konstituenata [47,48].

Metode istraživanja

U sklopu ovog rada provedena je višerazinska eksperimentalna analiza sinteriranog čelika Astaloy™ Mo+0,2C za tri različite gustoće sinteriranja. Materijalni parametri dobiveni eksperimentalnim mjerenjima korišteni su u numeričkom modeliranju metodom faznog polja gdje je mehanički odziv uspoređen s eksperimentalnim odzivom. Grafički prikaz rezultata eksperimentalnih istraživanja i numeričkih analiza na pojedinim materijalnim razinama te način primjene dobivenih rezultata prikazuje slika 1. P1, P2, P3 i P4 na slici 1 označavaju radove koji su sastavni dio ove disertacije, odnosno, P1 je prvi priloženi rad [49], P2 je drugi predloženi rad [50], P3 je treći priloženi rad [51] te P4 četvrti rad [52].

Tijekom istraživanja korišten je sinterirani predlegirani čelični prah Astaloy™ Mo+0,2C proizveden od Höganäs AB, Sweden [53]. Takav prah je kompaktiran u tri gustoće: 6,5 g/cm^3, 6,8 g/cm^3 i 7,1 g/cm^3. Standardni uzorci, izrađeni prema ASTM E8 standardu, korišteni su kroz istraživanje kako bi se pokazao utjecaj poroznosti na globalni odziv materijala. Prema procesu koji je opisan dalje u radu dobivena je porozna, heterogena mikrostruktura.

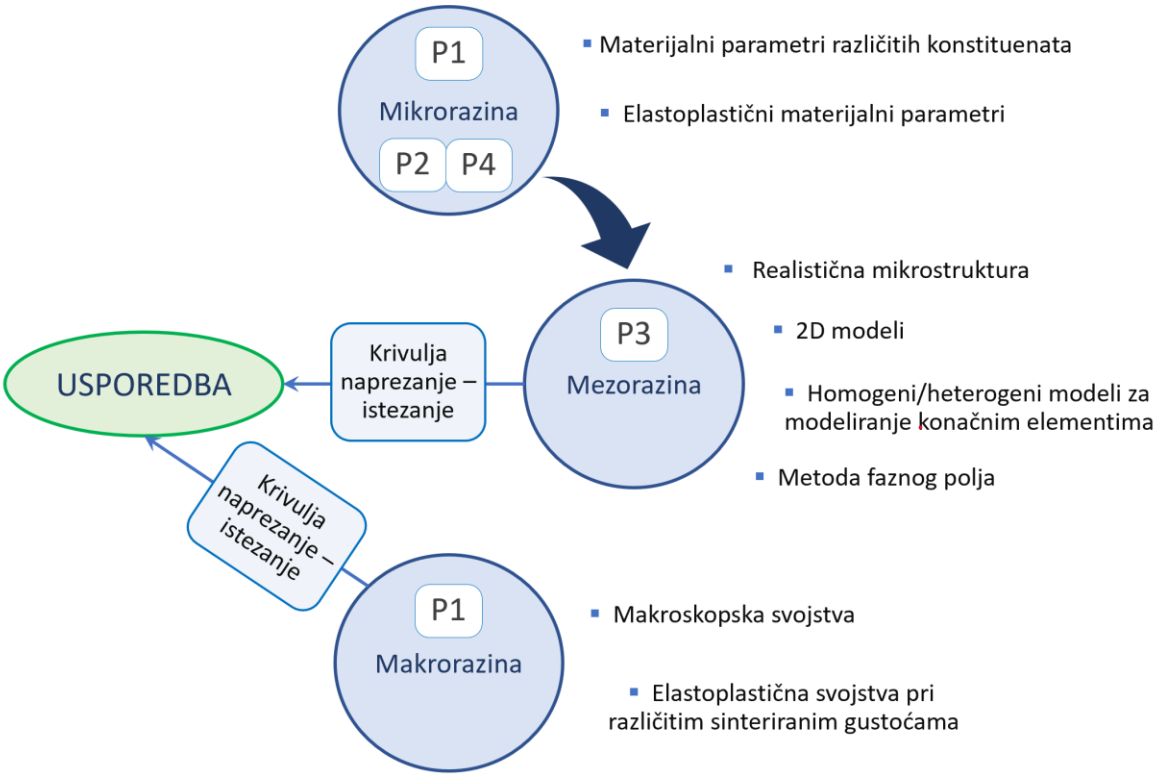

Slika 1. Višerazinsko istraživanje i usporedba numeričkih i eksperimentalnih rezultata

U prvom radu (P1 – [49]) prikazani su rezultati statičkog vlačnog makroskopskog testa na spomenute tri gustoće materijala. Također, istodobno je na mikrorazini instrumentiranom indentacijom analizirano elastično ponašanje mikrokonstituenata metalne matrice: ferita i bainita. Analizom je utvrđeno kako su elastična svojstva mikrokonstituenata (ferita i bainita) kroz različite gustoće ista, dok je makroodziv značajno degradiran povećanjem poroznosti. Na osnovi rezultata predložena je jedinstvena empirijska jednadžba pomoću koje je moguće odrediti efektivni modul elastičnosti uzorka obzirom na udio pojedinog konstituenta i udio poroznosti.

U drugom radu (P2 - [50]) izvršena je validacija formulacije metode faznog polja za krhko ponašanje materijala. Kvalitativni i kvantitativni rezultati modeliranja Vickersove indentacije silicijeva dioksida (eng. *fused silica*) uspoređeni su s rezultatima eksperimentalnih mjerenja. U radu je detaljno objašnjena i uspoređena upotreba različitih energijskih dekompozicija, bez primjene kojih dolazi do nefizikalnog rasta pukotine, a koje su neizbježne tijekom modeliranja metodom faznog polja gdje je primarno tlačna deformacija. Formulacija metode faznog polja primijenjena u ovom radu preuzeta kao nastavak istraživanja istraživačke skupine na temelju doktorskog rada Karla Seleša [54].

U trećem radu (P3 – [51]) rezultati mikrostrukturne karakterizacije dva rada (P1 i P4), korišteni su kako bi se opisalo materijalno ponašanje mikrostrukturnih konstituenata materijala u numeričkim modelima. Realistični modeli, na osnovi metalografske analize iz prethodnog rada (P1), izrađeni su za sve tri spomenute gustoće u tri veličine kako bi se ispitao utjecaj efekta veličine. Rezultati numeričkog modeliranja mikrostrukture uspoređeni su s rezultatima s makrorazine (P1), dok je paralelno proučavan nastanak i rast mikropukotine, jedinstven kod poroznih sinteriranih uzoraka.

U četvrtom radu (P4 - [52]) detaljno je prikazan postupak rekonstrukcije dijagrama naprezanje-istezanje iz krivulja indentacije za pojedine konstituente metalne matrice. U radu su navedeni svi problemi vezani za rekonstrukciju dijagrama te ispitane su različite metode koje su predložene u literaturi. Također, provedene su numeričke analize na volumenskim elementima te su rezultati elasto-plastičnog ponašanja uspoređeni s rezultatima eksperimenta jednoosnog vlačnog testa.

Cilj i hipoteza istraživanja

Glavni cilj je eksperimentalno istražiti i numerički modelirati proces akumuliranja oštećenja i loma sinteriranih materijala na makrorazini, uzimanjem u obzir heterogenosti materijala na mikrorazini. Namjera je poboljšati postojeći numerički model faznog polja za predviđanje zamornog loma te ga validirati primjenom računalne mikrotomografije, instrumentirane indentacije i makroskopskih ispitivanja.

Hipoteze:

1. Moguće je izvesti numerički model temeljen na teoriji faznog polja za simulaciju kvazistatičkog i zamornog rasta pukotina na mikro i makrorazini sinteriranih materijala.
2. Moguće je procijeniti materijalna svojstva poroznog sinteriranog materijala na makrorazini numeričkim modeliranjem ponašanja materijala na mikrorazini.

Znanstveni doprinos rada

Doprinosi koji proizlaze iz predstavljenog rada:

1. Izvršena je validacija formulacije metode faznog polja za slučaj krhkog ponašanja materijala. Predloženim 3D modelom indentacije silicijeva dioksida dobiveni su dodatni uvidi u formiranje pukotine ispod Vickersova indentora, što prije nije bilo

moguće s 2D modelom. Dodatno, istraživanje otkriva nove zaključke vezane uz dekompoziciju energije kod formulacije metode faznog polja.

2. Na temelju rezultata eksperimentalnih istraživanja na makrorazini (statički vlačni test) i mikrorazini (instrumentirana indentacija) predložen je novi empirijski izraz pomoću kojeg je moguće odrediti efektivni makroskopski modul elastičnosti poroznog heterogenog materijala na osnovi modula elastičnosti pojedinih mikrokonstituenata matrice i udjela poroznosti.
3. Eksperimentalno je pokazano kako se vrijednosti modula elastičnosti i tvrdoće sinteriranog čelika na mikrorazini dobivene indentacijom, ne mijenjaju bitno u ovisnosti o gustoći kompaktiranja, odnosno poroznosti.
4. Numeričkim modeliranjem heterogene mikrostrukture s različitim udjelima poroznosti, sa svojstvima pojedinih konstituenata dobivenih preko indentacije, pokazano je da je moguće dobiti efektivni modul elastičnosti dobiven statičkim vlačnim testom što odgovara predloženom empirijskom izrazu.
5. Pokazano je kako je primjenom metode faznog polja moguće obuhvatiti glavne fenomene i značajke razvoja mikropukotina kod poroznog sinteriranog čelika.

Ključne riječi: pukotina, zamorna pukotina, metoda faznog polja, sinterirani čelik, mikrorazina, makrorazina, instrumentirana indentacija

CONTENTS

LIST OF FIGURES

LIST OF TABLES

LIST OF ABREVIATIONS

PM	-	Powder metallurgy
3D	-	Three dimensional
SEM	-	Scanning Electron Microscopy
UTT	-	Uniaxial tension test
FEM	-	Finite element method
2D	-	Two dimensional
3D	-	Three dimensional
XFEM	-	Extended finite elements methods
CZM	-	Cohesive zone modelling
PF	-	Phase-field
DIC	-	Digital image correlation
LCF	-	Low cycle fatigue
HCF	-	High cycle fatigue
DNS	-	Direct numerical analysis
RVE	-	Representative volume elements
MVE	-	Microscopic volume element
FAMENA	-	Faculty of Mechanical Engineering and Naval Architecture

LIST OF AUTHOR'S PUBLICATION

List of Scientific Journal Papers

1. **Tomić Z**, Gubeljak N, Jarak T, Polančec T, Tonković Z. Micro - and macromechanical properties of sintered steel with different porosity. Scr Mater **2022**; 217:114787. https://doi.org/10.1016/j.scriptamat.2022.114787.
2. **Tomić Z**, Jukić K, Jarak T, Fabijanić TA, Tonković Z. Phase-Field Modelling of Fused Silica Cone-Crack Vickers Indentation. Nanomaterials **2022**; 12. https://doi.org/10.3390/nano12142356.
3. Seleš K, **Tomić Z**, Tonković Z. Microcrack propagation under monotonic and cyclic loading conditions using generalised phase-field formulation. Eng Fract Mech **2021**: 107973. https://doi.org/10.1016/j.engfracmech.2021.107973.
4. **Tomić Z**, Jarak T, Lesičar T, Gubeljak N, Tonković Z, Modelling of Fatigue Microfracture in Porous Sintered Steel Using a Phase-Field Method, Materials 16 **2023**. https://doi.org/10.3390/ma16114174.
5. **Tomić Z**, Jarak T, Pavlović B, Tonković Z. On extracting stress-strain curves of porous multi-phase sintered steels by microindentation, Exp Tech **2023**. https://doi.org/10.1007/s40799-023-00684-8

List of Scientific Conference Papers

1. **Tomić Z**, Seleš K, Tonković Z, Fabijanić T.A, Jarak T, Gubeljak N, The 2D microcrack phase-field modelling of sintered steel, AIP Conf. Proc. 2848 **2023** 20052. https://doi.org/10.1063/5.0145040.

2. Seleš K, **Tomić Z**, Tonković Z, Gubeljak N. Validation of the Phase-Field Model for Brittle Fracture. Procedia Struct Integr **2022**; 42: 1721–7. https://doi.org/10.1016/j.prostr.2022.12.218.
3. **Tomić Z**, Tonković Z, Jarak T, Gubeljak N. The 2D microcrack phase-field modelling of sintered steel. 11th Eur. Solid Mech. Conf., Galway, Ireland: **2022**.
4. **Tomić Z**, Seleš K, Tonković Z, Aleksandrov Fabijanić T, Jarak T, Gubeljak N. The 2D Microcrack Phase-Field Modelling of Sintered Steel. 20th Int. Conf. Fract. Damage Mech., Malaga, Spain: **2022**.
5. Stanić M, Lesičar T, **Tomić Z**, Gubeljak N. Modeliranje elastičnog ponašanja polimetilmetakrilata primjenom neuronske mreže. Zb. Rad. 11. Susr. Hrvat. društva za Meh., Rijeka, Croatia: **2021**, p. 259–67.
6. Seleš K, **Tomić Z**, Tonković Z, Sorić J. Rješavanje problema krhkog, duktilnog i zamornog loma primjenom poopćenog modela faznih polja implementiranog u programski paket ABAQUS. Zb. Rad. 10. Susr. Hrvat. društva za Meh., Slavonski Brod, Croatia: **2020**, p. 251–6.
7. **Tomić Z**, Seleš K, Tonković Z. Modeliranje rasta pukotine u mikrostrukturi sinteriranog materijala metodom faznog polja. Zb. Rad. 10. Susr. Hrvat. društva za Meh., Slavonski Brod, Croatia: **2020**, p. 283–8.
8. Jelušić T, Perić M, **Tomić Z**, Lesičar T, Tonković Z, Bubalo A. Modeliranje polimernog materijala ojačanog staklenim vlaknima primjenom Mori-Tanaka metode. Zb. Rad. 9. Susr. Hrvat. društva za Meh., Zagreb, Croatia: **2019**, p. 175–80.
9. Škugor T, **Tomić Z**, Živić J, Smoljkić M, Karšaj I. Numerical and experimental evaluation of 3D printed carotid replicas. 25th Congr. Eur. Soc. Biomech., Wien: **2019**, p. 656.
10. **Tomić Z**, Smoljkić M, Škugor T, Karšaj I. Numeričko modeliranje ponašanja karotidnih arterija dvokomponentnim materijalima. Zb. Rad. 9. Susr. Hrvat. društva za Meh., Zagreb, Croatia: **2019**, p. 331–6.
11. Škugor T, Smoljkić M, **Tomić Z**, Karšaj I. Eksperimentalno dvoosno ispitivanje 3D ispisanih polimernih uzoraka. Zb. Rad. 9. Susr. Hrvat. društva za Meh., Zagreb, Croatia: **2019**, p. 319–24.

1. INTRODUCTION

1.1. Motivation

The usage of advanced materials in recent years, along with acceptable production costs, plays significant role in modern machine components. Even though conventional machining processes (like milling, turning, computer CNC multi-axis processing) are still dominant, in recent years, other more exploitable techniques are utilized. In this sense, powder metallurgy (PM) gained huge popularity. Their huge raw material utilization (in some cases more than 95% [2]), low production costs, as well as good noise reduction [3] makes PM technology attractive to many industries, especially automotive industry. Due to low manufacturing costs, high utilization in large series of components, makes PM a good tool for components like gears, spurs and similar power train components [1].

With the introduction of electrified vehicles, where noise and vibration damping are of great interest, the use of porous sintered gears in different sort of drive trains could become a major factor in design process [1]. The porosity in such components acts as a damper, producing lower noise and vibrations [4,5]. In that way, porosity is not a negative feature, but the influence of the porosity ratio must be taken into account through design of such components since pores at different material scales act as crack initiatiors due to static or cyclic loading. In this way, the mechanical behaviour of materials with different density and the influence of the porosity have to be investigated.

1.2. Literature review and related studies

1.2.1. Sintering

The PM technology today exists in two forms: as an additive technology (known as 3D printing) and sintering processes. Both of these technologies are based on metallic powder, but the process of component solidification is different. While in additive technology the powder

is heated, melted and later added in layers to build the component, in the sintering technology the metallic powder is firstly compressed in a tool to desired dimensions and shape, after which a compressed powder is heated so the solidification process can be finished [6]. During the heating (sintering) process, which is usually above recrystallisation temperature of the metallic alloy, the connection between particles is established forming bridges between the particles [7,8]. Even though the sintering can be related only to heating process in whole production process, during this work, sintering will relate to whole manufacturing process unless otherwise stated. The resulting microstructure (after heating-sintering process) differs from the initial, compacted microstructure. The *in-situ* investigation by Lame et al. [7,8] showed that smaller pores have disappeared while larger pores did not change size nor shape. After sintering, the cooling phase is also important. The cooling rate and environment determine the final microstructure. The bridge establishment between particles during compression as well as sintering (heating process), will be shown later as the primary feature during microfracture and microfatigue.

The microstructural characterisation investigated by Chawla et al. [12,15] shows that irregular pores are usually interconnected, especially in samples with low density. The authors concluded that samples with a porosity higher than 5% have pores that tend to be interconnected. Moreover, as established in various studies, e.g. [9–11], the macroscopic mechanical behaviour is mostly affected by microstructural porosity. The microstructural porosity causes significant decrease in static strength. The macromechanical behaviour is governed by effective material microvolumes which transfers the applied external load [16]. As reported by [9,12,13], the degressive characteristic is observed in elastic modulus, yield stress as well as tensile strength with increase of porosity (decrease of density). A good recent review on behaviour of static mechanical parameters with respect to porosity increase is given by Ternero et al. [14]. It is shown that elastic modulus decreases linearly, while yield stress and tensile strength decrease nonlinearly (for porosities up to 30%).

1.2.2. Fractography of sintered steels

It is well known that microstructural irregularities like pores cause strain localization and crack initiation. The failure process in sintered steels is influenced by different factors, which are not present in conventional wrought steel samples, like pores, heterogeneous distribution along with pore agglomerations, condition of particle surfaces before sintering,

grain boundaries, etc. As mentioned, pores reduce effective macroscopic mechanical parameters and represents the locations of high stress and strain localization. Since the sintered components are usually compacted from a prealloyed powder, the microstructure of the metallic matrix is generally heterogeneous. Investigations by Kabatova and Dudrova [16–18], Chawla [12,15] and others show that crack nucleation is localized close to the larger pore agglomerates and interfaces (bridges between two pores). Moreover, the small particle bridges (necks) act as critical microvolumes. Higher localized plastic flow, due to their low load-bearing capacity, result in lower deformation at failure. With higher porosity smaller bridges form, resulting in lower static mechanical parameters (elastic modulus, yield stress and tensile strength) [16].

The multiscale fractography of sintered specimens after uniaxial tension test (UTT) reveals complex patterns that cannot be differentiated binary as solely brittle or ductile behaviour. In the literature, the failure in these kinds of materials is often called quasi-brittle fracture. At the macroscopic level, a generally straight fracture plane perpendicular to the loading direction is observed, similar to the brittle fracture (Figure 1b,) but it is preceded by a low amount of plastic deformation (Figure 1a).

a)

b)

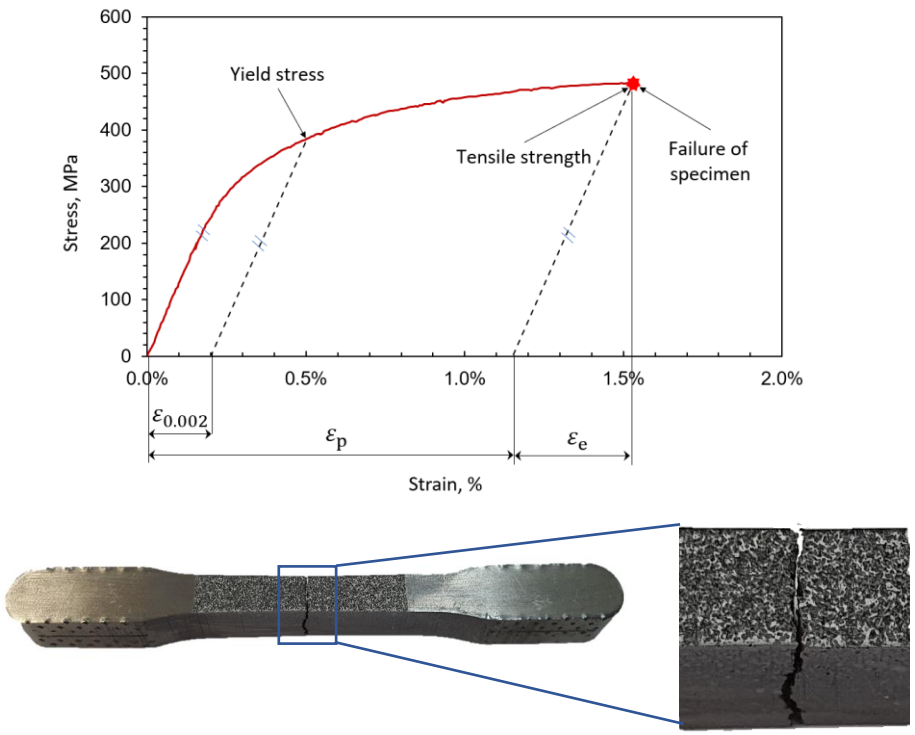

Figure 1. a) Typical UTT stress-strain curve of sintered specimen. Figure shows UTT stress-strain curve of Astaloy Mo+0.2C 7.1 g/cm^3 density. ε_e, ε_p and $\varepsilon_{0.002}$ are elastic, plastic strain and strain at 0.02%, respectively. b) standard ASTM E8 PM specimen after UTT

On the other hand, cracks appearing at the microscale cannot be differentiated as clear brittle fracture. In general, a fracture surface is made of transgranular and intragranular microcracks with a clear evidence of plastic deformation which is a consequence of crack propagation caused by the linking of smaller collapsed bridges between the particles, mentioned previously [9,16]. This microstructural behaviour can be investigated with a scanning electron microscope (SEM) of fracture surface (Figure 2). The figure on the right shows the area of ductile microcrack (green line) surrounded with free surfaces of grain boundaries around pores.

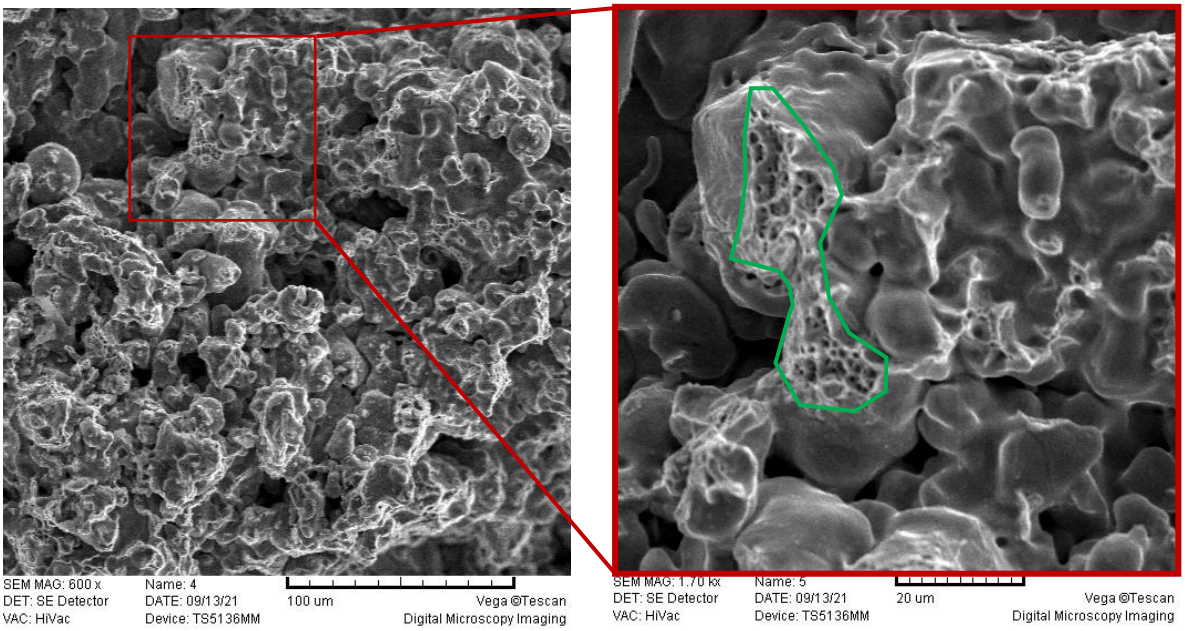

Figure 2. SEM image of fracture surface of monotonically loaded sintered specimen (Astaloy Mo+0.2C powder, 7.1 g/cm^3 density)

In general, macroscopic fracture and failure in materials start at the micro/nanoscale and is greatly influenced by the material microstructure. Experimental investigation of such multiscale processes of novel materials is expensive. Knowing local material properties, it is possible to develop various numerical models, which can be utilized to investigate complex inelastic material behaviour of new materials with advanced properties. For example, the Direct Numerical Simulation (DNS) performed at the Microstructural Volume Elements (MVEs) or the Representative Volume Element (RVEs) requires defining elastoplastic and fracture material parameters of individual constituents for analysing crack initiation and propagation in heterogeneous materials.

To encompass multiscale features of a material, different experimental measurements have to be taken on different material scales to obtain all necessary material parameters. At the

macroscale, the determination of macroscale mechanical properties is quite straightforward. On the other hand it is costly and time consuming. Regarding the microscale mechanical testing, micro tensile tests are similar to the standardized UTT, but the manufacture of single-grain micro tensile samples is difficult and expensive, and the repeatability of such tests is significantly compared to the macroscopic UTT. As described by Magagnosc [55], the use of femtosecond laser machining can be applied for the micro UTT sample machining, but it is less available and costly, among other restrictions. To conquer these restrictions, the non-destructive simple hardness test can be utilised to reconstruct material behaviour at the micro- or even at the nano-level, as defined by ISO 14577-1 [56]. Regarding the nano/microscale, in the last decade instrumented indentation gained huge popularity caused by relatively easy, low-cost determination of nano/microscale properties.

1.2.3. Instrumented indentation and reconstruction of indentation stress-strain curve

During UTT measurements, the contributions of microscopic defects like grain boundaries, porosity and other irregularities, such as inclusions and dislocations, are implicitly accounted. The demand of determining microstructural properties on individual grains (phases) in recent years gained popularity with the introduction of instrumented indentation. In the last decade of 20th century, the Oliver and Pharr [19] proposed a method for determining elastic modulus from single indentation. Until that moment, the hardness of the materials has been measured in similar manner. Vickers or Berkovich indenters were used, where a residual indent in material is measured, and the size of the indent, according to applied load, is converted to hardness. Instrumented indentation uses same indenters (along with spherical, conical and others), but the applied load and the displacement of indenter into the investigated material is continuously measured. The result is the so-called indentation curve: the force versus penetration depth graph. In their work, Oliver and Pharr proposed that the curve slope at the maximum load, just before unloading, corresponds to elastic modulus (Figure 3).

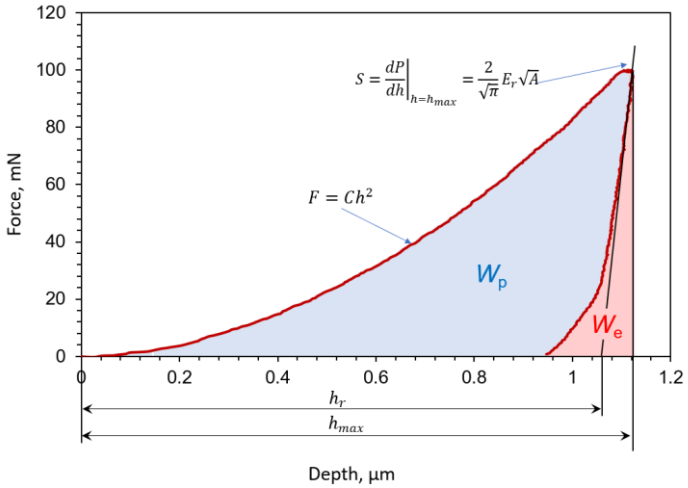

Figure 3. Typical Vickers indentation curve

In subsequent years many researchers showed excellent correlation with different macroscopic and microscopic tests, proving the validity of the method. As proposed by Oliver and Pharr, it is possible to determine only elastic modulus (along with hardness and creep which are not of interest for this research) but elastoplastic parameters remain undefined. However, knowing elastic modulus and assuming the value of Poisson's ratio, it is possible to simulate only elastic mechanical behaviour by the results of the by Oliver and Pharr method.

To determine elastoplastic material behaviour, or complete stress-strain curve of the individual material phases at the microscale, different reconstruction methods need to be utilized. Two basic groups of indentation stress-strain reconstruction methods can be differentiated: methods based on sharp indenters (Vickers or Berkovich) and spherical indenters. Shortly after Oliver and Pharr proposed their method, based on the contact mechanics of Hertz [57] and Johnson [58], Giannakopoulos and Suresh [20] presented an effective, numerical-based inverse method of extracting yield stress from indentation data: the modulus of elasticity and indentation curve. The authors proposed inverse empirical equations based on a high number of numerical finite element simulations of a sharp indentation, performed for a wide range of material properties. Dao *et al.* [21] used dimensional analysis to develop their empirical equations, where they expanded the Giannakopoulos method by assuming finite strain deformation and compared the reconstructed stress-strain curve with UTT results. In addition, they also proposed a simple equation for low hardening materials. Bucaille [59] further derived dimensionless equations for a reverse method where the dependence on the apex angle of a sharp indenter is added.

On the other hand, a stress-strain reconstruction by means of a spherical indenter is more commonly used due to greater simplicity. The stress-strain distribution under the spherical indenter has a more homogeneous distribution in comparison to sharp indenter, where significant discontinuities appear around indenter tip and edges. Another difference is that for spherical methods, multiple partial loading cycles are essential, while for sharp methods, only a single indentation curve is needed. Based on the Tabor's approach [60], where a relation of hardness and tensile strength is introduced, Filed and Swain [22] proposed a simple equation for the determination of indentation strain. Herbert [24] later compared the spherical indentation result with UTT and showed ±3% error in relation to UTT. Since the contact behaviour plays a crucial role (initial contact and contact radius) Kalidindi and Pathak [23] proposed a new method, which showed better consistency with the Hertz's theory. The contact radius proposed by Hertz yields larger deviation than the one used by Herbert [24,61]. A good overview of spherical indentation stress-strain reconstruction methods is given by Donohue et al. [26] and Pathak and Kalidindi [25]. The ease of data collection and relatively low cost made spherical reconstruction stress-strain methods attractive to many industries such as nuclear power plants [62], additively printed samples for space industry [63], or to the research of heterogeneous anisotropic materials [64,65]. Due to the need for a large amount of data, efforts are made in the field of artificial neural networks and data-driven models to reduce data collection and time [66].

In most works, the heterogeneous materials with a significant difference between the material parameters of different constituents are investigated. For example, in [27] the correlation between tensile properties and hardness tests results of an Al–Cu–Mg alloy reinforced with SiC particles was investigated, while in [28] the influence of a soft matrix and embedded hard particles was analysed. Some more recent works [29,30] studied the influence of hard particles and their interaction with the indenter during the nano-indentation response. Kannan *et al.*[31], investigated the duplex steel microstructure and the effect of local Young's modulus of inverse bainite, while Cheng *et al*. [32] investigated local plastic parameters of a multi-phase steel, consisting of austenite and martensite phases. As showed by the above-mentioned references, nowadays there exists a significant potential for the extraction of micro/nanoscale stress-strain curves by means of instrumented indentation, but it is still not clear how to efficiently apply the indentation results for obtaining local material data of specific heterogeneous materials.

In recent years, the micromechanical determination of individual constituents in heterogeneous materials is getting more attention since accurate heterogeneous numerical models can be utilized to investigate multiscale behaviour. By doing so, it is possible to investigate elastoplastic behaviour by using simpler finite element methods (FEM) or, fracture or fatigue failure analysis, accompanying microcrack initiation and propagation by using more advanced FEM based techniques. Such detailed simulations can result with accurate data about microplasticity or microfracture, which can be later linked to the macroscale behaviour. In this way, the design of desired macroscopic properties can be achieved, reducing environmental impact (through a better exploitation of raw material, reducing overdesigned components, less experimental testing) with components possessing custom-made properties.

1.2.4. Numerical modelling of heterogeneous materials

When dealing with the modelling of heterogeneous materials, most commonly various FEM approaches are employed. By performing such simulations, it is possible to gain an insight into microstructural behaviour of heterogeneous microstructure, interaction between the constituents and effects caused by different inclusions and irregularities during static and dynamic loading conditions. Using commercially available FEM 2D and 3D formulations, it is possible to investigate only elastoplastic behaviour. By employing more advanced methods, like Extended Finite Element Method (XFEM) it is possible to analyse crack initiation and propagation. For example, in [33,34], the microcrack transition between inter- and transgranular is observed in polycrystalline materials. However, the application of XFEM is often problematic in complex 2D problems and especially 3D problems due to difficult crack-tracking. A good alternative to XFEM is Cohesive Zone Modelling (CZM). Prechtel et al. [35] used CZM to simulate the fracture of heterogeneous elastic materials, while Wei et al. [36] simulated the grain separation in polycrystalline heterogeneous materials. To deal with the CZM's most important drawbacks, definition of crack path and mesh dependency, in [37] cohesive elements were used along all element edges, causing significant increase in computational time.

To overcome existing problems of XFEM and CZM, in the last decade, the Phase-Field (PF) modelling gained huge popularity in scientific community. Since no *ad hoc* criteria are needed for the determination of crack initiation and propagation, very complex crack patterns (merging, branching, multiple crack fronts…) can be obtained on complex 2D and 3D

geometries. A lot of effort has been made by different research groups to make the PF method potent in solving different complex geometries. When modelling heterogenous structure, few authors utilized a PF formulation to observe failure mechanisms at the microscale. In a recent work by the authors [38], a nodular cast iron is investigated using a generalized PF formulation [67] in both brittle and ductile regime. Due to implementation in the commercial package ABAQUS [68], it was possible to investigate different interaction features, like the friction contact between each constituent, elastic nodules and elastoplastic metallic matrix, shown in [38]. For polycrystalline materials, Abdollahi and Arias [39] used a PF brittle formulation to model crack propagation in ferroelectric materials, while Emdadi and Zaeem [40] simulated anisotropy influence of a single material phase and a different crack surface energy at grain boundaries. Nguyen et al. [41–43] simulated crack propagation in an idealized heterogeneous polycrystalline anisotropic material, where a PF formulation is enriched with cohesive zones. Similarly, Li et al. [69] used a PF method coupled with CZM for the simulation of cracks around fibres in a fibre-reinforced cement. With coupling of the PF with CZM, the interaction between individual phases can be analysed. Crack propagation between (interphase/intergranular) or through (transphase/transgranular) the specific phase can be observed. Later, this approach was extended to investigate complex 3D crack features in concrete materials [44,45]. A lot of effort has been made to compare 2D and 3D simulation results with experimental investigation data, which became possible with the introduction of microcomputed tomography and other imaging techniques [70–74].

As presented in this short review, the applied numerical models for fracture at the microscale are in general characterized by material parameters obtained experimentally at the macroscale or fictive parameters are used to show capabilities of proposed formulations. None of above-mentioned research have included experimentally obtained microscopic parameters and comparison with macroscopic UTT results.

1.3. Objectives and hypotheses

The objective of this research is the experimental and numerical modelling of damage accumulation in sintered materials on the macroscale, with respect to material heterogeneity on the microscale. The main intention is to upgrade an existing numerical model based on the

phase-field method to fatigue crack prediction (developed at the Laboratory for Numerical Mechanics, Faculty of Mechanical Engineering and Naval Architecture (FAMENA), University of Zagreb, and presented in [54]) and its experimental validation using microcomputed tomography, instrumented indentation and macroscopic testing.

Hypotheses of the research are:

1. It is possible to develop a numerical phase-field model for the quasistatic and fatigue crack simulation of sintered materials on micro- and macroscale.
2. It is possible to evaluate the mechanical macroscale properties of porous sintered material properties through numerical modelling on a microscale.

1.4. Scientific contribution

The existing numerical models for inspection of porous heterogeneous materials, like sintered steels, are usually described by regular or idealized representation of pores and inclusion on microscale. Even though such models gave satisfying results, accurate modelling and investigation on multiple materials scales demands modelling of heterogeneous materials with complicated microstructure as well as corresponding microstructural material properties. In this thesis those factors are both included and successfully implemented.

Therefore, the main scientific contribution of this thesis is development of 2D numerical model for simulation of deformation processes of porous heterogeneous sintered steel that couples the microscale mechanical properties of individual constituents and detailed microstructural representation with novel phase-field method. Such modelling enables better insight into microscale fracture and fatigue behaviour. Furthermore, using proposed methodology, it is possible to compare macroscale response using microscale mechanical properties. Based on experimental observations on micro- and macro scale the new empirical equation is proposed for determination of the effective macroscopic modulus of elasticity of porous heterogeneous material based on modulus of elasticity of individual microconstituents and porosity percentage. This allows prediction of both mechanical response as well as initiation and propagation of microcrack under monotonic or fatigue loading. Compared to existing numerical models of porous heterogeneous sintered steels, the developed model enables better insight between interphase or transphase microcrack propagation.

Using experimental test on different material scales and different porosity, a new empirical equation is proposed for determination of macroscale elastic modulus based on elastic modulus of individual constituents and porosity percentage.

Moreover, the numerical phase-field modelling and experimental investigation of fused silica certified glass specimen gives satisfying validation of phase-field formulation. Proposed 3D modelling of indentation test gives new insight into cone crack formation under Vickers indenter which is not possible with previously proposed 2D models. Additionally, investigation unveils new findings regarding energy decomposition in phase-field formulation.

A more accurate numerical modelling of quasi-static and fatigue scenarios presented in this thesis, compared to existing algorithms, allows the development of sintered materials with advanced mechanical properties and sintered components for demanding high-cyclic loading scenarios.

2. DISCUSSION ON METHODS AND RESULTS

In this thesis a multiscale experimental analysis is conducted on the sintered steel, with the aim of investigating the influence of density (porosity) on the fracture behaviour of the considered steel. Along with the experimental analysis, the numerical modelling on mesostructure of the sintered steel is performed. The elastoplastic material parameters from microscale are fed into mesoscale finite element model with PF formulation in order to investigate elastoplastic and fracture properties of investigated models. The investigation compares both qualitative results as well as quantitative features that are present in porous heterogeneous microstructure. Flow chart depicted in Figure 4 shows the detailed workflow of the thesis and investigation conducted herein.

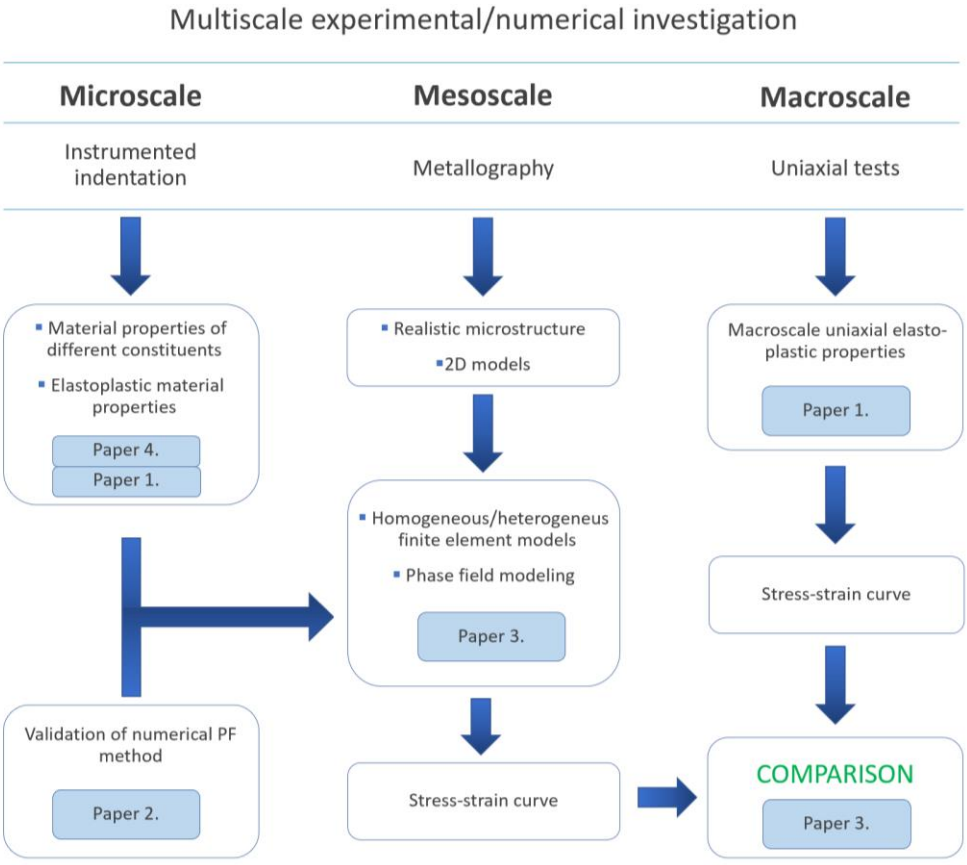

Figure 4. Flow-chart of experimental analysis on different material scales and numerical modelling conducted in the thesis. The key contribution of each paper is indicated in the text boxes.

2.1. Sintered steel Astaloy Mo + 0,2C

The material investigated in this thesis is a sintered steel, cold-compacted from prealloyed Astaloy™ Mo+0,2C produced by Höganäs AB, Sweden [53]. Three distinct densities are considered: 6.5 g/cm^3, 6.8 g/cm^3 and 7.1 g/cm^3. The compaction pressures required to gain aforementioned densities are shown in Table 1.

Table 1. Sintered densities and compaction pressures

Compaction density, g/cm^3	Compaction pressure, MPa
6.5	360
6.8	440
7.1	600

The geometry of the specimens (Figure 5) is defined by ASTM E8 for PM samples [75].

Figure 5. Geometry of different density (6.5 g/cm^3, 6.8 g/cm^3 and 7.1 g/cm^3) sintered specimens after compaction and sintering process

After compaction, specimens are isothermally sintered at 1120°C for 30 minutes and then cooled first, to 70°C, followed by a slow cooling to room temperature (25°C) in duration of approximately 40 minutes. No additional thermal or mechanical treatment was done on the specimens. The process described above generates heterogeneous porous microstructure consisting of ferrite and bainite microstructural constituents, along with pores.

2.2. Experimental investigation

To analyse mechanical behaviour (elastic, elastoplastic, fracture and fatigue), the experimental investigation is conducted for all mentioned densities at 3 distinct material scales:

- Microscale: sharp and spherical instrumented indentation and the reconstruction of stress-strain curves,

- Mesoscale: high-resolution metallography imaging,
- Macroscale: static and dynamic uniaxial tension test (UTT).

In this chapter, the methodology and results of individual experimental testing will be shown.

2.2.1. Microscale test

As mentioned before, the micromechanical properties are determined by instrumented indentation at the microscale. All measurements are conducted in the Mechanical Testing Laboratory of FAMENA by an Anton Paar Micro Combi Tester with the load resolution of 6 μN and the depth resolution of 0.03 nm. Throughout the investigation, instrumented indentations are force-controlled. The sintered specimens for instrumented indentation (Figure 6b) are prepared by mechanical polishing as described in the following chapter.

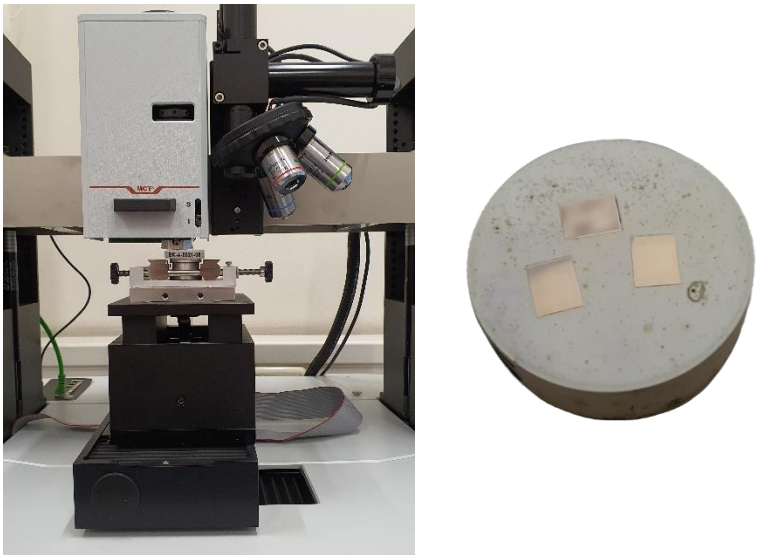

a) b)

Figure 6. a) Anton Paar MCT^3 indentation device installed at the Mechanical Testing Laboratory of FAMENA and setup used for instrumented indentation testing, b) polished three sintered samples for instrumented indentation and metallography analysis

2.2.2. Determination of elastic properties

To determine elastic properties, the standard diamond Vickers indenter is used. The maximum force of indentations was 100 mN. The choice for such force converges from three reasons:

- due to a high porosity of the tested samples, there is high probability that a pore will be positioned under the tested phase, invoking larger indent depth than expected and
- indent could encompass the phase boundary if the force is higher than needed,
- while on the other hand, since bainite phase (as later will be shown) has more heterogeneous structure, the force should be high enough to capture the bainite's heterogeneity.

A minimum of 20 indentations per phase is conducted for all sample densities. Before performing the indentation on the considered sintered metal, the indenter was calibrated on a fused silica sample with certified values. The mean indentation curves for both phases are shown in Figure 7a, while Figure 7b shows the comparison of mean penetration-time curves with the corresponding force-time characteristic. The dashed lines in Figure 7a are showing individual indentations while the mean indentation curve is marked with a solid line. The deviation (difference in indentation curve) is greater in ferrite than in bainite phase.

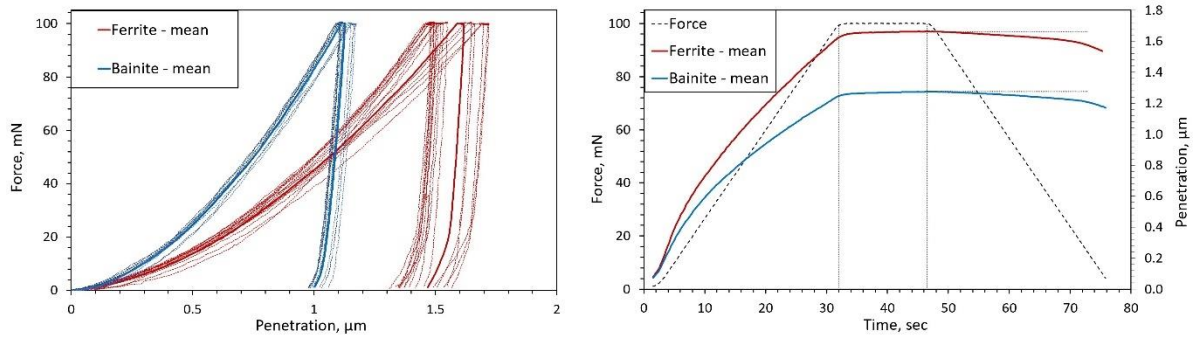

a) b)

Figure 7. Indentation curves for ferrite and bainite obtained from samples with three different densities. a) force-penetration curves with minimum/maximum deviation and mean indentation curve, b) ferrite and bainite mean penetration-time curves with corresponding force-time characteristic [49]

As visible from Figure 7a and b, bainite has a stiffer response than ferrite, mostly because of the presence of iron carbide (FeC). Moreover, the indentation curves show a significant plastic deformation for both phases, i.e., the elastic-to-plastic work ratio is very small (less than 5%). This implies that both phases have a distinct nonlinear behaviour. More about the determination of elastic properties one can find in the attached work P1. The results for different densities show almost no variation of the values of elastic (reduced) modulus for either ferrite or bainite, see Table 2.

Table 2. Microscopic properties of sintered steel with different porosity [49]

Sintered density, g/cm^3	Phase volume fraction, %			Microproperties			
	Porosity, $k_p = V_p/V_0$	Ferrite, $k_f = V_f/V_0$	Bainite, $k_b = 1-k_f$	Ferrite	Bainite	Ferrite	Bainite
				Modulus of elasticity, GPa		Vickers hardness, HV	
6.5	20	33 ±2.5	1-k_f	185.3 ± 29.5	238.4 ± 29.6	147 ± 5.9	290.8 ± 21.4
6.8	14.7	30 ±3.7	1-k_f	189.1 ± 22.8	240 ± 17.2	148.7 ± 15.4	285.5 ± 20.2
7.1	9,9	31±4.1	1-k_f	183.6 ± 20.7	238 ± 22.4	146.1 ± 10.2	296.6 ± 12.5

2.2.3. Reconstruction of indentation stress-strain curve

As described in section 1.2.3, the stress-strain curve cannot be obtained directly from indentation data, and some of the reconstruction methods must be utilized. From the indentation curves for ferrite and bainite (Figure 7a), gained by the Vickers indenter, it is possible to obtain the stress-strain curves according to the methods by Giannakopoulos [20] or Dao *et al*. [21]. Also, it is possible to utilize the spherical indenter to obtain the stress-strain relations. More about this reader can find in the work P4.

The stress-strain curves are described by the simple Holomon elastoplastic power-law material model:

$$\sigma = E \cdot \varepsilon \text{ for } \sigma \le \sigma_y \quad \& \quad \sigma = K \cdot \varepsilon^n \text{ for } \sigma \ge \sigma_y \tag{2.1}$$

where σ and ε are the effective stress and strain, respectively. E is the elastic modulus, while K and n are the strength index and the hardening exponent, respectively. The reasons of choosing such material law are in detail described in author works, attached paper P1, P4 and [76]. The values of elastic modulus (Table 2) are taken according to the Vickers indentation and the Oliver and Pharr method.

The methods by Giannakopoulos [20] and Dao *et al*. [21] are utilized herein to obtain the values of yield stress and the indentation stress-strain curve. The results from the Vickers indentation curves and the mentioned reconstruction methods are shown in Figure 8 and Table 3.

.

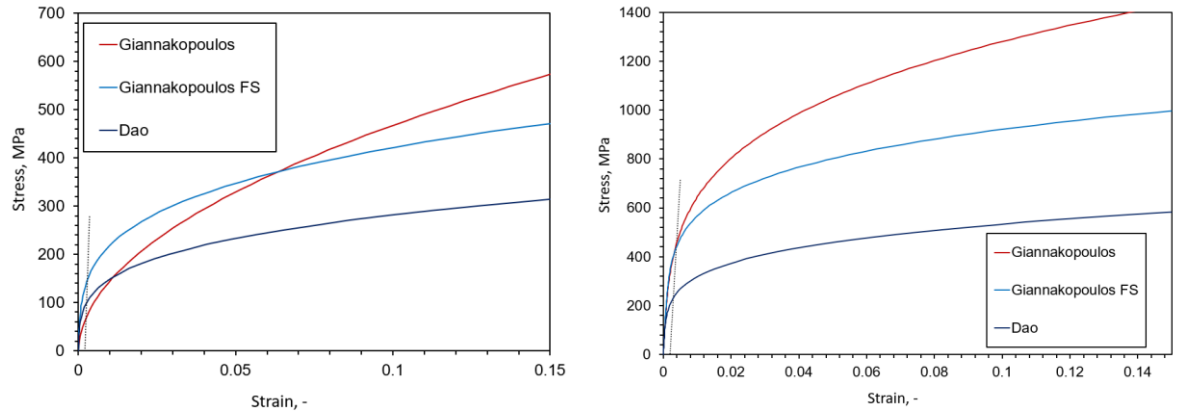

a) b)

Figure 8. Stress-strain curves of ferrite a) and bainite b) gained by reconstruction methods. The curve denoted as Giannakopoulos is extracted according to [20], Giannakopoulos FS and Dao according to [21]

In general, it can be concluded that the Vickers-based stress-strain relations for bainite and ferrite have adequate qualitative character in the sense that bainite has got higher strength than ferrite. This is expected, because bainite is a microstructure (here called the phase for simplicity) that consists of iron carbide and ferrite, rich with dislocations, providing elevated strength properties in comparison to pure ferrite. From Table 3 it is clearly visible that all methods predict a higher yield stress and strength index K for bainite. On the other hand, it seems that bit higher values of the hardening index n are predicted for ferrite. Again, the methods based on the large strains assumption predict more compliant behaviour for larger strains.

The quantitative results from indentation on microscale are in the range of macroscopic values. Due to complicated and sensitive manufacturing process (compacting, heating and cooling) as well as different alloying elements, it is difficult to compare the values with the one published in other works available. Moreover, the indentation technique is also sensitive to small environment changes and device settings, so it is not meaningful to compare the results with other publications.

Table 3. Elasto-plastic parameters of ferrite and bainite phases and homogenized matrix of sintered steel

	Name of reconstruction method	Modulus of elasticity, *E*, GPa	Poisson ratio, *v*, -	Yield stress, MPa	Strength index, *K*, MPa	Hardening exponent, *n*, -
Heterogeneous values	Ferrite					
	Giannakopoulos	186±28.8	0.3	67.4	1484	0.4994
	Giannakopoulos FS			159	772	0.2547
	Dao			98.2	526	0.2704
	Bainite					
	Giannakopoulos	239±29.6	0.3	453	2386	0.274
	Giannakopoulos FS			438	1424	0.1936
	Dao			232	874	0.2143
Homogeneous values	Homogenized values of metallic matrix					
	Giannakopoulos FS	294	0.3	233	795	0.4512

For the purposes of numerical investigation, as will be shown in the upcoming sections, the homogenized values of metallic matrix are taken. The homogenization is conducted in the sense that a number of indentations (in the form of matrix) is made across the sintered sample, regardless of indentation position: whether it is in ferrite, bainite or on the grain boundaries (Figure 9). The mean curve calculated from such indentations is used for the stress-strain curve reconstruction by the Giannakopoulos FS method and the obtained results are shown in Table 3.

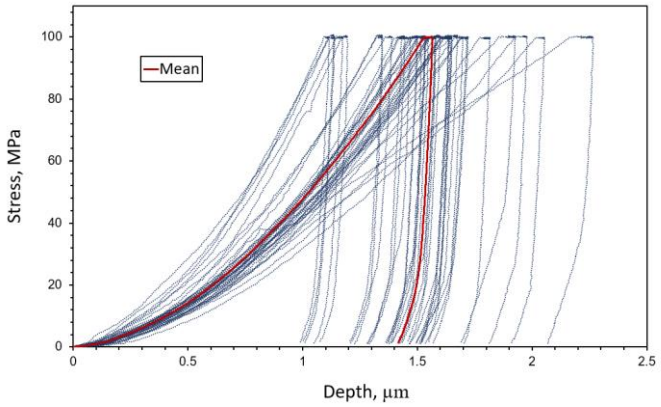

Figure 9. Individual indentation curves and mean indentation curve for the matrix of sintered steel

The determination of fracture toughness of ductile materials using instrumented indentation at the microscale is a difficult task, because no crack appears on the surface of indented specimens. In a brittle material, the determination of fracture toughness by Berkovich

or Vickers indentation is possible since cracks initiate and propagate from the edges of the indenter. Therefore, several methods are proposed for ductile materials, like those of Palmquist or Anstist [77,78]. But a sharp indentation of ductile material phases, like ferrite and bainite, again did not initiate cracks along the indenter edges (the Vickers indentation results and residual indents can be found in the attached papers P1 and P4). Due to this reason, only a few proposals have been made for an estimation of the fracture toughness of ductile materials using instrumented indentation. The method used here is proposed by Jeon et al. [79]. It utilizes multicycle spherical indentation and the theoretical background of plasticity evolution under the indenter. In this contribution, the indentation was conducted using a spherical indenter with the 50 μm radius on Anton Paar Micro Combi Tester MCT^3 at room temperature. At least 15 individual indentations were conducted for each phase.

By using the mentioned method for estimating the fracture toughness from [79] and the above-described multicycle spherical indentation, the fracture toughness of bainite and ferrite is calculated and shown in Table 4. More details reader can find in authors work P3.

Table 4. Fracture toughness estimation of microstructural constituents obtained by multicycle spherical indentation

	Fracture toughness (Energy release rate), G_C, N/mm
Bainite	8.45
Ferrite	14.5

2.2.4. Mesoscale test

The sintered specimens are prepared for metallography imaging by mechanical polishing. Different grade sanding papers are used after which 3μm diamond paste is applied, and in the end, 0.03 μm diamond fluid are applied. Besides polishing, samples are immersed in 3% Nital etching fluid to reveal heterogeneous microstructure. High resolution metallography imaging is obtained with Keyence® 4K optical microscope. The panoramic images are taken across the entire cross section (Figure 10b and c). The metallography analysis shows an uneven distribution of pores across the cross section (Figure 10b). Against the expectations, in all densities and sections, porosity is smaller in the interior of the sample and increasing towards the edge of specimen (Figure 10b).

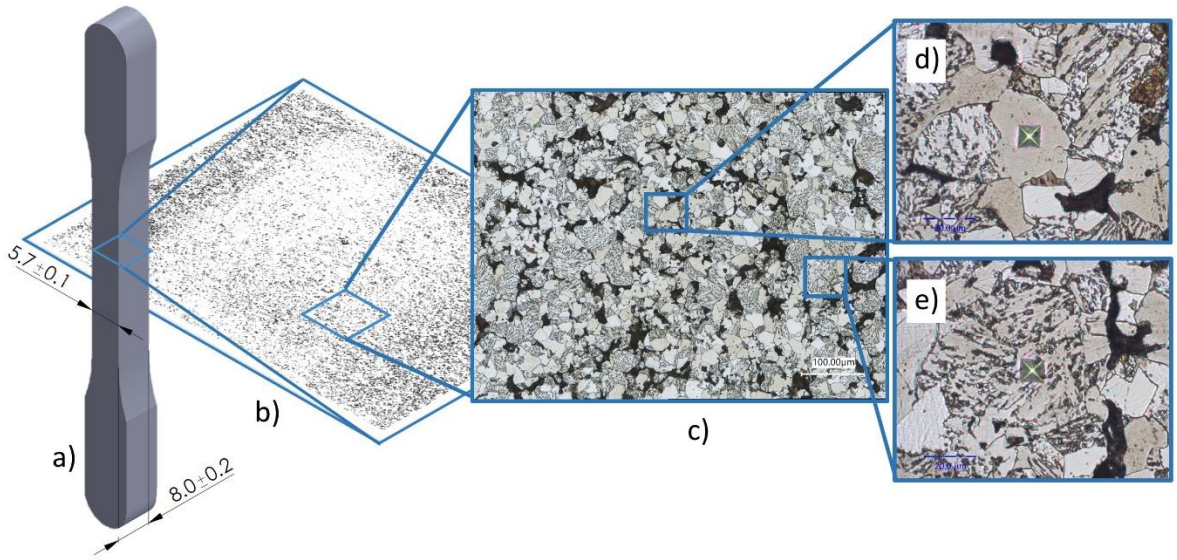

Figure 10. Metallography imaging of cross section of sintered specimen [49]. a) macroscopic specimen according to ASTM E8, b) cross-section of the sample where irregular pore distribution is visible, c) etched heterogeneous microstructure, d) ferrite phase with residual Vickers indent, e) bainite phase with residual Vickers indent

As visible from Figure 10c, the microstructure consist of two phases: ferrite (light yellow colour-Figure 10d) and bainite (light yellow with grey lines-Figure 10). The ferrite phase is homogenous, while bainite is the pseudophase with lamellas of iron carbide (FeC). During this thesis, bainite is considered as homogeneous due to the complexity of its structure. The segmentation of heterogeneous microstructure is conducted to determine the ratio of porosity, as well as the ratio of ferrite and bainite at each density. The open access ImageJ® software with Fiji extension is used in the segmentation process. The results for all three densities are shown in Table 5.

2.2.5. Macroscale test

The static uniaxial tension tests (UTT) are conducted on the Instron servo-hydraulic machine. All specimens are tested in the strain-controlled loop accompanying GOM® Aramis™ 12M DIC system with the constant strain rate of 1 mm/min. The mean results for three densities, shown in Table 5 and Figure 11a, are extracted from 8-9 specimens per density.

The results show a significant drop of considered mechanical properties (elastic modulus, yield stress and tensile strength) with the decrease of density (the increase of porosity).

Table 5. Compaction pressures, porosity ratio and macroscopic UTT properties of different density sintered stell specimens from Astaloy™ Mo+0,2C

Compaction density, g/cm^3	Porosity, %	Modulus of elasticity, GPa	Yield stress, MPa	Tensile strength, MPa
6.5	20	98.2	218.9	269.8
6.8	14.7	115.1	242.5	326.7
7.1	9.9	131	369.0	471.7

Along with the decrease of these properties, all tested samples demonstrated a distinct brittle behaviour, with brittle fracture pattern and a low amount of strain hardening (Figure 11a), where the strain at failure increases with the increase of density. As mentioned before, this kind of failure mode is indicated as quasi-brittle which possesses fracture surface perpendicular to loading direction and low amount of plastic deformation (in range from 1 to 2%).

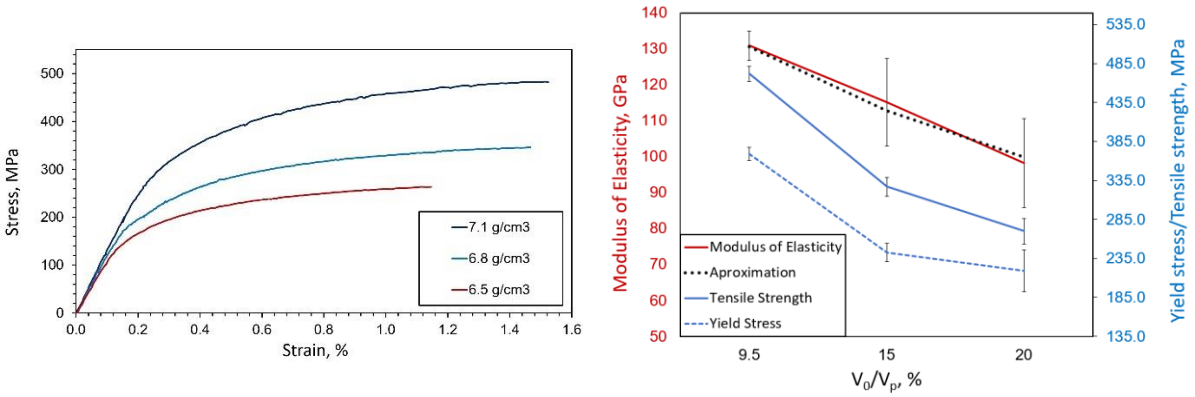

a) b)

Figure 11. Macroscopic UTT properties, a) stress-strain curves, b) macroscopic mechanical parameters in relation to sample porosity [49]

Such a strong degressive characteristic of all macromechanical properties (with respect to the increase of porosity) is also noticed in [9,11,13,80]. A most recent review by Ternero et al. [14] showed an almost linear decrease of elastic modulus (for up to 30% of porosity) and a nonlinear decrease of yield stress and tensile strength. As proposed in authors work [49] (attached paper P1), the effective macromechanical elastic modulus can be easily calculated for the considered steel by a simple equation involving the elastic moduli of microscale constituents along with the volume ratios of constituents and porosity as:

$$E_{\text{eff}} = \left[k_f \cdot E_f + k_b \cdot E_b\right] \cdot (1 - (k_p)^c), \tag{2.2}$$

where k_f, E_f, k_b, E_b are the ferrite or bainite volume ratios and elastic moduli, respectively, while k_p is the sample porosity and c is an arbitrary non-zero constant factor.

As visible from Figure 11a, a small plastic deformation is present before failure. Thereby, the elongation at failure and yield stress decrease with increased porosity. The porosity increases the compliance of the material, i.e., causes higher plastic deformation the microstructure and decreases the final elongation. On the other hand, more pores increase the possibility of microcrack initiation and speed up the microcrack propagation, because they alleviate the coalescence of microcracks. The loading-unloading experiments show that the plasticity might be the dominant mechanism at the microscale until the significant propagation of microcracks. After that, the brutal (sudden) failure occurs, as in typical brittle materials. The measurements are conducted with Rumul® Testronic 50kN as the loading device, coupled with the GOM® Aramis™ 12M DIC as a video-extensometer where live tension-relaxation supervision is possible. The results of tension – relaxation test (Figure 12) of 7.1 g/cm^3 density specimen show that there is no change in the elastic slope after an unloading cycle (except for the measuring error up to 2%). This means that the plastic deformation is present in porous sintered samples and that the microfracture events (if present) are not visible at the macroscale. The reader can find tension – relaxation test for other two densities in the attached paper P2.

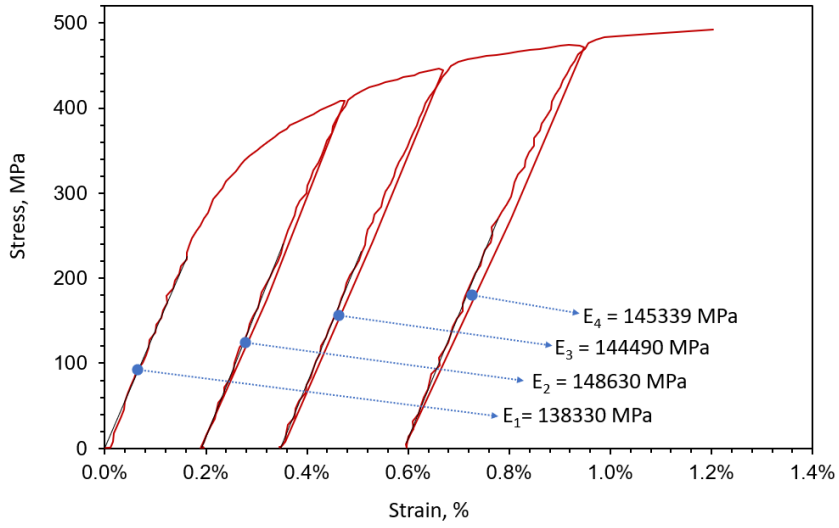

Figure 12. Tension-relaxation uniaxial test for 7.1 g/cm^3

Besides the static testing, fatigue tests are conducted on identical PM samples (Figure 5). For this, the Rumul Testronic 50kN frequency resonant machine is used. The average testing frequency was around 70 Hz for the low cycle fatigue (LCF) and around 130 Hz for the high cycle fatigue (HCF). All samples are mechanically polished with different sanding papers to

avoid surface roughness influence as well as to make better traceability among samples. The uniform cycling loading with the loading ratio, $R = \sigma_{min} / \sigma_{max} = F_{min} / F_{max}$ =0.05 was applied. All tests are force-controlled and the Wöhler curves (Figure 13) for all three densities are constructed.

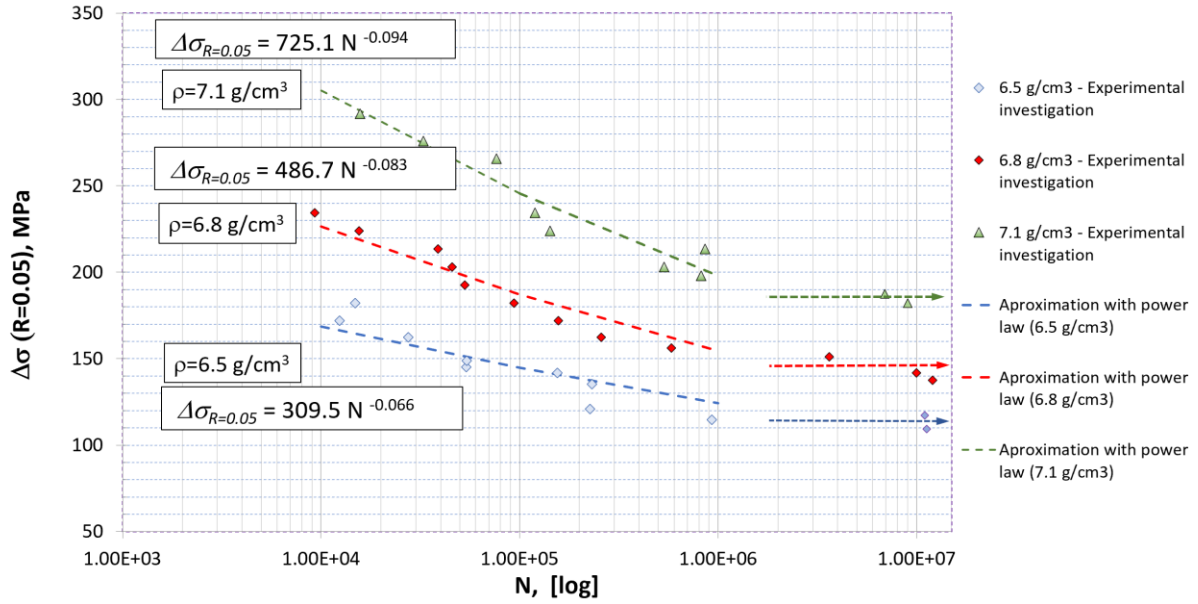

Figure 13. Wöhler curves of sintered steel specimens. Arrows pointing towards right represent fatigue limit determined as load that doesn't cause collapse at 10^7 cycles

From Figure 13 it is visible that there is a significant loss of fatigue resistance between the three considered densities. For example, at the load with the maximum force of approx. 9 kN the 7.1 g/cm3 density steel reaches the fatigue limit, while the 6.5 g/cm^3 density steel exhibits the low cyclic behaviour with only few thousands of cycles needed to complete the failure of specimen. Moreover, each density in the Wöhler diagram can be approximated with a nonlinear, exponential curve $\Delta\sigma = \mathrm{A} \cdot N^{\mathrm{B}}$, where $\Delta\sigma$ is the applied cyclic stress range, N is the number of cycles until fatigue failure, while A and B are nondimensional material parameters. The approximated values of parameters A and B are shown in Figure 13 for each density. Now, it is possible to relate the values of nondimensional parameters, A and B, to the density (Figure 14).

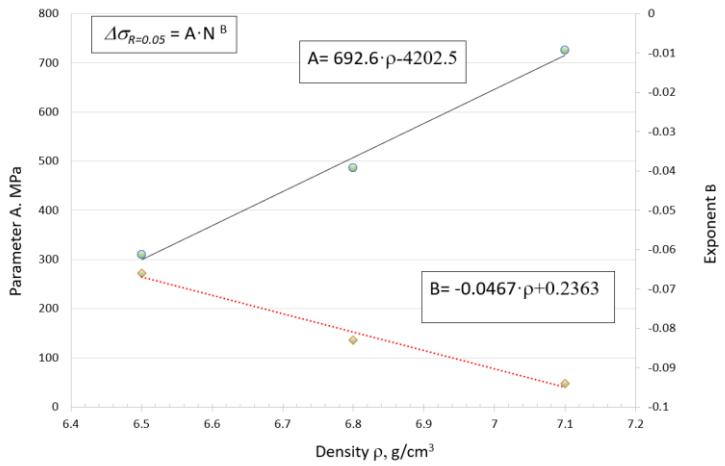

Figure 14. Change of nondimensional parameters A and B with respect to the sintered density change

It is possible to monitor the development of the internal microcrack propagation on resonant frequency machine. During the experimental testing resonant frequency can be monitored continuously. The observation of resonant frequency change can be related to microcrack propagation inside the tested specimen (collapse of bridges internally) since cross section of the specimen is reducing and resonant frequency is dropping. Such finding is a good basis for future work, where amount of damage can be correlated to frequency change. Such change in the resonant frequency is displayed in Figure 15, where the sudden drop is visible just few hundred cycles before the final failure. Similar frequency patterns were observed in both the LCF as well as the HCF regime.

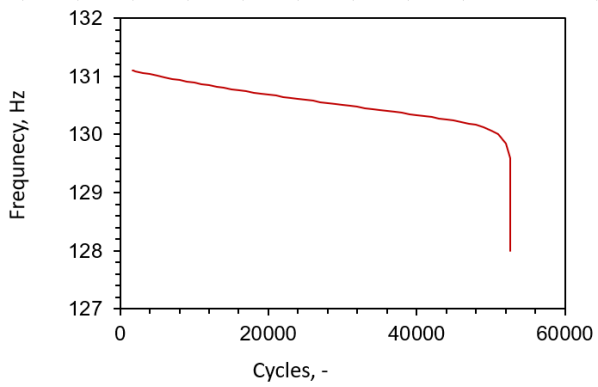

Figure 15. Frequency change with respect to number of loading cycles in low cyclic regime for specimen with 6.5 g/cm^3 density

2.3. Numerical modelling

In order to validate the applicability of the extracted elastoplastic material parameters in micro-(meso-)scale numerical simulations, the FE elastoplastic modelling of the microstructure of the heterogeneous sintered steel has been undertaken. For this purpose, the Direct Numerical Analysis (DNS) of the assumed Microscopic Volume Elements (MVE) has been performed, where the geometries of the individual material phases have been modelled realistically from high-resolution metallography images (like the one shown in Figure 16). Two-dimensional (2D) MVEs have been created, where the geometrical models of microstructures are extracted directly from the metallographic photographs by using the AutoCAD software. Although the considered microstructures have been modelled to a high degree of accuracy, the grain and pore boundaries are approximated by spline curves. The obtained graphical models have been exported to the ABAQUS software [39], where adequate meshes have been generated.

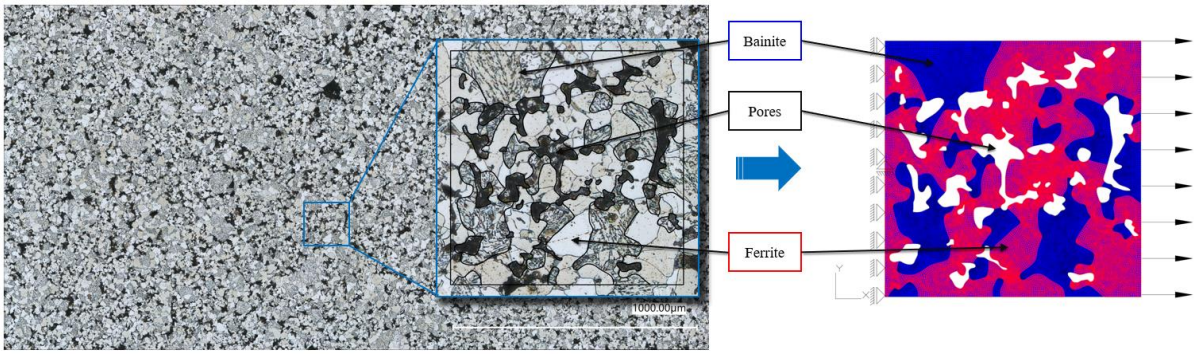

Figure 16. Metallography image of microstructure and generation of MVE numerical model.

The displacement boundary conditions that simulate the uniaxial tension are imposed on the outer MVE boundary, as depicted in right image of Figure 16, and are consistent with the macroscopic UTT. Moreover, three different sizes of thus obtained MVE models with the edge lengths of 0.2, 0.3 and 0.4 mm are considered (Figure 17). Numerical model names and sizes are shown in Table 6. In this way the size effects can be investigated, together with the representativeness of the models. The boundary conditions corresponding to UTT are prescribed by imposing the displacements on the left and right vertical edges, while considering the remaining outer edges as free surfaces (Figure 16). In this work, the individual material phases are connected node-to-node at their interfaces without defining any special contact interactions.

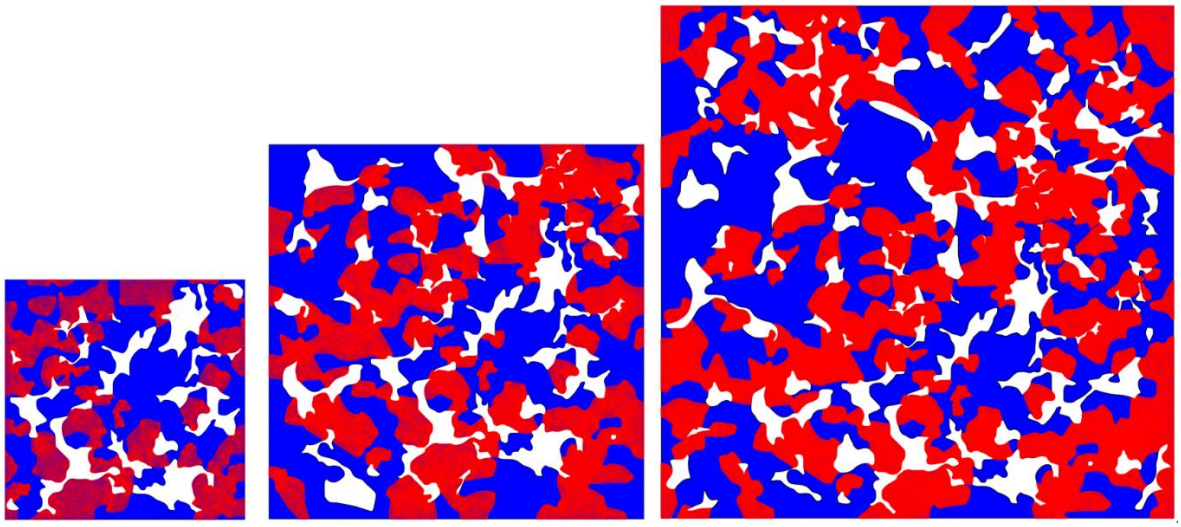

a) b) c)

Figure 17. Different sizes of MVE models for 6.5 g/cm³ density. Red regions corresponds to bainite phase, while blue region correspond to ferrite phase, a) 0.2 mm – Model S, b) 0.3 mm – Model M, c) 0.4 mm – Model L [81]***. Analogue models are extracted from other densities, 6.8 and 7.1 g/cm³***

The results of elastic, elastoplastic and PF simulation, and their comparison to the experimental results, are expressed through stress-strain diagrams. The stress-strain response of numerical models is determined as:

$$\sigma = \frac{RF}{L}, \quad \varepsilon = \frac{u}{L} \tag{2.3}$$

where *RF*, *u*, and *L* are the resultant reactive force, displacement along the right (loaded) edge, and the length of the right edge.

Table 6. Numerical model names and sizes

Name	Size
Model S	0.2 x 0.2 mm
Model M	0.3 x 0.3 mm
Model L	0.4 x 0.4 mm

2.3.1. Modelling of elastoplastic behaviour

The numerical analyses are conducted with the ABAQUS Simulia software [68]. The elasto-plastic material properties of individual phases obtained by the indentation methods, presented in Table 2, Table 3 and Table 4, are prescribed to the corresponding regions of the numerical

models. The stress-strain curves obtained by the indentation are fitted by the simple power-law material model and fed up to the numerical models. The small strain quasistatic elastoplastic analyses have been performed. All models are discretized by the 2D 4-node quadrilateral plane strain finite elements (CPE4) [68]. Approximate numbers of finite elements for S, M and L model are around 30 000, 70 000 and 130 000, respectively. The stress-strain data obtained by the numerical modelling are compared to those obtained by the macroscale UTT (Table 5).

In the first step, only elastic behaviour is investigated.Eeven though macroscopic and microscopic behaviour is elastoplastic, for the acquisition of microscopic parameters. The elastic moduli of individual phases are experimental data, obtained directly by the Oliver and Pharr method, unlike the plastic parameters, which are "indirect" estimates obtained from the indentation curve data by applying an inverse method based on dimensional analysis. Thereby, the methods of identifying certain curve data, such as curve inclination angle $\left(\mathrm{d}F_u / \mathrm{d}h\right)\big|_{h_{\max}}$, and the choice of considered functional forms in dimensional analysis, are not unanimous and may influence the results, contributing to the initial measuring errors.

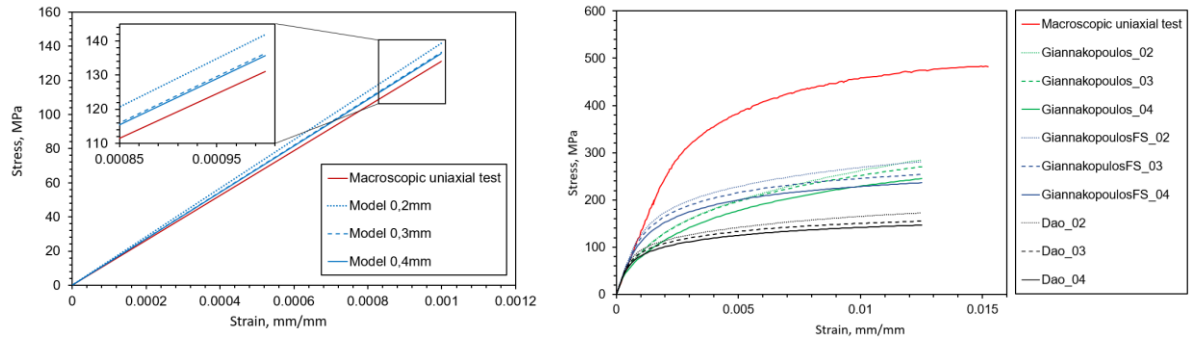

a) b)

Figure 18. a) Numerical analysis of different size 7.1g/cm^3 density models with elastic properties only and comparison to macroscopic UTT, b) numerical analysis of different size 7.1 g/cm^3 density models with elasoplastic properties and with comparison to macroscopic UTT

From Figure 18a, it is visible that the numerical results converge to the experimental value of elastic modulus (the curve slope) with increasing the model size, clearly exhibiting the size effect. The bulk elastic response of porous heterogeneous materials can also be determined using the empirical equation proposed in the authors' previous work [49] (attached work P1).

In the second step, elastoplastic analysis is conducted using proposed reconstruction methods, denoted as Giannakopoulos FS. The obtained numerical stress-strain results are compared with the macroscopic UTT stress-strain curve (Figure 18b). It is obvious that for the

sintered steel the applied numerical model significantly underestimates the expected experimentally observed macroscopic behaviour, regardless of the method applied for the extraction of the stress-strain curves of individual metallic phases. Qualitatively speaking, these results are physically incorrect, because it is expected that at lower length scales the yield and ultimate stresses should be higher and the behaviour stiffer than the corresponding macroscopic values due to the size effect, see e.g. [38] and references therein. Such large deviation from the experimental data can partly be explained by the erroneous estimation of plasticity parameter values of individual material phases, especially of ferrite. A large scattering of measured indentation curves has been recorded for the ferrite phase, see [49]. This phenomenon could be explained by the influence of the harder bainite phase on the indentation response of ferrite. The location of an indentation inside the ferrite phase and the spatial distribution of bainite surrounding the investigated ferrite patch probably significantly modify the force-penetration curve. Analogous conclusions were proposed in the very recent work [30] dealing with the influence of hard inclusions on the soft matrix indentation, and in [32], where the boundary effects have been analyzed in a multiphase steel, consisting of austenite and martensite phases. In the samples, the surrounding pores could also have an analogous effect on the indentation results. However, it can be concluded that the averaged indentation curves of individual phases may produce inaccurate curve data, which are used in the inverse analysis for extracting local plastic parameters.

One simple way to improve the accuracy of the numerical modelling of sintered specimens is by using the homogenized properties of the metallic matrix. The homogenized mean values of material properties are given in Table 3. They are obtained from the mean indentation curve, which is obtained from averaging all bainite and ferrite indentations, see Figure 9 or for more details attached paper P3 and P4.

As visible from Figure 19 much better approximation of macroscopic response is possible by utilizing the homogeneous values of microscale elastoplastic stress-strain data. A possible reason for such a difference between numerical results obtained by heterogeneous and “homogenized” metallic matrix could lie in overly pronounced plastic strain localization in the ferrite phase, whose plastic properties might be underestimated by the indentation methods. This effect is possibly “smeared out” by homogenizing the properties of the metallic matrix.

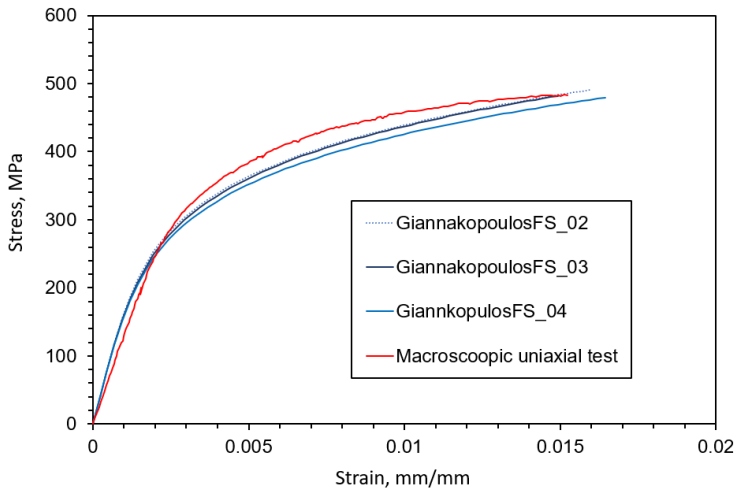

Figure 19. Stress-strain comparison of uniaxial test against numerical modelling with homogenised values of elastoplastic parameters

2.3.2. Damage modelling by phase-field method

The PF formulation used within this contribution is based on the work by Seleš [38,82–84], and is implemented in the commercial FE software ABAQUS. Here, only a brief overview of basic governing equations is shown.

As proposed by Francfort and Marigo [85] in their variational approach, which is an expansion of the Griffith's fracture theory, the fracture process is governed by the minimization of internal energy functional Ψ:

$$\Psi = \Psi^{\mathrm{b}} + \Psi^{\mathrm{f}} \approx \int_{\Omega/\Gamma} \psi_e(\varepsilon)\mathrm{d}\Omega + \int_{\Gamma} G_{\mathrm{C}}\,\gamma\left(\phi,\nabla\phi\right)\mathrm{d}\Gamma\,. \tag{2.4}$$

The total internal energy Ψ consists of the bulk energy Ψ^{b} accumulated in a body Ω with the crack defined by its surface Γ and the dissipated surface energy Ψ^{f}, induced by fracture. $\psi_{\mathrm{e}}(\boldsymbol{\varepsilon})$ is the strain energy density function, $\boldsymbol{\varepsilon}$ represents the small strain tensor, while G_c denotes the critical energy release rate (fracture toughness), representing the energy needed for forming the fracture of the unit surface area. The scalar parameter ϕ is called the phase-field parameter and is used to define the intensity of damage in the material. It is a smooth scalar field that describes transition from the intact material ($\phi = 0$) to the completely broken ($\phi = 1$) material. Therein, $\gamma\left(\phi,\nabla\phi\right)$ is the so-called crack surface density function that typically depends on the phase-field ϕ and its gradient $\nabla\phi$, and is defined over some small local subdomain (band) used to smear the crack. Starting from the works [86,87], in the general case

of brittle fracture the regularized internal energy functional Ψ of a body can be written as follows

$$\Psi = \Psi^b + \Psi^f \approx \int_{\Omega/\Gamma} g(\phi)\psi_e(\boldsymbol{\varepsilon})\, dV + \int_{\Omega} \psi^c(\bar{\psi})\,(2\phi + l|\nabla\phi|^2) dV \tag{2.5}$$

Herein ϕ is the monotonically decreasing degradation function which accounts for the loss of stiffness caused by the fracture initiation and propagation. Throughout this work, the standard quadratic function $g(\phi) = (1-\phi)^2$ is adopted. In Eq. (2.5) l is the length scale parameter corresponding to the width of the approximated crack band. To prevent the unphysical crack propagation in compressive stress states, an appropriate strain energy decomposition should be introduced, which considerably increases the computational costs. Consequently, in the paper P2 the energy decomposition is introduced as explained therein, while in the paper P3 due to only tension loading energy decomposition is deactivated.

The fracture energy Ψ^f can be approximated according to Miehe et al. [87] as domain integral, where ψ^c stands for a specific fracture energy. The ψ^c serves as an energetic threshold for fracture initiation. The ψ^c is the constant parameter in the case of quasi-static fracture but in fatigue formulations such as [86], it is assumed that the fracture resistance degrades under repeated cycling load. This can be achieved by making ψ^c dependent on the energy accumulation variable $\bar{\psi}$, which measures the "mileage" of the material subjected to repeated cycling loading. More about this, one can find in [54]. Here $\bar{\psi}$ is calculated at a certain moment *t* of the loading process as

$$\bar{\psi}(t) = \int_0^t \dot{\psi}_e(\tau)\, H\left(\dot{\psi}_e(\tau)\right) \mathrm{d}\tau. \tag{2.6}$$

The *H* in the previous equation represents Heaviside function, where the value of 0 is during energy decrease ($\dot{\psi}_e \le 0$) and the value of 1 when the strain energy increases ($\dot{\psi}_e > 0$).

In order to quantify ψ^c, in [38,88] the fracture energy was represented in a way typical for brittle PF models based on the Griffith's theory as:

$$\Psi^f \approx \int_\Omega \psi^c(\bar{\psi})\left(2\phi + l\left|\nabla\phi\right|^2\right)\mathrm{d}V = \int_\Omega G_c(\bar{\psi})\,\gamma(\phi,\nabla\phi)\,\mathrm{d}V \tag{2.7}$$

where $\gamma(\phi,\nabla\phi)$ is the surface crack density function defined as

$$\gamma(\phi,\nabla\phi) = \frac{3}{8\sqrt{2}}\left(\frac{2\phi}{l} + l^2\left|\nabla\phi\right|^2\right). \tag{2.8}$$

In this case, it follows:

$$\psi^c = \frac{3}{8\sqrt{2}} \frac{G_c}{l} . \tag{2.9}$$

Therefore, in the simulations shown herein, the initial value of ψ^c is defined as in (2.9) by using the experimentally estimated values for G_c. The length scale parameter can then be calculated as follows:

$$l = \frac{3}{4\sqrt{2}} \frac{G_C E}{\left(\sigma_{\max}\right)^2}, \tag{2.10}$$

where $\sigma_{\max}$ corresponds to the ultimate tensile stress.

In the case of fatigue loading the degradation of the fracture energy caused by fatigue is defined by a fatigue degradation function $\hat{F}(\bar{\psi})$ as:

$$\psi^c(\bar{\psi}) = \frac{3}{8\sqrt{2}} \frac{G_c(\bar{\psi})}{l}, \; G_c(\bar{\psi}) = \hat{F}(\bar{\psi}) G_c . \tag{2.11}$$

In the paper P3 the fatigue degradation function is chosen as logarithmic function as described in detail therein.

Governing equations, in the strong form, are the standard equilibrium equations with the corresponding natural and displacements boundary conditions (see [87] and [88] for the derivations). After introducing a few modifications, the evolution equation can be written as:

$$-l^2 \Delta \phi + \left[1 + \mathscr{H}\right] \phi = \mathscr{H} . \tag{2.12}$$

The $\mathscr{H}$ is the history field parameter introduced to impose the irreversibility of the phase field. Throughout this work, the history field parameter is defined as:

$$\mathscr{H}(t) := \max_{\tau \in [0,t]} \tilde{D}\left(\psi_e(\tau)\right), \tag{2.13}$$

where

$$\tilde{D}\left(\psi_e(\tau)\right) = \left\langle \frac{\psi_e(\tau)}{\psi^c\left(\bar{\psi}(\tau)\right)} - 1 \right\rangle_+ \text{ for } \forall \tau \in [0,t]. \tag{2.14}$$

The all numerical examples considered in this dissertation are based on above described formulation, implemented in ABAQUS FE software [68]. Detailed explanation about

numerical implementation reader can find in [54], authors previous work [38] and attached paper P3.

2.3.3. Validation of the brittle phase-field formulation

In order to validate presented phase-field formulation, since the lack of the same is still missing, the simulation of instrumented indentation is conducted. This paragraph corresponds to attached paper P2. In the paper, validation is shown through Vickers indentation of fused silica glass reference block. The fused silica glass is extremely brittle material. The material properties of the fused silica block are constant, regardless of the temperature or other environment conditions. Moreover, the values of the modulus of elasticity and Poisson's factor are certified with each glass block, so this makes fused silica as great material for validation of the brittle formulation. The typical force – displacement curve of the fused silica Vickers indentation is shown in Figure 20a while the residual indent is shown in Figure 20b.

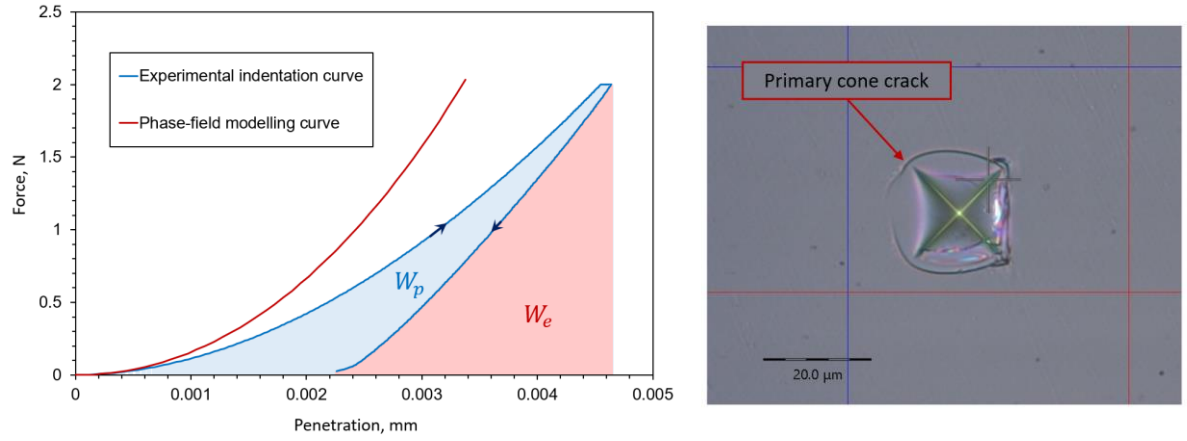

a) b)

Figure 20. a) Indentation curve comparison between numerical brittle phase-field formulation and experimental measurement. Area under the experimental indentation curve corresponds to elastic (W_e) and plastic (W_p) indentation work, b) residual indent and fracture pattern after Vickers indentation on fused silica glass.

From both Figure 20a and Figure 20b it is visible that even such brittle material like fused silica contains some plasticity. This is in detailed discussed in attached paper P2. Moreover, the typical fracture pattern after Vickers indentation of the fused silica is cone crack, visible in the Figure 20b.

The experimental instrumented indentation test is conducted on a certified reference material - round fused silica block produced and certified by Anton Paar TriTec, Switzerland. The measurements were performed on Micro Combi Tester MCT^3 according to EN ISO 14577-

1:2016 at room temperature using a certified Vickers diamond pyramidal indenter. The measurements were performed using different loads. The load of 50 mN was selected to determine the plane strain modulus E^* and the indentation modulus E_{IT} in accordance with recommendations from the calibration certificate. The values of the modulus of elasticity, both measured and certified, are shown in Table 7.

Table 7. Material properties of fused silica glass

	***Plane strain modulus E*,* MPa**	***Poisson's ratio ν, -***
Certified value	75 100±300	0.16
Measured value	74 990	-
StdDev	1360	-

Other required material properties necessary for the PF modelling, σ_{max} and the K_{IC}, are taken from literature [89]. The values of the σ_{max} and K_{IC} are 4000 MPa and 0.006 N/mm, respectively.

The modelling results show that phenomenological crack pattern, that is cone crack, can be obtained with PF brittle formulation (Figure 21) if appropriate energy split is used. Discussion on the energy split during indentation modelling is in detailed described in attached paper P2.

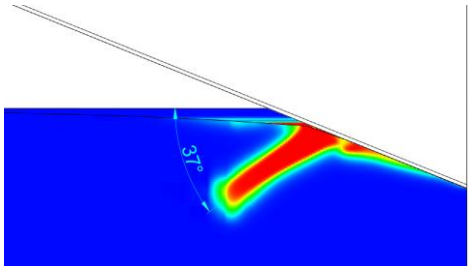

Figure 21. Cone crack during fused silica Vickers indentation modelling. Figure shows position of the indenter at max loading (2000 mN of force) and inclination angle of the cone crack in respect to the surface, typical for this kind of indentation.

The initiation ring, typical for Vickers indentation, can also be obtained with such modelling (attached paper P2) outside of the contact region between the indenter and the material. This is in fact in accordance with the Lawn and Evans theory [90] that says that the cone crack is the dominant crack mode in the indentation of intact fused silica and that radial-median (half penny) or lateral cracks are formed due to specimen irregularities or flaws beneath the indenter.

2.3.4. PF modelling of sintered steel microstructure

The comparison of experimentally obtained bulk modulus of elasticity and effective modulus of elasticity obtained by the PF formulation, assuming brittle fracture, is shown in Figure 22. The simulation results for the 6.5 g/cm^3 density sintered steel show greater scattering and inaccuracy than the results for other two densities, indicating more pronounced size effect. Further reasons for this could lie in the greater porosity and the boundary conditions applied at the MVE boundaries, leading to the localization at weakened model cross sections and overly compliant response of the models.

Moreover, for lowest density the value of effective elastic modulus increases with increasing the size of MVE, which is not a physical behaviour, which indicates that for this density larger MVEs should be considered to establish a representative volume element (RVE) for elastic behaviour.

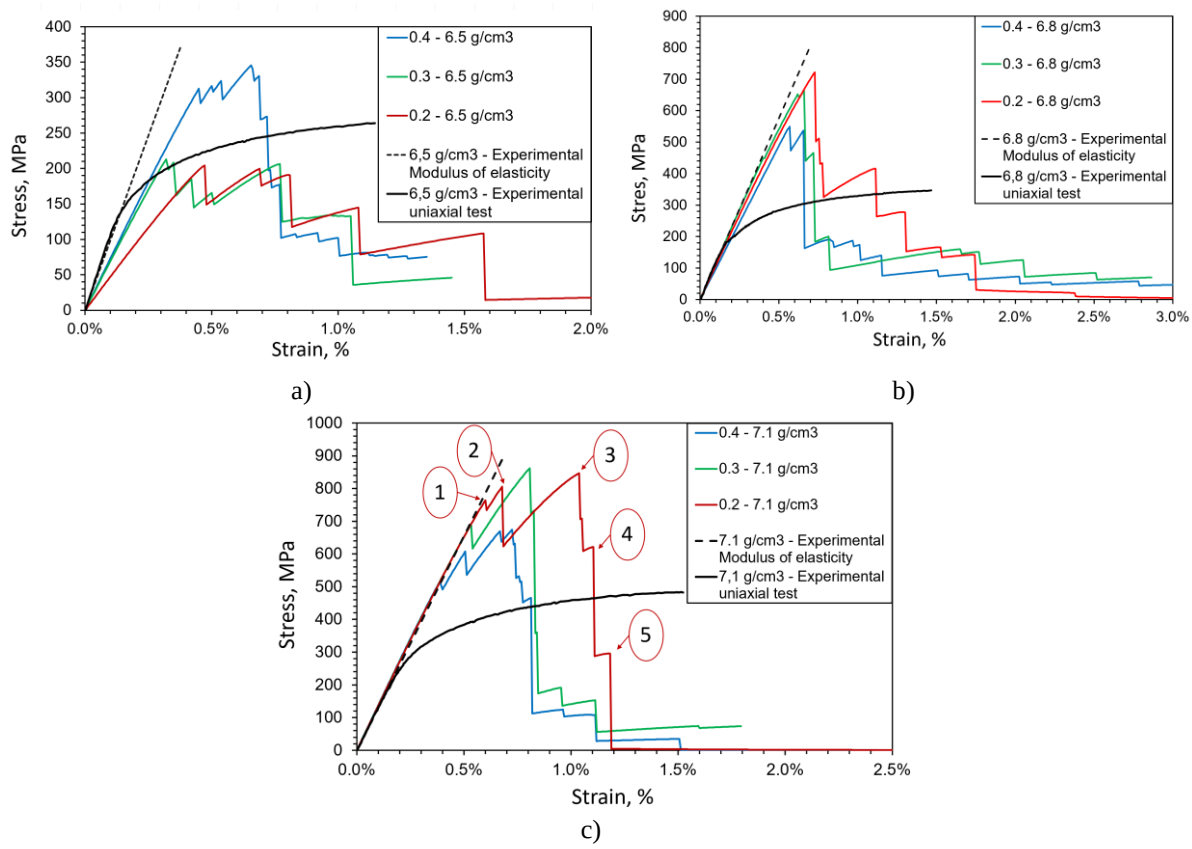

Figure 22. Numerically obtained stress-strain curve using brittle PF formulation for a) 6.5 g/cm^3, b) 6.8 g/cm^3, c) 7.1 g/cm^3 density models. The points marked by numbers from 1 to 5 in fig. c) are used to present the evolution of microcracks in Figure 24

Important to note here is that the bulk (macro) modulus of elasticity can be predicted quite accurately using numerical models of heterogeneous microstructure, with the local elastic

material parameters (the moduli of elasticity of different metallic phases) obtained by instrumented microindentation.

Numerical models for all densities considered yield a distinct perpendicular cracking pattern with respect to the load direction, which is common to the brittle fracture (see Figure 23). Also, from the Figure 22a, b and c, stress peaks and sudden vertical drops in stress are visible. This is caused by the brittle fractures of small “bridges” in the microstructure, which were formed during the early sintering process as bonds between powder particles were formed. A small bridge breaks when a microfracture that initiates at a pore at one end of the bridge propagates until a pore positioned at another side of the bridge. The final fracture pattern develops when these microcracks coalesce with neighbouring pores into one large crack (see images on Figure 24). This fracture propagation at the microscale is typical for sintered materials, as reported in the literature [9,16,17,91].

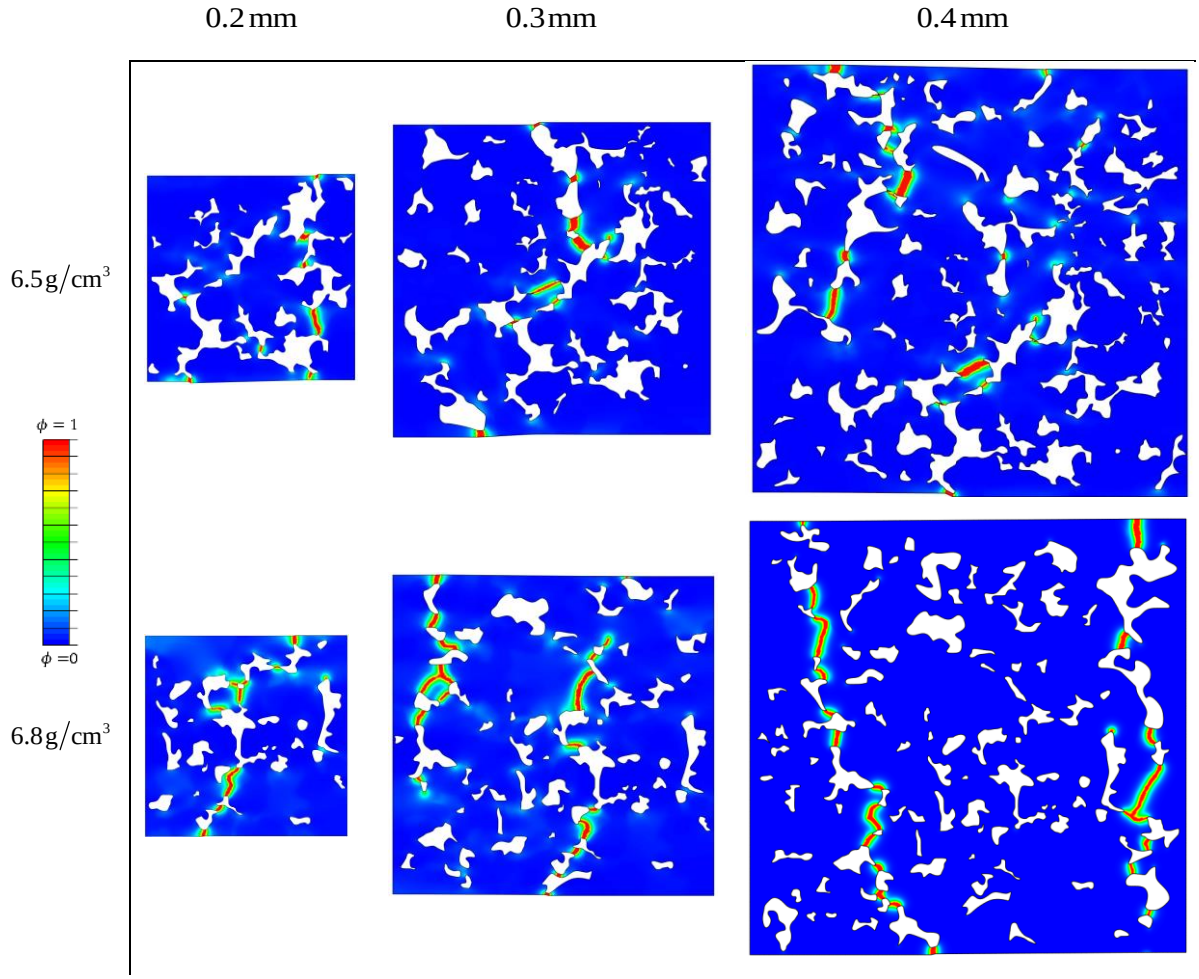

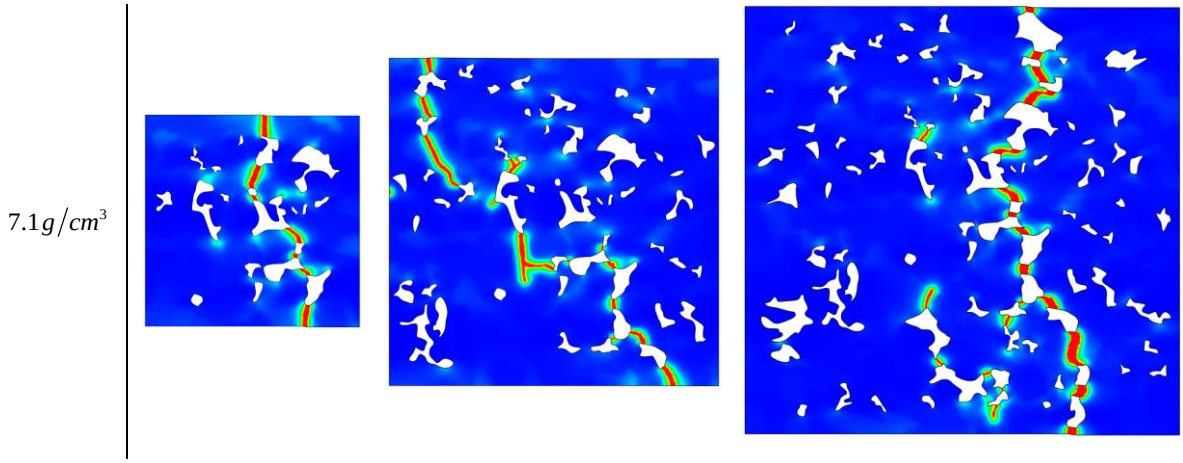

Figure 23. Microfracture patterns on different sizes and different density samples of sintered steel obtained with brittle PF formulation

Observations that arise from PF modelling of sintered microstructure can also be experimentally observed by SEM of fracture surface. The reader can find the results of SEM analysis in the attached paper P2 accompanying the detailed description. Moreover, the modelling of heterogeneous material employed herein can be utilized to show microcrack propagation with respect to different phases.

It is showed, since bainite has lower fracture toughness, the crack propagates in bainite. For a small bridge consists of ferrite phase, the microcrack initiates and propagates in those microlocations, regardless of better fracture resistance of ferrite. The cracks propagate from one pore to another until they coalesce into larger cracks, which finally results in a macroscopic fracture (Figure 24).

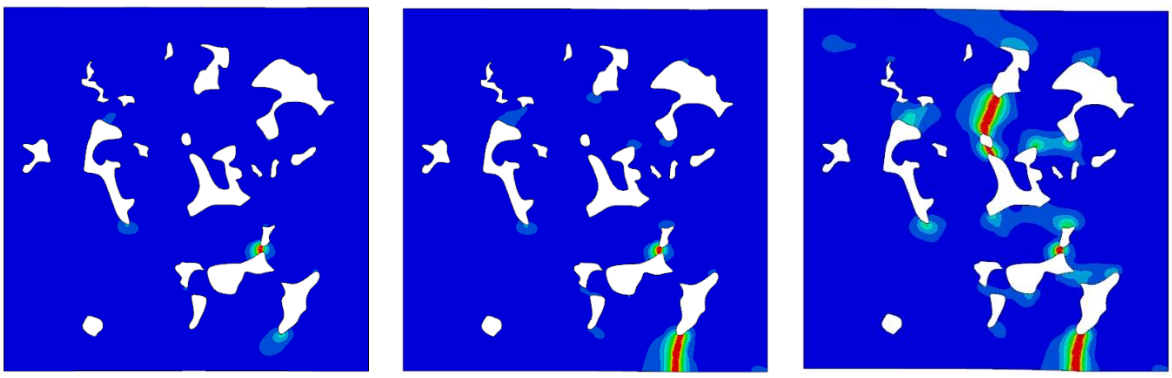

1 2 3

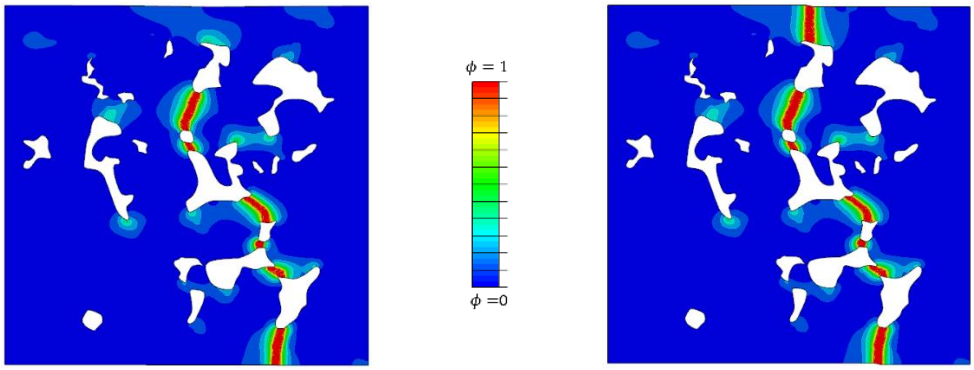

4 5

Figure 24. Microcracks propagation in S model with 7.1 g/cm^3 density. Figures 1-5 show the phase field distribution in the model for the loading states that correspond to points marked as 1-5 on the stress-strain curve in Figure 22

Investigation also shows interesting phenomenon, where a ferrite phase stops the propagation of a microcrack which indicates that it could be necessary to include the intergranular crack propagation into the future numerical modelling of the porous sintered models. Regardless of the material phase, if the minimum of the strain energy is found in ferrite zone, crack propagates further. This usually occurs if the ferrite zone is located along a small “bridge” between two pores. Reader can find more information about this phenomenon in attached paper P3.

3. CONCLUSION AND FUTURE WORK

Understanding and relating microscopic features with macroscopic behaviour is a very demanding task. Numerical models should envelope all microscopic features, boundary conditions and material properties, whose identification is not trivial. From the results that are presented in this brief overview and detailed in attached papers, it is visible that modelling of the real microstructure can benefit the understanding of macroscopic behaviour of the material.

As expected, the microscopic features, like pores and different constituents, have huge impact on the macroscopic behaviour of sintered steel. The investigation conducted on microscale using instrumented indentation and on macroscale using uniaxial tension test, shows that elastic moduluses of individual phases can be related to macroscopic (bulk) modulus of sintered steel, with respect to porosity level. The main aim of this thesis and study is to numerically investigate macroscopic behaviour based on microscopic properties, with respect to fracture and fatigue behaviour.

Paper 1 – P1 [49] shows that porosity is indeed the main influence factor for the decrease of mechanical properties in sintered steel. Using instrumented indentation it is shown that mechanical properties of two microphases (ferrite and bainite) remain almost constant, regardless of considered density of sintered specimens. Also, the equation is proposed which can be used to calculate macroscopic modulus of elasticity based on microscopic modulus of elasticity of individual constituents, with regard to porosity level. Also, from the indentation curves, it is visible that behaviour of the individual constituents is distinctly elastoplastic while the macroscopic behaviour is still quite brittle, probably due to a large porosity.

While the Paper 1 is based on multiscale experimental investigation, Paper 2 – P2 [50] focuses on numerical validation of phase-field formulation. The proposed phase-field formulation is implemented in the commercial ABAQUS software, which enables different features like contact between different parts, stabilization and other. In this paper, the numerical modelling of sharp Vickers indentation is conducted using 3D hexahedral phase-field elements. The material parameters are taken from experimental observations of fused silica Vickers

indentation. The investigated material, the fused silica, has certified mechanical parameters, and is often used in calibration purposes, due to constant properties, regardless of outside factors. Moreover, in the paper, different energy decompositions are investigated as one of biggest drawbacks of the phase-field. The results proposed in this paper shows that it is possible to mimic fracture of fused silica under Vicker indentation. The well-known, dominant fracture pattern, cone crack can be obtained using different strategies and energy decompositions. The validation is also obtained through the comparison of numerical and experimental results.

Paper 3 – P3 [51] finally focuses on microscopic behaviour of detailed heterogeneous microstructure of sintered steel and comparison with macroscopic behaviour. A numerical method is proposed for estimating total life of sintered steel microstructure using phase-field modelling of fracture and fatigue. The model captures well known features of microcrack initiation and propagation in sintered steel. Those features include initiation on, so called ‘’bridges’’ between pores and further propagation by connecting similar bridge collapse into single crack. Those observations are noticed in literature and experimental investigations conducted herein and in literature. Also, regarding fatigue analysis, results are showing that model is suitable for porosity influence investigation on a total fatigue life in a high cyclic fatigue regime.

Paper 4 – P4 [52] focuses on stress-strain reconstruction from indentation curves of multiphase porous material. The paper describes in detail the main advantages and disadvantages of reconstruction methods proposed by different authors. The main contribution of the paper is also numerical validation. Different size MVEs with very precise heterogeneous microstructure are compared with experimental uniaxial macroscopic stress-strain curve. The results indicate that microindentation is adequate for the identification of elastic properties of individual material phases, but local plastic parameters are inconclusive. Nevertheless, it seems that macroscopic stress-strain curves could be captured more accurately by matrix homogenization.

Future work:

In the future, more detailed numerical modelling will be conducted. Especially concerning ductile formulation of phase field method which could enable better correspondence with experimental stress-strain curves. Regarding the microscopic properties of individual phases, nanoindentation will be used. With this scale transition, more reliable indentation curves will be obtained along with reconstruction of indentation stress-strain diagram. Also, it is desirable

to use indentation device with continuous stiffness measurement option which enables better reconstruction of data and more precise capturing of plastic properties. Such elastoplastic modelling could describe quasi-brittle and plastic behaviour better than just elastic. Moreover, elastoplastic modelling will give insight into formation and propagation of microfracture in porous heterogeneous materials which will enable better understanding of deformation process and how to prevent component failure.

BIBLIOGPRAHY

[1] H. Danninger, What Will Be the Future of Powder Metallurgy?, Powder Metall. Prog. 18 (**2018**) 70–79. doi.org/10.1515/pmp-2018-0008.

[2] B. Leupold, V. Janzen, G. Kotthoff, D. Eichholz, Validation approach of PM gears for eDrive applications, in: V.D.I.W. GmbH (Ed.), Int. Conf. Gears 2017 2 Bände, 1st ed., VDI Verlag, Düsseldorf, **2017**: pp. 119–130. https://doi.org/10.51202/9783181022948-119.

[3] S. Dizdar, High-Performance Sintered-Steel Gears for Transmissions and Machinery : A Critical Review, Gear Technol. (**2012**) 60–65.

[4] T. Frech, P. Scholzen, P. Schäflein, C. Löpenhaus, P. Kauffmann, F. Klocke, Design for PM Challenges and Opportunities for Powder Metal Components in Transmission Technology, Procedia CIRP. 70 (**2018**) 186–191. https://doi.org/10.1016/j.procir.2018.03.267.

[5] C. Brecher, C. Löpenhaus, M. Schroers, T. Frech, P. Scholzen, Optimization of NVH behavior of gears by alternative gear materials, in: Int. Conf. Gears 2017 2 Bände, **2017**: pp. 539–552. https://doi.org/10.51202/9783181022948-539.

[6] H. Ab, Production of Sintered Components: Höganäs Handbook for Sintered Components, **2013**.

[7] O. Lame, D. Bellet, M. Di Michiel, D. Bouvard, Bulk observation of metal powder sintering by X-ray synchrotron microtomography, Acta Mater. 52 (**2004**) 977–984. https://doi.org/https://doi.org/10.1016/j.actamat.2003.10.032.

[8] O. Lame, D. Bellet, M. Di Michiel, D. Bouvard, In situ microtomography investigation of metal powder compacts during sintering, Nucl. Instruments Methods Phys. Res. Sect. B Beam Interact. with Mater. Atoms. 200 (**2003**) 287–294. https://doi.org/10.1016/S0168-583X(02)01690-7.

[9] A. Falkowska, A. Seweryn, Fatigue life of 316L steel sinters of varying porosity under conditions of uniaxial periodically variable loading at a fixed stress amplitude, Int. J. Fatigue. 117 (**2018**) 496–510. https://doi.org/10.1016/j.ijfatigue.2018.07.025.

[10] M. Doroszko, A. Seweryn, A new numerical modelling method for deformation behaviour of metallic porous materials using X-ray computed microtomography, Mater. Sci. Eng. A. 689 (**2017**) 142–156. https://doi.org/10.1016/j.msea.2017.02.055.

[11] A. Ataee, Y. Li, M. Brandt, C. Wen, Ultrahigh-strength titanium gyroid scaffolds manufactured by selective laser melting (SLM) for bone implant applications, Acta Mater. 158 (**2018**) 354–368. https://doi.org/https://doi.org/10.1016/j.actamat.2018.08.005.

[12] N. Chawla, X. Deng, Microstructure and mechanical behavior of porous sintered steels, Mater. Sci. Eng. A. 390 (**2005**) 98–112. https://doi.org/10.1016/j.msea.2004.08.046.

[13] T. Uhlířová, W. Pabst, Conductivity and Young's modulus of porous metamaterials based on Gibson-Ashby cells, Scr. Mater. 159 (**2019**) 1–4. https://doi.org/https://doi.org/10.1016/j.scriptamat.2018.09.005.

[14] F. Ternero, L.G. Rosa, P. Urban, J.M. Montes, F.G. Cuevas, Influence of the Total Porosity on the Properties of Sintered Materials—A Review, Met. . 11 (**2021**). https://doi.org/10.3390/met11050730.

[15] N. Chawla, J. Williams, X. Deng, C. McClimon, Three dimensional (3D) characterization and modeling of porosity in powder metallurgy (P/M) steels, Int J Powder Met. 45 (**2009**) 19–27.

[16] E. Dudrova, M. Kabatova, Fractography of sintered steels, Powder Metall. Process. 8 (**2004**) 59–75.

[17] E. Dudrova, M. Kabátova, A review of failure of sintered steels: fractography of static and dynamic crack nucleation, coalescence, growth and propagation, Powder Metall. 59 (**2016**) 148–167. https://doi.org/10.1080/00325899.2016.1145786.

[18] M. KABATOVA, E. DUDROVA, A.S. WRONSKI, Microcrack nucleation, growth, coalescence and propagation in the fatigue failure of a powder metallurgy steel, Fatigue Fract. Eng. Mater. Struct. 32 (**2009**) 214–222. https://doi.org/https://doi.org/10.1111/j.1460-2695.2009.01328.x.

[19] W.C. Oliver, G.M. Pharr, An improved technique for determining hardness and elastic modulus using load and displacement sensing indentation experiments, J. Mater. Res. 7 (**1992**) 1564–1583. https://doi.org/DOI: 10.1557/JMR.1992.1564.

[20] A.E. Giannakopoulos, S. Suresh, Determiantion of elastoplastic properties by instrumented sharp indentation, Scr. Mater. 40 (**1999**) 1191–1198.

[21] M. Dao, N. Chollacoop, K.J. Van Vliet, A. Venkatesh, S. Suresh, Computational modeling of the forward and reverse problems in instrumented sharp indentation, Acta Mater. 49 (**2001**) 3899–3918.

[22] J.S. Field, M. V Swain, A simple predictive model for spherical indentation, J. Mater. Res. 8 (**1993**) 297–306.

[23] S.R. Kalidindi, S. Pathak, Determination of the effective zero-point and the extraction of spherical nanoindentation stress–strain curves, Acta Mater. 56 (**2008**) 3523–3532. https://doi.org/https://doi.org/10.1016/j.actamat.2008.03.036.

[24] E.G. Herbert, G.M. Pharr, W.C. Oliver, B.N. Lucas, J.L. Hay, On the measurement of stress–strain curves by spherical indentation, Thin Solid Films. 398–399 (**2001**) 331–335. https://doi.org/https://doi.org/10.1016/S0040-6090(01)01439-0.

[25] S. Pathak, S.R. Kalidindi, Spherical nanoindentation stress–strain curves, Mater. Sci. Eng. R Reports. 91 (**2015**) 1–36. https://doi.org/https://doi.org/10.1016/j.mser.2015.02.001.

[26] B.R. Donohue, A. Ambrus, S.R. Kalidindi, Critical evaluation of the indentation data analyses methods for the extraction of isotropic uniaxial mechanical properties using finite element models, Acta Mater. 60 (**2012**) 3943–3952. https://doi.org/https://doi.org/10.1016/j.actamat.2012.03.034.

[27] Y.-L. Shen, Y.L. Guo, Indentation modelling of heterogeneous materials, Model. Simul. Mater. Sci. Eng. 9 (**2001**) 391–398. https://doi.org/10.1088/0965-0393/9/5/304.

[28] F. Pöhl, S. Huth, W. Theisen, Finite element method-assisted acquisition of the matrix influence on the indentation results of an embedded hard phase, Mater. Sci. Eng. A. 559 (**2013**) 822–828. https://doi.org/https://doi.org/10.1016/j.msea.2012.09.029.

[29] M. Heidari, A. Karimzadeh, M.R. Ayatollahi, M.Y. Yahya, Effects of particle distribution and calculation method on results of nano-indentation technique in heterogeneous nanocomposites-experimental and numerical approaches, Int. J. Solids Struct. 225 (**2021**) 111054. https://doi.org/https://doi.org/10.1016/j.ijsolstr.2021.111054.

[30] H.S. Tran, C. Bouffioux, O. Dedry, C. Rojas-Ulloa, L. Duchêne, A. Mertens, A.M. Habraken, Identification of a soft matrix-hard inclusion material by indentation, Int. J. Mech. Sci. 235 (**2022**) 107723. https://doi.org/https://doi.org/10.1016/j.ijmecsci.2022.107723.

[31] R. Kannan, Y. Wang, M. Nouri, D. Li, L. Li, Materials Science & Engineering A Instrumented indentation study of bainite / martensite duplex microstructure, Mater. Sci. Eng. A. 713 (**2018**) 1–6. https://doi.org/10.1016/j.msea.2017.12.052.

[32] G. Cheng, K.S. Choi, X. Hu, X. Sun, Determining individual phase properties in a multi-phase Q&P steel using multi-scale indentation tests, Mater. Sci. Eng. A. 652 (**2016**) 384–395. https://doi.org/https://doi.org/10.1016/j.msea.2015.11.072.

[33] N. Sukumar, D.J. Srolovitz, T.J. Baker, J.-H. Prévost, Brittle fracture in polycrystalline microstructures with the extended finite element method, Int. J. Numer. Methods Eng. 56 (**2003**) 2015–2037. https://doi.org/10.1002/nme.653.

[34] K. Shibanuma, Y. Suzuki, K. Kiriyama, K. Suzuki, H. Shirahata, A model of cleavage crack propagation in a BCC polycrystalline solid based on the extended finite element method, Acta Mater. 176 (**2019**) 232–241. https://doi.org/https://doi.org/10.1016/j.actamat.2019.07.013.

[35] M. Prechtel, P.L. Ronda, R. Janisch, A. Hartmaier, G. Leugering, P. Steinmann, M. Stingl, Simulation of fracture in heterogeneous elastic materials with cohesive zone models, Int. J. Fract. 168 (**2011**) 15–29. https://doi.org/10.1007/s10704-010-9552-z.

[36] Y.J. Wei, L. Anand, Grain-boundary sliding and separation in polycrystalline metals: application to nanocrystalline fcc metals, J. Mech. Phys. Solids. 52 (**2004**) 2587–2616. https://doi.org/https://doi.org/10.1016/j.jmps.2004.04.006.

[37] S.M. Taheri Mousavi, N. Richart, C. Wolff, J.F. Molinari, Dynamic crack propagation in a heterogeneous ceramic microstructure, insights from a cohesive model, Acta Mater. 88 (**2015**) 136–146. https://doi.org/https://doi.org/10.1016/j.actamat.2015.01.003.

[38] K. Seleš, Z. Tomić, Z. Tonković, Microcrack propagation under monotonic and cyclic loading conditions using generalised phase-field formulation, Eng. Fract. Mech. (**2021**) 107973. https://doi.org/https://doi.org/10.1016/j.engfracmech.2021.107973.

[39] A. Abdollahi, I. Arias, Numerical simulation of intergranular and transgranular crack propagation in ferroelectric polycrystals, Int. J. Fract. 174 (**2012**) 3–15. https://doi.org/10.1007/s10704-011-9664-0.

[40] A. Emdadi, M. Asle Zaeem, Phase-field modeling of crack propagation in polycrystalline materials, Comput. Mater. Sci. 186 (**2021**) 110057. https://doi.org/https://doi.org/10.1016/j.commatsci.2020.110057.

[41] T.-T. Nguyen, J. Réthoré, J. Yvonnet, M.-C. Baietto, Multi-phase-field modeling of anisotropic crack propagation for polycrystalline materials, Comput. Mech. 60 (**2017**) 289–314. https://doi.org/10.1007/s00466-017-1409-0.

[42] T.-T. Nguyen, J. Rethore, M.-C. Baietto, Phase field modelling of anisotropic crack propagation, Eur. J. Mech. a-Solids. 65 (**2017**) 279–288. https://doi.org/10.1016/j.euromechsol.2017.05.002.

[43] T.-T. Nguyen, J. Yvonnet, D. Waldmann, Q.-C. He, Phase field modeling of interfacial damage in heterogeneous media with stiff and soft interphases, Eng. Fract. Mech. 218 (**2019**) 106574. https://doi.org/https://doi.org/10.1016/j.engfracmech.2019.106574.

[44] T.T. Nguyen, J. Yvonnet, Q.Z. Zhu, M. Bornert, C. Chateau, A phase field method to simulate crack nucleation and propagation in strongly heterogeneous materials from direct imaging of their microstructure, Eng. Fract. Mech. 139 (**2015**) 18–39. https://doi.org/10.1016/j.engfracmech.2015.03.045.

[45] T.T. Nguyen, J. Yvonnet, M. Bornert, C. Chateau, Initiation and propagation of complex 3D networks of cracks in heterogeneous quasi-brittle materials: Direct comparison between in situ testing-microCT experiments and phase field simulations, J. Mech. Phys. Solids. 95 (**2016**) 320–350. https://doi.org/https://doi.org/10.1016/j.jmps.2016.06.004.

[46] K. Oshima, T. Takaki, M. Muramatsu, Development of multi-phase-field crack model for crack propagation in polycrystal, Int. J. Comput. Mater. Sci. Eng. 03 (**2014**) 1450009. https://doi.org/10.1142/S2047684114500092.

[47] J.D. Clayton, J. Knap, Phase field modeling of directional fracture in anisotropic polycrystals, Comput. Mater. Sci. 98 (**2015**) 158–169. https://doi.org/https://doi.org/10.1016/j.commatsci.2014.11.009.

[48] J.D. Clayton, Modeling Deformation and Fracture of Boron-Based Ceramics with Nonuniform Grain and Phase Boundaries and Thermal-Residual Stress, Solids. 3 (**2022**) 643–664. https://doi.org/10.3390/solids3040040.

[49] Z. Tomić, N. Gubeljak, T. Jarak, T. Polančec, Z. Tonković, Micro - and macromechanical properties of sintered steel with different porosity, Scr. Mater. 217 (**2022**) 114787. https://doi.org/https://doi.org/10.1016/j.scriptamat.2022.114787.

[50] Z. Tomić, K. Jukić, T. Jarak, T.A. Fabijanić, Z. Tonković, Phase-Field Modeling of Fused Silica Cone-Crack Vickers Indentation, Nanomater. . 12 (**2022**). https://doi.org/10.3390/nano12142356.

[51] Z. Tomić, T. Jarak, T. Lesičar, N. Gubeljak, Z. Tonković, Modelling of Fatigue Microfracture in Porous Sintered Steel Using a Phase-Field Method, Materials (Basel). 16 (**2023**). https://doi.org/10.3390/ma16114174.

[52] Z. Tomić, T. Jarak, P. Benjamin, Z. Tonkovic, On extracting stress-strain curves of porous multi-phase sintered steels by microindentation, Exp. Tech. *accepted for publication*.

[53] Höganäs, Iron and steel powders for sintered components: Höganäs Handbook for Sintered Components, **2017**.

[54] K. Seleš, Numerical Phase-Field Modeling of Damage in Heterogeneous Materials, University of Zagreb, **2020**.

[55] D.J. Magagnosc, J.P. Ligda, T. Sano, B.E. Schuster, Femtosecond laser machining of micro-tensile specimens for high throughput mechanical testing, in: L. Starman, J. Hay (Eds.), Conf. Proc. Soc. Exp. Mech. Ser., Springer International Publishing, Cham, **2018**: pp. 7–9. https://doi.org/10.1007/978-3-319-63405-0_2.

[56] ISO 14577-1 Metallic materials - Instrumented indentation test for hardness and materials parameters, **2002**.

[57] H. Hertz, Ueber die Berührung fester elastischer Körper., 1882 (**1882**) 156–171. https://doi.org/doi:10.1515/crll.1882.92.156.

[58] K.L. Johnson, Contact Mechanics, Cambridge University Press, Cambridge, **1985**. https://doi.org/DOI: 10.1017/CBO9781139171731.

[59] J.L. Bucaille, S. Stauss, E. Felder, J. Michler, Determination of plastic properties of metals by instrumented indentation using different sharp indenters, Acta Mater. 51 (**2003**) 1663–1678.

[60] D. Tabor, The Hardness of Metals, 1st ed., Oxford University Press, Londkon, **1951**.

[61] E.G. Herbert, W.C. Oliver, G.M. Pharr, On the measurement of yield strength by spherical indentation, Philos. Mag. 86 (**2006**) 5521–5539. https://doi.org/10.1080/14786430600825103.

[62] A. Ruiz-Moreno, P. Hähner, F. Fumagalli, V. Haiblikova, M. Conte, N. Randall, Stress−strain curves and derived mechanical parameters of P91 steel from spherical nanoindentation at a range of temperatures, Mater. Des. 194 (**2020**) 108950. https://doi.org/https://doi.org/10.1016/j.matdes.2020.108950.

[63] Z.S. Courtright, N.P. Leclerc, H.N. Kim, S.R. Kalidindi, Critical Comparison of Spherical Microindentation, Small Punch Test, and Uniaxial Tensile Testing for Selective Laser Melted Inconel 718, Appl. Sci. . 11 (**2021**). https://doi.org/10.3390/app11031061.

[64] A.R.H. Midawi, N. Huda, C.H.M. Simha, A.P. Gerlich, Characterization of Anisotropy of Strength in API-X80 Line Pipe Welds Through Instrumented Indentation, Metallogr. Microstruct. Anal. 9 (**2020**) 884–894. https://doi.org/10.1007/s13632-020-00693-8.

[65] N. Millan-Espitia, S. Mohan, A.L. Pilchak, S.R. Kalidindi, Mechanical Responses of Primary-α Ti Grains in Polycrystalline Samples: Part I—Measurements of Spherical Indentation Stress–Strain Curves, Integr. Mater. Manuf. Innov. 10 (**2021**) 82–98. https://doi.org/10.1007/s40192-021-00203-w.

[66] K. Jeong, H. Lee, O.M. Kwon, J. Jung, D. Kwon, H.N. Han, Prediction of uniaxial tensile flow using finite element-based indentation and optimized artificial neural networks, Mater. Des. 196 (**2020**) 109104. https://doi.org/https://doi.org/10.1016/j.matdes.2020.109104.

[67] K. Seleš, F. Aldakheel, Z. Tonkovic, J. Sorić, P. Wriggers, A General Phase-Field Model for Fatigue Failure in Brittle and Ductile Solids, (n.d.).

[68] Abaqus 6.14-1, Dassault Systems Simulia Corp., Providence, RI, USA, (**2014**).

[69] G. Li, B.B. Yin, L.W. Zhang, K.M. Liew, Modeling microfracture evolution in heterogeneous composites: A coupled cohesive phase-field model, J. Mech. Phys. Solids. 142 (**2020**) 103968. https://doi.org/https://doi.org/10.1016/j.jmps.2020.103968.

[70] A.M. Boyce, E. Martínez-Pañeda, A. Wade, Y.S. Zhang, J.J. Bailey, T.M.M. Heenan, D.J.L. Brett, P.R. Shearing, Cracking predictions of lithium-ion battery electrodes by X-ray computed tomography and modelling, J. Power Sources. 526 (**2022**) 231119. https://doi.org/https://doi.org/10.1016/j.jpowsour.2022.231119.

[71] A. Yin, X. Yang, G. Zeng, H. Gao, Fracture simulation of pre-cracked heterogeneous asphalt mixture beam with movable three-point bending load, Constr. Build. Mater. 65 (**2014**) 232–242. https://doi.org/https://doi.org/10.1016/j.conbuildmat.2014.04.119.

[72] A. Yin, X. Yang, C. Zhang, G. Zeng, Z. Yang, Three-dimensional heterogeneous fracture simulation of asphalt mixture under uniaxial tension with cohesive crack model, Constr. Build. Mater. 76 (**2015**) 103–117. https://doi.org/https://doi.org/10.1016/j.conbuildmat.2014.11.065.

[73] T.T. Nguyen, J. Yvonnet, M. Bornert, C. Chateau, Initiation and propagation of complex 3D networks of cracks in heterogeneous quasi-brittle materials: Direct comparison between in situ testing-microCT experiments and phase field simulations, J. Mech. Phys. Solids. 95 (**2016**) 320–350. https://doi.org/https://doi.org/10.1016/j.jmps.2016.06.004.

[74] Y.J. Cao, W.Q. Shen, J.F. Shao, W. Wang, A novel FFT-based phase field model for damage and cracking behavior of heterogeneous materials, Int. J. Plast. 133 (**2020**) 102786. https://doi.org/https://doi.org/10.1016/j.ijplas.2020.102786.

[75] ASTM E8, ASTM E8 - Standard Testing Methods for Tension Testing of Metallic Materials, Am. Soc. Test. Mater. (**2016**).

[76] Z. Tomić, Z. Tonković, T. Jarak, N. Gubeljak, The 2D microcrack phase-field modelling of sintered steel, in: 11th Eur. Solid Mech. Conf., Galway, Ireland, **2022**.

[77] G.R. ANSTIS, P. CHANTIKUL, B.R. LAWN, D.B. MARSHALL, A Critical Evaluation of Indentation Techniques for Measuring Fracture Toughness: I, Direct Crack Measurements, J. Am. Ceram. Soc. 64 (**1981**) 533–538. https://doi.org/https://doi.org/10.1111/j.1151-2916.1981.tb10320.x.

[78] T. Aleksandrov Fabijanić, D. Ćorić, M. Šnajdar Musa, M. Sakoman, Vickers indentation fracture toughness of near-nano and nanostructured WC-Co cemented carbides, Metals (Basel). 7 (**2017**). https://doi.org/10.3390/met7040143.

[79] S.-W. Jeon, K.-W. Lee, J.Y. Kim, W.J. Kim, C.-P. Park, D. Kwon, Estimation of Fracture Toughness of Metallic Materials Using Instrumented Indentation: Critical Indentation Stress and Strain Model, Exp. Mech. 57 (**2017**) 1013–1025. https://doi.org/10.1007/s11340-016-0226-2.

[80] E. Alabort, D. Barba, R.C. Reed, Design of metallic bone by additive manufacturing, Scr. Mater. 164 (**2019**) 110–114. https://doi.org/https://doi.org/10.1016/j.scriptamat.2019.01.022.

[81] Z. Tomić, T. Jarak, Z. Tonković, Stress-strain curve in sharp and spherical indentation: a comparative study [Submitted for publication], **2022**.

[82] K. Seleš, Abaqus Code for a Residual Control Staggered solution Scheme for the Phase-Field Modeling of Brittle Fracture, (**2019**). https://data.mendeley.com/datasets/p77tsyrbx2/3.

[83] K. Seleš, T. Lesičar, Z. Tonković, J. Sorić, A Phase Field Staggered Algorithm for Fracture Modeling in Heterogeneous Microstructure, Key Eng. Mater. 774 (**2018**) 632–637. https://doi.org/10.4028/www.scientific.net/kem.774.632.

[84] K. Seleš, Numerical phase-field modeling of damage in heterogeneous materials, University of Zagreb, **2020**.

[85] G.A. Francfort, J.J. Marigo, Revisiting brittle fracture as an energy minimization problem, J. Mech. Phys. Solids. 46 (**1998**) 1319–1342. https://doi.org/10.1016/s0022-5096(98)00034-9.

[86] P. Carrara, M. Ambati, R. Alessi, L. De Lorenzis, A framework to model the fatigue behavior of brittle materials based on a variational phase-field approach, Comput. Methods Appl. Mech. Eng. 361 (**2020**) 29. https://doi.org/10.1016/j.cma.2019.112731.

[87] C. Miehe, L.M. Schanzel, H. Ulmer, Phase field modeling of fracture in multi-physics problems. Part I. Balance of crack surface and failure criteria for brittle crack propagation in thermo-elastic solids, Comput. Methods Appl. Mech. Eng. 294 (**2015**) 449–485. https://doi.org/10.1016/j.cma.2014.11.016.

[88] K. Seleš, F. Aldakheel, Z. Tonković, J. Sorić, P. Wriggers, A general phase-field model for fatigue failure in brittle and ductile solids, Comput. Mech. 67 (**2021**) 1431–1452. https://doi.org/10.1007/s00466-021-01996-5.

[89] S. Bruns, The Indentation Densification and Cracking Behavior of Fused Silica, **2020**.

[90] B.R. Lawn, A.G. Evans, A model for crack initiation in elastic/plastic indentation fields, J. Mater. Sci. 12 (**1977**) 2195–2199. https://doi.org/10.1007/BF00552240.

[91] M. Doroszko, A. Seweryn, Numerical modelling of the mesofracture process of sintered 316L steel under tension using microtomography, Eng. Fract. Mech. 255 (**2021**) 107965. https://doi.org/https://doi.org/10.1016/j.engfracmech.2021.107965.

CURRICULUM VITAE

Zoran Tomić was born 7th of January 1995 in Tomislavgrad, Bosnia and Herzegovina. In 2014, he finished High school Marko Marulić in Tomislavgrad after which he enrolled to University of Zagreb, Faculty of Mechanical Engineering and Naval Architecture. He defended his master thesis in 2019 under the title ‘’Numerical modelling of deformation processes of porous connector housing’’ under the supervision of Prof. Zdenko Tonković, PhD. and Yazaki Europe Ltd. where he worked for more than a year as a part-time employee. During his master studies he received the Rector’s award for individual scientific and research work under supervision of Prof. Igor Karšaj, PhD.

In February 2020 he started working as a Research Assistant at the Faculty of Mechanical Engineering and Naval Architecture (University of Zagreb) on a scientific project ‘’Multiscale Numerical Modelling and Experimental Investigation of Aging Processes in Sintered Structural Components’’ led by Prof. Zdenko Tonković, PhD. The project was realized with collaboration with University of Maribor (Slovenia) where he spent one month as a visiting student. Also, he participated as researcher in another project “Nanostructured hardmetals - New challenges for Powder Metallurgy” led by Tamara Aleksandrov Fabijanić, PhD.

In his scientific domain, he authored and co-authored five scientific papers published in high cited journals and more than ten as part of international or domestic conferences.

PAPER 1.

Reproduced with permission.

Authors:	Zoran Tomić, Nenad Gubeljak, Tomislav Jarak, Tomislav Polančec, Zdenko Tonković
Title:	Micro - and macromechanical properties of sintered steel with different porosity
Journal:	Scripta Materialia
Quartile/Impact Factor	Q1/6.302
Bibliography data:	Volume 217, Year 2022, 114787, ISSN 1359-6462
DOI:	https://doi.org/10.1016/j.scriptamat.2022.114787

Scripta Materialia 217 (2022) 114787

Contents lists available at ScienceDirect

Scripta Materialia

journal homepage: www.journals.elsevier.com/scripta-materialia

Micro - and macromechanical properties of sintered steel with different porosity

Zoran Tomić [a,*], Nenad Gubeljak [b], Tomislav Jarak [c,1], Tomislav Polančec [a], Zdenko Tonković [a]

[a] University of Zagreb, Faculty of Mechanical Engineering and Naval Architecture, Croatia
[b] University of Maribor, Faculty of Mechanical Engineering, Slovenia
[c] ITAP, School of Industrial Engineering, University of Valladolid, Spain

ARTICLE INFO

Keywords:
Sintering
Multiphase material
Porous material
Microindentation
Tension test

ABSTRACT

To assess the behaviour of porous materials, it is important to consider the influence of material microstructure. In this study, a multiscale experimental analysis is conducted to investigate the influence of micromechanical parameters, such as the material properties of metallic phases and porosity, on the macromechanical properties of a porous sintered steel. At the microlevel, indentation is conducted to identify microphases and metallographic analysis has been used on mesoscale to measure porosity. Tension uniaxial tests have been applied to characterize macro properties. The results of the tests suggest that the macromechanical properties of porous sintered metallic materials might be mostly influenced by the porosity, while at the microlevel no significant variation in the mechanical properties of microphases has been detected in samples with different density, i.e., porosity. In addition, porosity is related to the sintering density experimentally and an empirical expression that relates density and porosity is proposed.

Sintered materials (or powder metallurgy-PM) are popular materials with advanced micro/macromaterial properties. Porous sintered steels is often used in gear manufacturing, especially in electrified vehicles, where good noise and vibration damping, as well as mass reduction, are beneficial [1,2]. There is an increased demand for a low NVH (noise--vibration-hardness) ratio, especially in the powertrain usage, due to the awareness of the harmful effects of ambient noise and higher living standards, especially in urban areas [2,3]. In the recent years, nanostructured sintered materials are gaining more attention because of high hardness and good wear properties. However, even though sintering is becoming more advanced and theoretical densities can be achieved, the residual porosity presents a problem in dynamically loaded machine parts because it reduces the fracture and fatigue resistance of sintered materials.

Irregular pores appearing in the sintered materials are usually interconnected [4,5], especially in heterogeneous materials with low density. Chawla et al. [6] conclude that in the samples with a porosity level higher than 5% the pores tend to be interconnected, with up to 90% of the pore volume connected into a single pore. The localisation of the micro-cracks takes place at the boundaries of pores and during the further deformation process the pores coalesce and form a larger crack [7]. Different authors [5,8,9] calculate a porosity level from a sintered density and a theoretical density of metallic powder, with an assumption that micromechanical properties do not depend on density. Their investigation of the dependence of macroproperties on material density has shown a drastic reduction of strength properties with the density decrease, leading to the conclusion that macroproperties are mostly affected by porosity. In the present paper, the validity of the generally accepted assumption that micromechanical properties do not depend on density has been investigated by measuring the micromaterial properties of different metallic microphases in a sintered steel of different density.

For this study, sample batches of three different densities were compacted and sintered from identical metallic powder, the low-prealloyed steel powder Astaloy™ Mo+0,2C produced by Höganäs AB, Sweden [10]. The uniaxial samples (Fig. 1a) are manufactured in three densities compacted with corresponding pressures:7.1 g/cm^3 under the pressure of 600 MPa, 6.8 g/cm^3 at the pressure of 440 MPa, and 6.5 g/cm^3 under the pressure of 360 MPa. After compacting, sintering is conducted at 1120°C for half an hour. Finally, the samples are cooled

* Corresponding author at: Institute of Applied Mechanics, Faculty of Mechanical Engineering and Naval Architecture, University of Zagreb, Ivana Lučića 5, 10002, Zagreb, Croatia.
E-mail address: zoran.tomic@fsb.hr (Z. Tomić).
[1] Permanent address: tomislav.jarak@fsb.hr, University of Zagreb, Faculty of Mechanical Engineering and Naval Architecture, Croatia

https://doi.org/10.1016/j.scriptamat.2022.114787
Received 23 March 2022; Received in revised form 29 April 2022; Accepted 29 April 2022

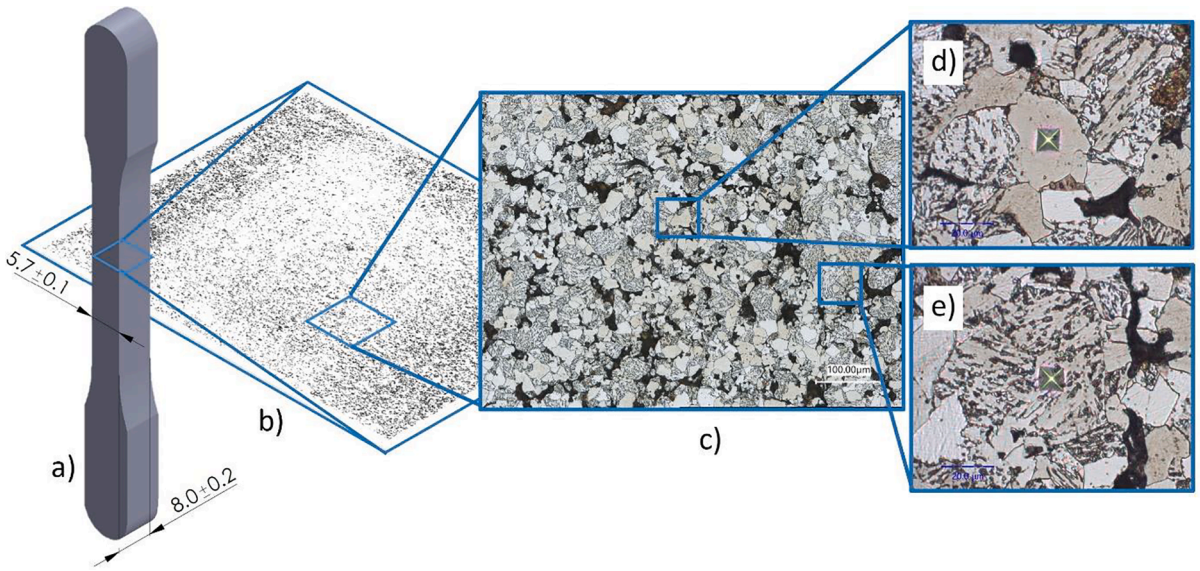

Fig. 1. Sintered sample, a) uniaxial sample according to ASTM E8, b) irregular porosity distribution, c) etched heterogeneous representation, d) Vickers indent in ferrite phase, e) Vickers indent in bainite phase.

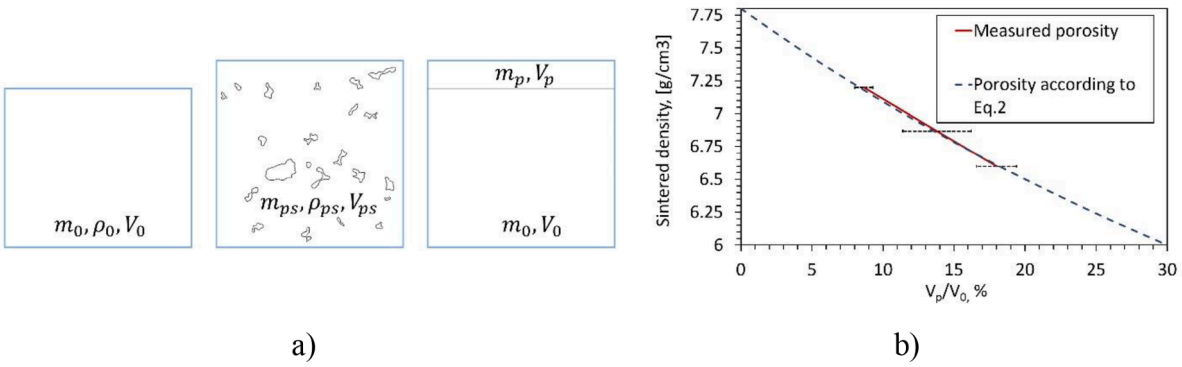

Fig. 2. a) theoretical volumes for bulk material without pores (left) and porous sample (middle and right), b) porosity distribution in relation to sintered density.

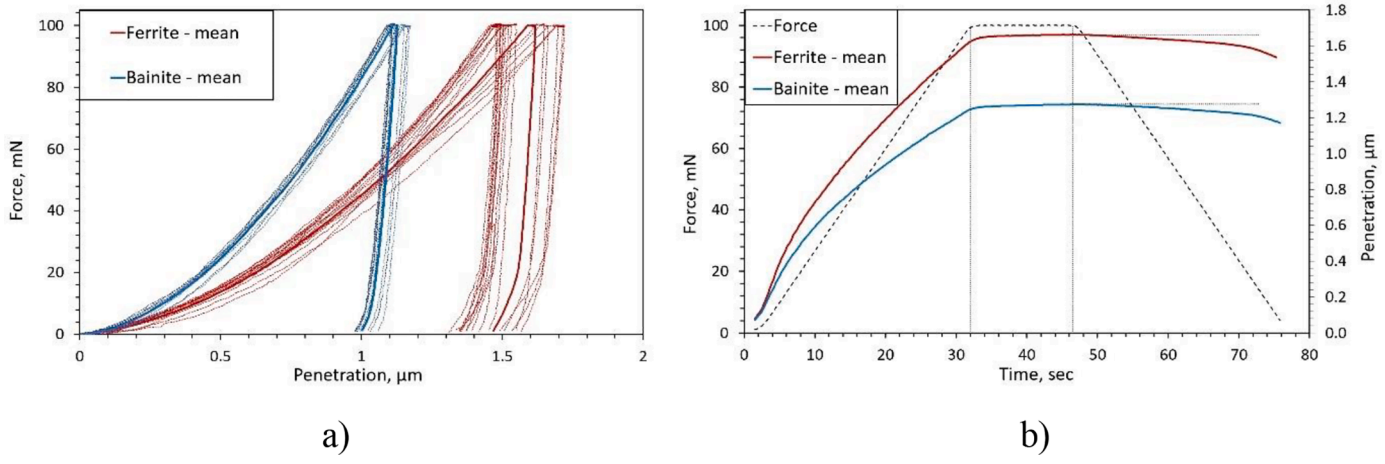

Fig. 3. Indentation curves for ferrite and bainite on three different densities, a) force-penetration curves with minimum/maximum deviation, b) comparison of ferrite and bainite mean penetration-time curves with corresponding force-time characteristic.

first to 70°C and then to room temperature (25°C) in duration of approximately 40 min. The theoretical density of the Astaloy metallic powder is 7.8 g /cm^3[10]. The geometry of the samples (Fig. 1a) corresponds to the one recommended by ASTM E8 for PM samples [11].

First, the metallography analysis was performed to acquire the material microstructure and assess porosity, and then the instrumented indentation method was undertaken on the microscale. Macromechanical strength properties were investigated by the uniaxial tension

Table 1
Micromechanical properties of sintered steel with different densities where k_p, k_f and k_b are porosity and ferrite volume ratio, respectively.

Sintered density, g/cm^3	Phase volume fraction, %			Microproperties			
	Porosity, $k_p = V_p/V_0$	Ferrite, k_f=V_f/V_0	Bainite, $k_b = 1\text{-}k_f$	Ferrite Modulus of elasticity, GPa	Bainite	Ferrite Vickers hardness, HV	Bainite
6.5	20	33 ±2.5	1-k_f	185.3 ± 29.5	238.4 ± 29.6	147 ± 5.9	290.8 ± 21.4
6.8	14.7	30 ±3.7	1-k_f	189.1 ± 22.8	240 ± 17.2	148.7 ± 15.4	285.5 ± 20.2
7.1	9,9	31±4.1	1-k_f	183.6 ± 20.7	238 ± 22.4	146.1 ± 10.2	296.6 ± 12.5

Table 2
Macromechanical properties obtained by indentation and uniaxial tests.

Sintered density, g/cm^3	Porosity (V_p/V_0), %	Macroproperties		
		Modulus of elasticity, GPa	Yield stress, MPa	Tensile strength, MPa
6.5	20	98.2 ± 4.1	218.9 ± 8.7	269.8 ± 9.4
6.8	14.7	115.1 ± 12.1	242.5 ± 11.6	326.7 ± 12.2
7.1	9,9	131 ± 12.3	369.0 ± 26.9	471.7 ± 16.5

test.

The metallography samples are prepared by mechanical polishing. Different sanding papers are used for polishing, and in the final steps the sanding 3μm diamond paste and 0.03μm fluid are applied. The samples are immersed in 3% Nital etching fluid for a few seconds to reveal the heterogeneous microstructure. The metallographic images reveal two phases (or one phase and one pseudophase): ferrite and bainite. A typical ferrite phase has an approximate size of around 30μm, while a typical bainite phase measures around 70μm. Also, it is visible (Fig. 1d and 1e) that a ferrite phase possesses a homogenous structure, while a bainite phase is distinctly heterogeneous (it contains the lamellas of iron carbide (FeC)).

Before the property identification, the porosity in the samples is calculated and measured using metallography images. A simple empirical approach that relates density and porosity is applied. Here, the volume (2D or 3D) of bulk material without pores (Fig. 2a left) is denoted by V_0 and its corresponding density by ρ_0, while the volume, density and mass of porous sample are denoted by V_{ps}, ρ_{ps} and m_{ps} (Fig. 2a middle), respectively. In addition, the total volume of pores is defined as V_p, with ρ_p and m_p as the total density and mass of the pore volume V_p, respectively (Fig. 2a right). Now it is assumed that the mass of the pores m_p is zero since the pores contain nothing but air. The second assumption is based on the premise that a building material of the steel (pore-free) sample is the same as a building material of the porous sample (Fig. 2a middle). In addition, as proposed by Bocchini [12], it is assumed that the pressure applied during compacting does not influence the volume of individual grains of powder and that the change in the density of the sintered material should be associated with the decrease of voids volume during compacting. Here we state in passing that this assumption corresponds to the widely used fact that material microstructural phases do not change density nor mechanical properties during the sintering process, as shown by our experimental results. We can then write for the density

$$\rho_0 = \frac{m_0}{V_0} \Rightarrow m_0 = \rho_0 \cdot V_0, \qquad \rho_{ps} = \frac{m_{ps}}{V_{ps}} = \frac{m_0 + \overline{)m_p}}{V_0 + V_p}. \tag{1}$$

The combination of these two equations gives us the porosity definition as a volume ratio (the volume of pores V_p to the volume of material without pores V_0) denoted as

$$\frac{V_p}{V_0} = \frac{\rho_0}{\rho_{ps}} - 1 \tag{2}$$

We can plot this relation as shown in Fig. 2b.

To validate the proposed empirical approach, a set of panoramic high-resolution metallographic images is analysed in the samples of different porosity. The Keyence® 4K microscope is used to record and collect a number of high-resolution images on a different cross- and longitudinal sections, which are analysed and segmented with the ImageJ® software and Fiji extension. The average scanned area was 5-6 mm^2. Then, the segmented binary images are analysed, and porosity is calculated according to Eq. (2). In addition, the ferrite and bainite volume percentage is calculated in a similar manner. The results show

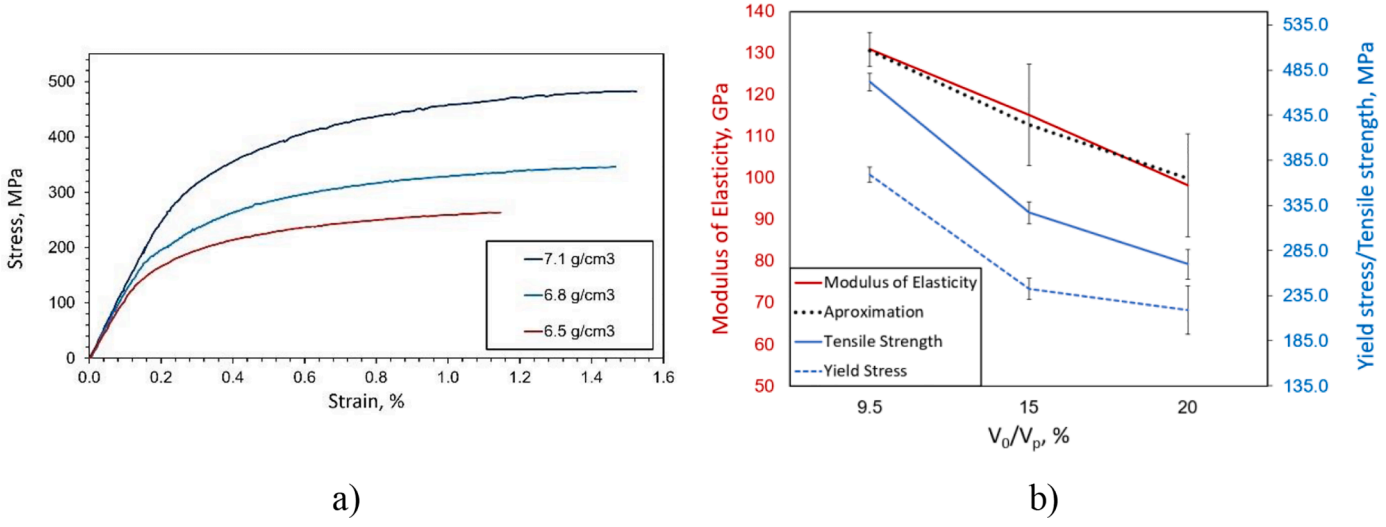

Fig. 4. Macroscopic uniaxial tensile properties, a) stress-strain curves, b) macroproperties in relation to sample porosity.

ferrite volume percentage in the range from 30-35% while the rest belongs to bainite, excluding the porosity percentage. We decided not to use the Microcomputed Tomography (CT) for determining porosity because the value of the greyscale threshold in CT drastically influences the porosity leading to unreliable results for porosity in the considered sintered metal [13–15]. The results of the porosity analysis, performed by using samples with three different densities, are shown in Fig. 2b where the red line (measured porosity) follows the theoretical trend, including the corresponding standard deviation. The scattering of the measured porosity is caused by the irregular distribution of porosity across a considered section (Fig. 1b).

To acquire the micromechanical properties of the sintered samples, instrumented indentation on the microscale is used. The measurements are conducted on a Micro Combi Tester by Anton Paar using the Vickers indenter. Due to large porosity, there is a high probability that a pore will be positioned under the considered phase. For that reason, the indentation forces are kept relatively low: 100 mN with a loading and unloading rate of 200 mN/min, held at the maximum force for 20 s. The characterisation force is kept the same for both phases to avoid the influence of the size effect. At lower forces heterogeneity effects of the bainite grain could not be captured, leading to an overly large scattering of the indentation results. On the other hand, the application of higher forces would lead to an indent positioned close to phase boundaries, invoking the influence of boundary effects. In addition, to further minimize the influence of phase boundaries, all indentations are conducted as far away from the visible pores as possible and in phases of similar, large size. A minimum of 20 indentations per phase is conducted for all sample densities. Before performing the indentation on the considered sintered metal, the indenter was calibrated on a fused silica sample with certified values. The indentation curves for both phases are presented in Fig. 3a, and encompass the results obtained from all samples, regardless of density. Fig. 3b shows comparison of ferrite and bainite mean penetration-time curves with the corresponding force-time characteristic.

As visible from Fig. 3, bainite has a stiffer response than ferrite, mostly because of the presence of FeC. The indentation curves imply a significant plastic deformation of both phases, i.e., the elastic to plastic work ratio is very small (less than 5%). This means that both microstructural phases, ferrite and bainite, have distinct nonlinear behaviour. The greater scattering of the ferrite indentations is likely caused by the phase boundary influence, which is more pronounced in smaller ferritic phases. Also, from the metallographic images, it is noticed that the ferrite phases usually form near the pores, which might further contribute to the scattering of ferrite measurement results. Even though all indents are located inside the phase boundaries, conditions below the considered phase are unknown, and the compacting of a pore located underneath the phase may influence the penetration of the indenter.

The results in Table 1 show that there is almost no difference between elastic (reduced) modulus across different density samples in both ferrite and bainite. However, like with the indentation curves (Fig. 3), one can spot a noticeable standard deviation between individual indents (Fig. 3a). As mentioned before, a pore located underneath an examined material phase may significantly contribute to such scattering since there is a high probability of such an event due to high porosity. Madej et al. [16] suggest that lower characterisation forces be used for porous materials in order to avoid the porosity influence, but since a significant noise occurs at lower forces and due to reasons described above, here the characterisation force is kept at 100 mN.

Furthermore, macroscopic quasistatic tensile tests are conducted on the Instron servo-hydraulic machine. All specimens are tested in the strain-controlled loop with the strain rate of 1 mm/min and the DIC GOM® Aramis™ 12M system. The elastic modulus at the macrolevel is determined as a slope of the linear part of the stress-strain curve for a material under tension. Mean values (Table 2) for the stress-strain curves (Fig. 4a) are extrapolated from the results obtained from 8-9 samples per density.

The curves show that the porosity increase leads to a significant drop in the considered macroscopic mechanical properties (Fig. 4b). It is important to emphasise that the macroscopic response of all tested samples demonstrated a distinct brittle behaviour with a strain hardening. One can also notice that the strain at failure increases with the increase of density.

A significant degressive characteristic in macromechanical properties with the increase of porosity is also noticed by other authors [5,9,17,18]. A recent review by Ternero et al. [19] also shows a linear decrease in the elastic modulus (for porosities up to 30%) and a nonlinear decrease for other mechanical strength properties. The macroscale (effective) behaviour of elastic modulus (E_{eff}) can be easily described with a simple linear equation which includes the microscale elastic moduli gained by the indentation of ferrite and bainite and the porosity percentage, as follows

$$E_{\text{eff}} = \left[k_{\text{f}} \cdot E_{\text{f}} + k_{\text{b}} \cdot E_{\text{b}}\right] \cdot \left(1 - \left(k_{\text{p}}\right)^{c}\right) \tag{3}$$

where $k_{\text{f}}, E_{\text{f}}, k_{\text{b}}, E_{\text{b}}$ are ferrite or bainite volume ratios and elastic moduli, respectively, while k_{p} is the sample porosity (V_{p}/V_0) and c is an arbitrary non-zero constant factor. Using the obtained values of elastic moduli (Table 2), assuming $c = 0.34$, the macroscale elastic modulus for different densities can be approximated using this novel proposed equation (Eq. 3), as shown in Fig. 4b (black dashed line).

A comparison of results obtained at the material micro- and macro scale leads to a conclusion that porosity is indeed the main influence factor for the decrease of the mechanical strength properties in the examined sintered metal because the mechanical properties of both microstructural phases remain almost constant, regardless of three considered densities. These findings confirm that the use of the empirical equation (3) and similar approaches used by other authors is indeed justified. In addition, even though the properties of the ferrite and bainite phases might be distinctly elastoplastic, as visible from the indentation curves, the macrobehaviour of the considered sintered steels is still quite brittle, probably due to a large porosity. Additionally, the effective (macro) elastic modulus of porous material can be related to the measured indentation (micro) moduli of different phases of heterogeneous material and porosity by a novel, simple linear function proposed herein. It is interesting to note here that the 3D printing of metallic components is based on a metal powder similar to the one at sintered metallurgy. In future research, the presented conclusion will be verified by numerical multiscale modelling of sintered materials which will also include fracture phenomena.

Declaration of competing interest

The authors declare that they have no known competing financial interests or personal relationships that could have appeared to influence the work reported in this paper.

Acknowledgment

This work has been fully supported by Croatian Science Foundation under the project “Multiscale Numerical Modelling and Experimental Investigation of Aging Processes in Sintered Structural Components” (MultiSintAge, PZS-1 2019-02-4177) and Slovenian research agency ARRS for part of the research supported by Program P2-0137 “Numerical and Experimental Analysis of Nonlinear Mechanical Systems”.

References

[1] C. Brecher, C. Löpenhaus, M. Schroers, T. Frech, P. Scholzen, Optimization of NVH behavior of gears by alternative gear materials, Int. Conf. Gears 2017 2 Bände (2017) 539–552.
[2] T. Frech, P. Scholzen, P. Schäflein, C. Löpenhaus, P. Kauffmann, F. Klocke, Procedia CIRP 70 (2018) 186–191.
[3] K.F. Steinberg, With all senses: the first book on how to eliminate interfering sound in the car, wjr-Verlag (2007).

[4] E. Dudrova, M. Kabátova, Powder Metall 59 (2016) 148–167.
[5] A. Falkowska, A. Seweryn, Int. J. Fatigue 117 (2018) 496–510.
[6] N. Chawla, J. Williams, X. Deng, C. McClimon, Int. J. Powder Met 45 (2009) 19–27.
[7] S.J. Polasik, J.J. Williams, N. Chawla, Metall. Mater. Trans. A. 33 (2002) 73–81.
[8] M. Doroszko, A. Seweryn, Mater. Sci. Eng. A. 689 (2017) 142–156.
[9] A. Ataee, Y. Li, M. Brandt, C. Wen, Acta Mater. 158 (2018) 354–368.
[10] Höganäs, Iron and steel powders for sintered components: Höganäs Handbook for Sintered Components (2017).
[11] ASTM E8, Am. Soc. Test. Mater. (2016).
[12] G.F. Bocchini, SAE Trans. 95 (1986) 790–805.
[13] M. Doroszko, A. Seweryn, Acta Mech. Autom. 9 (2015) 70–74.
[14] R. Kopp, J. Joseph, X. Ni, N. Roy, B.L. Wardle, Adv. Mater. 34 (2022), 2107817.
[15] E. Beckers, E. Plougonven, C. Roisin, S. Hapca, A. Léonard, A. Degré, Geoderma. 219-220 (2014) 145–154.
[16] L. Madej, A. Legwand, M. Setty, M. Mojzeszko, K. Perzyński, S. Roskosz, J. Chrapoński, Arch. Civ. Mech. Eng. 22 (2021) 21.
[17] T. Uhlířová, W. Pabst, Scr. Mater. 159 (2019) 1–4.
[18] E. Alabort, D. Barba, R.C. Reed, Scr. Mater. 164 (2019) 110–114.
[19] F. Ternero, L.G. Rosa, P. Urban, J.M. Montes, F.G. Cuevas, Met. 11 (2021).

PAPER 2.

Reproduced with permission.

Authors:	Zoran Tomić, Krešimir Jukić, Tomislav Jarak, Tamara Aleksandrov Fabijanić, Zdenko Tonković
Title:	Phase-Field Modelling of Fused Silica Cone-Crack Vickers Indentation
Journal:	Nanomaterials
Quartile/Impact Factor	Q1/5.719
Bibliography data:	Volume 12, no. 14, Year 2022, 2356
DOI:	https://doi.org/10.3390/nano12142356

nanomaterials

MDPI

Article

Phase-Field Modeling of Fused Silica Cone-Crack Vickers Indentation

Zoran Tomić [1,*], Krešimir Jukić [1], Tomislav Jarak [1,2], Tamara Aleksandrov Fabijanić [1] and Zdenko Tonković [1]

[1] Faculty of Mechanical Engineering and Naval Architecture, University of Zagreb, Ivana Lučića 5, 10000 Zagreb, Croatia; kresimir.jukic@fsb.hr (K.J.); tomislav.jarak@fsb.hr (T.J.); tamara.aleksandrov@fsb.hr (T.A.F.); zdenko.tonkovic@fsb.hr (Z.T.)

[2] ITAP, School of Industrial Engineering, University of Valladolid, Paseo de Cauce 59, 47011 Valladolid, Spain

* Correspondence: zoran.tomic@fsb.hr

Abstract: In this paper, a 3D phase-field model for brittle fracture is applied for analyzing the complex fracture patterns appearing during the Vickers indentation of fused silica. Although recent phase-field models for the fracture caused by the indentation loading have been verified by some simpler academic axis-symmetric examples, a proper validation of such models is still missing. In addition, heavy computational costs, and a complicated compression stress field under the indenter, which demands different energy decompositions, have been identified as the most important impediments for the successful application of the phase-field method for such problems. An adaptive strategy is utilized for reducing the computational costs, and some modifications are introduced, which enable an accurate simulation of the Vickers indentation fracture. Here, the fracture initiation ring outside the contact zone is detected by using different energy decompositions, and the dominant cone-crack formation under the Vickers indenter is observed. Different contact conditions are investigated. The proposed model is validated by experimental measurements, and a quantitative and qualitative comparison between experimental and numerical results is conducted.

Keywords: phase-field modeling; fused silica; Vickers indentation; cone crack

Citation: Tomić, Z.; Jukić, K.; Jarak, T.; Fabijanić, T.A.; Tonković, Z. Phase-Field Modeling of Fused Silica Cone-Crack Vickers Indentation. *Nanomaterials* **2022**, *12*, 2356. https://doi.org/10.3390/nano12142356

Academic Editor: Sam Zhang

Received: 31 May 2022
Accepted: 5 July 2022
Published: 9 July 2022

1. Introduction

In recent years, the instrumented indentation test has gained massive popularity to determine the mechanical behavior of different materials due to its straightforward and standardized experimental procedure. The method requires only a small volume of material for measurement, minimal specimen preparation, and low costs, at the same time enabling the evaluation of the indentation by considering both the force and the displacement during plastic and elastic deformation [1]. By monitoring the complete loading cycle of increasing and removing the test force, a wide range of mechanical properties, such as the Martens hardness (*Ms*), the indentation hardness (H_{IT}), the indentation modulus (E_{IT}), the plane strain modulus (E^*), the indentation creep (C_{IT}), the indentation relaxation (R_{IT}), and the elasto-plastic behavior (work, *W*), can be determined in one measurement [1]. Based on the measurement results, it is possible to construct stress–strain diagrams, which are of great importance for materials and coatings for which the conventional static tensile test is not applicable. In addition to the above-mentioned mechanical properties, by applying higher loads, it is possible to estimate the indentation fracture toughness of the material based on the cracks at the tips of the Vickers indent.

These mechanical quantities are calculated based on the indenter's contact (projected) area. Crucial differences can arise when comparing the actual contact area with the area calculated assuming an ideal indenter geometry, particularly at small, measured indentation depths. These differences occur due to the rounding and wear of the indenter's tip following use. For that reason, it is necessary to determine the actual indenter's contact surface (area) and use it to calculate the material parameters, ensuring the accuracy and repeatability of

the measured values. An indirect way to determine the actual contact area is periodical calibration by utilizing indentations into a material of certified indentation modulus and Poisson's ratio, known as the reference material [1].

The reference materials known as the reference blocks are specially produced to assure the structure's necessary homogeneity, uniformity, and long-term stability. In that way, the homogeneity of mechanical properties is confirmed. Stable temperature and humidity properties, as well as an amorphous molecular structure and an almost pure homogenous microstructure, established the position of the fused silica glass as the most investigated/most used reference material for instrumented indentation tests. Since it has a relatively low modulus of elasticity and Poisson's ratio, fused silica is supremely brittle. According to the calibration certificate, it is not recommended to perform indentations over 100 mN using the Berkovich or Vickers indenter due to cracks that may influence the results. During this research, the indentation forces were increased to initiate a crack on the corner of Vickers indentations.

The crack shapes appearing in brittle materials are related to the indenter shape and to the nature of the material [2]. According to Lee et al. [3], there are five major crack types formed after unloading the sample: radial, lateral, median, half-penny, and Hertzian cone cracks [2]. Independently of the indenter's geometry (sharp Vickers or Berkovich, spherical, flat punch), similar crack patterns can be observed in fused silica, with the preferential mode being a cone crack or other types of median-radial cracking [4]. The initiation of the cone crack is formed on the specimen surface outside the contact zone of the indenter and the fused silica specimen. The propagation of the cone crack has the incline angle, α, in a range from 30°, as reported by Hagan [5], to 45°, as reported by Michel et al. [6]. In addition, it has also been established that the incline angle depends mainly on the Poisson's ratio [7].

Hagan [5] concluded that the cone-crack formation is driven only by the elastic stress during the indentation, and the initiation ring is formed only due to positive (tensile) radial stress outside the contact region [8]. One of the indentation fracture theories presented by Lawn and Evans [9] indicates that medial (radial, half-penny) cracks are driven by the stress nucleation caused by material flaws under the indenter, and that a flaw has to have a finite size to initiate a median crack. These conclusions are compared with our numerical modeling in the following sections.

Currently, for the modeling of the indentation crack nucleation and propagation, the most used numerical approach is the cohesive zone modeling (CZM). Bruns et al. [2] modeled the cracking of fused silica under the Berkovich indenter. The authors proposed using the Drucker-Prager Cap plasticity model, which is able to reproduce elasto-plastic material behavior and the hardening due to material densification. Lee et al. [3] also used CZM to analyze the cracking of a brittle material under a four-sided pyramid (Vickers indenter). The biggest drawback of CZM is that the crack nucleation and propagation directions have to be determined a priori: cracking appears only in the a priori defined cohesive planes. This makes CZM suitable only for capturing the radial or half-penny cracks, but not the cone cracks, which are not planar. Among other possible approaches, the extended finite element method (XFEM) [10] and the peridynamics [11] have been attempted. Although both methods are capable of reproducing complex crack patterns, their usage in 3D modeling is still a daunting task, because they tend to become extremely complex due to problems associated with the crack tracking in XFEM, or a proper definition of internal forces and efficient numerical implementation in peridynamics.

The phase-field (PF) method seems to be an appropriate approach to overcome the latter problems. It does not require ad hoc criteria for the nucleation, propagation, or branching of cracks, and its numerical implementation in the existing FEM codes is relatively simple and straightforward. However, due to high computational costs, mainly caused by the need to use very dense meshes in the regions where damage appears, only 2D models have so far been proposed. In general, it has been shown that one of the main problems in phase-field modeling of the indentation process is accurate modeling of crack

initiation in an otherwise defect-free material. Additional considerable problems include the proper definition of the length scale parameter value or the definition of the crack driving force. Strobl and Seeling [8] proposed a 2D phase-field brittle formulation for the simulation of cone-crack formation under the flat indenter. They have studied various modifications of standard AT1 and AT2 models, which render the phase-field method more suitable for indentation simulations. In doing so, they identified the most important problems and proposed certain conditions that have to be fulfilled by the brittle phase-field models in indentation simulations, such as: using appropriate energy decompositions and crack driving functions to account for the tension-compression behavior and crack boundary conditions, using small length scale parameter values in comparison to characteristic crack dimensions to ensure the accurate capture of crack initiation, defining appropriate degradation functions that prevent erroneous phase-field evolution and ensure the linear response before the initiation of damage, and incorporating the material's tensile strength and fracture toughness as independent material parameters. In their work, they utilized a hybrid approach, where no split is used for the Cauchy stress tensor because the cracks remain opened during the indentation, while the directional split proposed by Steinke and Kaliske [12] is used for the crack driving function to avoid the crack evolution being driven by a compression stress state. Thereby, the crack driving function itself is formulated by using positive principal stresses as it is deemed more appropriate than by using strains. Small values of length parameters had to be used to capture the spontaneous crack initiation, leading to restrictions on the minimal values of the tension strength in their AT2 model. Fourth-order degradation functions were used to ensure the linear elastic response prior to the onset of damage, but such choice compromises the crack propagation to the fully broken state. The overestimation of the surface crack energy, caused by an over-smearing of the phase-field if a relatively large value of length parameter is used, is avoided by a recalibration of the length parameter and yield functions. The irreversibility of the phase-field is ensured by employing the "crack-like" constraint, allowing for irreversibility of the damage before the onset of a well-defined crack. However, such approach does not work well for all simulation setups. Despite all mentioned restrictions, for a certain choice of input variables for which all required conditions are satisfied, their modified model was able to reproduce the main features of cone-crack initiation and propagation: the formation of the initiation ring around the indenter, a vertical crack propagation, and the conical crack propagation with an inclination to the sample surface. Kindrachuk and Klunker [13] used a similar brittle phase-field formulation for the axis-symmetric 2D simulation of spherical indentation to investigate a kinked cone-crack propagation, caused by the changing contact conditions between the propagating spherical indenter and the sample surface. They performed a frictionless contact analysis by employing an ad-hoc crack driving force based on the strain measure, similar to the Beltrami criterion of failure, instead of a stress-based crack driving force. The irreversibility was enforced in a "damage-like" manner by employing a history variable. Only one problem setup was analyzed, and the applicability of the method was not studied in detail. In a very recent work, Wu et al. [14] used an axis-symmetric phase-field cohesive zone model to investigate the flat punch indentation of a homogeneous material with borosilicate glass properties. Therein, the cohesive zone model has been applied to correctly capture the crack nucleation in the otherwise defect-free material. Here, the failure strength can be chosen independently from the fracture toughness by applying the Wu-Nguyen phase-field model for quasi-brittle fracture, where the length parameter is introduced as an independent parameter. This allows for the choice of the length parameter value that is small enough to accurately capture the crack initiation and to prevent the unphysical widening of the damaged zone during the crack propagation. That approach shows impressive potential for correctly capturing all important details of the cracking process caused by the indentation, including the initiation. However, its implementation is more complex than the phase-field models based on the AT2 model, as it requires special solvers for the imposition of the irreversibility condition on the phase-field.

In comparison to the similar phase-field models for the indentation problem, encountered in the available literature, the novelties of the present work are:

- To the authors' knowledge, the present paper represents the first 3D phase-field model of the Vickers indentation fracture to this date.
- An asymmetric model, where the energy decomposition is applied for both the crack driving force and the stress field, is used.
- Contact analysis with friction is applied.

The proposed numerical model is validated by experimental indentation, showing that the formation of a cone crack is accurately predicted by the current model in the Vickers indentation.

The paper is organized as follows. The experimental setup is presented in Section 2. Afterwards, the most important details of the used phase-field formulation are exposed, along with the energy decomposition, which has a significant influence on the indentation modeling. Then, the numerical model is described in detail. In Section 3, the obtained numerical results are compared with the experimental data. Finally, some conclusions are presented in Section 4.

2. Materials and Methods

2.1. Material and Experimental Setup

The experimental instrumented indentation test was conducted on a certified reference material—a round fused silica block (ϕ 25 mm $\times$ 5 mm), produced and certified by Anton Paar, TriTec SA, (Corcelles-Cormondrèche, Switzerland) calibrated by the Berkovich indenter. The measurements were performed on the Micro Combi Tester (MCT^3) produced by Anton Paar, TriTec SA, (Corcelles-Cormondrèche, Switzerland) according to EN ISO 14577-1:2016, at room temperature using a certified Vickers diamond pyramidal indenter. The measurements were performed using different loads. The load of 50 mN was selected to determine the plane strain modulus, E^*, and the indentation modulus, E_{IT}, in accordance with recommendations from the calibration certificate not to perform indentations over 100 mN using the Berkovich or the Vickers indenter. Higher loads could cause cracks that may influence the results. Based on the measurement, it was concluded that the measured values of E^* are in excellent correlation with certified values. The certified and the measured E^*, the certified Poisson's ratio, ν, and the fracture toughness value, K_{IC}, from the literature, used for further phase-field modeling, are shown in Table 1.

Table 1. Material properties of fused silica glass.

Type of Value	Plane Strain Modulus, E^* (MPa)	Poisson's Ratio, ν(-)
Certified value	75,100 $\pm$ 300	0.16
Measured value	74,990	-
SD	1360	-

The fracture toughness, K_{IC}, could not be directly measured by the instrumented indentation test, but it could be calculated by measuring the total length of cracks emanating from the corners of indentations at loads higher then critical force, Pc, at which the first cracks occur. The model used for the calculation of K_{IC} is dependent on the type of crack, median, radial, half-penny, cone, or lateral, using the Palmquist method [15] or the method proposed by Anstis et al. [16]. As mentioned in the Introduction Section, during indentation, the load was increased to determine the critical force, to pinpoint the start of crack formation, and possibly, to calculate K_{IC}.

Such behavior starts to become clearly visible when applying a force of 2000 mN. Finally, the instrumented indentation test was conducted with a load control loop and 2000 mN of force, with the loading and unloading speed of 4000 mN/min and the hold on maximum load for 30 s. The average indentation depth was around 4 µm, and the mean indentation curve is shown in Figure 1 with the displacement resolution of 30 nm.

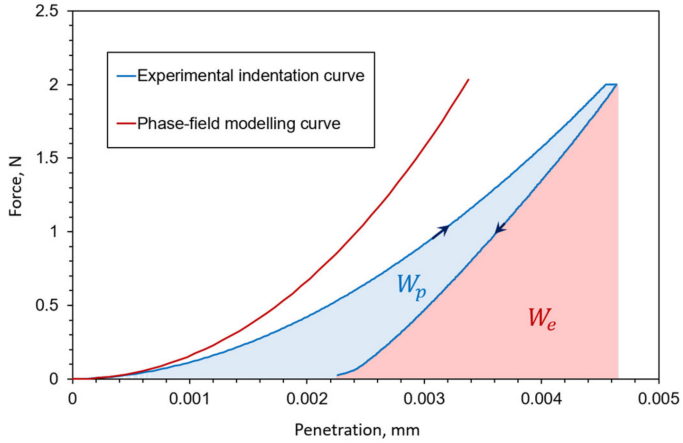

Figure 1. Indentation curve comparison between numerical brittle phase-field formulation and experimental measurement. Area under the experimental indentation curve corresponds to elastic (W_e) and plastic (W_p) indentation work.

Around 15 indentations were conducted, and similar cone-crack patterns were observed (Figure 2). The indentations were optically analyzed on a video microscope and residual indents are presented in Figure 2.

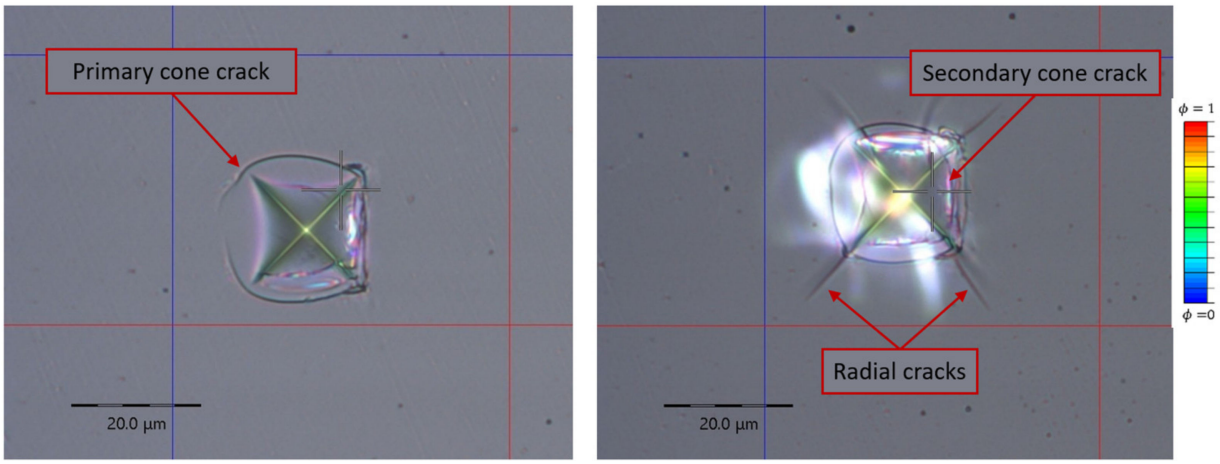

Figure 2. Residual indents and different fracture patterns after Vickers indentation on fused silica glass, (**a**) indent showing only primary cone crack, (**b**) indent with secondary cone crack and radial cracks at the edge of the indent.

The yield strength, σ_y, of fused silica cannot be directly measured from the indentation measurements. Even though different methods for extraction of elasto-plastic parameters from indentation do exist, such as the one for the low-hardening materials proposed by Giannakopoulos et al. [17] and later upgraded by Dao et al. [18], the yield strength of the fused silica is taken from the literature. Bruns et al. [4] concluded from the values obtained by various measurements that the σ_y value of fused silica is in the interval from 4000 to 7000 MPa.

As it will be later explained in detail, the phase-field method is very mesh-dependent, at least with the presented formulation, and mesh dependance is linked to material parameters. This means that the characteristic element length, l, is a function of material properties, $l = f(E, \nu, \sigma_{max})$. Since fused silica is a brittle material, the value of ultimate strength can be taken as the same as the yield strength. For the purposes of this research, σ_{max} has the value of 4000 MPa.

2.2. Numerical Modeling

2.2.1. Phase-Field Formulation

Herein, the brittle phase-field formulation is used [19]. The phase-field approach regularizes the sharp discontinuity with a scalar parameter ϕ, which has the value from 0 to 1, distinguishing between the fractured state ($\phi = 1$) and the intact state ($\phi = 0$). A strain energy degradation function is introduced (in this case a simple quadratic function, Equation (5)) to account for the loss of stiffness due to fracture propagation. In that case, in regions where $\phi = 1$, the stress and stiffness drop to zero. For more details about the phase-field method, see [20–22]. The basic equations of the applied phase-field formulation are presented in Table 2. Here, Ψ is the energy functional of the body occupying a volume, Ω, containing a crack, with Γ as a crack surface. According to Equation (1), the total energy, Ψ, consists of the stored energy, Ψ^b, due to deformation and the energy dissipated in the fracture process, Ψ^s. Therein, ψ_e is the elastic strain-energy density function (Equation (2)), and G_c is the fracture toughness or the critical energy release rate denotes the small strain tensor, defined as the symmetric part of the displacement gradient, $\varepsilon = \mathrm{sym}(\nabla \mathrm{u})$, with u as the displacement field. According to the phase-field method for fracture [23], the functional Ψ can be regularized as in Equation (3), where l is the length scale parameter, which is here chosen to be a material parameter and can be calculated by Equation (7), according to [24]. In Equation (4), $\mathrm{F}^{\mathrm{ext}}$ represents the vector of external forces. The history field, $H(t)$, in Equation (4) is employed instead of ψ_e to prevent the crack "healing".

Table 2. Basic equations of brittle phase-field formulation.

Total Energy Functional	
$\Psi = \Psi^b + \Psi^s = \int_{\Omega/\Gamma} \psi_e(\varepsilon) d\Omega + \int_\Gamma G_c d\Gamma$	(1)
Elastic deformation energy density	
$\psi_e = \frac{1}{2}\lambda tr^2(\varepsilon) + \mu tr(\varepsilon^2)$	(2)
Regularized energy functional	
$\Psi(u,\phi) = \int_\Omega g(\phi)\psi_e(\varepsilon(u)) d\Omega + \int_\Omega \frac{G_c}{2}\left[l(\nabla\phi)^2 + \frac{1}{l}\phi^2\right] d\Omega$	(3)
Governing equations through the principle of virtual work	
$\int_\Omega (1-\phi)^2 \frac{\partial \psi_e(\varepsilon)}{\partial \varepsilon}\delta\varepsilon d\Omega = F^{\mathrm{ext}}\delta u$ $\int_\Omega \left\{ G_c l \Delta\phi\Delta(\delta\phi) + \frac{G_c}{l}\phi\delta\phi \right\} d\Omega = \int_\Omega 2(1-\phi)H(t)\delta\phi d\Omega$ $H(t) := \max_{\tau=[0,t]} \psi_e(\tau)$	(4)
Degradation function	
$g(\phi) = (1-\phi)^2$	(5)
Crack density function (AT2—Ambrosio-Tortorelli [24,25])	
$\gamma(\phi, \nabla\phi) = \frac{1}{2}\left[\frac{1}{l}\phi^2 + l\lvert\nabla\phi\rvert^2\right]$	(6)
Length scale parameter	
$l = \frac{27}{256}\frac{G_C E}{(\sigma^{max})^2}$	(7)

Although in [5,11] the usage of stress-based energy splits is advocated in phase-field numerical simulations, herein, three different strain-based energy splits are tested: two spectral splits, one proposed by Miehe et al. [20] and the other by Freddi [26], and a volumetric-deviatoric split, proposed by Amor et al. [27].

2.2.2. Energy Split

One of the major aspects of the phase-field modeling of fracture is the choice of energy split. It determines the mechanical behavior of the damaged material and enables the simulation of crack closure. Additionally, the energy split determines the way in which the crack grows, as the crack driving force is determined by the energy split. It is important

to emphasize that in real situations, cracks cannot initiate under compressive stress. In its nature, the material during indentation is predominantly in a compressive stress state. From this aspect, the use of an appropriate energy split is the most important part in the process of indentation modeling with the phase-field method.

There exist three basic families of energy splits: the well-established spectral energy splits, spherical-deviatoric energy splits, and the more recently developed directional splits. As noticed in [5,11], in the phase-field indentation simulations, defining a proper energy split is essential for defining the crack driving force to prevent the crack evolution due to compressive stress. On the other hand, so far, no split has been applied for computing the stresses, apparently because in the axis-symmetric cases, such as spherical or flat punch indentation, cracks remain open once they appear. However, for a more general purpose, employing some convenient energy split would be more than beneficial, see, e.g., [9,28,29]. The directional splits are the most promising tools in resolving the problem of crack closure, as the knowledge about crack direction is necessary for its description. Since such splits are relatively new and are still the object of intense research, they are not considered in this work.

Among spherical-deviatoric splits, the most popular one is Amor's split [4], with positive and negative energies defined as:

$$\psi_0^+ = \frac{1}{2}\left(\lambda + \frac{2}{3}\mu\right)\langle \mathrm{tr}\,(\varepsilon)\rangle_+^2 + \mu\varepsilon_D : \varepsilon_D,\ \psi_0^- = \frac{1}{2}\left(\lambda + \frac{2}{3}\mu\right)\langle \mathrm{tr}\,(\varepsilon)\rangle_-^2, \tag{8}$$

where $x_\pm = \frac{1}{2}(x + |x|)$ are the Macaulay brackets, λ and μ are the Lame's constants, while ε_D stands for the deviatoric part of the strain tensor. Despite its popularity, this split has some serious flaws. If a simple uniaxial compressive case is considered, the nonzero deviatoric part of the strain tensor leads to cracking with a fixed compressive-tensile strength ratio. Additionally, nondegraded energy due to the negative strain tensor trace should lead to the transmission of compressive stresses if the specimen is fully broken. However, in most cases, this split cannot transmit any compressive stresses, because for the fully damaged material it does not take the deviatoric strain into consideration, and therefore the material starts to act as a fluid. For those reasons, such split is not a good choice for the simulation of indentation, where the expected contact-induced compressive stresses are high and lead to cracking in the contact zone and to the fluid-like behavior of the material.

Spectral splits utilize a spectral decomposition of the strain/stress tensor to define the positive strain energy. Some notable spectral splits have been proposed by Miehe [20], Freddi [26], Lo [30] (a 3D generalization of the Freddi split), He [31] (the 'orthogonal' split implemented in the phase-field framework by Nguyen [32]), or Wu and Nguyen [33]. In the highly popular split by Miehe, energies are computed as:

$$\psi_0^\pm = \frac{1}{2}\lambda\langle \mathrm{tr}\,(\varepsilon)\rangle_\pm^2 + \mu\mathrm{tr}\left(\varepsilon_\pm^2\right), \tag{9}$$

with positive and negative strain tensor parts, $\varepsilon_\pm$, defined as:

$$\varepsilon_\pm = \sum_{i=1}^{3}\langle\varepsilon_i\rangle_\pm n_i \otimes n_i \tag{10}$$

Herein, $\langle\varepsilon_i\rangle_\pm$ and n_i are the positive/negative eigenvalues and corresponding eigenvectors of the strain tensor. Although this split does not degrade energy related to the negative principal strains, it does not completely prevent cracking in compression, which can be caused by the Poisson's effect. For example, a uniaxial compressive stress state will lead to one negative and two positive principal strains. Those positive principal strains will form a positive strain energy density and will lead to the growth of the phase-field. Consequently, such split is not suitable for contact problems.

In this work, we rely on the spectral split defined by Lo [30]. With the principal strains defined as $\varepsilon_3 \geq \varepsilon_2 \geq \varepsilon_1$, such split is defined by the equations in Table 3.

Table 3. Spectral split energy decomposition main equations, In the table, the well-known formula of the model firstly proposed in [30] are given for completeness.

if $\varepsilon_1 > 0$
$\psi_0^+ = \frac{Ev}{2(1+v)(1-2v)}(\varepsilon_1+\varepsilon_2+\varepsilon_3)^2 + \frac{E}{2(1+v)}(\varepsilon_1^2+\varepsilon_2^2+\varepsilon_3^3), \psi_0^- = 0$ (11)
else if $\varepsilon_2 + v\varepsilon_1 > 0$
$\psi_0^+ = \frac{Ev}{2(1+v)(1-2v)}(\varepsilon_3+\varepsilon_2+2v\varepsilon_1)^2 + \frac{E}{2(1+v)}\left((\varepsilon_3+v\varepsilon_1)^2+(\varepsilon_2+v\varepsilon_1)^2\right),\ \psi_0^- = \frac{E}{2}\varepsilon_1^2$ (12)
else if $(1-v)\varepsilon_3 + v(\varepsilon_1+\varepsilon_2) > 0$
$\psi_0^+ = \frac{E}{2(1-v^2)(1-2v)}((1-v)\varepsilon_3+v\varepsilon_2+v\varepsilon_1)^2,\ \psi_0^- = \frac{E}{2(1-v^2)}(\varepsilon_1^2+\varepsilon_2^2+2v\varepsilon_1\varepsilon_2)$ (13)
else
$\psi_0^- = \frac{Ev}{2(1+v)(1-2v)}(\varepsilon_1+\varepsilon_2+\varepsilon_3)^2 + \frac{E}{2(1+v)}(\varepsilon_1^2+\varepsilon_2^2+\varepsilon_3^3)$ (14)

However, this set of equations can also be written as:

$$\psi_0^{\pm} = \frac{1}{2}\lambda(\mathrm{tr}(\varepsilon_{\pm}^*))^2 + \mu\mathrm{tr}\left((\varepsilon_{\pm}^*)^2\right) \tag{15}$$

where $\varepsilon_{\pm}^*$ is defined as:

$$\varepsilon_{\pm}^* = \sum_i^3 \varepsilon_{i,\pm}^* n_i \otimes n_i \tag{16}$$

where n_i are eigenvectors of ε and ε_i^* are functions of eigenvalues of ε, defined as:
if $\varepsilon_1 > 0$

$$\varepsilon_{1,+}^* = \varepsilon_1,\ \varepsilon_{2,+}^* = \varepsilon_2,\ \varepsilon_{3,+}^* = \varepsilon_3,\ \varepsilon_{1,-}^* = 0,\ \varepsilon_{2,-}^* = 0,\ \varepsilon_{3,-}^* = 0 \tag{17}$$

else if $\varepsilon_2 + v\varepsilon_1 > 0$

$$\begin{gathered}\varepsilon_{1,+}^* = 0,\ \varepsilon_{2,+}^* = \varepsilon_2 + v\varepsilon_1,\ \varepsilon_{3,+}^* = \varepsilon_3 + v\varepsilon_1,\\ \varepsilon_{1,-}^* = \varepsilon_1,\ \varepsilon_{2,-}^* = -v\varepsilon_1,\ \varepsilon_{3,-}^* = -v\varepsilon_1\end{gathered} \tag{18}$$

else if $(1-v)\varepsilon_3 + v(\varepsilon_1+\varepsilon_2) > 0$

$$\begin{gathered}\varepsilon_{1,+}^* = 0,\ \varepsilon_{2,+}^* = 0,\ \varepsilon_{3,+}^* = \varepsilon_3 + \tfrac{v}{1-v}(\varepsilon_1+\varepsilon_2),\\ \varepsilon_{1,-}^* = \varepsilon_1,\ \varepsilon_{2,-}^* = \varepsilon_2,\ ,\ \varepsilon_{3,-}^* = -\tfrac{v}{1-v}(\varepsilon_1+\varepsilon_2)\end{gathered} \tag{19}$$

else

$$\begin{gathered}\varepsilon_{1,+}^* = 0,\ \varepsilon_{2,+}^* = 0,\ \varepsilon_{3,+}^* = 0,\\ \varepsilon_{1,-}^* = \varepsilon_1,\ \varepsilon_{2,-}^* = \varepsilon_2,\ \varepsilon_{3,-}^* = \varepsilon_3\end{gathered} \tag{20}$$

Note that the following two properties always stand:

$$\begin{gathered}\varepsilon_+^* + \varepsilon_-^* = \varepsilon,\\ \psi_0 = (\varepsilon_+^* + \varepsilon_-^*) : C : (\varepsilon_+^* + \varepsilon_-^*) = \varepsilon_+^* : C : \varepsilon_+^* + \varepsilon_-^* : C : \varepsilon_-^*,\\ \varepsilon_+^* : C : \varepsilon_-^* = \varepsilon_-^* : C : \varepsilon_+^* = 0,\end{gathered} \tag{21}$$

where C stands for the elasticity tensor of undamaged isotropic material. While the Miehe's split degrades energy related to positive principal strains, the Lo's split degrades energy related to positive principal stresses. Therefore, the Lo's split does not lead to the growth of cracks in compression. However, like all other spectral splits, it still suffers from the transmission of shear stresses through the crack. However, in our opinion, this split is the most suitable spectral split for problems with contact, such as indentation. As used split of

Lo's is 3D version of spectral split given in work of Freddi, in rest of the work we denote it as Freddi split.

Figure 3 shows a comparison between the splits by Miehe and Amor. Both energy decompositions fail to mimic the crack propagation under the indenter. In both examples, the scalar phase-field, ϕ, grows under the indenter where the compression stress field occurs. In the case of Amor, a similar growth of damage can be spotted under the indenter, along with the fact that elements lose their integrity and the excessive distortion of individual nodes appears.

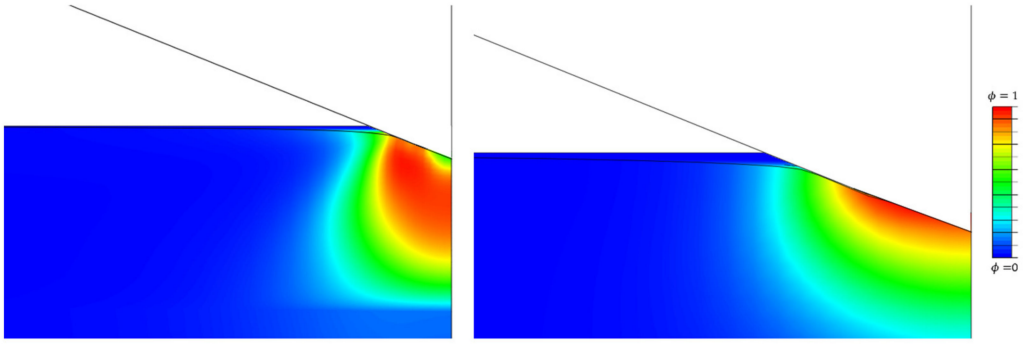

(**a**) (**b**)

Figure 3. Comparison of (**a**) Miehe and (**b**) Amor energy decomposition.

The above formulation was implemented in the first-order, eight-node hexahedral finite element into the ABAQUS program package (2020., 2020, Dassault Systèmes, Vélizy-Villacoublayu, France) [34] by following a procedure proposed by Seleš et al. [35], using a three-layered system. In this way, since the second layer is a standard ABAQUS finite element, different interaction features between two (or more) surfaces (or nodes) can be prescribed.

2.2.3. Indentation Modeling

To reduce the number of degrees of freedom (DOFs), a two-times symmetrical model was used (Figure 4a), with symmetrical boundary conditions defined by Figure 4b. The size of the specimen model is 50 µm × 35 µm × 50 µm. The loading is prescribed as the displacement as the flat top side of the indenter, which is assumed to be rigid. This assumption has been adopted by different finite element studies [8,13,36], where simulations have exhibited little or no difference between the simulations with a rigid or deformable indenter.

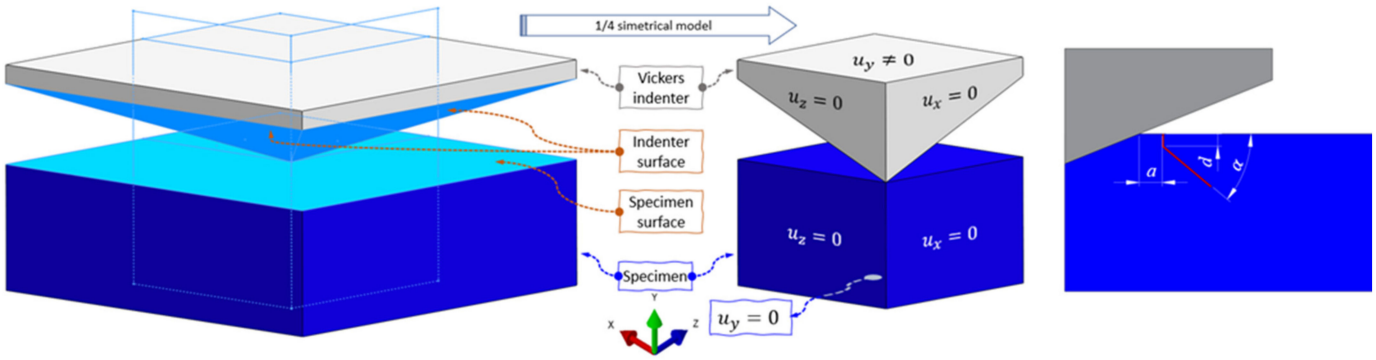

(**a**) (**b**) (**c**)

Figure 4. Numerical model of Vickers indentation: (**a**) full model, (**b**) quarter symmetrical model with symmetry boundary conditions, and (**c**) idealized crack.

Material parameters for our brittle fracture phase-field formulation are shown in Table 4. The length scale parameter has been calculated according to Equation (7) and has the value of approximately 3×10^{-6} mm. Elements with an appropriate edge length are placed only below the indenter and in the contact area (Figure 5). The quarter model is discretized by approximately 3.5 M hexahedral elements.

Table 4. Elastic material parameters for brittle phase-field formulation used in this study.

Modulus of Elasticity, E, MPa	Poisson's Ratio, ν	Fracture Toughness/Energy Release Rate, G_C, N/mm	Tensile Strength, σ^{max}, MPa
75,000	0.16	0.006	4000

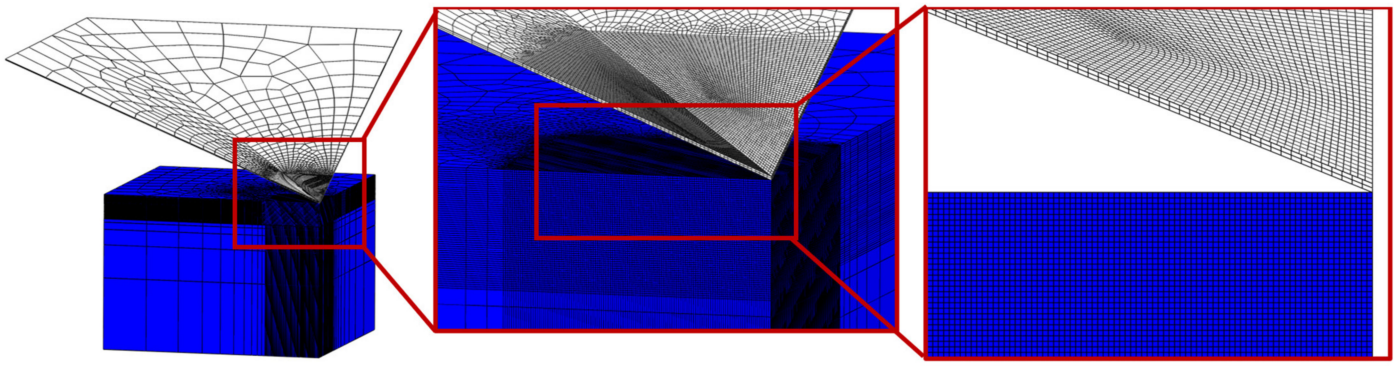

Figure 5. Mesh distribution on the indentation model.

Regarding the contact properties, the indenter surface is taken as the master surface, while a specimen's penetrated surface is the slave surface. Moreover, the master surface (indenter) has a coarser mesh than the slave surface (Figure 5). The contact behavior is established as a surface-to-surface finite sliding, i.e., the sliding between the master and the slave surface nodes is possible [34]. Furthermore, the contact in the normal direction is presumed as the Lagrange formulation hard contact with a relatively small node penetration, and in the tangential direction as the Lagrange formulation with a friction coefficient.

The applied phase-field model was implemented in the ABAQUS software package (2020, 2020, Dassault Systèmes, Vélizy-Villacoublayu, France) along the lines described in [22]. Herein, presented numerical examples were conducted on a single workstation with the AMD® processor, with a 3.80 GHz clock speed and 128 GB RAM memory. Additionally, ABAQUS was accelerated with a NVidia® RTX™ GPU unit. The average duration of the simulations was around 10 days.

3. Results and Discussion

The experimental measurements clearly demonstrate the occurrence of a significant plastic deformation during the Vickers indentation. It is visible as a residual indent after unloading (Figure 2) and the residual plastic energy in Figure 1. Even though the elasto-plastic deformation has been detected by other authors, such as in [2], as an important phenomenon during the Vickers indentation of fused silica, here we applied a brittle phase-field formulation due to the high costs of the phase-field simulations and a complex coupling of damage and plasticity phenomena in the phase-field models. It can be seen from the indentation curve comparison (Figure 1) that the numerical, brittle formulation, can describe the experimental indentation loading curve relatively well, although with a significantly stiffer response caused by the lack of plastic deformation. Therefore, the implementation of a plastic material model will be in the focus of future research since

the authors believe that an adaptive elasto-plastic phase-field formulation is a well-suited approach to model the complex Vickers indentation.

Since the presented phase-field formulation is implemented in the commercial FE software ABAQUS, the use of all interaction features is possible. In this model, the contact interaction is prescribed on the contact surfaces, as described in a later section.

The use of other contact parameters did not afford good results, such as small sliding contact formulation or the penalty contact method. Investigation has shown that the indentation curve did not change (quantitatively) in comparison with the final contact modeling (finite sliding and the Lagrange formulation), but the formation of the cracks, i.e., the growth of the scalar phase-field parameter on the surface, did change. Cracks form in the early stages of the loading process and below the indenter itself. The small sliding contact does not allow the motion of the nodes of adjacent surfaces when the contact is established. This means that the slave nodes stick to the master surface as soon as the contact is established. With the progress of the loading process, they stay stuck to the master surface, unlike the finite sliding formulation, which allows the motion of the nodes in the contact.

Friction between the indenter surface and the specimen surface is also an influential parameter (Figure 6). As friction increases, the initial ring forms closer to the indenter centerline. Moreover, the initiation ring of the secondary cone crack (Figure 2b) propagates deeper as friction decreases.

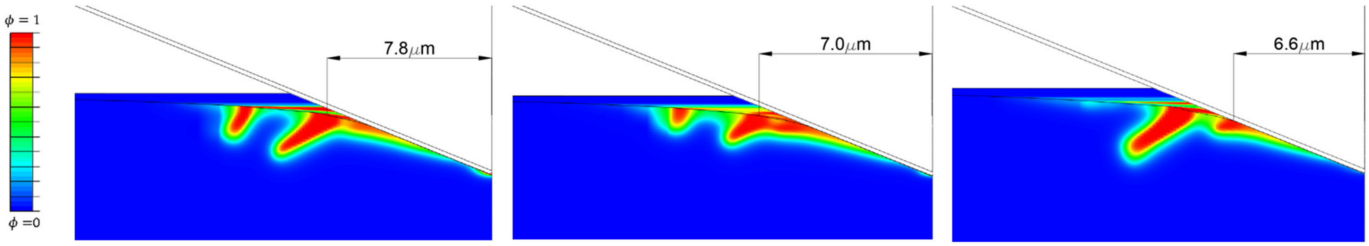

Figure 6. Comparison of the crack growth for different values of the friction coefficient, μ. All deformed models are under the same indenter penetration, i.e., $h = 3$ µm.

Unlike Strobl and Seelig [8], who concluded that the energy decomposition proposed by Freddi cannot replicate the cone crack under the flat indenter with their 2D phase-field formulation, it was shown here that it is possible to model the cone crack with the Vickers indenter by our 3D formulation employing the above-proposed Freddi decomposition.

At the beginning of the loading phase, as soon as the contact is established, the phase-field starts to rise slowly. Since the Freddi energy decomposition is introduced, the negative compression stress does not influence the crack initiation. Only after the indenter notably penetrates the specimen does the phase-field start to intensely rise. The formation of the damage below the indenter is not noticed, unlike in the model with the Miehe energy decomposition (Figure 3).

As reported by Strobl and Seelig [8], the tensile stress on the specimen surface is responsible for the cone-crack initiation. It is visible that the initiation is governed by a weak surface-positive stress field (Figure 7a,b) that forms crack initiation in the shape of a ring. The initiation ring (Figure 7) is located outside the contact region at a certain distance from the indenter contact edge.

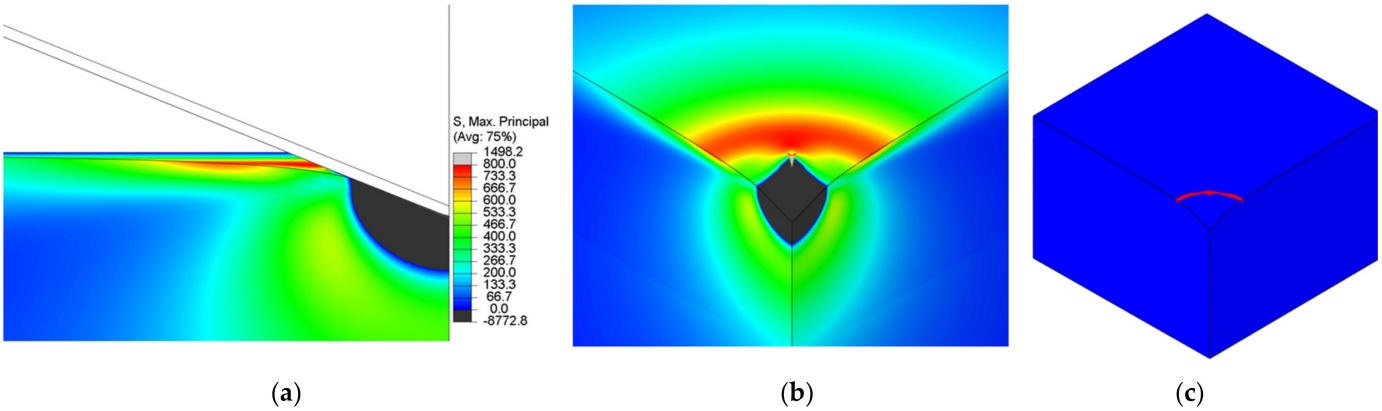

(**a**) (**b**) (**c**)

Figure 7. Positive maximum principal stress (in MPa) on specimen surface as a cause of cone-crack initiation, (**a**) stress distribution (in MPa) in front plane, (**b**) stress distribution in isometric view (without the indenter), showing ring-like distribution outside the contact region, and (**c**) isometric view (without the indenter) of the initiation ring.

By increasing the load, the crack starts to propagate orthogonally to the surface towards the interior of the material (see the dimension, d, in Figure 4c). This propagation direction has been well-captured in both 2D numerical [8,13] and 3D experimental [5,6] observations. With increasing load, the crack continues to propagate with an incline angle of around 45° with respect to the surface (Figure 4b).

As reported by recent phase-field modeling by Strobl and Seeling [8] and Wu et al. [14], and an experimental investigation by Kocer and Collins [7], the Poisson's ratio is the most influential material parameter that influences the angle of the cone crack (in case of a flat punch indenter). However, in the case of an inclined indenter (Vickers or Berkovich), the angle of the cone crack is around 40–45°, as reported by Hagan [5] and Michel et al. [6], which is significantly higher than the angle encountered in the flat punch indentation. In our simulation, a somewhat smaller inclination angle of the cone crack has been observed, as shown in Figure 8f.

The primary and secondary cracks are visible in Figure 8b. The size of the primary (small) cone crack is dependent on the friction coefficient (Figure 6), but both are noticed in experimental measurements (Figure 2), as well as in the relevant literature [37].

Unlike the flat punch, where the contact area is constant, in the Vickers indentation we can expect that the indenter will pass through the crack at some point during the indentation. In terms of the numerical analysis, the crack starts to thicken. This happens when the force is just below 2000 mN. At this force, a new cone crack starts to form, again outside the contact region. Further loading leads to the formation of a new cone crack (Figure 8g), but with a slightly smaller inclination angle.

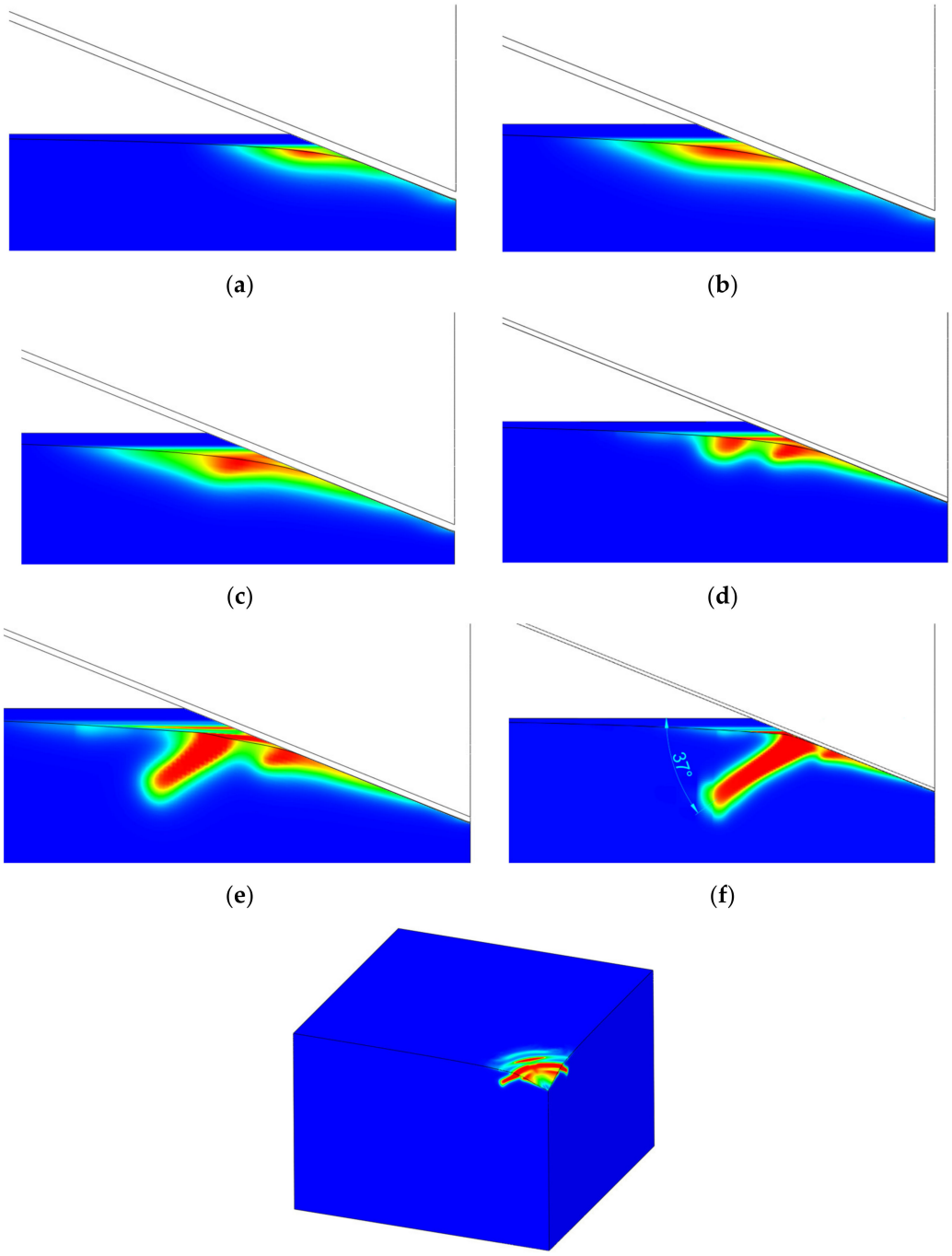

Figure 8. Stable crack growth with inclination angle at different penetration depths: (**a**) $u = 1.2$ µm, (**b**) $u = 1.65$ µm, (**c**) $u = 2.025$ µm, (**d**) $u = 2.4$ µm, (**e**) $u = 2.8$ µm, (**f**) $u = 3.375$ µm, front view for different penetration depths, and (**g**) isometric view without indenter at $u = 3.375$ µm (max. loading).

4. Conclusions

As shown in Section 2, from the considered energy splits, only the spectral energy split proposed by Freddi can accurately replicate cone-crack behavior. The decomposition proposed by Amor fails to model the crack since finite elements in the compression state lose their stiffness and excessive distortion of elements occurs. A similar growth of the scalar damage field was observed using the decomposition proposed by Miehe.

As can be seen from the presented results, the phase-field method is capable of modeling the cone crack formation during the Vickers indentation in fused silica if an appropriate energy split is used. The phase-field numerical model can initiate a ring on the specimen surface outside of the contact region of the indenter, as noticed by Hagan [5] and Lawn and Evans [9]. These indentation crack phenomena are also visible in Figure 2, where a cone crack is formed outside the residual indent. This fact is in accordance with the Lawn and Evans theory that says that the cone crack is the dominant crack mode in the indentation of intact fused silica and that radial-median (half-penny) or lateral cracks are formed due to specimen irregularities or flaws beneath the indenter. A crack in the ideal numerical model without flaws is initiated only by a positive stress field on the surface (Figure 7a,b). From the aspect of linear fracture mechanics (assuming brittle materials), fracture occurs, according to the principal stress hypothesis, when the maximum principal stress reaches the fracture strength of a material [4]. This statement can also be corelated with the phase-field formulation and energy splits, where fracture occurs when one positive stress reaches the critical value.

Regarding the contact formulation, as described, the finite sliding contact is the accordance formulation, since small sliding cannot replicate the conditions appearing in the investigated cone crack. The reason for this lies in small sliding formulation, which "glues" the corresponding nodes from the master and slave surfaces. With further penetration, the nodes of the slave surface are dragged by the corresponding master nodes, which creates positive tensile stress on the specimen, i.e., the slave surface.

By further increasing the load, the crack starts to propagate orthogonally to the surface to a certain depth, firstly in the direction parallel to the loading direction and then at a certain incline angle, which corresponds well to the numerical and experimental observations conducted in the relevant literature.

Even though fused silica is usually presented as an elastic, brittle material, from the obtained experimental indentation curve (Figure 1), it is visible that there occurs a significant plastic deformation, also visible after unloading in the form of a residual indent. The authors' opinion is that no significant change in the crack pattern, with the introduction of a ductile phase-field formulation, will appear since the crack is still driven by only elastic deformation energy.

This research creates new questions in the numerical modeling of indentation cracking, as well as the validation of different phase-field formulations, since fused silica consists of pure silicon dioxide, SiO_2, and can be assumed to be homogeneous. The use of graphic accelerated servers will enhance the computational speeds in future investigations, especially in combination with efficient adaptive remeshing and faster equation solvers. The use of a ductile formulation instead of a brittle one will possibly describe the real indentation curve even better. Additionally, the use of ductile formulation with different energy decompositions could possibly describe the radial (also median and half-penny) cracks, which appear as the second-dominant crack pattern in the fused silica indentation. This could explain why different crack patterns appear on the same specimen at the same indentation force.

Author Contributions: Conceptualization, writing, and numerical simulations, Z.T. (Zoran Tomić); programing and writing, K.J.; experimental investigation, T.A.F.; writing—review and editing, T.J. and Z.T. (Zdenko Tonković). All authors have read and agreed to the published version of the manuscript.

Funding: This work has been fully supported by Croatian Science Foundation under the project "Multiscale Numerical Modelling and Experimental Investigation of Aging Processes in Sintered Structural Components" (MultiSintAge, PZS-1 2019-02-4177), and the project "Nanostructured Hard Metals—New Challenges for Powder Metallurgy" (Nano-PM, UIP-2017-05-6538).

Institutional Review Board Statement: Not applicable.

Informed Consent Statement: Not applicable.

Data Availability Statement: Not applicable.

Conflicts of Interest: The authors declare no conflict of interest.

References

1. *EN ISO 14577-1:2015*; Metallic Materials–Instrumented Indentation Test for Hardness and Materials Parameters–Part 1: Test Method. ISO: Geneva, Switzerland, 2015.
2. Bruns, S.; Johanns, K.E.; Rehman, H.U.R.; Pharr, G.M.; Durst, K. Constitutive modeling of indentation cracking in fused silica. *J. Am. Ceram. Soc.* **2017**, *100*, 1928–1940. [CrossRef]
3. Lee, J.H.; Gao, Y.F.; Johanns, K.E.; Pharr, G.M. Cohesive interface simulations of indentation cracking as a fracture toughness measurement method for brittle materials. *Acta Mater.* **2012**, *60*, 5448–5467. [CrossRef]
4. Bruns, S. The Indentation Densification and Cracking Behavior of Fused Silica. 2020. Available online: https://www.semanticscholar.org/paper/The-Indentation-Densification-and-Cracking-Behavior-Bruns/4b0a4ca825c17178367a0c2db4fc1b252d2b088c (accessed on 30 May 2022).
5. Hagan, J.T. Cone cracks around Vickers indentations in fused silica glass. *J. Mater. Sci.* **1979**, *14*, 462–466. [CrossRef]
6. Michel, M.D.; Serbena, F.C.; Lepienski, C.M. Effect of temperature on hardness and indentation cracking of fused silica. *J. Non. Cryst. Solids* **2006**, *352*, 3550–3555. [CrossRef]
7. Kocer, C.; Collins, R.E. Angle of Hertzian Cone Cracks. *J. Am. Ceram. Soc.* **1998**, *81*, 1736–1742. [CrossRef]
8. Strobl, M.; Seelig, T. Phase field modeling of Hertzian indentation fracture. *J. Mech. Phys. Solids* **2020**, *143*, 104026. [CrossRef]
9. Lawn, B.R.; Evans, A.G. A model for crack initiation in elastic/plastic indentation fields. *J. Mater. Sci.* **1977**, *12*, 2195–2199. [CrossRef]
10. Rickhey, F.; Marimuthu, K.P.; Lee, H. Investigation on Indentation Cracking-Based Approaches for Residual Stress Evaluation. *Materials* **2017**, *10*, 404. [CrossRef] [PubMed]
11. Cao, Y.; Kazembeyki, M.; Tang, L.; Krishnan, N.M.A.; Smedskjaer, M.M.; Hoover, C.G.; Bauchy, M. Modeling the nanoindentation response of silicate glasses by peridynamic simulations. *J. Am. Ceram. Soc.* **2021**, *104*, 3531–3544. [CrossRef]
12. Steinke, C.; Kaliske, M. A phase-field crack model based on directional stress decomposition. *Comput. Mech.* **2019**, *63*, 1019–1046. [CrossRef]
13. Kindrachuk, V.M.; Klunker, A. Phase Field Modeling of Hertzian Cone Cracks Under Spherical Indentation. *Strength Mater.* **2020**, *52*, 967–974. [CrossRef]
14. Wu, J.-Y.; Huang, Y.; Nguyen, V.P.; Mandal, T.K. Crack nucleation and propagation in the phase-field cohesive zone model with application to Hertzian indentation fracture. *Int. J. Solids Struct.* **2022**, *241*, 111462. [CrossRef]
15. Roebuck, B.; Bennett, E.; Lay, L.; Morrell, R. *Palmqvist Toughness for Hard and Brittle Materials Measurement Good Practice Guide No. 9*; National Physical Laboratory: Teddington, UK, 2008; p. 48.
16. Anstis, G.R.; Chantikul, P.; Lawn, B.R.; Marshall, D.B. A Critical Evaluation of Indentation Techniques for Measuring Fracture Toughness: I, Direct Crack Measurements. *J. Am. Ceram. Soc.* **1981**, *64*, 533–538. [CrossRef]
17. Giannakopoulos, A.E.; Suresh, S. Determiantion of elastoplastic properties by instrumented sharp indentation. *Scr. Mater.* **1999**, *40*, 1191–1198. [CrossRef]
18. Dao, M.; Chollacoop, N.; Van Vliet, K.J.; Venkatesh, A.; Suresh, S. Computational modeling of the forward and reverse problems in instrumented sharp indentation. *Acta Mater.* **2001**, *49*, 3899–3918. [CrossRef]
19. Seleš, K. Abaqus Code for a Residual Control Staggered solution Scheme for the Phase-Field Modeling of Brittle Fracture. *Eng. Fract. Mech.* **2019**, *205*, 370–386. [CrossRef]
20. Miehe, C.; Welschinger, F.; Hofacker, M. Thermodynamically consistent phase-field models of fracture: Variational principles and multi-field FE implementations. *Int. J. Numer. Methods Eng.* **2010**, *83*, 1273–1311. [CrossRef]
21. Seleš, K.; Aldakheel, F.; Tonkovic, Z.; Sorić, J.; Wriggers, P. A General Phase-Field Model for Fatigue Failure in Brittle and Ductile Solids. *Comput. Mech.* **2021**, *67*, 1431–1452.
22. Seleš, K. Numerical Phase-Field Modeling of Damage in Heterogeneous Materials. Ph.D. Thesis, University of Zagreb, Zagreb, Croatia, 2020.
23. Ambrosio, L.; Tortorelli, V.M. On The Approximation of Free Discontinuity Problems. *Boll. Della Unione Mat. Ital.* **1992**, *6*, 105–123.
24. Alessi, R.; Ambati, M.; Gerasimov, T.; Vidoli, S.; De Lorenzis, L. Comparison of Phase-Field Models of Fracture Coupled with Plasticity. In *Advances in Computational Plasticity*; Oñate, E., Peric, D., de Souza Neto, E., Chiumenti, M., Eds.; Springer: Cham, Switzerland, 2018. [CrossRef]
25. De Lorenzis, L.; Gerasimov, T. Numerical implementation of phase-field models of brittle fracture. In *Modeling in Engineering Using Innovative Numerical Methods for Solids and Fluids*; De Lorenzis, L., Ed.; Springer: Berlin/Heidelberg, Germany, 2020; pp. 75–101. [CrossRef]
26. Freddi, F.; Royer-Carfagni, G. Regularized variational theories of fracture: A unified approach. *J. Mech. Phys. Solids* **2010**, *58*, 1154–1174. [CrossRef]
27. Amor, H.; Marigo, J.J.; Maurini, C. Regularized formulation of the variational brittle fracture with unilateral contact: Numerical experiments. *J. Mech. Phys. Solids* **2009**, *57*, 1209–1229. [CrossRef]
28. Strobl, M.; Seelig, T. On constitutive assumptions in phase field approaches to brittle fracture. *Procedia Struct. Integr.* **2016**, *2*, 3705–3712. [CrossRef]
29. Fan, M.; Jin, Y.; Wick, T. A quasi-monolithic phase-field description for mixed-mode fracture using predictor–corrector mesh adaptivity. *Eng. Comput.* **2021**, 1–25. [CrossRef]

30. Yu-Sheng, L.; Michael, J.; Borden, K.; Ravi-Chandar, C.M.L. A phase-field model for fatigue crack growth. *J. Mech. Phys. Solids* **2019**, *132*. ISSN 0022-5096.
31. He, Q.-C.; Shao, Q. Closed-Form Coordinate-Free Decompositions of the Two-Dimensional Strain and Stress for Modeling Tension–Compression Dissymmetry. *J. Appl. Mech.* **2019**, *86*, 031007. [CrossRef]
32. Nguyen, T.-T.; Yvonnet, J.; Waldmann, D.; He, Q.-C. Implementation of a new strain split to model unilateral contact within the phase field method. *Int. J. Numer. Methods Eng.* **2020**, *121*, 4717–4733. [CrossRef]
33. Wu, J.-Y.; Nguyen, V.P. A length scale insensitive phase-field damage model for brittle fracture. *J. Mech. Phys. Solids* **2018**, *119*, 20–42. [CrossRef]
34. Abaqus 6.14-1, Dassault Systems Simulia Corp., Providence, RI, USA. 2014. Available online: http://130.149.89.49:2080/v6.14/pdf_books/ANALYSIS_4.pdf (accessed on 30 May 2022).
35. Seleš, K.; Tomić, Z.; Tonković, Z. Microcrack propagation under monotonic and cyclic loading conditions using generalised phase-field formulation. *Eng. Fract. Mech.* **2021**, *255*, 107973. [CrossRef]
36. Bruns, S.; Petho, L.; Minnert, C.; Michler, J.; Durst, K. Fracture toughness determination of fused silica by cube corner indentation cracking and pillar splitting. *Mater. Des.* **2020**, *186*, 108311. [CrossRef]
37. Li, C.; Ding, J.; Zhang, L.; Wu, C.; Sun, L.; Lin, Q.; Liu, Y.; Jiang, Z. Densification effects on the fracture in fused silica under Vickers indentation. *Ceram. Int.* **2021**, *48*, 9330–9341. [CrossRef]

PAPER 3.

Reproduced with permission.

Authors:	Zoran Tomić, Tomislav Jarak, Tomislav Lesičar, Nenad Gubeljak, Zdenko Tonković
Title:	Modelling of Fatigue Microfracture in Porous Sintered Steel Using a Phase-Field Method
Journal:	Materials
Quartile/Impact Factor	Q2/3.748
Bibliography data:	Volume: 16 (11) Year: 2023, 4174
DOI:	https://doi.org/10.3390/ma16114174

materials

MDPI

Article

Modelling of Fatigue Microfracture in Porous Sintered Steel Using a Phase-Field Method

Zoran Tomić [1], Tomislav Jarak [1,2,*], Tomislav Lesičar [1], Nenad Gubeljak [3] and Zdenko Tonković [1]

[1] Faculty of Mechanical Engineering and Naval Architecture, University of Zagreb, 10000 Zagreb, Croatia; zoran.tomic@fsb.hr (Z.T.); tomislav.lesicar@fsb.hr (T.L.); zdenko.tonkovic@fsb.hr (Z.T.)
[2] ITAP, School of Industrial Engineering, University of Valladolid, Paseo de Cauce 59, 47011 Valladolid, Spain
[3] Faculty of Mechanical Engineering, University of Maribor, 2000 Maribor, Slovenia; nenad.gubeljak@um.si
* Correspondence: tomislav.jarak@uva.es

Abstract: Porosity in sintered materials negatively affects its fatigue properties. In investigating its influence, the application of numerical simulations reduces experimental testing, but they are computationally very expensive. In this work, the application of a relatively simple numerical phase-field (PF) model for fatigue fracture is proposed for estimation of the fatigue life of sintered steels by analysis of microcrack evolution. A model for brittle fracture and a new cycle skipping algorithm are used to reduce computational costs. A multiphase sintered steel, consisting of bainite and ferrite, is examined. Detailed finite element models of the microstructure are generated from high-resolution metallography images. Microstructural elastic material parameters are obtained using instrumented indentation, while fracture model parameters are estimated from experimental S–N curves. Numerical results obtained for monotonous and fatigue fracture are compared with data from experimental measurements. The proposed methodology is able to capture some important fracture phenomena in the considered material, such as the initiation of the first damage in the microstructure, the forming of larger cracks at the macroscopic level, and the total life in a high cycle fatigue regime. However, due to the adopted simplifications, the model is not suitable for predicting accurate and realistic crack patterns of microcracks.

Keywords: sintered steel; microcracks; fatigue; phase-field method; porosity

Citation: Tomić, Z.; Jarak, T.; Lesičar, T.; Gubeljak, N.; Tonković, Z. Modelling of Fatigue Microfracture in Porous Sintered Steel Using a Phase-Field Method. *Materials* **2023**, *16*, 4174. https://doi.org/10.3390/ma16114174

Academic Editors: Lucjan Śnieżek and Jaroslaw Galkiewicz

Received: 30 April 2023
Revised: 23 May 2023
Accepted: 30 May 2023
Published: 3 June 2023

1. Introduction

In recent years, much effort has been made in investigating the influence of material microstructure on the failure mechanisms of highly heterogeneous materials, such as sintered materials, using various numerical and experimental techniques. This is especially important when they are subjected to cyclic loading conditions. Structural components manufactured with various sintering or additive technologies are becoming attractive due to their good vibration and noise reduction properties, accompanied by a very high rate of raw material utilization in such processes [1]. This is especially favorable for large-series production of machine components with complex geometry, such as gears, spurs or bearings. However, pores appear in sintered materials, which are often a predominant factor in failure mechanisms in dynamically loaded sintered parts [2,3]. Microcracks usually initiate around smaller closely packed pores, propagate to nearby pores and eventually mutually coalesce, creating a macrocrack which can finally cause the failure of a component. Being able to predict the relationship between material microstructure and fracture behaviour by means of numerical modelling could significantly reduce the amount of time and costs needed for identifying the "optimal" microstructure.

Most often, models based on the Finite Element Method (FEM) have been used for investigating material microfracture, due to the robustness and availability of FEM. The Extended Finite Element Method (XFEM), based on enriching the approximation functions space with discontinuous functions, has sometimes been used; see, e.g., [4,5]. Nevertheless,

in XFEM it is difficult to accurately track crack geometries in problems where multiple cracks evolve, branch or merge. Cohesive Zone Modelling (CZM) has sometimes been viewed as a good alternative to XFEM, see, e.g., [6,7], but to predict the paths of arbitrary cracks, cohesive elements have to be used along all finite element edges [8], which is computationally expensive. Further interesting models to be considered for understanding microfracture might be models with embedded and smeared discontinuities [9]. In problems with arbitrary crack paths, remeshing techniques are often used, but they require special numerical procedures and special attention has to be dedicated to avoiding loss of accuracy during mapping. Recently, the moving mesh method [10] has been proposed to tackle this problem, where the Arbitrary Lagrangian formulation (ALE) is used to simulate the evolution of material discontinuities.

During the last decade, phase-field (PF) modelling of fracture experienced significant popularity, since no ad hoc criteria are needed for crack initiation or propagation, and complex crack patterns can be modelled without the need to explicitly track crack geometries. Therefore, such PF methods seem to be appropriate for modelling cracking in the microstructures of heterogeneous materials. Thereby, some important issues are the modelling of cracking along material interfaces or crystal grains and model calibration.

Simple multiphase PF models for fracture, where the effects of interfacing between the particles or grains or anisotropy are not modelled, have been considered in the literature for reproducing global material responses. In [11] the topology of a highly heterogeneous realistic microstructure was extracted from X-ray CT images, and the improved formulation proposed by Miehe et al. [12] was used to analyse fracture. A similar formulation was used for 3D analysis [13] using models created from microtomography. To cut computational costs, Seleš et al. [14] proposed a staggered solution procedure based on a residual norm with improved convergence properties to study size effects associated with microscale fracture in a hypothetical material.

More sophisticated models have been developed to include the anisotropy of grains or to describe intergranular cracks [15–23]. The grain boundaries are often modelled as smeared internal layers between grains with fracture toughness dependent on the surrounding bulk material [15,17], or as an additional material phase appearing as a thin layer between grains [19,20]. Alternatively, a Cohesive Zone Model (CZM) might be used to model intergranular cracks [21,22]. Various models with multiple phase field parameters may also be found in the literature [17,18,23]. Common issues in such sophisticated models are the mechanical characterization of the boundaries and the increased complexity. They also demand a higher computational burden, which is in general one of the main obstacles in the practical use of PF models. This could become even more pronounced in fatigue computations for porous sintered materials, where complex geometries require the application of dense finite element meshes everywhere in the model to accurately capture geometry and phase-field evolution. The recent work by the authors of [24] represents an early attempt at fatigue microfracture analysis, where a fatigue fracture in nodular cast iron was simulated using a generalized PF model [25], featuring friction contact between elastic graphite nodules and the elasto-plastic metallic matrix. However, in that work, validation results for total life estimation were not offered, and the calibration of such a model is still an open question.

In general, one of the main problems in numerical material modelling at the microstructural level is the mechanical characterization of material phases. Using different indenters and different forces, it is possible to characterize single grains of material from nano- to macroscale. The basic method was proposed by Oliver and Pharr [26], which enables reliable estimation of elastic properties. Later, various methods for extracting complete stress–strain curves of individual grains were presented [27–29]. Recently, instrumented indentation has been applied for the mechanical characterization of plastic parameters in a multi-phase steel [30], but the reliability and accuracy of such data may be questionable, and from our experience depend significantly on the equipment used and the inverse method for characterization of plastic parameters.

This work deals with investigating the influence of porosity on fatigue failure in a sintered steel by employing PF modelling to observe the evolution of microcracks due to cyclic loading. A simplified PF model for brittle fatigue fracture with a threshold is applied. Fatigue is modelled by degrading the fracture toughness. It is derived from the general PF model presented in [24] by neglecting plastic deformation. Elastic local (microstructural) material properties are identified using instrumented indentation. In addition, the fracture toughness of individual phases is also estimated via indentation and used in the model as the initial fracture toughness (the fracture toughness of material undegraded by fatigue). The degradation of fracture toughness is modelled by a logarithmic function with one material fatigue parameter, which is calibrated from experimental S–N curves. Two-dimensional (2D) microscopic volume elements (MVEs) of different sizes are extracted from high-resolution metallography imaging and divided into spatial zones corresponding to the metallic phases observed in metallography images. In this work, it is assumed that the main driving feature for crack initiation and propagation through the microstructure in the considered material is porosity. The influence of grain boundaries and grain anisotropy is not accounted for in order to simplify the model and reduce the computational burden. The results of numerical simulations are compared with macroscale quasi-static uniaxial tension test (UTT) data and images obtained with a scanning electron microscope (SEM) to interpret the obtained results. Although material interfaces and plastic deformation could have significant impacts that cannot be captured by the present model, the obtained results indicate that the applied strategy is still capable of capturing some important phenomenological fatigue features, such as S–N curves.

The main highlights of the paper are:

- simplified numerical modelling based on the PF method for estimating the fatigue life of sintered steels is presented,
- mechanical characterization of the applied PF fatigue model based on the degradation of fracture energy is critically discussed,
- the influence of the porosity of the considered sintered steel on the estimated fatigue life is analysed using the proposed numerical method.

The paper is structured as follows: in Section 2 basic information about the applied numerical and experimental methods is given, including the governing equations of numerical phase-field formulations. The modelling process is also described. Afterwards, in Section 3 numerical results for monotonic quasi-static and dynamic fatigue fracture are presented, together with discussion of the results. Finally, some concluding remarks and future lines of research are proposed in Section 4.

2. Materials and Methods

2.1. Experimental Testing

For the purposes of this study, sintered samples (Figure 1) were compacted from Astaloy Mo+0.2C steel according to Höganäs [31]. Three densities were compacted: 6.5 g/cm^3, 6.8 g/cm^3 and 7.1 g/cm^3, with dimensions according to the ASTM E8 standard [32]. More details about the compacting, sintering and cooling procedure can be found in the authors' previous work [33]. The specimens in Figure 1 were used for the macroscopic uniaxial tension test (UTT), and smaller material samples were extracted from them for the purpose of metallographic and instrumental indentation testing.

2.1.1. Microscale

The microstructure consists of two distinct phases, ferrite and bainite, and is of relatively high porosity. Typical microstructure of the sintered steel is shown in Figure 2.

Table 1 shows some of the micromechanical properties for all three densities, obtained via instrumented Vickers indentation and high-resolution metallography imaging. The elastic modulus of different constituents was determined by the standard Oliver and Pharr method [26]. Indentation testing was conducted on an Anton Paar MCT^3 testing device

applying a standard diamond Vickers indenter. For more information about the indentation procedure, please see [33].

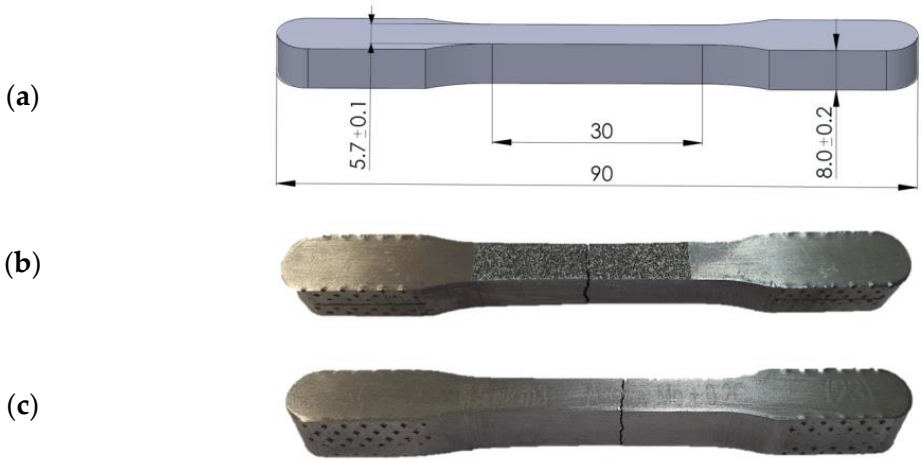

Figure 1. Sintered specimen according to ASTM E8: (**a**) dimensions, (**b**) fracture after quasi-static uniaxial tension test, (**c**) fatigue crack after cyclic uniaxial test.

Figure 2. Typical microstructure of sintered Astaloy Mo+0.2C steel (here shown for specimen with 6.5 g/cm^3). Metallography image shows a heterogeneous microstructure consisting of ferrite and bainite phases and pores (black color).

Table 1. Microstructural properties according to metallographic imaging and instrumented indentation [33]. V_0 is the volume of bulk material without pores (material matrix), V_p is the total volume of the pores.

Sintered Density, g/cm^3	Phase Volume Fraction, %			Microproperties	
	Porosity, $k_p = V_p/V_0$	Ferrite, $k_f = V_f/V_0$	Bainite, $k_b = 1 - k_f$	Ferrite	Bainite
				Modulus of Elasticity, GPa	
6.5	20	33 ±2.5	xxx	185.3 ± 29.5	238 ± 29.6
6.8	14.7	30 ±3.7	xxx	189.1 ± 22.8	240 ± 17.2
7.1	9,9	31 ± 4.1	xxx	183.6 ± 20.7	238 ± 22.4

As reported in [33], the local (microscopic) values of the elastic properties for bainite and ferrite are almost identical for different densities, as shown in Table 1. This finding implies that the elastic macroscopic response of the considered material is driven mostly by porosity.

Besides the elastic properties of ferrite and bainite, the PF model for brittle fracture presented in Section 2.2 requires the material fracture toughness value. Although this parameter itself is not actually relevant for our analysis, here the fracture toughness of each material constituent was estimated via instrumental indentation and used to calculate the initial values of critical fracture energy (critical fracture energy before the onset of fatigue damage) in the model. At the moment there exist few works dealing with estimation of the fracture toughness of ductile materials using instrumented indentation; several methods have been proposed, such as those of Palmquist or Anstis [34,35] or Jeon et al. [36]. However, determination of the fracture toughness of ductile materials using indentation is a difficult task, because no cracks appear on the surface even when Berkovich or Vickers indenters are used; see Figure 3.

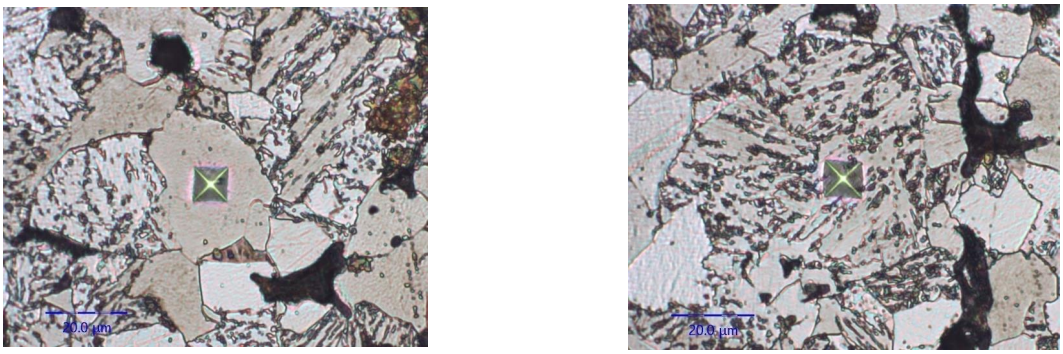

(**a**) (**b**)

Figure 3. Typical residual Vickers indent in sintered steel: (**a**) ferrite phase, (**b**) bainite phase.

The method used here was proposed by Jeon et al. [36]. It utilizes multicycle spherical indentation and is based on the theoretical background of plasticity evolution under an indenter proposed by Hertz. Multicycle indentation was used to obtain the required information, which was fed into an empirical equation. Indentation was conducted using a spherical indenter with a 50 µm radius and an Anton Paar Micro Combi Tester MCT^3 at room temperature. At least 15 individual indentations were conducted for each phase. For the ferrite phase, the maximum force of 200 mN was achieved in 15 steps (Figure 4a), while for the bainite phase, the maximum force of 1000 mN was reached in 20 steps (Figure 4b). The load in each step was increased in an approximately linear fashion (see the red line in Figure 4). The sample surface was prepared according to the procedure described in [33]. Different maximum forces were chosen for testing each phase, with the maximum forces chosen so as to minimize the influence of phase interfaces and material surrounding the tested phase. However, since in this work bainite is considered an isotropic homogeneous material phase in numerical models, relatively high force was applied for bainite indentation to implicitly capture the influence of the heterogeneity of the bainite phase in the obtained results. The obtained fracture toughness values for bainite and ferrite are given in Table 2.

Table 2. Fracture toughness of microstructural constituents obtained via multicyclic spherical indentation.

	Fracture Toughness (Energy Release Rate), G_C, N/mm
bainite	8.45
ferrite	14.5

2.1.2. Macroscale

The sintered specimens were subjected to quasi-static tension loading in UTT. The obtained stress–strain curves, shown in Figure 5, serve in this article only for comparison with the results of numerical simulations of microfracture caused by quasi-static monotonous loading. More information about the static testing procedure undertaken can be found in [33].

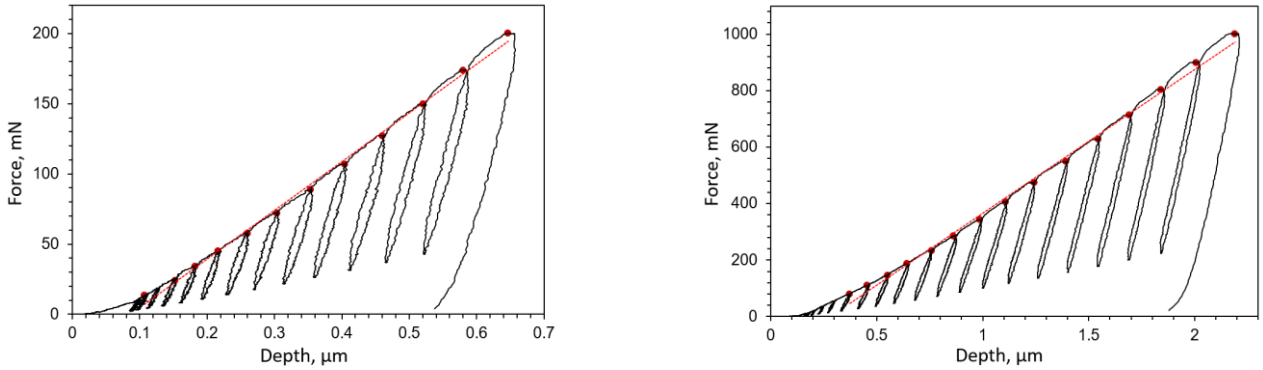

Figure 4. Force–displacement curves obtained via multicycle spherical indentation used for fracture toughness estimation of material constituents: (**a**) ferrite, (**b**) bainite.

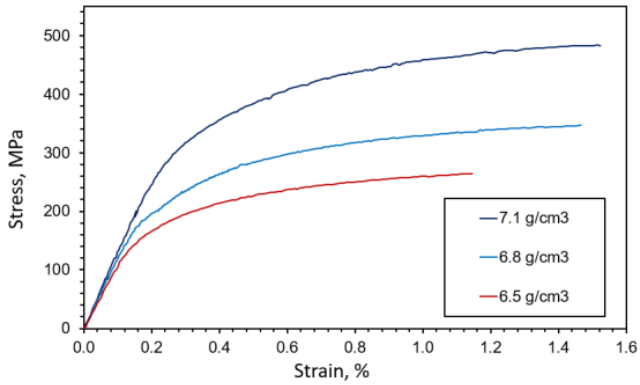

Figure 5. Mean stress–strain curves at a macroscopic level [35].

As visible from Figure 5, a small plastic deformation is present at the macroscopic level before failure. In addition, elongation before failure decreases with increased porosity. This could be explained by the fact that in porous materials smaller particle necks between two adjacent pores promote higher localized plastic flows, which contribute to faster damage evolution at the microlevel and finally result in lower deformation of the loaded system, which is consistent with the observations in [2]. As is visible from metallographic imaging (Figure 2) and other presented figures from numerical models, in specimens with higher porosity there is a high probability that a larger number of small particle necks is encountered. This increases the number of probable locations for microcrack initiation, and a larger number of simultaneously propagating microcracks facilitates their coalescence and causes complete material failure before significant macroscopic plastic deformation occurs. Porosity also decreased the macroscopic yield stress, tensile strength and elastic modulus of the considered sintered steel. For all three considered microstructures, after the onset of fracture, a sudden failure producing a very sudden drop in stress was observed, typical for brittle fracture.

Next, loading–unloading experiments were conducted with a Rumul Testronic 50 kN loading device, coupled with a GOM Aramis as a video-extensometer, making live tension–relaxation supervision possible. In the results of the loading–unloading tests (Figure 6), no change in elastic slope after unloading–loading cycles is visible (except for measurement error up to 2%). This means that microfracture events (if present) were not observable on the macroscale at stress levels lower than the ultimate tensile strength. This absence of damage at the macroscale before the occurrence of failure implies that plasticity could be a driving mechanism of failure in the considered material.

Fatigue tests were conducted on a Rumul 50 kN frequency resonant machine. The average testing frequency was around 130 Hz for High Cycle Fatigue (HCF). The surfaces

of all sintered samples were previously polished using polishing paper of identical grade in order to maintain traceability. The loading ratio $R = F_{max}/F_{min} = \sigma_{max}/\sigma_{min}$ was maintained at 0.05. All tests were controlled by force. The Wöhler curves for all three densities are shown in Figure 7, together with the corresponding identified curve exponents and coefficients.

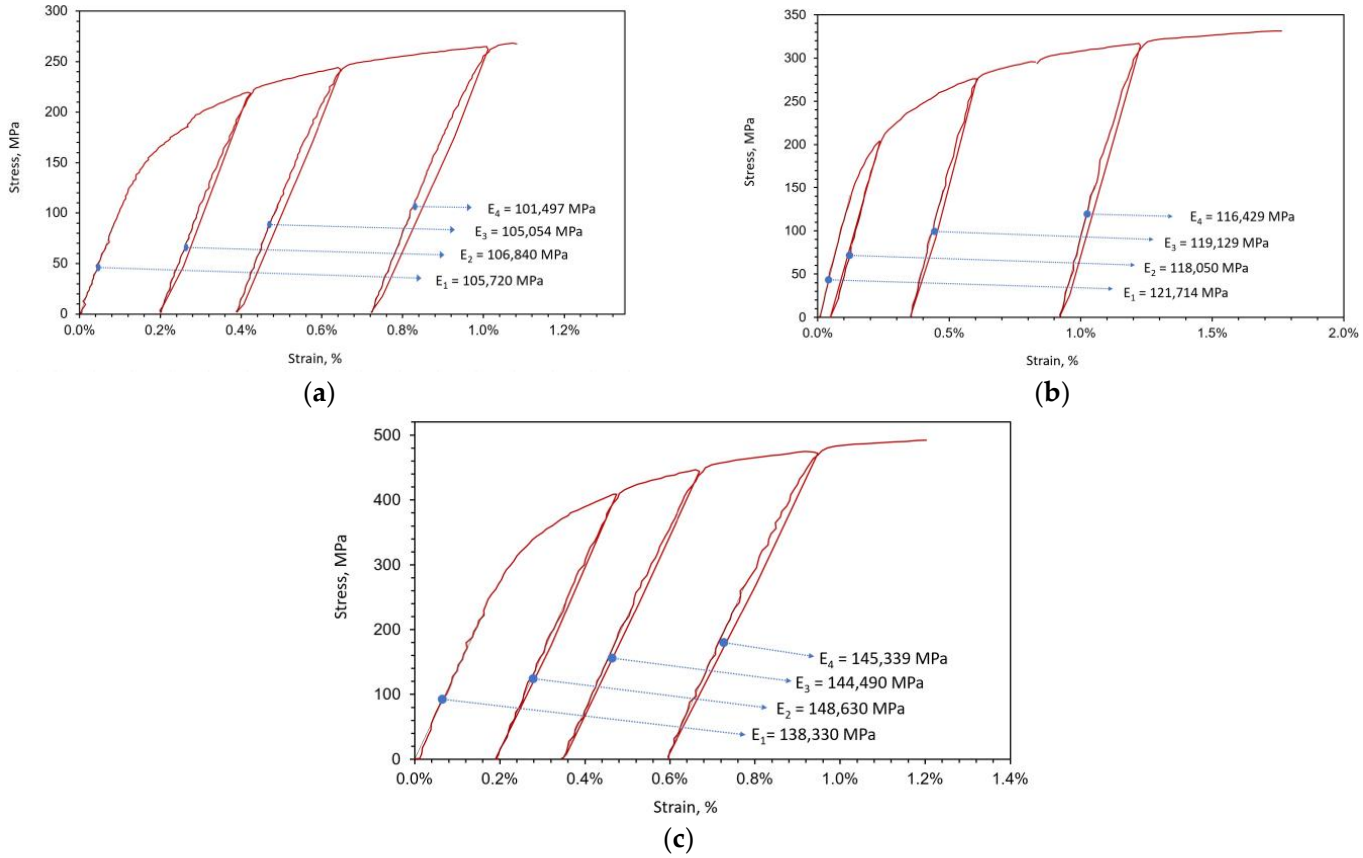

Figure 6. Uniaxial tension loading–unloading cycles for (**a**) 6.5 g/cm^3, (**b**) 6.8 g/cm^3, (**c**) 7.1 g/cm^3.

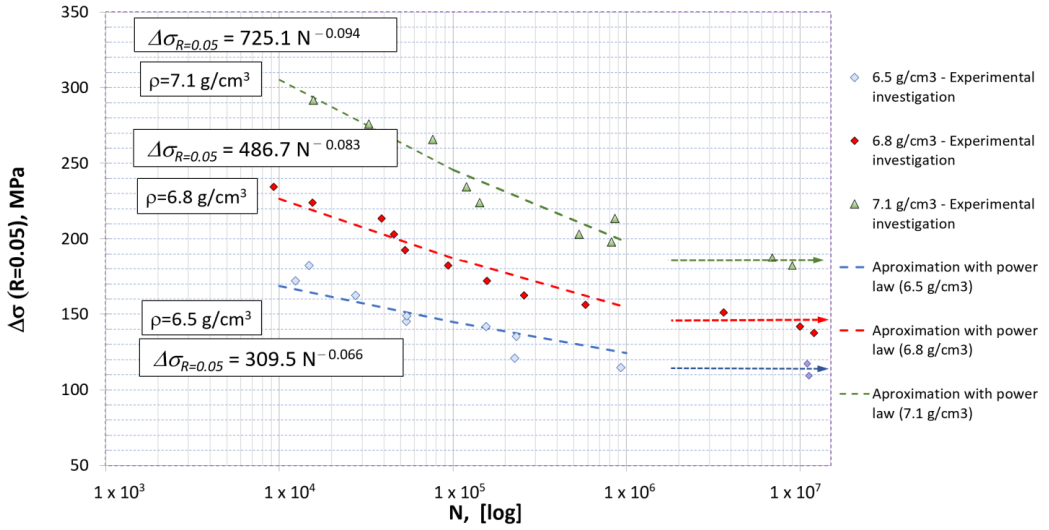

Figure 7. Wöhler curves for sintered steel specimens with 6.5, 6.8 and 7.1 g/cm^3. The arrows pointing rightwards represent specimens that reached the fatigue limit, determined as more than 10^7 cycles.

From Figure 7 it is visible that the total fatigue life significantly decreased with respect to increased porosity. For an identical loading cycle the 7.1 g/cm^3 density steel might reach

its fatigue endurance limit, while the 6.5 g/cm^3 density steel might exhibit LCF behavior with only a few thousand cycles needed to reach the failure of the specimen.

2.1.3. Fractographic Observations

The results of the UTT suggest that plastic deformation should be the prominent process at the microscale as well, causing or contributing to the initiation of the first microcracks. Indeed, the crack surfaces observed in Scanning Electron Microscopy (SEM) images created after quasi-static uniaxial testing (Figure 8) were similar in all considered samples and correspond to the ductile dimple fracture mode. This is consistent with the findings from [3], where microfractographic analysis of Astaloy CRL + 0.7 wt-%C sintered steel was performed for both static and fatigue failure. In addition, similarly to the observations from [2,3,37], the microcrack patterns clearly show that a crack surface (marked by a yellow curve in Figure 8) is generally formed by a collapse of a ''bridge'' between two pores (i.e., fracture of the neck joining two adjacent powder particles). The free surfaces marked in Figure 8 represent the walls of the surrounding pores. This also means that in such cases the microcrack is often formed as a transgranular crack (a crack passing though only one material phase), because metallographic analyses have shown that often only one material phase is present along the small bridge.

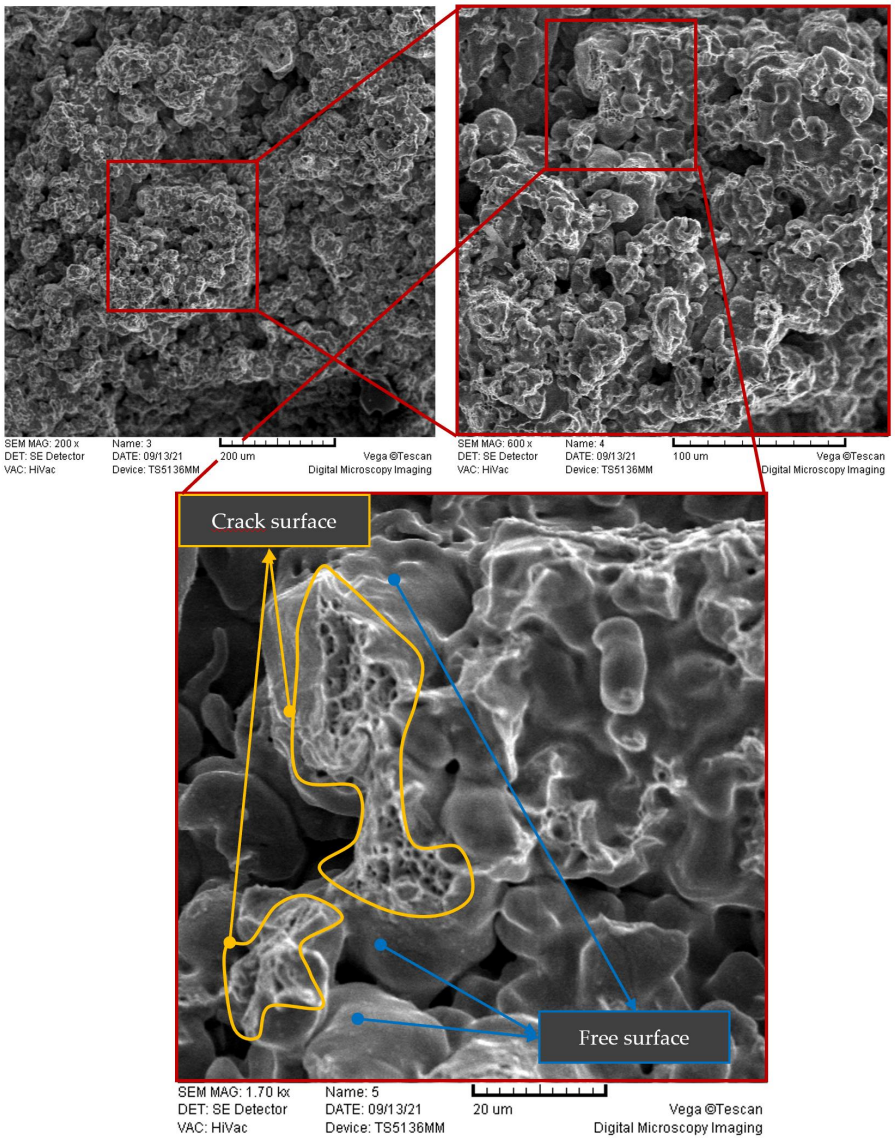

Figure 8. SEM imaging of the crack surface at different magnifications.

2.2. Numerical Phase-Field Model for Fatigue Fracture

The brittle PF model for fatigue fracture applied in this work is derived from the general plane strain PF formulation proposed in [25], omitting plastic deformation. The model was implemented in the commercial FE software Abaqus using UMAT and UEL user-defined functions.

In the following, only a brief overview is given, as more details can be found in [24,25]. Here, however, we will correct certain errors and clear out some ambiguities regarding this model that are encountered in previous works [24,25].

2.2.1. Governing Equations

Starting from [38,39], in the general case of brittle fracture, the internal energy functional Ψ^{int} of a body Ω bounded by an outer surface $\partial\Omega$ and containing a crack with surface Γ can be defined as a sum of the strain energy in the bulk material Ψ^{b} and the fracture energy Ψ^{f} (energy dissipated by the fracture):

$$\Psi^{\text{int}} = \Psi^{\text{b}} + \Psi^{\text{f}} \approx \int_{\Omega/\Gamma} g(\phi)\psi_e(\varepsilon)\,\mathrm{d}V + \int_{\Omega} \psi^c(\overline{\psi})\left(2\phi + l\,|\nabla\phi|^2\right)\mathrm{d}V \tag{1}$$

The scalar parameter ϕ is called the phase-field parameter and is used to define the intensity of damage in the material. It is a smooth scalar field that describes a transition from an intact material ($\phi = 0$) to a completely broken material ($\phi = 1$). Since fracture causes the loss of the initial stiffness of a material, strain energy is reduced by introducing a monotonically decreasing degradation function $g(\phi)$, with $\psi_e(\varepsilon)$ being the elastic strain energy density of the intact material (effective strain energy). In this work, the standard quadratic function $g(\phi) = (1-\phi)^2$ is adopted. In passing, we note that in [24,25], the contribution of plastic deformation is included in the strain energy to model ductile fracture. To prevent unphysical crack propagation in compressive stress states, an appropriate strain energy decomposition should be introduced, which considerably increases the computational costs. However, in this work only problems with tension loading are studied, and it is deemed that in such cases, tensile stress states are predominant. Therefore, in Equation (1) an isotropic degradation of strain energy is employed, where the entire strain energy is degraded, and this issue of implementing an energy decomposition method is outside of the scope of this article.

The fracture energy Ψ^{f} can be approximated as a domain integral according to Miehe et al. [39], where ψ^c stands for a specific fracture energy. It can be shown that ψ^c serves as the energetic threshold for fracture initiation in the material, and therefore such models are sometimes called PF models with thresholds (or threshold PF models). ψ^c is the constant parameter in the case of quasi-static fracture caused by monotonous loading, but in fatigue formulations such as [38], it is assumed that fracture resistance degrades under the influence of repeated cycling load. This can be achieved by making ψ^c dependent on the energy accumulation variable $\overline{\psi}$, which measures the "mileage" of the material subjected to repeated cycling loading by memorizing repeated strain energy changes during the loading history. Here $\overline{\psi}$ is calculated at a certain moment t of the loading process as

$$\overline{\psi}(t) = \int_0^t \dot{\psi}_e(\tau)\,H\left(\dot{\psi}_e(\tau)\right)\mathrm{d}\tau \tag{2}$$

where H is the Heaviside step function, with a value of 0 when the strain energy in the material decreases ($\dot{\psi}_e \leq 0$) and a value of 1 when the strain energy in the material increases ($\dot{\psi}_e > 0$) during the loading cycle. It is obvious that $\overline{\psi}$ has the character of a loading history(path-dependent) variable that increases only when strain energy grows during the loading process. It is of note that this definition of (2) is by no means the unique one. Finally, l denotes the length-scale parameter that controls the width of the transition zone between intact and completely broken material, where the damage intensity is described by the distribution of the phase-field ϕ.

Remark. *In an attempt to quantify* ψ^c*, in* [24,25] *the fracture energy was represented in a manner typical for brittle PF models based on Griffith's theory:*

$$\Psi^{\mathrm{f}} \approx \int_{\Omega} \psi^c(\overline{\psi}) \left(2\phi + l\,|\nabla\phi|^2\right) \mathrm{d}V = \int_{\Omega} G_c(\overline{\psi})\,\gamma(\phi, \nabla\phi) \mathrm{d}V \tag{3}$$

where $\gamma(\phi, \nabla\phi)$ *is the surface crack density function, defined as*

$$\gamma(\phi, \nabla\phi) = \frac{3}{8\sqrt{2}} \left(\frac{2\phi}{l} + l^2 |\nabla\phi|^2\right) \tag{4}$$

and G_c *stands for the critical energy release rate (fracture toughness), which was considered the material property in* [24,25]*. In that case, it follows that:*

$$\psi^c = \frac{3}{8\sqrt{2}} \frac{G_c}{l} \tag{5}$$

However, note that according to the original threshold formulations proposed by Miehe et al. in [39,40]*, in the case of a general elasto-plastic cyclic deformation process,* ψ^c *should be considered the material fracture model parameter, to be defined either experimentally or empirically through numerical experiments. Therefore, it is not clear if the approach proposed in* [24] *is actually able to produce quantitatively meaningful results if an experimentally defined Gc were used to define* ψ^c *according to Equation (5). On the contrary, it seems that in that case* G_c *should be treated as a purely numerical parameter, to be calculated from Equation (5) using* ψ^c *defined from experimental stress–strain curves, making the approach given by (3)–(5) superfluous. Moreover, it can be shown that (5) is strictly valid only for brittle fracture. It corresponds to the definition* $\psi^c = 0.5\,\sigma_c \varepsilon_c$*, with* σ_c *and* ε_c *being the critical (peak) stress and its corresponding strain, respectively, obtained by analytically solving a 1-D problem; see, e.g.,* [41].

Here the problem described in the Remark was avoided because we adopted a brittle fracture model, and ψ^c has to be modified anyway in fatigue analyses due to the action of cyclic loading. Therefore, in the presented simulations, the initial value of ψ^c is defined as in (5) using the experimentally estimated values for G_c, identified with the procedures described in Section 2.1.1. The length scale parameter can then be calculated using the following expression:

$$l = \frac{3}{4\sqrt{2}} \frac{G_{\mathrm{C}} E}{(\sigma^c)^2} \tag{6}$$

where σ^c corresponds to the ultimate tensile stress.

The degradation in fracture energy caused by fatigue is defined by a fatigue degradation function $\hat{F}(\overline{\psi})$ as

$$\psi^c(\overline{\psi}) = \frac{3}{8\sqrt{2}} \frac{G_c(\overline{\psi})}{l}, \; G_c(\overline{\psi}) = \hat{F}(\overline{\psi})\, G_c \tag{7}$$

In this work, the logarithmic fatigue degradation function (reported in [24,25] in an erroneous form) is defined as

$$\hat{F}(\overline{\psi}) = \left(1 - \log \frac{\overline{\psi}_{\infty}}{\overline{\psi}}\right)^2, \; \text{for}\, \overline{\psi} \in \left[\overline{\psi}_{\infty}, 10\,\overline{\psi}_{\infty}\right] \tag{8}$$

with $\overline{\psi}_{\infty}$ as the fatigue model parameter, which here is calibrated to capture the total life of the examined material given by an experimental S–N curve.

The governing equations in the strong form are the standard equilibrium equations with the corresponding natural and displacement boundary conditions, and the evolution equation of the phase-field, both obtained by adopting homogeneous natural boundary

conditions for the phase-field (see [25,39] for the derivations). After introducing a few modifications, the evolution equation of the phase-field can be written as

$$-l^2\Delta\phi + [1+\mathcal{H}]\phi = \mathcal{H} \tag{9}$$

Herein, $\mathcal{H}$ is the history field parameter introduced to impose the irreversibility condition of the phase field ($\dot{\phi}(t) \geq 0$), according to Miehe et al. [42]. Here it is defined as

$$\mathcal{H}(t) := \max_{\tau\in[0,t]} \widetilde{D}(\psi_e(\tau)), \tag{10}$$

with

$$\widetilde{D}(\psi_e(\tau)) = \left\langle \frac{\psi_e(\tau)}{\psi^c(\overline{\psi}(\tau))} - 1 \right\rangle_+ \quad \text{for } \forall\tau \in [0,t] \tag{11}$$

being the crack driving state function at some moment τ during the loading process. The Macaulay bracket was introduced in order to keep the phase-field bounded ($\phi \geq 0$).

The governing equations in the weak form are obtained by introducing definitions (7), (8), (10) and (11) in the internal weak form (1), and applying the principle of virtual work, as described in [24,25].

2.2.2. Numerical Implementation

An interested reader can find important details about the discretization procedures for and numerical implementation of numerical models in the commercial program package Abaqus in [24,25,43]. An important modification to those works is a new cyclic skipping procedure developed in order to reduce computational time and memory demands.

Numerical PF models based on FEM are computationally demanding due to the requirement for dense mesh discretization around cracks, which requires a large computational time and memory resources. When solving HCF problems, these requirements are multiplied because of the large number of loading cycles that have to be simulated until reaching total failure. To reduce computational costs, herein a two-step cycle skipping technique is embedded into the existing numerical routines for the presented PF formulation, relying on the energy accumulation variable $\overline{\psi}$. The first cycle skipping step seeks the cycle in which the initial degradation of the bulk material occurs, satisfying the condition:

$$\hat{F}(\overline{\psi})\psi_c < \psi_e \tag{12}$$

as in [24]. Since prior to damage initiation a constant loading amplitude leads to a constant change in the strain energy density $\Delta\psi$ inside each cycle, the accumulated energy variable value can be calculated as

$$\overline{\psi} = N_1\Delta\psi \tag{13}$$

By inserting (8) and (13) into (12), the number of cycles to crack initiation, which can be skipped after the first step, is computed via

$$N_1 = \frac{\overline{\psi}}{\Delta\psi} 10^{-\sqrt{\frac{\overline{\psi}}{\psi_c}}} \tag{14}$$

After the onset of damage, further cycle skipping is performed as described below. It is based on the extrapolation procedure proposed in [44]. For two consecutive loading cycles exhibiting changes in the accumulation variables $\Delta\overline{\psi}_1$ and $\Delta\overline{\psi}_2$, respectively, the number of cycles skipped is computed using the relation

$$\Delta N_2 = q\frac{\Delta\overline{\psi}_2}{\Delta\overline{\psi}_2 - \Delta\overline{\psi}_1} \tag{15}$$

where q represents a fidelity parameter, which controls the maximum allowed number of skipped cycles. After finding the appropriate number of skipped cycles according to

Equation (15), the result is used for extrapolation of the accumulation variable from the previously achieved value after N cycles as

$$\overline{\psi}(\mathrm{N}+\Delta\mathrm{N}_2) = \overline{\psi}(\mathrm{N}) + \Delta\overline{\psi}_2\Delta\mathrm{N}_2 + \frac{1}{2}(\Delta\overline{\psi}_2 - \Delta\overline{\psi}_1)(\Delta\mathrm{N}_2)^2 \tag{16}$$

The presented procedure is embedded into the FE software Abaqus by means of the subroutine UEXTERNALDB.

2.3. Numerical Modelling of Microstructure

Two-dimensional (2D) models of heterogeneous microstructures were extracted from high-resolution 4K metallography images, the specimens previously being polished and etched for a few seconds in 3% Nital fluid. Figure 9 shows the microstructure of the 6.5 g/cm^3 sample and the process of extracting a corresponding numerical model. The models were chosen in a such way that the ferrite percentage is around 30% [32] for all densities. To acknowledge the fact that the aim of this contribution is studying fracture processes at the material microlevel, in this work the considered parts of the microstructure are called the Microscopic Volume Elements (MVE), rather than the Representative Volume Elements (RVE).

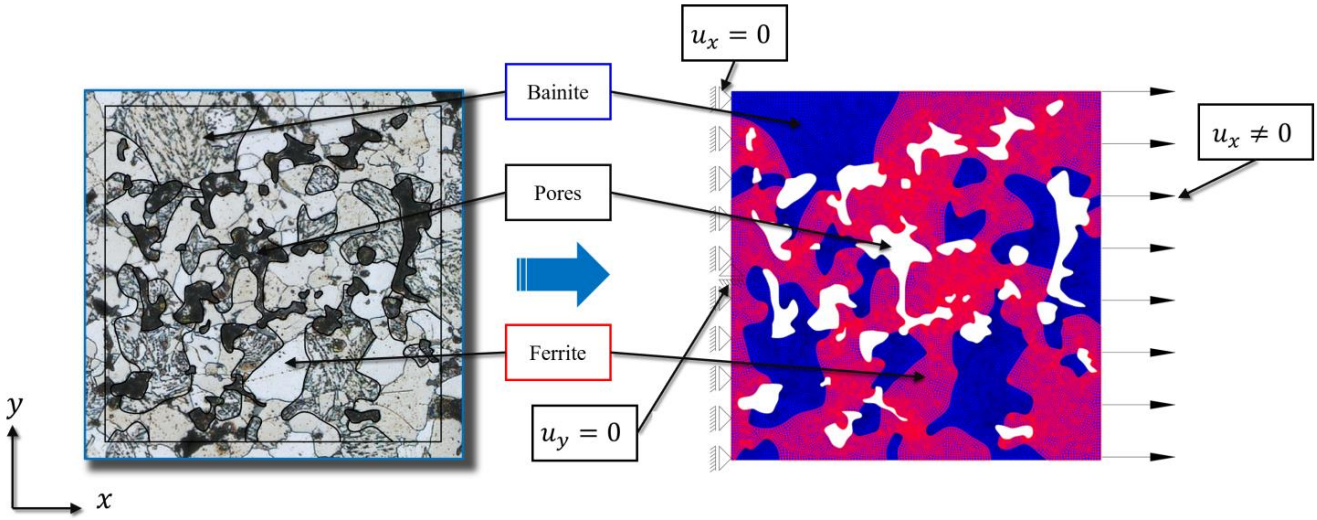

Figure 9. Metallography image of microstructure and extraction of 2D numerical model with corresponding boundary conditions.

Two-dimensional (2D) MVEs were created, where the geometrical models of the microstructures were directly extracted from metallographic photographs using AutoCAD software. The considered microstructures were modelled to a high degree of accuracy, but the grain and pore boundaries were approximated by spline curves. The thus obtained graphical models were then exported into Abaqus software [45], where adequate meshes were generated. Since the pores and different phases are described with spline lines, the discretization process was not dependent on the resolution of lines, which would be the case if polylines were used.

Three different sizes of MVEs with side lengths of 0.2, 0.3 and 0.4 mm were modelled for each density in order to investigate size effects. The boundary conditions corresponding to the uniaxial tensile test (UTT) were prescribed on the MVE models by imposing displacements on the left and right vertical edges, while considering the remaining outer edges to be free surfaces (Figure 9). In all models non-zero horizontal displacements were imposed along the right edge, which correspond to the loading and vary during the loading process. Along the left edge, the horizontal degree of freedom (x axis) was suppressed. Moreover, at the node in the middle of the left edge, the vertical degree of freedom (y axis) was also

suppressed in order to avoid rigid body motion. Homogeneous zero natural boundary conditions were defined along the upper and lower horizontal edges.

The models presented were discretized using approximately 30,000, 70,000 and 130,000 quadrilateral finite elements for the 0.2 (Model S), 0.3 (Model M) and 0.4 (Model L) mm models, respectively, for all three densities (Figure 10). The average element size was h = 1.5 µm, chosen so that the microstructural topology could be captured in detail. The size of the elements is therefore much smaller than the size of individual grains and pores. Ferrite grains have the approximate size of 30 µm and the approximate size of bainite grains is 70 µm, while the pores range from 20–80 µm [33]. At the same time, the demand that $h < 1/2l$, necessary to accurately resolve the phase field using the applied PF formulation, is satisfied. Numerical simulations were conducted on a workstation with an AMD CPU with 3.80 GHz base clock, 128 GB of RAM and acceleration with a NVidia RTX™ GPU card. The duration of each simulation was around 20, 30 and 54 h for the S, M and L models, respectively.

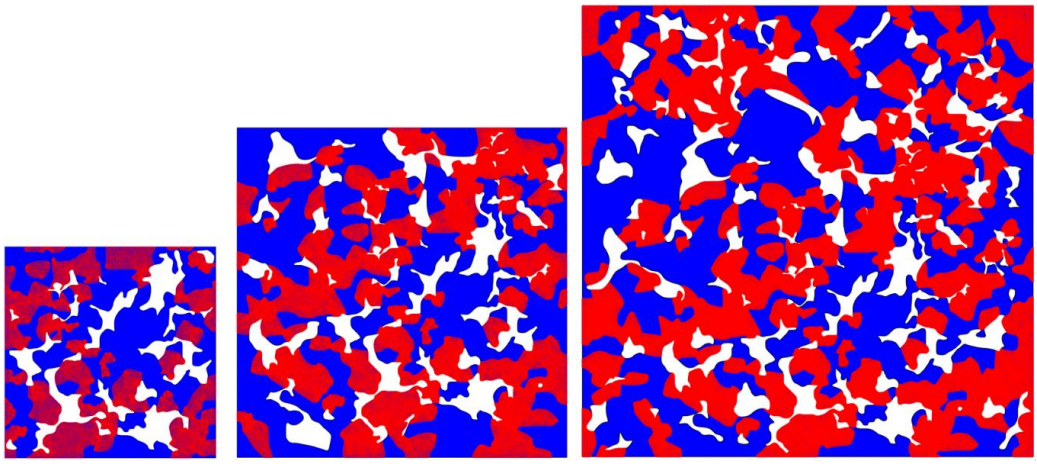

(**a**) (**b**) (**c**)

Figure 10. Different MVE size models for 6.5 g/cm^3 density. The red region corresponds to the bainite phase, while the blue region corresponds to the ferrite phase. (**a**) 0.2 mm—Model S, (**b**) 0.3 mm—Model M, (**c**) 0.4—Model L.

The average strains and stresses for the numerically obtained stress–strain diagrams presented in the following chapter are calculated for each MVE as:

$$\sigma = \frac{RF}{L}, \quad \varepsilon = \frac{u}{L} \tag{17}$$

where RF, u, and L are the total reactive force, average horizontal displacement at the loaded side, and side length of MVE, respectively.

As presented in the introduction, various sophisticated PF models for microfracture in heterogeneous materials have been proposed, but they demand significant computational costs, and this problem would only be further exacerbated in HCF simulations with complex geometries, such as those encountered in the microstructures of sintered steels. Therefore, the following simplifications are adopted here:

- The interfaces between individual material phases are not modelled as separate entities or properties. Consequently, the present model is unable to simulate interphase fracture.
- Both material phases are considered to be elastically isotropic, with properties given in Table 3, with bainite regarded as being homogenous.
- The isotropic fracture surface energy defined in Equation (1) is adopted.
- Plastic deformation, which can normally be expected during the microfracture of sintered metals, is neglected.

Table 3. Identified elastic properties [33] and fracture toughness of material phases.

	Bainite	**Ferrite**
Modulus of elasticity, E, MPa	239,000	186,000
Poisson ratio, v, -	0.28	
Energy release rate (Fracture toughness), G_C, N/mm	8.5	14.5

From the above, it can be concluded that this model can be called a simplified PF model for HCF in multiphase sintered materials.

The present model is not suitable for accurate modelling of microfracture patterns in polycrystals, as anisotropy is not taken into account. However, in this work we observed our heterogeneous material at a higher length scale, where the material phases are homogenized and are not considered polycrystals.

3. Results and Discussion

3.1. Quasi-Static Fracture

First, only the elastic response from the numerical model of the microstructure was investigated. A comparison of the experimentally obtained macroscopic modulus of elasticity and the effective modulus of elasticity obtained using the numerical model is presented in Figure 11. The simulation results for the specimen with a density of 6.5 g/cm^3 exhibit a larger scattering of results and higher error than the results for the other two densities, indicating a more pronounced size effect. In addition, for this density the value of the effective elastic modulus increases with increasing MVE size, which is not a physical behavior. This indicates that, for this density, larger MVEs should be considered to establish a representative volume element (RVE) for elastic behavior.

Important to note here is that, for smaller porosity levels, the bulk (macro) modulus of elasticity can be predicted quite accurately using these numerical models for a heterogeneous microstructure, with the local elastic material parameters (the moduli of elasticity of different metallic phases) obtained using the applied instrumented micro-indentation.

Microcrack initiation and propagation were analyzed next. From the average stress–strain responses presented in Figure 11 it is obvious that the present model is unable to accurately capture the global nonlinear response, mainly because the plastic deformation of individual material phases is neglected in the numerical model. Due to the absence of plastic deformation in the numerical models, the final elongation is generally grossly underestimated, and overly early advent of sudden fracture (unstable global crack propagation) through the material is predicted. However, the size effect is still visible, in accordance with the observations in [14]. The modelled MVEs (except for the S model with 6.5 g/cm^3) predict a higher peak stress (the tensile strength) than the macroscopic sample, which is again consistent with size effect phenomena. Sudden vertical drops in stress values are visible in post-peak (softening) responses, which are caused by the brittle fractures of small "bridges" between the pores (particle necks appearing during the sintering process as bonds formed between powder particles). A small bridge breaks when a microfracture initiated at a pore at one end of the bridge propagates until reaching a pore positioned at another side of the bridge. In addition, note that the numerical model correctly predicts that tensile strength increases with a reducing porosity level in the material, which is clearly visible at the macrolevel [33]. This could be attributed to greater distances between the initiated microcracks in the material with higher density, i.e., lower porosity. In that case, higher loading is needed to cause growth and coalescence of microcracks sufficient to trigger global softening.

The predicted fracture patterns were examined next. The propagation of microcracks during the loading process is illustrated in Figure 12. The areas with high values of the phase field correspond to highly damaged materials. Theoretically, the points where $\phi = 1$ define well-formed microcracks, i.e., crack paths. On the other hand, in areas where the phase field is equal to zero, the material is intact. For points where the phase field is

in between these extreme values, the material stiffness and fracture properties, i.e., the modulus of elasticity and fracture toughness, degrade due to sustained damage. The cracks propagate from one pore to another until they coalesce into larger cracks, which finally results in a macroscopic fracture.

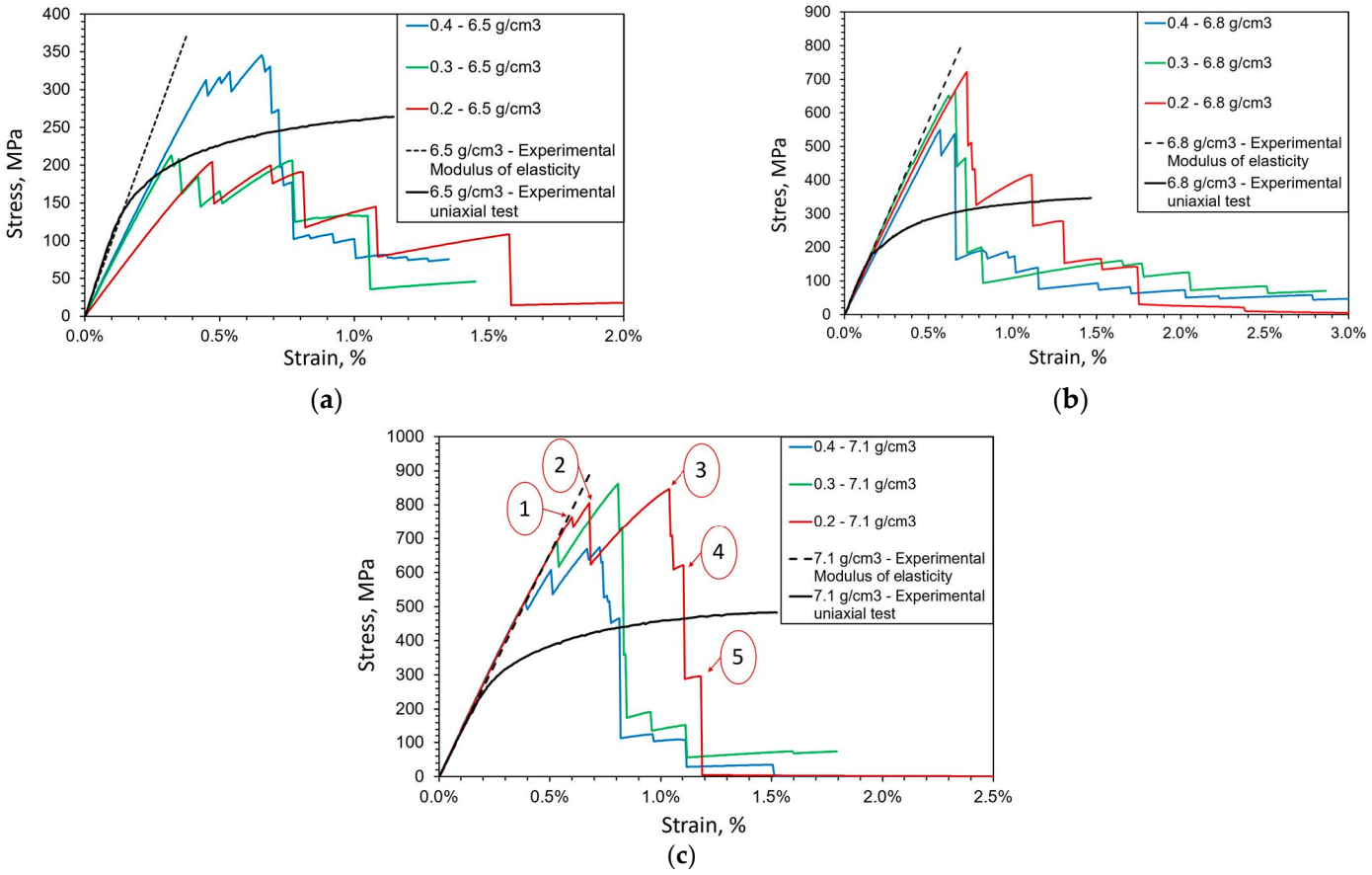

Figure 11. Average stress–strain response with respect to size in numerical models of microstructure for different densities: (**a**) 6.5 g/cm^3, (**b**) 6.8 g/cm^3, (**c**) 7.1 g/cm^3. The points marked by numbers from 1 to 5 in Figure (**c**) are used to present the evolution of microcracks in Figure 12.

A closer inspection of crack patterns reveals that, in accordance with expectations, the model predicts transgranular microcracks, where cracks pass through different phases (ferrite or bainite). In Figure 13 it is visible that in most cases the microcracks propagate through a bainite zone, since bainite has stiffer behavior (higher modulus of elasticity) and lower fracture resistance (lower fracture toughness) than ferrite. Cracks typically initiate in bainite zones at the edge of pores, which act as stress concentrators. The further propagation of a microcrack is driven by the microstructure's topology, because the relative distribution of material phases and pores in the microstructure dictates the stress distribution and fracture energy.

An interesting phenomenon where a ferrite phase stops the further propagation of a crack may be clearly observed in Figure 13c. This indicates that it could be necessary to include intergranular crack propagation into the model if realistic crack patterns are to be captured using the proposed strategy. Exceptionally, if the minimum strain energy is found for crack propagation through a ferrite zone, the crack continues to propagate through the ferrite zone. This can occur if the ferrite zone is located along a small "bridge" between two pores (in Figure 13c some small "bridges" pass through ferrite). The microcracks often merge or branch, as is visible in Figure 13a–c.

From the presented results it can be concluded that the presented model is qualitatively able to capture the propagation of microcracks by the mechanism of collapsing "bridges" between pores, also visible in the SEM images (Figure 8).

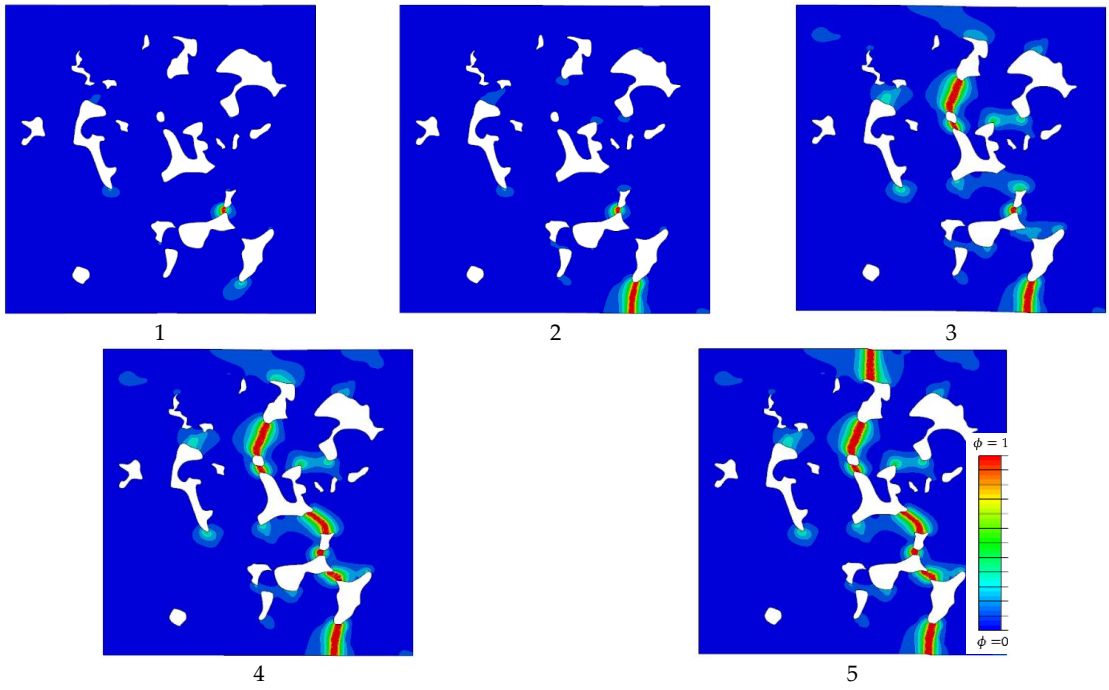

Figure 12. Microcrack propagation in S model (size 0.2 × 0.2 mm) with 7.1 g/cm^3. 1–5 show phase field distribution in the model for the loading states that correspond to the points marked 1–5 on the stress–strain curve in Figure 11c.

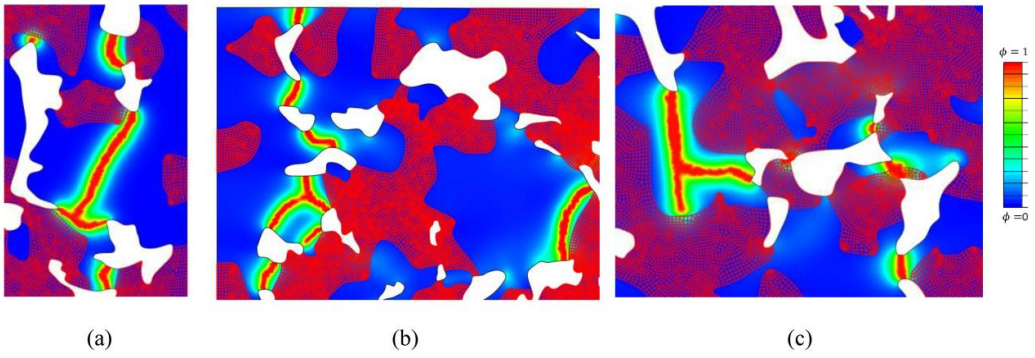

Figure 13. Transgranular cracks predicted using the PF model. Blue areas correspond to bainite and red to ferrite. (**a**) detail of L model of 6.8 g/cm^3, (**b**) detail of M model of 6.8 g/cm^3, (**c**) detail of M model of 7.1 g/cm^3.

3.2. Cyclic Loading

The PF model for fatigue failure, employing the degrading fracture energy defined by (7) and the cycle skipping technique for speeding up the calculations, was used for all fatigue simulations. Identical geometric models of the microstructure and finite element meshes as those for monotonous quasi-static fracture analysis were used. For the purpose of brevity, here only the results obtained from L-size microstructure models are presented. Instead of the loading used in the static case, herein loading conditions were imposed on the microstructure by means of kinematic restraints, where the concentrated nodal force F_{cyc} is prescribed to a reference node coupled via the imposed kinematic constraints to all nodes positioned at the loaded edge (Figure 14). Moreover, the left edge was restrained in the x direction and the middle node on the left edge in the y direction.

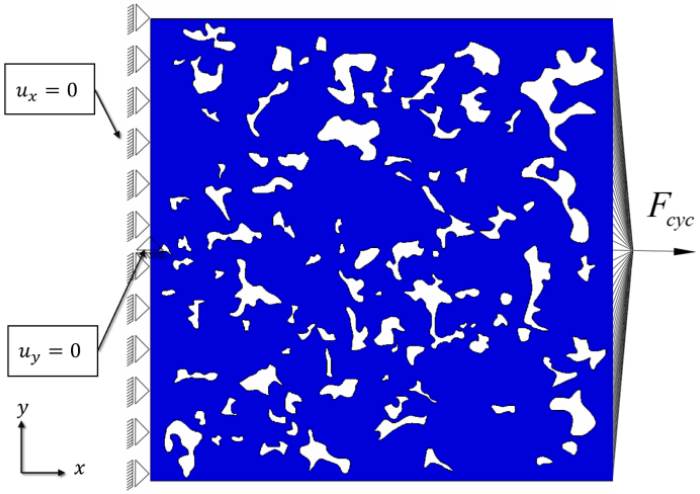

Figure 14. Boundary conditions of the 6.8 g/cm^3 L model for fatigue modelling.

The material parameters given in Tables 1 and 2 were used in simulations, and the loading ratio for all densities was kept at $R = 0.05$, as in the experimental testing discussed in Section 2.1.2. The value of fatigue parameter $\overline{\psi}_\infty$ was chosen as 50 (for both phases) in order to best fit the experimental S–N curves.

Using the cycle skipping feature explained in Section 2.2, the duration of simulations was reduced from a few weeks (5–6) to a few (4–5) days. Another benefit in comparison to the formulation from [24] was a significant reduction in memory demands. For an HCF test with $N_f \approx 10^7$ the present algorithm does not require more than 150 GB (for a numerical model with more than 100 000 finite elements), which is available in most desktop computers nowadays. The authors believe that a similar HCF simulation without a cycle skipping feature would possibly require a few terabytes of data.

Numerically obtained Wöhler curves are presented Figure 15. The model predicted the fatigue total life relatively well in the HCF regime. For a smaller number of cycles it seems that the model tended to overestimate the experimentally determined total life, probably due to neglecting plastic deformation and intergranular cracks. This could be important because the local plastic flow could be significant, especially around small "bridges" between pores, and could contribute significantly to the formation of microcracks [3]. In addition, it seems that in the present model the ferrite phases sometimes stop the further propagation of microcracks, similarly to pores, while in reality the crack could propagate along the interface between the adjacent ferrite and bainite phases. On the other hand, a slight underestimation of the total life could be observed for low loading, possibly because stress concentrations in MVEs lead to large energy accumulation per cycle and therefore the energy accumulation variable $\overline{\psi}$ grows faster, resulting in the underestimation of critical fracture energy during the process.

As already explained, for accurate simulation of microfractures, elasto-plastic analysis would be a preferable approach, but characterizing the plastic parameters of individual material phases in multi-phase materials is by no means a simple task and requires appropriate nano-indenters. Even then, its accuracy depends greatly on the method applied for reconstructing stress–strain curves [27,29]. During our research, we were not able to obtain reliable data for plastic parameters of ferrite and bainite. In addition, in elasto-plastic PF models with a threshold, the critical fracture energy per volume (the specific fracture energy) and not the critical release energy release rate G_c should figure as the model parameter, as explained in Section 2.2. This, however, demands that the maximum stress (i.e., the tension strength) be characterized for each phase, which is another challenge in instrumental indentation. Although plasticity is not included in the proposed model, it could nevertheless be said that the influence of plastic deformation is implicitly captured in the present modelling paradigm in HCF regime. It is also noted that in [24] a way

to fine-tune the fatigue degradation function $\hat{F}(\overline{\psi})$ is proposed, which, however, is not pursued in the scope of this work.

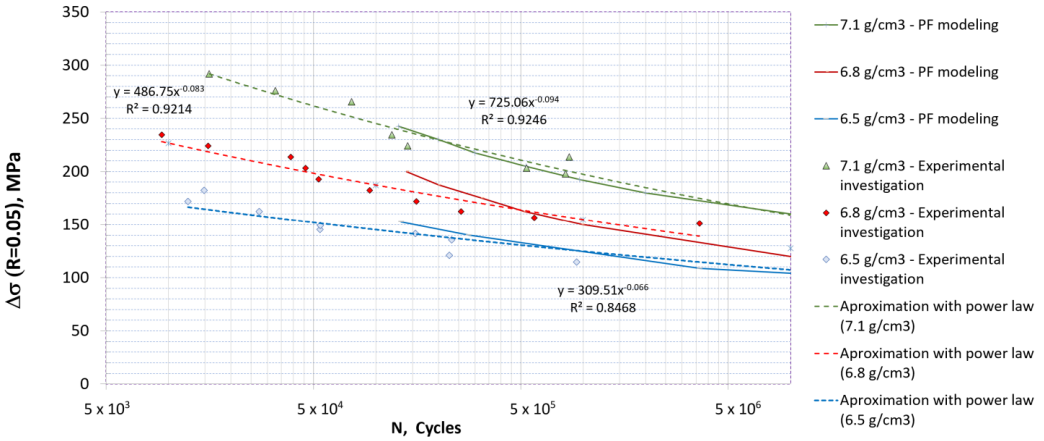

Figure 15. Wöhler curves obtained using the PF model for fatigue fracture for different densities of sintered steel. The L-size numerical model of the material microstructure is applied for all curves.

In Figure 16 the microcrack patterns in MVEs just before the onset of total failure are shown for the same loading case with $\Delta\sigma$ = 152 MPa. For higher densities, the microcracks coalesce into larger cracks vertical to the loading direction (horizontal in images) in the "weakest" cross sections (those with the largest ratio of pores along the section). This behavior qualitatively corresponds well to the brittle fatigue fracture observed in macroscopic samples during UTT (see Figure 1c). In the sample with the highest level of porosity, it seems that large cracks are formed in a more "diffuse" manner by joining the cracks in the smallest "bridges" in the microstructure.

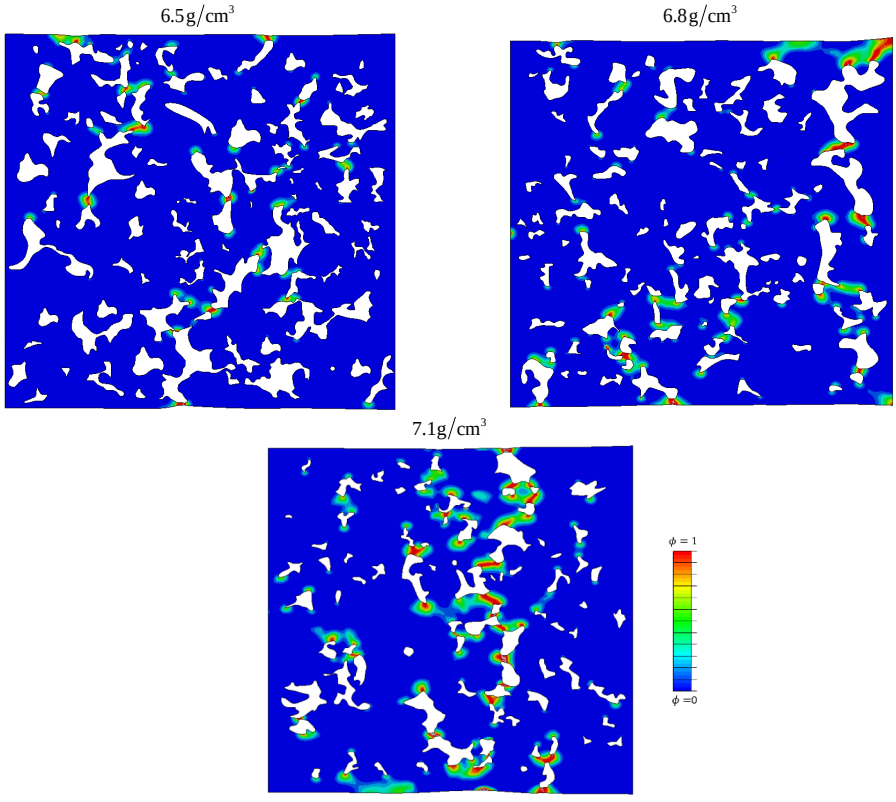

Figure 16. Numerically obtained microcrack patterns before the onset of total failure for identical loading cases with $\Delta\sigma$ = 152 MPa. Figures show the distribution of the phase field at the moment right before complete failure.

This is further demonstrated in Figure 17, where the evolution of microcracks in the microstructure with 7.1 g/cm^3 density is presented. The first microcracks appear at certain small bridges (Figure 17c,d). Gradually, other bridges collapse (Figure 17e) with a tendency to connect and create one larger microcrack (Figure 17f). A similar observation was noticed by Falkowska and Seweryn [46] in their experimental SEM observation of sintered steel samples with different densities submitted to cyclic loading.

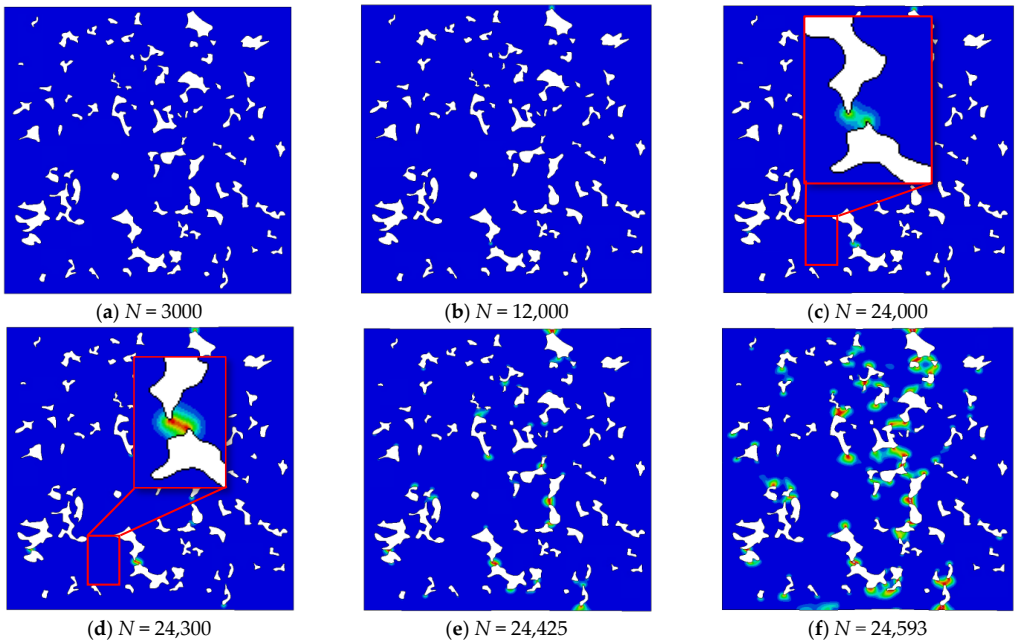

Figure 17. Evolution of fatigue microcracks for density 7.1 g/cm^3 and $\Delta\sigma = 152$ MPa. (**a**–**f**) show phase field distribution in the model after different numbers of loading cycles.

In addition, the simulation results (see Figure 17) imply that most of the fatigue degradation takes place in the last few hundred cycles before complete failure. Such behavior is typical for the degradation function (Equation (8)) used in this paper, and is similar to the observations gained by inspecting loading–unloading cycles under static loading (Figure 6), which also suggest that the fracture appears suddenly after the material suffers a certain amount of degradation. To confirm this result, measurement of resonant frequency during experimental testing was performed, since any deviation in frequency can be continuously monitored and directly coupled to microcrack propagation inside the tested specimen (while maintaining a fixed room temperature). Such a change in the resonant frequency is displayed in Figure 18, where a sudden drop is visible just a few hundred cycles before the final failure.

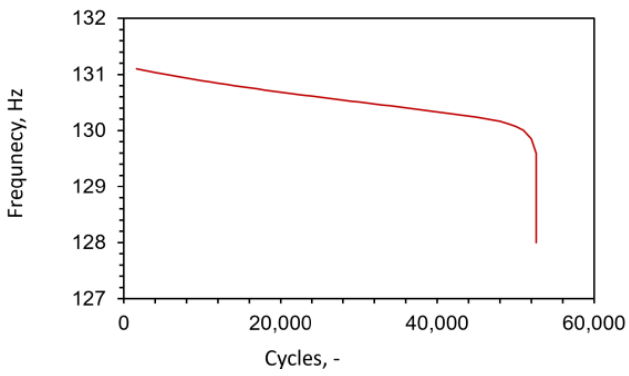

Figure 18. Resonant frequency with respect to number of loading cycles for a specimen with density 6.5 g/cm^3.

4. Conclusions

A fast numerical method based on a phase-field model for fracture is proposed for estimating the fatigue total life of multiphase sintered steels through simulations of fatigue microfracture in the material. In contrast to existing models for multiphase materials, herein a simplified numerical phase-field model for fatigue fracture based on the Finite Element Method is employed in order to reduce the large computational resources needed for numerical fatigue simulations. Plastic deformation is neglected in the present model, the influence of material interfaces is not modelled, and the material phases are assumed to be isotropic. A new cycle-skipping algorithm is also proposed, which can yield further savings in computation costs. The model can be calibrated by identifying microscopic elastic material parameters using instrumented indentation, while fracture parameters are calibrated from experimental S–N curves.

The model exhibits some size effects, such as reducing the effective maximum stress and elastic modulus of sintered steel with increasing sizes of considered microscopic volume elements (MVEs). The results indicate that the model captures well the initiation of the first damage in the microstructure, where microcracks first appear in the narrowest bridges between two closely located pores. In addition, the initiation and propagation of larger fatigue cracks in the material, corresponding to the brittle fracture observed experimentally in the examined material, are qualitatively captured. This confirms the experimentally confirmed fact that fracture propagation in porous sintered steels is strongly driven by porosity. However, the proposed model is unable to yield realistic crack patterns in the microstructure due to the assumed simplifications. Nevertheless, the obtained results indicate that the proposed approach is suitable for investigating the influence of porosity on the fatigue total life in a high cycle fatigue (HCF) regime. Therefore, it could be used for preliminary investigation in research dealing with the influence of microstructure on fatigue failure in similar sintered steels.

In order to obtain more accurate predictions for fracture patterns, future research will be dedicated to extending the model to ductile failure by including plastic deformation, as well as including models of intergranular crack propagation. Thereby, special attention should be paid to the mechanical characterization of local material plastic and fracture parameters. Besides improvements in constitutive modelling of the microstructure, an extension towards 3D modelling will be also considered. Based on the results obtained for fatigue response at the material microscale, a procedure will be proposed for the assessment of macroscopic fatigue parameters based on explicit numerical modelling of material fatigue at the microscale.

Author Contributions: Z.T. (Zoran Tomić): Conceptualization, Methodology, Experimental investigation, Numerical calculations, Results preparation, Writing—original draft, T.J.: Conceptualization, Methodology, Writing—original draft, review and editing, Supervision, T.L.: Coding, Writing—review and editing, Numerical calculations. N.G.: Experimental investigation, Z.T. (Zdenko Tonković): Supervision, Resources. All authors have read and agreed to the published version of the manuscript.

Funding: This work was fully supported by the Croatian Science Foundation under the project "Multiscale Numerical Modelling and Experimental Investigation of Aging Processes in Sintered Structural Components" (MultiSintAge, PZS-1 2019-02-4177).

Institutional Review Board Statement: Not applicable.

Informed Consent Statement: Not applicable.

Data Availability Statement: Data sharing not applicable.

Conflicts of Interest: The authors declare that they have no known competing financial interests or personal relationships that could have appeared to influence the work reported in this paper.

References

1. Danninger, H. What will Be the Future of Powder Metallurgy? *Powder Metall. Prog.* **2018**, *18*, 70–79. [CrossRef]
2. Dudrova, E.; Kabatova, M. Fractography of sintered iron and steels. *Powder Metall. Prog.* **2008**, *8*, 59–75.

3. Dudrova, E.; Kabátova, M. A review of failure of sintered steels: Fractography of static and dynamic crack nucleation, coalescence, growth and propagation. *Powder Metall.* **2016**, *59*, 148–167. [CrossRef]
4. Sukumar, N.; Srolovitz, D.J.; Baker, T.J.; Prévost, J.-H. Brittle fracture in polycrystalline microstructures with the extended finite element method. *Int. J. Numer. Methods Eng.* **2003**, *56*, 2015–2037. [CrossRef]
5. Shibanuma, K.; Suzuki, Y.; Kiriyama, K.; Suzuki, K.; Shirahata, H. A model of cleavage crack propagation in a BCC polycrystalline solid based on the extended finite element method. *Acta Mater.* **2019**, *176*, 232–241. [CrossRef]
6. Prechtel, M.; Ronda, P.L.; Janisch, R.; Hartmaier, A.; Leugering, G.; Steinmann, P.; Stingl, M. Simulation of fracture in heterogeneous elastic materials with cohesive zone models. *Int. J. Fract.* **2011**, *168*, 15–29. [CrossRef]
7. Wei, Y.J.; Anand, L. Grain-boundary sliding and separation in polycrystalline metals: Application to nanocrystalline fcc metals. *J. Mech. Phys. Solids.* **2004**, *52*, 2587–2616. [CrossRef]
8. Mousavi, S.M.T.; Richart, N.; Wolff, C.; Molinari, J.F. Dynamic crack propagation in a heterogeneous ceramic microstructure, insights from a cohesive model. *Acta Mater.* **2015**, *88*, 136–146. [CrossRef]
9. Cervera, M.; Wu, J.-Y. On the conformity of strong, regularized, embedded and smeared discontinuity approaches for the modeling of localized failure in solids. *Int. J. Solids Struct.* **2015**, *71*, 19–38. [CrossRef]
10. Funari, M.F.; Lonetti, P.; Spadea, S. A crack growth strategy based on moving mesh method and fracture mechanics. *Theor. Appl. Fract. Mech.* **2019**, *102*, 103–115. [CrossRef]
11. Nguyen, T.T.; Yvonnet, J.; Zhu, Q.Z.; Bornert, M.; Chateau, C. A phase field method to simulate crack nucleation and propagation in strongly heterogeneous materials from direct imaging of their microstructure. *Eng. Fract. Mech.* **2015**, *139*, 18–39. [CrossRef]
12. Miehe, C.; Hofacker, M.; Welschinger, F. A phase field model for rate-independent crack propagation: Robust algorithmic implementation based on operator splits. *Comput. Methods Appl. Mech. Eng.* **2010**, *199*, 2765–2778. [CrossRef]
13. Nguyen, T.T.; Yvonnet, J.; Bornert, M.; Chateau, C. Initiation and propagation of complex 3D networks of cracks in heterogeneous quasi-brittle materials: Direct comparison between in situ testing-microCT experiments and phase field simulations. *J. Mech. Phys. Solids* **2016**, *95*, 320–350. [CrossRef]
14. Seleš, K.; Jurčević, A.; Tonković, Z.; Sorić, J. Crack propagation prediction in heterogeneous microstructure using an efficient phase-field algorithm. *Theor. Appl. Fract. Mech.* **2019**, *100*, 289–297. [CrossRef]
15. Abdollahi, A.; Arias, I. Numerical simulation of intergranular and transgranular crack propagation in ferroelectric polycrystals. *Int. J. Fract.* **2012**, *174*, 3–15. [CrossRef]
16. Emdadi, A.; Zaeem, M.A. Phase-field modeling of crack propagation in polycrystalline materials. *Comput. Mater. Sci.* **2021**, *186*, 110057. [CrossRef]
17. Oshima, K.; Takaki, T.; Muramatsu, M. Development of multi-phase-field crack model for crack propagation in polycrystal. *Int. J. Comput. Mater. Sci. Eng.* **2014**, *3*, 1450009. [CrossRef]
18. Schneider, D.; Schoof, E.; Huang, Y.; Selzer, M.; Nestler, B. Phase-field modeling of crack propagation in multiphase systems. *Comput. Methods Appl. Mech. Eng.* **2016**, *312*, 186–195. [CrossRef]
19. Clayton, J.D.; Knap, J. Phase field modeling of directional fracture in anisotropic polycrystals. *Comput. Mater. Sci.* **2015**, *98*, 158–169. [CrossRef]
20. Clayton, J.D. Modeling Deformation and Fracture of Boron-Based Ceramics with Nonuniform Grain and Phase Boundaries and Thermal-Residual Stress. *Solids* **2022**, *3*, 643–664. [CrossRef]
21. Nguyen, T.-T.; Réthoré, J.; Yvonnet, J.; Baietto, M.-C. Multi-phase-field modeling of anisotropic crack propagation for polycrystalline materials. *Comput. Mech.* **2017**, *60*, 289–314. [CrossRef]
22. Nguyen, T.T.; Yvonnet, J.; Zhu, Q.-Z.; Bornert, M.; Chateau, C. A phase-field method for computational modeling of interfacial damage interacting with crack propagation in realistic microstructures obtained by microtomography. *Comput. Methods Appl. Mech. Eng.* **2016**, *312*, 567–595. [CrossRef]
23. Li, G.; Yin, B.B.; Zhang, L.W.; Liew, K.M. Modeling microfracture evolution in heterogeneous composites: A coupled cohesive phase-field model. *J. Mech. Phys. Solids* **2020**, *142*, 103968. [CrossRef]
24. Seleš, K.; Tomić, Z.; Tonković, Z. Microcrack propagation under monotonic and cyclic loading conditions using generalised phase-field formulation. *Eng. Fract. Mech.* **2021**, *255*, 107973. [CrossRef]
25. Seleš, K.; Aldakheel, F.; Tonković, Z.; Sorić, J.; Wriggers, P. A general phase-field model for fatigue failure in brittle and ductile solids. *Comput. Mech.* **2021**, *67*, 1431–1452. [CrossRef]
26. Oliver, W.C.; Pharr, G.M. An improved technique for determining hardness and elastic modulus using load and displacement sensing indentation experiments. *J. Mater. Res.* **1992**, *7*, 1564–1583. [CrossRef]
27. Giannakopoulos, A.E.; Suresh, S. Determiantion of elastoplastic properties by instrumented sharp indentation. *Scr. Mater.* **1999**, *40*, 1191–1198. [CrossRef]
28. Lu, L.; Dao, M.; Kumar, P.; Ramamurty, U.; Karniadakis, G.E.; Suresh, S. Extraction of mechanical properties of materials through deep learning from instrumented indentation. *Proc. Natl. Acad. Sci. USA* **2020**, *117*, 7052–7062. [CrossRef]
29. Donohue, B.R.; Ambrus, A.; Kalidindi, S.R. Critical evaluation of the indentation data analyses methods for the extraction of isotropic uniaxial mechanical properties using finite element models. *Acta Mater.* **2012**, *60*, 3943–3952. [CrossRef]
30. Cheng, G.; Choi, K.S.; Hu, X.; Sun, X. Determining individual phase properties in a multi-phase Q&P steel using multi-scale indentation tests. *Mater. Sci. Eng. A* **2016**, *652*, 384–395. [CrossRef]

31. Höganäs, A.B. *Iron-Based Materials, Design and Mechanical Properties—Höganäs Handbook for Sintered Components*; Höganäs: Halmstad, Sweden, 2015; pp. 45–90.
32. *ASTM E8*; Standard Testing Methods for Tension Testing of Metallic Materials. ASTM: West Conshohocken, PA, USA, 2016.
33. Tomić, Z.; Gubeljak, N.; Jarak, T.; Polančec, T.; Tonković, Z. Micro—And macromechanical properties of sintered steel with different porosity. *Scr. Mater.* **2022**, *217*, 114787. [CrossRef]
34. Anstis, G.R.; Chantikul, P.; Lawn, B.R.; Marshall, D.B. A Critical Evaluation of Indentation Techniques for Measuring Fracture Toughness: I, Direct Crack Measurements. *J. Am. Ceram. Soc.* **1981**, *64*, 533–538. [CrossRef]
35. TFabijanić, A.; Ćorić, D.; Musa, M.Š.; Sakoman, M. Vickers indentation fracture toughness of near-nano and nanostructured WC-Co cemented carbides. *Metals* **2017**, *7*, 143. [CrossRef]
36. Jeon, S.-W.; Lee, K.-W.; Kim, J.Y.; Kim, W.J.; Park, C.-P.; Kwon, D. Estimation of Fracture Toughness of Metallic Materials Using Instrumented Indentation: Critical Indentation Stress and Strain Model. *Exp. Mech.* **2016**, *57*, 1013–1025. [CrossRef]
37. Doroszko, M.; Seweryn, A. Modeling of the tension and compression behavior of sintered 316L using micro computed tomography. *Acta Mech. Autom.* **2015**, *9*, 70–74. [CrossRef]
38. Carrara, P.; Ambati, M.; Alessi, R.; De Lorenzis, L. A framework to model the fatigue behavior of brittle materials based on a variational phase-field approach. *Comput. Methods Appl. Mech. Eng.* **2020**, *361*, 112731. [CrossRef]
39. Miehe, C.; Schanzel, L.M.; Ulmer, H. Phase field modeling of fracture in multi-physics problems. Part I. Balance of crack surface and failure criteria for brittle crack propagation in thermo-elastic solids. *Comput. Methods Appl. Mech. Eng.* **2015**, *294*, 449–485. [CrossRef]
40. Miehe, C.; Hofacker, M.; Schanzel, L.M.; Aldakheel, F. Phase field modeling of fracture in multi-physics problems. Part II. Coupled brittle-to-ductile failure criteria and crack propagation in thermo-elastic-plastic solids. *Comput. Methods Appl. Mech. Eng.* **2015**, *294*, 486–522. [CrossRef]
41. Wu, J.-Y.; Nguyen, V.P.; Nguyen, C.T.; Sutula, D.; Sinaie, S.; Bordas, S.P.A. Chapter One—Phase-field modeling of fracture. *Adv. Appl. Mech.* **2020**, *53*, 1–183. [CrossRef]
42. Miehe, C.; Welschinger, F.; Hofacker, M. Thermodynamically consistent phase-field models of fracture: Variational principles and multi-field FE implementations. *Int. J. Numer. Methods Eng.* **2010**, *83*, 1273–1311. [CrossRef]
43. Seleš, K.; Lesičar, T.; Tonković, Z.; Sorić, J. A residual control staggered solution scheme for the phase-field modeling of brittle fracture. *Eng. Fract. Mech.* **2018**, *205*, 370–386. [CrossRef]
44. Cojocaru, D.; Karlsson, A. A simple numerical method of cycle jumps for cyclically loaded structures. *Int. J. Fatigue* **2006**, *28*, 1677–1689. [CrossRef]
45. *Abaqus 6.14-1, Abaqus/CAE User's Guide*; Dassault Systems Simulia Corp.: Providence, RI, USA, 2014.
46. Falkowska, A.; Seweryn, A. Fatigue life of 316L steel sinters of varying porosity under conditions of uniaxial periodically variable loading at a fixed stress amplitude. *Int. J. Fatigue* **2018**, *117*, 496–510. [CrossRef]

PAPER 4.

Reproduced with permission.

Authors:	Zoran Tomić, Tomislav Jarak, Benjamin Pavlović, Zdenko Tonković
Title:	On extracting stress-strain curves of porous multi-phase sintered steels by microindentation
Journal:	Experimental Techniques
Quartile/Impact Factor	Q2/1.6
Bibliography data:	Year: 2023
DOI:	https://doi.org/10.1007/s40799-023-00684-8

Experimental Techniques
https://doi.org/10.1007/s40799-023-00684-8

RESEARCH PAPER

On Extracting Stress–Strain Curves of Porous Multi-Phase Sintered Steels by Microindentation

Z. Tomić[1] · T. Jarak[1,2] · B. Pavlović[1] · Z. Tonković[1]

Received: 15 January 2023 / Accepted: 25 October 2023

Abstract

The efficient characterization of material properties of porous multi-phase sintered steels by instrumental indentation is still an open question. To the authors' knowledge, so far only a characterization of single-phase porous sintered steel by nanoindenation has been reported in literature. This paper for the first time offers a study about the applicability of microindentation techniques for characterizing the matrix material in a multi-phase sintered steel. This preliminary study is motivated by the relatively wide availability of necessary equipment, and simplicity of material identification procedures.

Herein, a dual-phase ferrite/bainite Astaloy steel with 9% porosity is studied. Various commonly used methods for the reconstruction of stress–strain curves from microindentation data are considered, whereby both Vickers and spherical tips are used. In addition, some homogeneous solid materials are investigated to better asses the performance of applied identification procedures. Two approaches for the mesoscale identification of the considered sintered steel are attempted. The first one is based on the identification of individual material phases, while in the other one the homogenization of the metallic matrix is adopted. To assess the reliability of obtained parameters, the direct numerical simulation of representative volume elements of realistic steel microstructure subjected to uniaxial tension is conducted. Numerical results are compared with the data from the macroscopic uniaxial tensile test.

The obtained results indicate that microindentation is adequate for the identification of elastic properties of individual material phases, but results for local plastic parameters are largely inconclusive and a further analysis is needed, focusing on applying smaller forces and investigating the influence of pores on identification results. Nevertheless, it seems that macroscopic stress–strain curves could be captured more accurately by the methodology based on the matrix homogenization if relatively large indentation forces are applied.

Keywords Microindentation · Porous multi-phase sintered steels · Plastic parameters · Stress–strain curve · Numerical mesoscale simulation

Introduction

In recent years, sintered steels are becoming a popular choice for the mass production of various machine components, such as gears in electrified vehicles [1], due to their good noise and vibration damping, and some good technological features of powder metallurgy (PM), such as a high percentage of material utilization or potential for producing very complex shapes. However, even though high theoretical densities can be achieved by modern sintering techniques, residual porosity still might present an important problem in dynamically loaded components. Pores in sintered material might have highly irregular shapes or spatial distribution, which during exploitation might cause stress concentrations and trigger significant local plastic deformation and fracture

✉ T. Jarak
tomislav.jarak@uva.es

Z. Tomić
zoran.tomic@fsb.hr

B. Pavlović
bp212419@stud.fsb.hr

Z. Tonković
zdenko.tonkovic@fsb.hr

[1] Faculty of Mechanical Engineering and Naval Architecture, University of Zagreb, I. Lučića 5, 10000 Zagreb, Croatia

[2] ITAP, School of Industrial Engineering, University of Valladolid, Paseo del Cauce 59, 47011 Valladolid, Spain

Published online: 29 November 2023

in microstructure, ultimately resulting in lower structural resistance to failure. In addition, the metallic matrix of such steels often consists of two or more distinct materials. Large efforts have been invested in investigating the influence of microstructure on the macroscopic behaviour of sintered porous steels by various experimental and numerical methods [2]-[9]. Thereby, the use of numerical methods greatly reduces costs and time needed for experimental testing, because it enables generating virtual hypothetical microstructural models. Usually, the Direct Numerical Simulation (DNS) is performed on the Representative Volume Elements (MVEs) or Microstructural Volume Elements (MVEs) of microstructure. However, meaningful nonlinear mesoscale numerical simulations can be obtained only by employing reasonably accurately identified local material parameters. This is especially important when investigating failure processes in sintered steels, see [3, 9].

Mechanical properties of individual material phases of multi-phase steels found in literature can be quite different from one another. Such discrepancies can be due to the limitations of the adopted experimental equipment and techniques, but also because different multi-phase steels are produced with different alloying elements and thermo-mechanical processing parameters, which lead to different mechanical properties of the individual phases. The works related to the identification of sintered steels at mesoscale are still relatively scarce. In [8], the influence of porosity on the macroscopic elastic behaviour of a dual-phase ferrite/bainite Astaloy steel was studied by experimental investigation across different length scales, and an analytical correlation between the elastic moduli of material phases and macroscopic elastic modulus was proposed. In the more recent work by the authors [9], the fracture and fatigue processes in the same sintered steel were modelled by a numerical phase-field model for fatigue based on brittle fracture, where plastic strains were not explicitly modelled. Although certain behaviour aspects in the high cycle fatigue regimen could be captured, experimental macroscopic monotonous uniaxial tension tests (UTTs) clearly pointed to the presence of small plastic deformation before failure, which could not be reproduced because plasticity was not included in the model. In addition, the fractographic analysis showed that significant local plastic flow takes place around small "bridges" between pores (which develop during sintering, when necks between two particles are being formed), which is critical in the formation and propagation of cracks through the microstructure, see also [2]. Therefore, it is necessary to include plastic deformation in any mesoscale numerical model for porous sintered steels. In [5] the influence of porosity on mesoscale elasto-plastic deformation processes in the single-phase austenitic steel 316L was investigated, and later this approach was extended to large plastic strains [4] and micro-fracture [3]. Although various techniques for generating faithful three-dimensional (3D) geometric models of RVEs of multi-phased and sintered steels are available [6, 7], often only 2D numerical models generated from a single metallographic photography are used in research in order to cut the costs of experimental testing needed for model generation and numerical simulations, see e.g. [9–15]. Regardless of which approach is adopted, characterizing local plastic parameters is essential, but by no means a simple task.

In [3–5] the local material properties of the porous single-phase 316L steel were obtained by inverse analysis from the results of macroscopic experiments performed on solid materials, i.e., the samples without pores. However, it is difficult and expensive to produce such samples, and in the case of multi-phase porous steels, it would require producing homogeneous macroscopic samples corresponding to each material phase. Alternatively, the in-situ high-energy X-ray diffraction [11], and microscale tests, such as micro-pillar compression test [16], microscopic tension test [17] or micro-grids [10], may be used. However, the manufacture of microscopic samples is complicated, and the repeatability of such tests is relatively low [18], in part due to size-effects associated with plasticity [19–21]. In addition, performing such tests requires appropriate equipment, which is not widely available. Some of these restrictions can be overcome by instrumented indentation, partly because it can be performed on the surface of small samples, acquired from local regions of interest in the analysed structure.

There are various methods for extracting material parameters from indentation data. Most often, elastic properties are extracted by the standard Oliver and Pharr [22] method, directly from the force–displacement curve obtained by a sharp tip. The methods for determining plastic parameters can be based either on sharp or spherical indenters. Giannakopoulos and Suresh [23] presented a simple inverse method for a sharp indenter, based on a high number of numerical finite element simulations of indentation process. Dao et al. [24] expanded that method by assuming finite strain deformation. Later, this approach has been further modified and extended to include the influence of various parameters, e.g., the apex angle of a sharp indenter [25]. The main problem of the methods based on sharp indentation is high sensitivity of result accuracy on any deviations in the shape of indentation force–displacement curve. These are however difficult to avoid due to strong stress localization occurring under a sharp indenter, which leads to fast transition between elastic and elasto-plastic deformation regime in the tested material. Determining a stress–strain relation by means of a spherical indenter is in principle somewhat simpler, since the stress field is smoother and the duration of elastic deformation during indentation larger. However, in this approach the exact determination of indent topology parameters, such as the contact radius, is a delicate task, because of pronounced pile-up and sink-in effects [26]. In spherical indentation

usually multiple partial unloading indents are necessary to obtain the indentation curve. The methodology has been studied extensively and tuned for better accuracy [27–29]. The application of the method that employs the Continuous Stiffness Measurement (CSM) to avoid multiple loading/unloading cycles was also reported [30], but it considerably raises the price of the equipment, which is not always available, and does not always produce more accurate results [30, 31]. Good overviews of different methods for the estimation of mechanical properties based on spherical indentation can be found in [26, 32].

When it comes to the multi-phase steels, indentation has been used mostly for solid materials, which are fully dense materials, i.e., materials without significant porosity [7, 14, 15, 30, 33, 34, 38]. Usually, sharp tips are used as they produce smaller indent than spherical tips, which is beneficial if only one grain is to be probed. In addition to usual problems, in various multi-phase materials the influence of harder particles that are positioned close to the indent location on indentation load–displacement curves has to be taken into account [34–37]. Kannan et al. [38] investigated the local Young's modulus of inverse bainite in a duplex steel microstructure, composed of bainite or martensite, by the Oliver-Pharr method [22] and showed how the transformation time influences the Young's modulus of inverse bainite. In [15], the influence of a harder phase on mechanical behaviour of ferrite–pearlite (FP), ferrite–bainite (FB) and ferrite–martensite (FM) microstructures was investigated by numerical mesoscale simulations on RVEs. Although it is claimed that nanoindentation was used to calibrate a hardening parameter of ferrite in the applied Rodriguez-Gutierrez hardening rule, no details about indentation procedure are given. In [33] the effect of hard particles (martensite) on the indentation load curves of ferrite in a dual-phase ferrite/martensite steel subjected to microindentation tests by Vickers indenter was evaluated by a similar plastic model, but it is not clear how the parameters for material models applied were identified. In [14] a ferrite/bainite steel was examined. The properties of individual phases were identified by microindentation by the Berkovich tip, indents were made approximately in the middle of regions corresponding to individual phases in order to avoid the influence of surrounding phase interfaces, elastic moduli were determined by the standard Oliver-Pharr method [22], and the methods proposed by Dao were used to determine the plastic parameters [24]. However, the details about experimental procedures for obtaining indentation curves, such as the number of indents, averaging procedures, statistical error or uncertainty analysis, were not exposed. A much more detailed analysis about obtaining average local plastic parameters of individual phases in a multi-phase quenched steel was given in [34], where nanoindentation by Berkovich tip was used to identify austenite and martensite phases. The elastic moduli were determined by the Oliver-Pharr method [22], and the Dao inverse method for estimating plastic parameters by microindentation [24] was modified by first determining the yield stress from nanohardness and by introducing a correlation coefficient to consider size effects. For each phase, first for each indentation a corresponding stress–strain curves was extracted, and then the average stress–strain curve was constructed from a thus obtained set of stress–strain curves. These average stress–strain curves tended to somewhat overestimate those obtained by the in-situ high energy X-ray diffraction (HEXRD) test. In addition, the influence of grain boundaries on the plastic parameter values was investigated and it was established that they caused certain strengthening in larger tempered martensite grains. Recently, spherical nanoindentation was used for a macroscopic characterization of a ferritic/martensitic steel [30] by employing different methods for defining the contact radius, and by fitting the elasto-plastic power law to the obtained indentation stress–strain curves. An interesting approach was proposed in [7], where an optimization inverse method was employed for the identification of material parameters of a ferrite/martensite steel, where the results of FEM elastoplastic simulations of nanoindentation process were fitted to the experimentally obtained nanoindentation load–displacement curves, obtained by the cube-corner tip. However, many numerical simulations of indentation process are needed for such identification process, which may demand significant computational costs and time.

Recently, the capability of nanoindentation for identification of material matrix in a single-phased ferritic Distaloy AB steel was evaluated in [39]. Therein, the influence of porosity was reduced by performing indentation further away from pores. The Berkovich tip and conical tips were used, and the indentation curves obtained by the conical tip were reproduced by axisymmetric 2D numerical models. The results indicate that size effects have to be taken into account if small force are used, while pile-up phenomenon might influence the results if larger forces are used. Using various loads during testing might be beneficial in detecting these effects and eventual porosity influence. Still, the selection of indentation curves for an inverse identification procedure remains unclear. In [39], no averaging was performed to take into account the dispersion of indentation curves, and the verification on realistic material mesoscale model was not performed. In addition, since only a single-phased material was analysed, no influence of phase interfaces or hard particles was present, which could be important in case of multi-phase steels. Recently, the authors have successfully used microindentation to identify elastic properties of individual material phases in a sintered dual-phase ferrite/bainite steel [8], and they correlated those local values to the macroscopic elastic properties.

To the best knowledge of the authors, instrumented indentation has still not been used to identify plastic parameters of individual phases in multi-phase sintered steels. So far, only the methods based on sharp indentation have been applied for estimating material properties of individual phases in multi-phase steels. It seems that accuracy might significantly depend on the techniques applied, but critical comparison between various existing methods is still missing. Further, as mostly solid solid-phase steels have been examined, it is unclear how these methods would work if applied to sintered steels with considerable porosity. Nanoindentation could be a preferred choice, but in that case size effects must be properly treated [34, 39]. On the other hand, the application of more available microindentation has still not been reported in the literature. In general, so far, there is still a lack of indentation procedures for sintered steels backed up by a proper statistical analysis.

This article attempts to address some of the abovementioned issues. Microindentation is for the first time applied for identifying local plastic parameters of multi-phase sintered porous steels. The purpose of this study is to investigate the potential of various well-known methods based on microindentation, such as the Giannakopoulos or Dao methods, to identify local plastic material parameters in a porous sintered material. In this work the dual-phase ferrite/bainite steel, sintered from the prealloyed Astaloy powder, is examined. Various methods for the extraction of stress–strain curves from the microindentation data are compared and commented. Besides the sharp Vickers tip, a spherical tip is also applied, which has so far not been used for the identification of porous sintered steels. First, the performance of all applied methods is critically assessed by characterizing a set of very brittle or ductile homogeneous materials, representing extreme cases that could be encountered in a multi-phase material. Then, the local properties of inspected realistic porous heterogeneous sintered steel are identified. The parameters of individual material phases and homogenized matrix material are identified by performing indents at the centres of a certain material phase or by grid indentation, respectively. In order to reduce the influence of pores on results, the indents are made further away from the visible pores. In order to take into account the scattering of indentation load–displacement curves, first the average indentation curve for the considered material constituent is constructed, which is then used for the estimation of elastic and plastic parameters. The behaviour of thus identified material at mesoscale is simulated by the Finite Element (FE) 2D plane strain models by using the commercial program package Abaqus [40]. Highly realistic geometrical models of RVE are generated from 2D metallographic photographs and then used to generate finite element (FE) models, whereby the identified material properties are assigned to the regions representing certain material phases. In all models the deformation plasticity theory adopting the small strain Ramberg–Osgood model is adopted to describe elasto-plastic behaviour of all material phases. The stress–strain curves obtained by the numerical mesoscale models are compared with the macroscopic experimental testing data obtained by the standard macroscopic UTT to assess the accuracy of proposed approaches.

The structure of the paper is as follows. In Sect. 2 the investigated materials, the applied equipment, methods for the stress–strain curves extraction and numerical modelling approach are described in few details. Section 3 exposes obtained experimental and numerical results, accompanied by a detailed discussion. Finally, in Sect. 4 conclusions and future lines of research are given.

Materials and methods

Investigated materials

Sintered Astaloy steel

In this contribution, a sintered Astaloy Mo + 0.2C steel, compacted from low-prealloyed metallic powder according to Höganäs [8], is considered. This steel is a dual-phase ferrite/bainite steel with the metallic matrix consisting of ferrite and bainite, as shown in Fig. 1. For clarity and simplicity of the text, in this work the bainite microstructure is referred to as a material phase, whose average mechanical properties are identified by indentation. More details about the sintering procedure can be found in the authors' previous work [8].

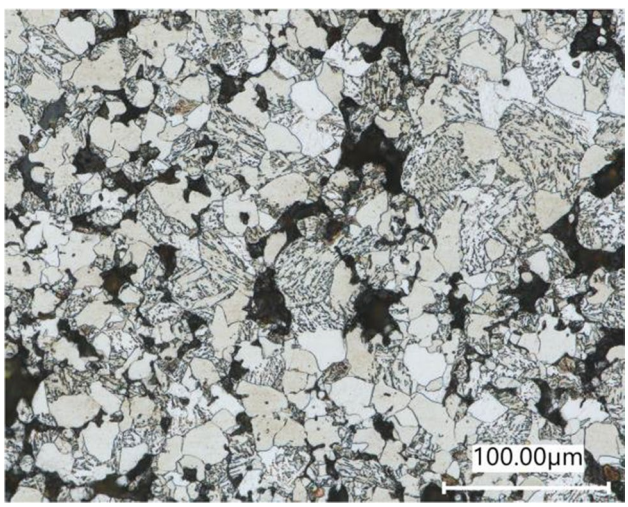

Fig. 1 Typical microstructure of sintered Astaloy Mo + 0.2C steel, consisting of ferrite (white colour), bainite phases (lamellar white-black regions) and pores (black colour)

In this work the steel with the compacting density of 7.1 g/cm^3 is investigated. It possesses substantial porosity, where the pores (shown by black colour in Fig. 1) are often agglomerated. The geometry of pores is highly irregular, so pores act as strong stress concentrators during loading. The volume ratio of the ferrite and bainite in the metallic matrix are around 31% and 69%, respectively, while porosity is around 9% of the total sample volume. The approximate sizes of ferrite and bainite grains are 30 µm and 70 µm, respectively, while the size of pores ranges from 20 to 80 µm.

Materials for calibration and verification of identification methods

The initial assessment of the material identification methods applied in this work is performed by inspecting a set of very brittle or ductile homogeneous materials. These materials might be considered as certain extreme cases of microstructures to be found in heterogeneous multi-phase materials. Here, brittle materials are represented by glass samples, made of fused silica (FS) and the borosilicate glass (BK7), with the certified values of elastic modulus of 75.1 GPa and 86.5 GPa, respectively. In addition, a highly ductile copper sample is investigated, manufactured from 99.9% pure Cu and possessing a distinct homogeneous microstructure (see figures in Table 2). Referent macroscopic properties values for pure copper, used here for the purpose of qualitative comparison, are taken from existing databases [41–43].

Preparation of material samples

For glass samples reference blocks are used, with the dimensions ϕ25 x 5 mm(Fig. 2a) for fused silica (FS), and ϕ40 x 5 mm the borosilicate glass (BK7) (Fig. 2b).

With the exception of the reference glass blocks shown in Fig. 2a and 2b, all materials samples investigated in this work are prepared with mechanical polishing, first with different sanding papers, then with the 3 µm diamond paste and finally with the 0.03 µm diamond fluid. The sintered steel samples (Fig. 2c) are immersed in the 3% Nital etching fluid for the duration of a few seconds to reveal their heterogeneous microstructures.

Indentation hardware and conditions

The experimental studies of sharp and spherical indentations are caried on a Micro Combi Tester (MCT) produced by Anton Paar with the depth resolution of 0.03 nm and the load resolution of 6 µN. In order to compare the performance of various well-established methods for material identification based on microindentation, both sharp and spherical tips are considered in this work. A standard diamond Vickers indenter is applied for sharp indentation, while a diamond spherical indenter with the nominal radius of 50 µm is used for the spherical-based characterization method. The values for the Young's modulus and Poisson coefficient of the indenters used in this article are $E_i = 1140$ GPa and $\nu_i = 0.07$, respectively. Indentations are conducted with the force control procedure, with the loading rate defined as $2 \cdot F_{\max}/\min$, $\left[F_{\max}\right] = \text{mN}$, where $F_{\max}$ is the maximum force. All indentations are conducted at the room ambiental temperature, which is approx. 23 °C.

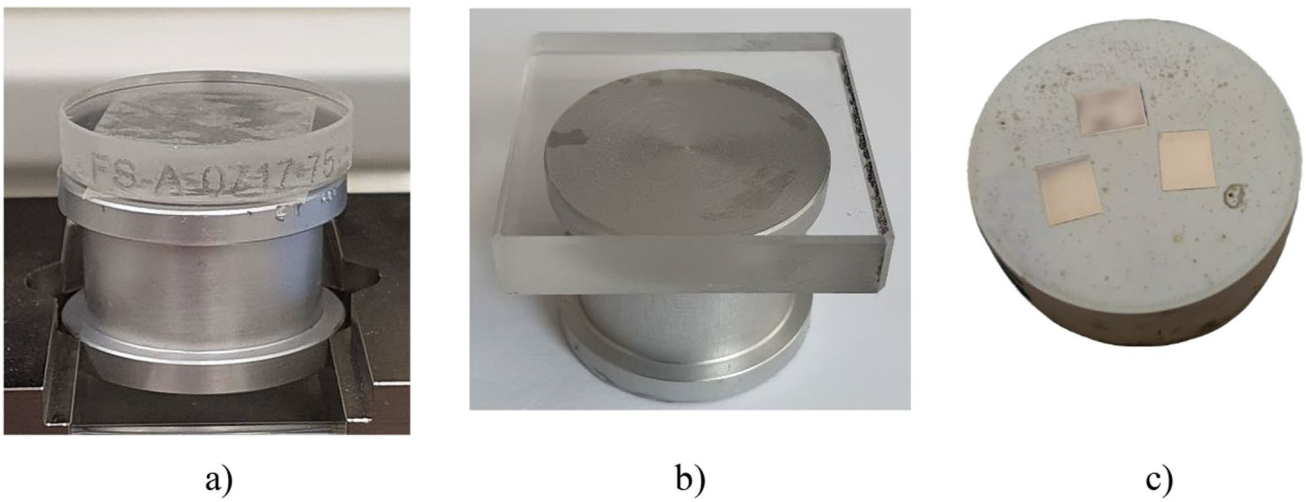

Fig. 2 Samples prepared for indentation: a) fused silica, b) borosilicate glass-BK7, c) sintered steel

Table 1 Maximum indentation forces for sharp indentation

Material	Phase	Maximum force F_{max}, mN	
		Vickers indentation	Spherical indentation
FS glass	-	50	8000
BK7 glass	-	200	4000
copper	-	200	1000
Sintered steel	ferrite	100	250
	bainite	100	150
	Matrix (grid indentation)	100	-

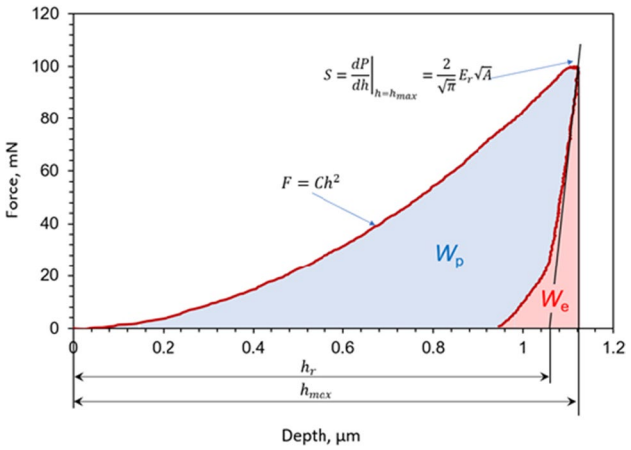

Fig. 3 Typical indentation curve obtained by sharp indentation

Material characterization based on sharp indentation

Procedures for sharp indentation

In this work, the standard Vickers indenter is used. The maximum forces applied for different material samples are shown in Table 1.

The maximum indentation force is different for each material. The maximum applied forces for the brittle FS and BK7 glasses are low enough to avoid the appearance of cracks (according to the sample certificates, cracks appear at the forces of around 200 mN and 400 mN, respectively). The maximum values of indentation forces used for individual material phases of the investigated sintered steel are restricted by the sizes of individual material phases, as the indent has to be small enough in comparison to the size of the tested grain in order to reduce the influence of surrounding material. In addition, large force cause a considerable pile-up phenomenon, which could significantly reduce the accuracy of the parameter identification procedure. On the other hand, minimal values for F_{max} in all cases are restricted by the configuration of the applied experimental equipment.

Material parameters have been identified from average indentation curves. To obtain these curves, first a number of indentations were performed for each material sample, and for each indent a corresponding indentation curve was recorded. Typical indentation force–displacement (indentation depth) curve obtained by sharp indentation is presented in Fig. 3. Then average curves were extracted from that set of indentation curves by Anton Paar Indentation Software. The average results for homogeneous materials were taken from 15 indentations. In the case of sintered steel, 20 indentations were performed for each individual phase, and the total of 49 indentations for the identification of homogenized parameters of the metallic matrix. The obtained average curves are shown in Sect. 3 in Fig. 9 for individual homogeneous materials and material phases, in and Fig. 13 for the homogenized matrix.

For the sintered steel, two approaches for characterizing microscopic material parameters are used, associated with the simplification level adopted in numerical modelling, as explained in Sect. 2.5. In the first one, the ferrite and bainite phases are characterized separately, whereby indents are made close to the centres of grains corresponding to the examined material phase, to minimize the possible influence of surrounding grains, phase interfaces and/or pores. For each homogeneous material phase, 20 indentation curves were extracted. In another approach, grid indentation is applied over the metallic matrix of the material sample, disregarding the influence of grain boundaries. In total, 49 indents were performed in 7×7 pattern, with 100μm between individual indents. The inspected zones were chosen to be as free from any visible pores as possible, but any indent closer than 100μm to a pore was discarded. In all tests, bainite is assumed to be a homogeneous phase whose average properties were identified, i.e., carbide and ferrite forming bainite are not characterized separately. More details about the sintered steel indentation can be found in the authors' previous work [8].

Methods for reconstruction of stress–strain curves from sharp indentation data

The methods proposed by Giannakopoulos and Suresh [23] and Dao et al. [24] are used in this work to identify plastic parameters from the sharp Vickers indentation. The maximum and residual contact depths, denoted as h_{max} and h_r, respectively, are measured directly. In all cases, the Young's modulus is determined from the unloading indentation force-depth curves according to the Oliver and Pharr method [22] using the Vickers tip. Further, for identifying plastic parameters, the loading force-depth curve

is approximated by a simple $F = C \cdot h^2$ quadratic equation (the Kick's law, see [23, 24, 44]), where F, h and C are the applied force, the indentation depth, and a dimensionless parameter, respectively. The flow charts of the considered methods are given in Fig. 4 and Fig. 5, followed by short descriptions containing few important details about their execution in this work.

The Giannakopoulos reverse method [23] estimates the elasto-plastic material properties from the indentation curve under the assumption about small strains. In this work, the elasticity effects are considered by computing the effective elastic modulus E^* directly from the elastic parameters of the considered material (E, ν), and the indenter (E_i, ν_i), instead of estimating it from the experimental F–h curve data. From the experimentally identified h_r and h_{max}, and the calculated E^*, first the values for the representative stress $\sigma_{0,29}$ and the yield stress σ_y are acquired in an iterative manner, followed by the strain hardening exponent n.

Dao et al. [24] expanded the Giannakopoulos approach to three new variants. These reverse methods take into account large strains phenomena, such as pile-up effects. The first expansion, called here the Giannakopoulos FS method, is simply a modification of the original Giannakopoulos method. The only resulting differences are the new values of the nondimensional parameters M_1 and M_2, which are now obtained by including large strains in numerical simulations of indentation process, see [24], and norming of E^* by $\sigma_{0.29}$ instead of σ_y in the expression for the loading curvature C (step 5 in Fig. 4). Other two methods, denoted in this paper as the Dao and the Low Hardening methods, are reversed

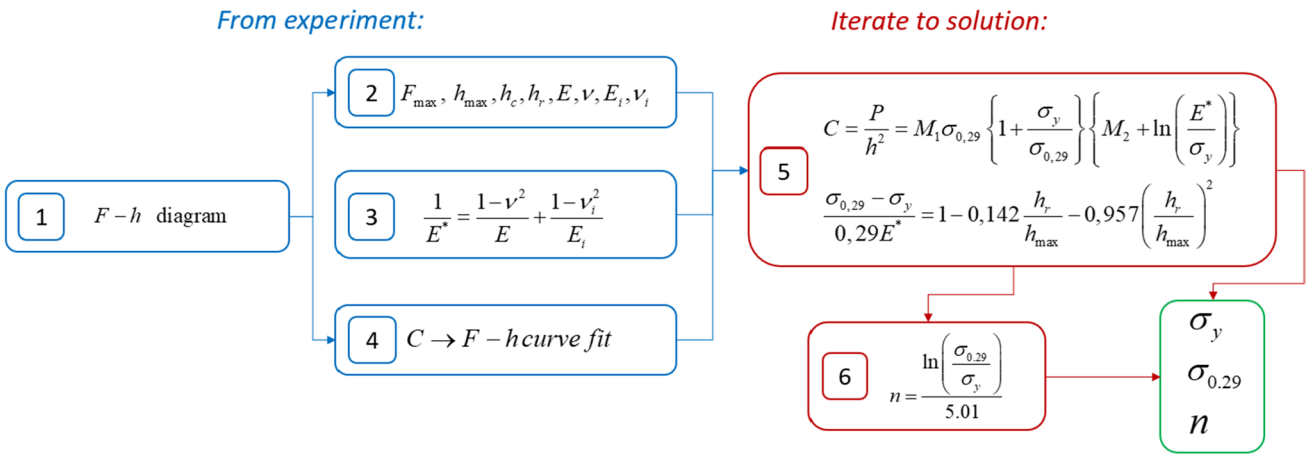

Fig. 4 Flow chart for Giannakopoulos method and Giannakopoulos FS method

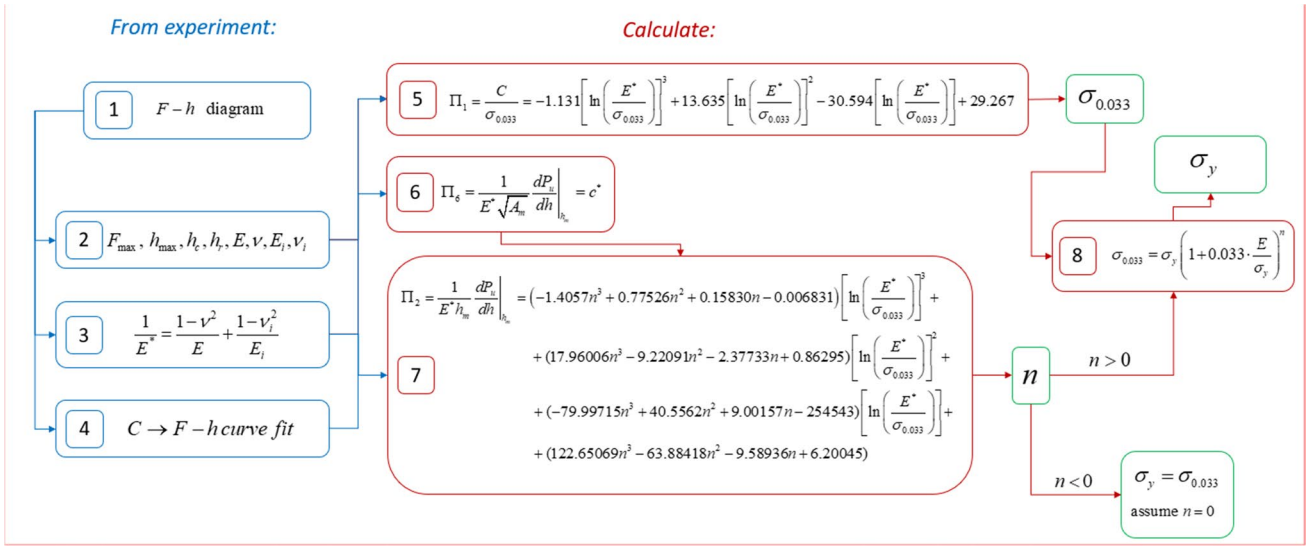

Fig. 5 Flow chart for Dao method and Low Hardening method

methods employing a set of equations obtained by dimensional analysis, see flow charts in Fig. 5. Thereby, the Low Hardening method is suitable only for low-hardening materials or materials with no pronounced plasticity before failure. For these methods the slope of unloading indentation curve at the maximum penetration depth, $\left(\mathrm{d}F_u/\mathrm{d}h\right)\Big|_{h_{\max}}$ has to be determined.

In the Dao and Low Hardening methods, the representative stress $\sigma_{0.033}$ is used, and is calculated by using the dimensionless function π_1 (step 5) employing the effective elastic modulus E^* and C, which are defined as in previous two methods. Thereafter, the strain hardening exponent n is obtained from the dimensionless function π_2 (step 7). Finally, the yield stress σ_y is calculated (step 8), which is defined as the zero offset yield strength. In this work, the dimensionless function π_6 served for estimating the maximum indentation contact area A_{m} in order to control the measured $h_{\max}$. In the Low Hardening method, which is applicable for $n \leq 0$, the yield stress is equal to the representative stress $\sigma_{0.033}$. In that case, the experimental values of indentation curve parameters have to be verified by using the estimated parameters in the dimensionless functions π_i.

The reconstructed stress–strain curves, except the Low Hardening method, are based on a simple power-law elasto-plastic material model:

$$\sigma = E \cdot \varepsilon \ \text{ for } \sigma \leq \sigma_y \ \ \& \ \ \sigma = K \cdot \varepsilon^n \ \text{ for } \sigma \geq \sigma_y \tag{1}$$

where σ and ε stand for the stress and strain, respectively. E is the Young's modulus, while K and n are the strength index and the hardening exponent, respectively. In the Low Hardening method, the behavior can be approximately described by the linear elastic law until $\sigma_y = \sigma_{0.033}$,i.e., the assumed advent of yielding.

Material characterization based on spherical indentation

Spherical indentations are conducted in a multicyclic mode, i.e., the repeated indentation is executed at the same spot with an increased load in every new cycle. Throughout this paper the quadratic load increase is used during 20 cycles (see Fig. 6) with the 50% unloading from the maximum force of a current cycle. The indentation force is kept at its maximum value for 30 s at every cycle. The applied values of total maximum force $F_{\max}$ (the maximum force at the last cycle) are given in Table 1 and depend on the investigated sample. They are chosen so as to capture the yield stress of the materials.

The method based on the spherical multicycle indentation without the CSM feature is used in this contribution. In contrast to the methods based on sharp indentation, here the plastic parameters are estimated directly from stress–strain

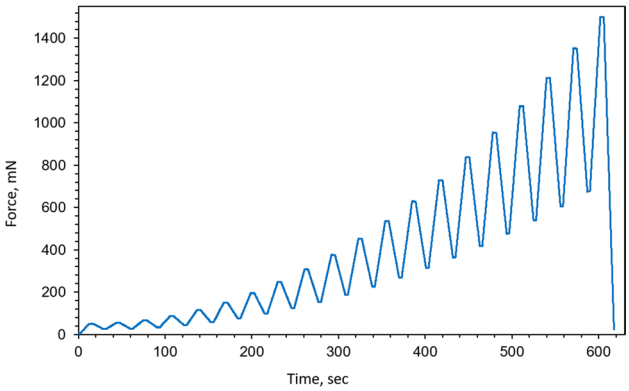

Fig. 6 Typical force–time curve for multicyclic spherical indentation

curve obtained by calculating strain and stress directly from the measured force and indent geometry data. Such approach circumvents errors caused by employing reverse methods used for sharp indentation, but its accuracy depends considerably on determining the indent geometry data during the procedure, such as the contact radius or contact depth, which is far from trivial task because of pile-up and sink-in effects. Here, these data were extracted from average indentation curves, obtained in the same manner as those for sharp indentation. The same number of indents was used as for sharp indentation procedure, described in Sect. 2.3.1.

The determination of the true (uniaxial) stress–strain relation is defined by the following equations [28, 32]:

$$\varepsilon = 0.2 \cdot \frac{a_c}{R}, \quad \sigma = \frac{p_m}{\psi}, \tag{2}$$

where a_c, R, $p_m = F/\pi a_c^2$ and ψ are the contact radius, the nominal indenter radius, the mean pressure and the indentation governing factor, respectively. The contact radius is defined as:

$$a_c = \sqrt{2h_cR - h_c^2}, \tag{3}$$

where h_c is the contact depth of the indenter defined by the Oliver and Pharr method [22]. The value of the dimensionless parameter ψ depends on the considered material and its value is in the range from 1.1 to 3 [26, 28, 44, 45]. For the fused silica and BK7 glasses the values of parameter ψ are determined by fitting the elastic part of the reconstructed strain–stress relation to the slope defined by the certified elastic modulus. According to this approach, the following values have been obtained:

$$\psi_{FUSED\ SILICA} = 1.4,\ \psi_{BK7} = 1.2. \tag{4}$$

For other materials investigated here, the values of ψ are:

$$\psi_{COPPER} = 3,\ \psi_{SINTERED\ STEEL} = 3 \tag{5}$$

Numerical modelling

In order to verify the identified local material parameters, the Direct Numerical Simulation (DNS) of the Representative Volume Elements (RVE) of the considered sintered steel was performed. For that purpose, two-dimensional (2D) RVEs were created, where geometrical models of microstructure had been extracted directly from metallographic photographs, with shapes of grains and pores approximated by spline curves. The thus obtained graphical models were then exported to the Abaqus general-purpose Finite Element (FE) software [40], where adequate meshes were generated. The average element size was h = 1.5 μm, chosen so that microstructural topology and steep stress gradients in the regions around stress concentrations could be captured in detail. The size of the elements is therefore much smaller than the size of individual grains and pores.

The procedure for extracting RVEs is shown in Fig. 7. In every model all pores are positioned completely inside the model of RVE, i.e., no pore intersects the outer RVE boundary. The displacement boundary conditions (BCs) corresponding to the uniaxial tension were imposed on the outer RVE boundary, as depicted in the right of Fig. 7.

To capture the size effects, RVEs of different sizes were extracted, each with the same porosity level (around 9%) and approximately equal ferrite-to-bainite ratio in the metallic matrix. Three sizes (with edge lengths of 0.2, 0.3 and 0.4 mm) of RVEs were created, as shown in Fig. 8.

The elasto-plastic material properties of individual phases obtained by indentation were prescribed to the

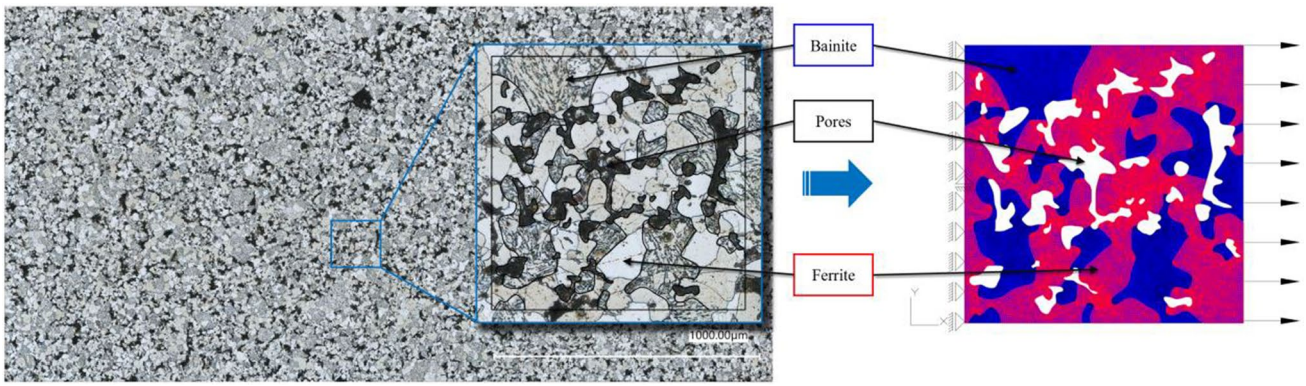

Fig. 7 Extraction of RVE from metallographic images of sintered steel (left: metallographic image, right: FE model of RVE with applied BCs)

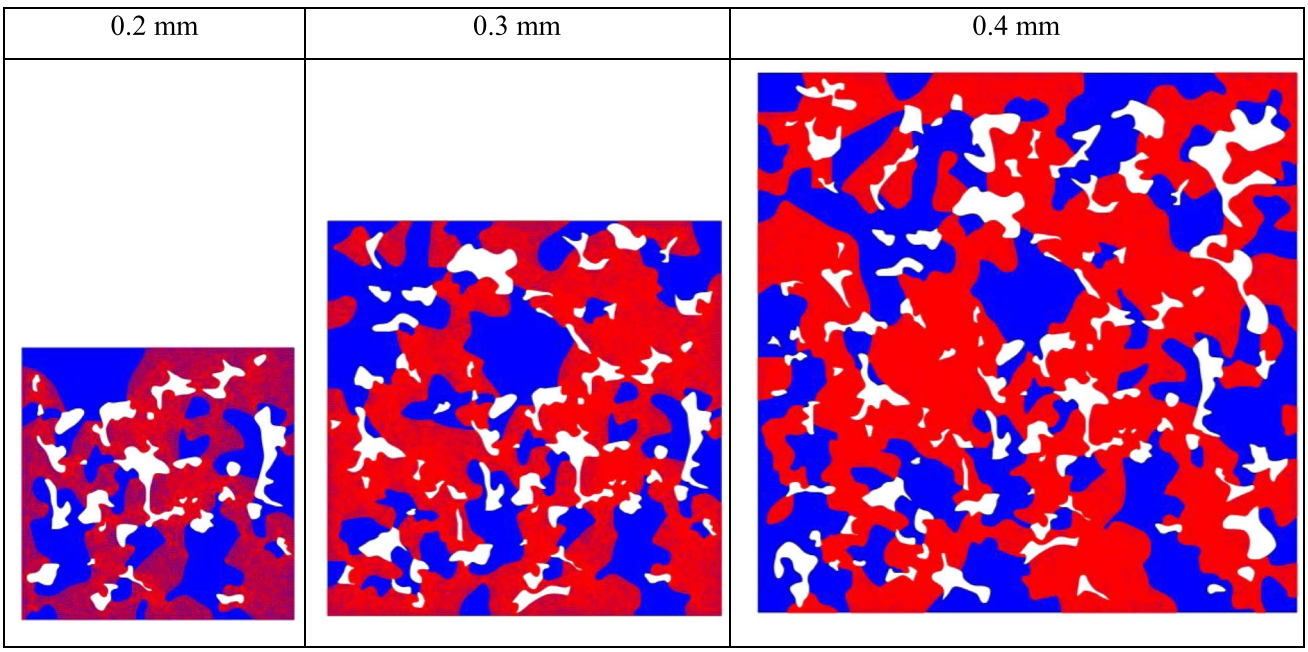

Fig. 8 Different sized of RVEs for sintered steel: bainite (blue), ferrite (red), pores (white)

corresponding regions of numerical models. For the models where each individual phase is characterized, separate regions for each phase are discerned in the models (in Fig. 8 blue regions represent bainite and red regions ferrite). In the models where the material matrix is assumed to be homogeneous, equal material properties estimated as explained in subsection 3.2.2 were assigned to all regions. Small strain quasi-static elasto-plastic analyses were performed in ABAQUS Simulia software [40] by utilizing the deformation plasticity Ramberg–Osgood model. All RVEs were discretized by the 2D 4-node quadrilateral plane strain finite elements (CPE4) [40]. Approximate numbers of finite elements for the RVE sizes of 0.2, 0.3 and 0.4 mm are around 30 000, 70 000 and 130 000, respectively.

Results and discussion

Indentation data

Average indentation curves for sharp indentation, obtained as explained in Sect. 2.3.1, are presented in Fig. 9 for each inspected homogeneous material or material phase. The average curve for the homogenized matrix is shown in Fig. 13. These curves were used for the characterization of material parameters by the methods based on sharp indentation. In all cases the residual indentation depth was > = 300 nm, indicating that size effects, typically occurring in nanoindentation, could be safely neglected.

Typical residual indents are shown in Table 2. Images shown herein were obtained using a light microscope with different magnifications lenses fitted on indentation devices. No cracks were observed in ductile materials (copper, bainite, ferrite), but in certain cases some radial cracks were noticeable in the BK7 glass sample at maximum forces.

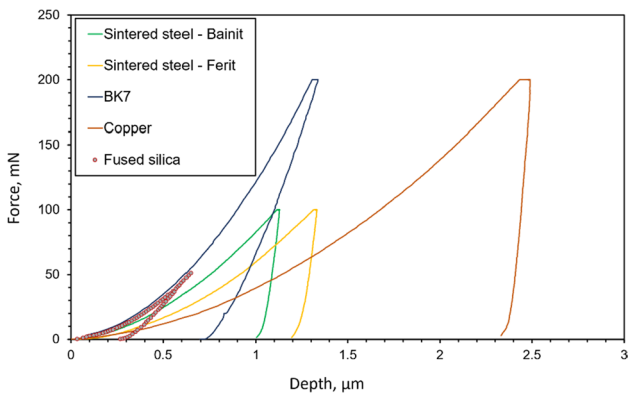

Fig. 9 Average indentation curves obtained by Vickers tips

Verification on homogeneous samples

For completeness, here initial investigation dealing with characterizing some common brittle and ductile homogeneous materials was performed to gain a more objective comparison of the employed indentation methods. Due to the homogeneity of inspected materials, the influence of features which may play a significant role in a multi-phase sintered steel, such as phase interfaces or pores, was not present in this initial study.

Brittle materials

Only the Low Hardening method and the method based on the special indentation were used to identify the yield stress of homogeneous brittle materials described in subsection 2.1.2 (the fused silica and BK7 glass), because these materials do not exhibit significant plastic deformations before failure. Figure 10 shows the estimated true stress–strain curves of fused silica (Fig. 10a) and the BK7 glass (Fig. 10b). The curves obtained by the Low-Hardening method are shown only schematically, since in that method it is usually assumed that material is linear-elastic until the advent of yielding, with the yield stress corresponding to the calculated representative stress $\sigma_{0.033}$.

The estimated yield stress values are given in Table 3. For fused silica the obtained values agree reasonably well with those reported in literature, see e.g. [46–48], which are usually in the range from 4000 to 5000 MPa. Note that for the BK7 glass the Low Hardening method yielded somewhat lower result (around 3500 MPa), which might be provoked by the appearance of radial cracks during spherical indentation, visible in Table 2 for the BK7 sample, indicating that lower forces should be applied for the BK7 glass. However, further testing is needed to confirm this assumption. On the other hand, for both glass samples the difference between the values estimated by the Vickers and spherical indentation is around 10%, which could be attributed to the inaccuracies in calculating the representative stress $\sigma_{0.033}$ in the Low Hardening method and the adopted assumption that $\sigma_y = \sigma_{0.033}$.

Ductile materials

The estimated stress–strain curves and identified parameters for the investigated copper sample, which is a pronouncedly ductile homogeneous material (see the figures of microstructure in Table 2), are shown in Fig. 11 and Table 4, respectively.

Herein, the predicted value of elastic modulus, estimated from the unloading indentation curve by the Oliver-Pharr method [22], is considerably higher than the typically reported values (approximately 110—132 GPa) [41]-[43]. This can occur due to pile-up effect during indentation

Table 2 Typical residual indents

Vickers indentation	Spherical indentation
Fused silica	
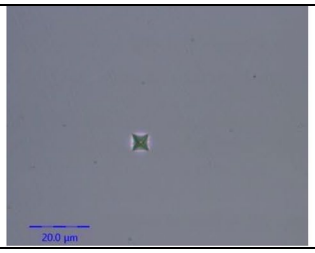	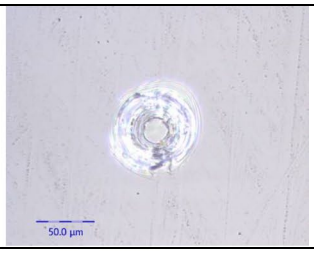
BK7	
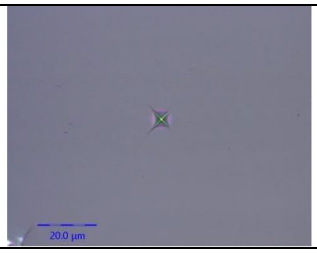	
Copper	
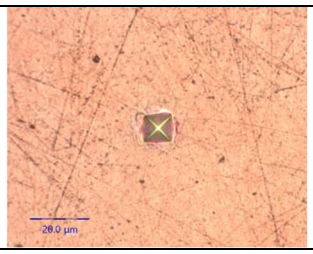	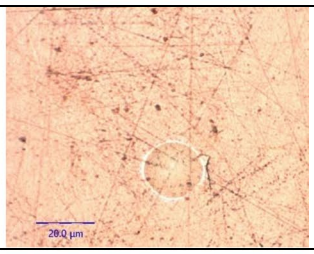
Sintered steel – Bainite phase	
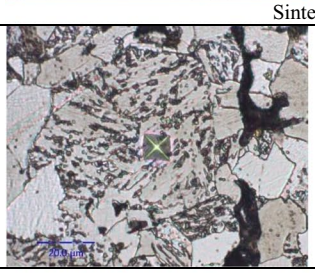	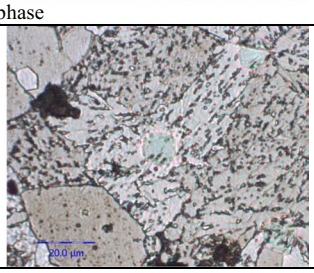
Sintered steel – Ferrite phase	
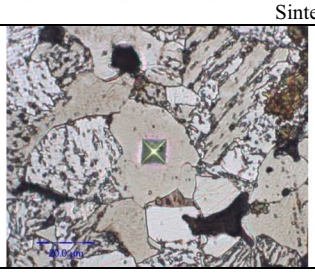	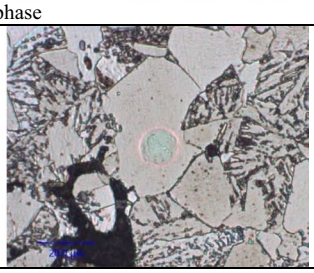

and/or reverse plasticity during unloading [49], caused by relatively large indentation forces. According to [49], the unloading curve method with forces sufficiently low to avoid reverse plasticity might work well, but they typically fall in range of nanoindentation, which is outside of the scope of this paper. Alternatively, for some metals a more accurate estimation might be obtained by applying the reload curve analysis in multicycle indentation procedure. Because here the Young's modulus value might be overrated, it is difficult to estimate accuracy of the identified plastic parameters in this example, but in passing we note that the estimated value of the yield stress for pure copper is between 40—90 MPa, which is still in a good correspondence with data reported in literature, see [41–43]. An exception is the Giannakopoulos FS method, where noticeably higher values were obtained.

As visible in Fig. 11, the stress–strain curves obtained by the Giannakopoulos method and the spherical indentation exhibit a good correspondence. This can be explained by the fact in the spherical indentation method the parameter ψ was calibrated to match the elastic slope, which is in both cases

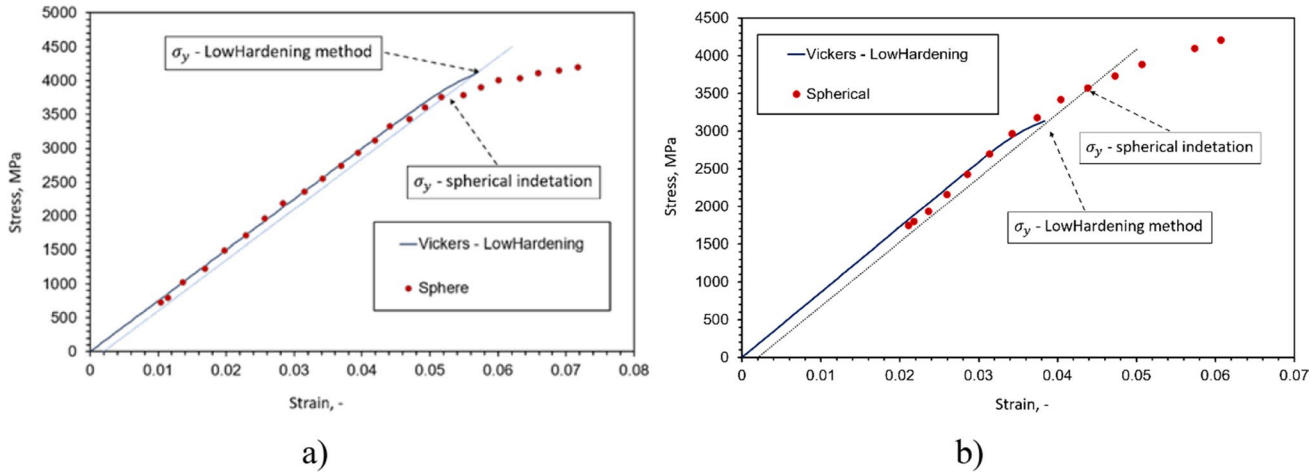

Fig. 10 Stress–strain diagrams for a) fused silica and b) BK7 obtained by Low Hardening method (LowHardening) and method based on spherical indentation (Spherical)

Table 3 Yield stress for fused silica and BK7 determined by Vickers and spherical indenter

Material	Indenter	Elastic modulus, E, GPa	Poisson ratio, ν, -	Yield stress, MPa
Fused silica	Vickers	75.1 ± 0.3	0.16	4110
	Sphere			3800
BK7	Vickers	86.5 ± 0.4	0.2	3130
	Sphere			3570

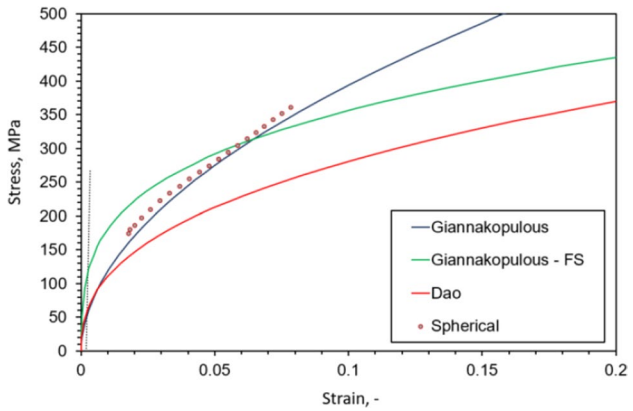

Fig. 11 Stress–strain curves based on Vickers and spherical indentation for copper sample

obtained by the Oliver-Pharr method. Therefore, in the small strain regime, the resulting curve follows closely the curve obtained by the Giannakopoulos method, derived under the assumption of small strains. On the other hand, the [24] Giannakopoulos FS and Dao methods, based on the finite strain theory, produced distinctly different curves. In contrast to the original Giannakopoulos method, in the Giannakopoulos FS method the proposed values of parameters M_1 and M_2 were obtained under the assumption about finite strains during indentation, and consequently different values of plastic parameters are calculated. On the other hand, the discrepancy between the Giannakopulous FS and Dao curves occurs probably due to the fact that in the Dao method the reverse analysis uses the slope of the indentation unloading curve at the maximum indentation penetration, $\left(\mathrm{d}F_u/\mathrm{d}h\right)\Big|_{h_{\max}}$, as an input parameter. As shown by the sensitivity analysis, in the Dao method the results are very sensitive on the value of this parameter of (see [24] and Table 5 for more details). Therefore, any errors in determining the unloading curve parameters will influence significantly the identified plastic parameters.

It can be concluded that the microindentation-based methods for estimating plastic parameters could yield significantly different solutions for very ductile metallic materials in certain testing conditions. Plastic parameters predicted by instrumented indentation can also be very sensitive to variations in parameters of the experimentally obtained indentation curve [24]. For the purpose of comparison, here the most important results of the sensitivity analysis are presented. The most influential parameters for the sharp indentation are the fitting parameter C and the slope of unloading curve at the maximum penetration depth, $\left(\mathrm{d}F_u/\mathrm{d}h\right)\Big|_{h_{\max}}$. On the other hand, the yield stress σ_y and hardening exponent n have been identified as the most sensitive plastic parameters. In Table 5 the conservative errors for σ_y and n are shown, obtained for the ± 4% variations of the influence parameters C and $\left(\mathrm{d}F_u/\mathrm{d}h\right)\Big|_{h_{\max}}$ around their respective values extracted from the average experimental indentation curves.

Table 4 Identified plastic parameters for copper

	Modulus of elasticity, *E,* GPa	Poisson ratio, *v*, -	Yield stress, MPa	Strength index, *K*, MPa	Hardening exponent, *n*, -
Giannakopoulos	186.9 ± 19	0.3	53	1295	0.514
Giannakopoulos FS			118	689.3	0.285
Dao			60	701.5	0.396
Sphere			66	1183.8	0.476

Table 5 Sensitivity analysis of methods based on sharp indentation

Method	Material parameter	Curve fitting parameter, *C*	Unloading slope, $\frac{dF_u}{dh}\Big\vert_{h_{\max}}$
		+4%/-4%	+4%/-4%
Dao	Yield stress, MPa	27.7%/41.7%	34.3%/81.9%
Giannakopoulos		51.3%/-12.4%	1.3%/1.7%
Giannakopoulos FS		16.5%/26.3%	3.1%/-3.6%
Dao	Hardening exponent, *n*, -	-10.0%/-7.9%	56.1%/-41.0%
Giannakopoulos		-32.7%/7.0%	-0.3%/-0.8%
Giannakopoulos FS		-10.9%/-11.7%	-1.9%/2.0%

Table 6 Sensitivity analysis of the method based on spherical indentation

	Contact depth, h_c, mm	
	+4%/-4%	
	Yield stress, MPa	Hardening exponent, *n*, -
Sphere	-1.52%/-13.6%	4.8%/5.1%

The variation of the parameter *C* caused a large scattering of σ_y in all methods. It had a less pronounced influence on the hardening parameter *n,* except in the Giannakopoulos method, where it was again pronounced. The observations for σ_y are similar to the conclusions in Dao et al. [24] for the materials with the hardening exponent $n > 0.1$. The variation of the slope of the unloading curve $\left(\mathrm{d}F_u/\mathrm{d}h\right)\Big\vert_{h_{\max}}$ has a high influence on both σ_y and *n* in the Dao method, and relatively low impact in the Giannakopoulos and the Giannakopoulos FS method.

In the spherical indentation, the influence of the variations in the contact depth was investigated, because it is difficult to accurately determine its values due to the sink-in or pile-up phenomena. The results are shown in Table 6. It was established that the contact depth h_c has a low influence on *n*, and that its impact on the values of σ_y is significantly lower than the influence of the most influential parameter (the loading curvature *C*) in sharp indentation.

Characterization of Astaloy sintered steel

The investigated sintered steel, compacted from Astaloy Mo + 0.2C low-prealloyed metallic powder, is porous with a heterogeneous metallic matrix consisting of ferrite and bainite. In this work, two different approaches for the mechanical characterization of the considered steel at the mesoscale level are adopted:

- The identification of individual material phases,
- The homogenization of the material matrix.

The experimental data obtained by both methods are applied in the numerical models of RVEs to verify the obtained results and to assess the applicability of both approaches.

Identification of individual material phases

For both phases indentation was always carried out inside a single-phase grain, as close as possible to the grain center, in order to minimize the influence of surrounding phase interfaces (see figures in Table 2). In the case of spherical indentation, larger grains were targeted, to ensure that the indent does not interfere with the phase interfaces. Indentation was performed away from the visible pores to reduce their influence, see figures in Table 2. Nevertheless, significant dispersion of the indentation curves was noted, especially for ferrite, see [8] for sharp indentation. In all methods, the elastic modulus of each material phase is identified by the standard Oliver-Pharr method [22] from the average

Table 7 Elasto-plastic parameters of ferrite and bainite phases in sintered steel

	Modulus of elasticity, *E*, GPa	Poisson ratio, *v*, -	Yield stress, MPa	Strength index, *K*, MPa	Hardening exponent, *n*, -
Ferrite					
Giannakopoulos	186 ± 28.8	0.3	67.4	1484	0.4994
Giannakopoulos FS			159	772	0.2547
Dao			98.2	526	0.2704
Sphere			-	-	-
Bainite					
Giannakopoulos	239 ± 29.6	0.3	453	2386	0.274
Giannakopoulos FS			438	1424	0.1936
Dao			232	874	0.2143
Sphere			-	-	-

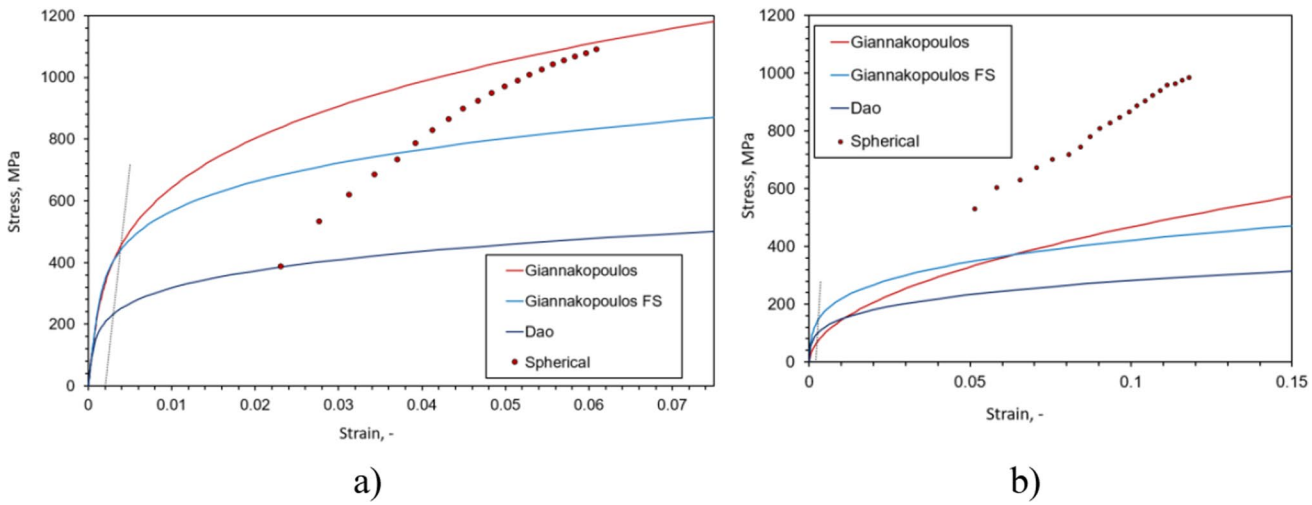

Fig. 12 Stress–strain relation of a) bainite and b) ferrite of sintered steel

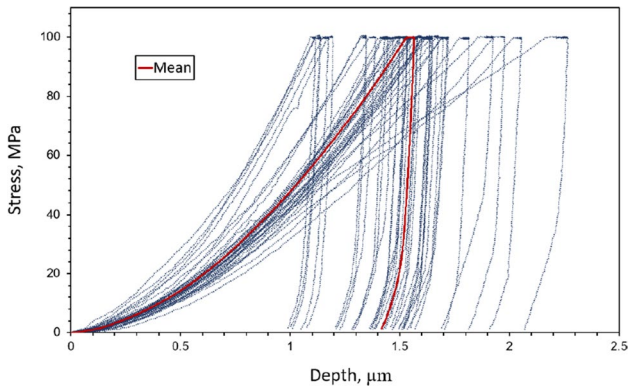

Fig. 13 Individual indentation curves and average indentation curve for metallic matrix (red line)

indentation curves of each phase, and results are presented in Table 7, where the mean value and standard deviation of the Young's modulus are given.

The estimated stress–strain curves and material parameter values of individual phases are presented in Fig. 12 and Table 7, respectively. The elastic properties are similar to those reported in [8], and it can be concluded that in contrast to the copper sample, here the standard Oliver-Pharr method based on microindentation is suitable for determining elastic properties of individual phases. However, in comparison to the values reported in the available literature for various multi-phase solid rolled steels [14, 50], here significantly lower values for the yield stress of individual phases have been obtained, especially for ferrite. This could be attributed to the fact that sintering procedure used the production of the sintered sample results in a microstructure which is significantly different than the one obtained by rolling. However, besides the presence of pores, larger forces applied in this work may also contribute to that discrepancy, and further research applying smaller forces in the nanoindentation regimen. following the approach proposed in [39], is needed to confirm this hypothesis.

The stress–strain curves obtained by different methods differ considerably, as seen in Fig. 12. In general, it can be concluded that the methods based on Vickers microindentation can predict the behavior of material phases qualitatively correctly, i.e., that bainite has got higher mechanical strength properties than ferrite, as expected. For ferrite the Giannakopoulos FS method again estimates a significantly higher value of the yield strength and less intense hardening in comparison to the Giannakopoulos method, due to the finite strain hypothesis. Likewise, the Dao method again predicts significantly more compliant behavior than other methods. In general, the presented results might be greatly influenced by pile-up effects caused by relatively large forces, but this has to be confirmed by further detailed studies. Further errors might be caused by extracting plastic parameters from the average indentation curves for each phase, shown in Fig. 9, because of a large scattering of curves, e.g., see [8]. The variation of the measured indentation data is especially pronounced for the ferrite phase, which could be the consequence of the influence of the surrounding harder bainite phase, similar to the phenomenon reported in [34–37] for various materials with harder inclusions immersed in a softer metallic matrix, and to the influence of surrounding porosity, which was noticed even in a single-phase sintered steel [39]. As demonstrated by the sensitivity analysis for copper presented in subsection 3.2.2, any variation in the curve indentation data could lead to substantial deviations in the estimated values of plastic parameters. A larger number of extracted indentation curves used for averaging could lead to a more accurate estimation, especially in the case of the Dao method. Alternatively, different statistical analysis of data could be attempted, where plastic parameters could be extracted from each individual indentation curve and then averaged, similar to the procedure proposed in [34]. However, such detailed analysis is out of the scope of this introductory investigation. It has to be noted that here no meaningful results have been obtained by spherical indentation, which might be caused by inaccurate recording of the indent geometry during the indentation process, due to the pile-up effect and relatively large indent that might interfere with the surrounding interfaces. To the authors' knowledge, a successful application of spherical indentation for characterizing individual phases in DP steels has so far not been reported.

Although microindentation is sometimes used for the identification of individual phases in multi-phase steels, see e.g. [14, 33], the presented results imply that it might not be an appropriate approach for porous multi-phase sintered steels, at least in the case of larger indentation forces. Nanoindentation-based methods should be considered instead, due to a smaller and shallower indent, but their application is out of the scope of this work.

Homogenization of metallic matrix

In the second approach, the metallic matrix is considered homogeneous. This simplified approach might be interesting if the main aim of analysis is investigating the influence of porosity on the global mechanical behavior of sintered porous steels, since porosity has been recognized as the dominant mechanism in the initiation and evolution of local plastic flow and fracture in such materials [2–5, 9]. However, it should be noted that exact distributions of plastic flow and fractures in the microstructure cannot be obtained by this approach, because it neglects the influence of phase boundaries or the spatial distribution of individual material phases, which could have very different properties.

In this approach, the metallic matrix is characterized by grid indentation over the metallic matrix, as explained in Sect. 2.3.1. The recorded indentation curves, shown in Fig. 13, exhibit a significant scattering. The average indentation curve is obtained (the red curve in Fig. 13) from all recorded indentation curves and used for extracting necessary data for estimating material parameters. It indirectly captures the influence of interfaces between different material phases, which in multi-phase steels might play a significant influence on the indentation data, as reported in [34].

The material parameter estimated from the average indentation curve are shown in Table 8. The Young's modulus of the matrix is again estimated by the Oliver-Pharr method [22]. Only the estimated plastic parameters obtained using the Giannakopoulos FS method are presented, since it has produced somewhat better results than other methods, probably because it better captures the pile-up effect caused by larger indentation forces than the original Giannakopoulos method, and is less sensitive to the slope of unloading indentation curve than the Dao method, as demonstrated in previous sections. However, here a larger Young's modulus of the metallic material than expected is obtained, probably due to a large dispersion of indentation curves used for obtaining the average indentation curve (see Fig. 13).

Table 8 Homogenized material parameters of metallic matrix obtained by the Giannakopoulos FS method

	Modulus of elasticity, E, GPa	Poisson ratio, ν, -	Yield stress, σ_y MPa	Strength index, K, MPa	Hardening exponent, n, -
Giannakopoulos FS	294	0.3	233	795	0.4512

Numerical mesoscale simulations

The identified parameters of individual material phases are used in numerical mesoscale models, with the aim of reproducing the results of the macroscopic uniaxial tension test (UTT). The macroscopic UTT is conducted with the displacement control and the strain rate of 1 mm/min. Mean values are extracted from at least 8 samples per density. The obtained macroscopic elastic and plastic parameters are given in Table 9. Further details about macroscopic testing can be found in [8].

As explained in Sect. 2.5, in numerical model with heterogenous matrix the identified material parameters of individual phases from Table 7 are prescribed to corresponding regions in the numerical models (presented by blue regions for bainite and red region for ferrite in Fig. 8). In the first step, only elastic behavior is analyzed, since the identification of elastic parameters is more reliable than that of plastic parameters. This is because a more complex reverse analysis is necessary to obtain plastic parameters, which generates further errors and uncertainties (see subsection 3.2.2). As visible in Fig. 14, the mesoscale numerical models are able to reproduce linear elastic behavior correctly and the numerical results converge towards the experimental value of macroscopic elastic modulus when the RVE size is increased, clearly exhibiting the size effect. The deviation of less than 5% from the experimental value is due to the plain strain assumption adopted in the numerical models. However, it is significantly smaller than the one expected for solid material, suggesting that the influence of porosity on elastic properties of sintered steel [52, 53] is captured by the numerical model.

Next, entire macroscopic stress–strain curves are calculated and compared to the corresponding experimental curves. The results are shown in Fig. 15, respectively. Therein, the labels {02,03,04} in the figure legend refer to the RVEs with sizes {0.2×0.2, 0.3×0.3, 0.4×0.4} mm. In Fig. 15, the stress–strain curves obtained by employing various methods for the characterization of individual phases are presented and compared with the experimental macroscopic curve.

It is obvious that the numerical mesoscopic models significantly underestimate the experimentally observed macroscopic behavior, regardless of the identification method applied. These results are physically incorrect, because it is expected that at lower length scales the yield and ultimate stresses should be higher than the corresponding macroscopic values, see e.g., [19] and references therein. Since the purely elastic

Table 9 Macroscopic properties of sintered steel, [8]

Modulus of elasticity, GPa	Yield stress, MPa	Tensile strength, MPa
Sintered steel, 7.1 g/cm^3		
131 ± 12.3	369.0 ± 26.9	471.7 ± 16.5

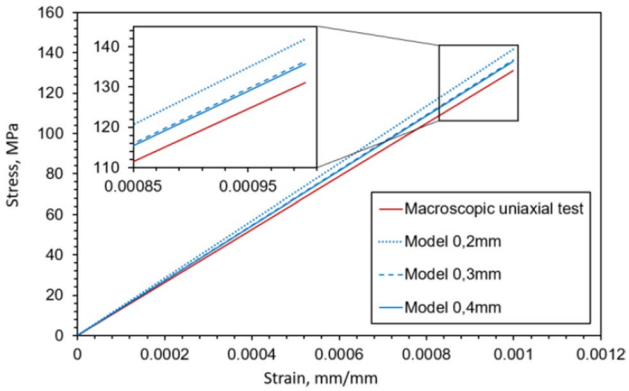

Fig. 14 Comparison of the macroscopic elastic behaviour obtained by DNS and UTT for sintered steel

macroscopic behavior of the considered sintered steel can be predicted accurately, these errors are caused by the erroneous estimation of plastic parameters. The severe underestimation of ferrite plastic properties, especially in the yield stress, leads to a premature and pronounced localization of plastic flow in the ferrite zones, which leads to the overly compliant global behavior of microstructure.

Figure 16 shows the stress–strain curves estimated by the Giannakopoulos FS method using the "homogenized" properties from Table 8, obtained as explained in subsections 2.3.2 and 3.3.2, which were employed over the entire metallic matrix. Interestingly, it seems that the global response of the microstructure significantly improves by this approach. This could be explained by the fact that errors in characterizing softer ferrite phase are "smoothed" by averaging the data collected by grid indentation, partly because the hardening of the ferrite phase caused by the nearby harder bainite phase interface is captured by the indents inside soft ferrite zones that are positioned closer to the interface with the surrounding harder bainite, similarly to the findings for an austenitic/martensitic steel in [34]. However, this has to be confirmed

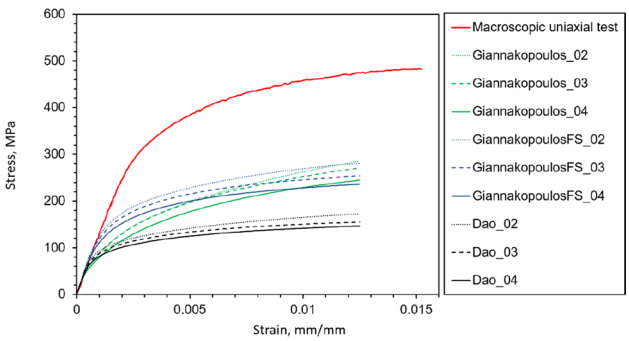

Fig. 15 Strain–stress curves obtained by DNS and UTT for sintered steel for numerical model with heterogeneous material matrix

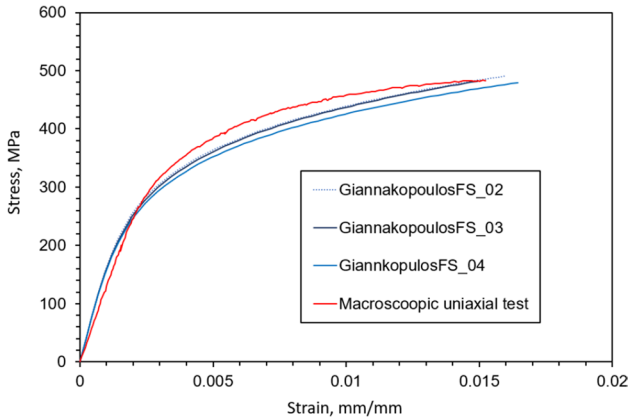

Fig. 16 Strain–stress curves obtained by DNS and UTT for sintered steel for numerical models employing homogenized metallic matrix properties

by more detailed research involving nanoindentation, which is outside of the scope of this work.

The size effect due to plastic deformation is somewhat more pronounced than in elastic regimen, which is common at lower length scales, see [19]. Although the global response of microstructure is somewhat stiffer in the elastic deformation regimen due to the overestimation of Young's modulus, once the plastic deformation becomes more pronounced, more compliant response is predicted due to considerable underestimation of the yield stress. Nevertheless, the overall predicted response agrees relatively well with the experimental curve. This further confirms the conclusion from the authors' recent work [9] that this homogenization procedure could be a useful approach for studying the influence of porosity on certain aspects of macroscopic behavior of sintered porous steels, especially because of reduced computational resources needed for the generation and execution of such simplified numerical models. Nevertheless, further research is needed to obtain more reliable material matrix data, including performing grid indentations at various locations in the matrix and more detailed statistical analysis of indentation results. However, by adopting this homogenization approach in general one cannot capture exactly inelastic deformation processes inside the metallic matrix, such as plastic flow localization or propagation of microfractures, due to significant simplifications adopted in the model, see [9] for a more detailed discussion about that issue.

Conclusion

Two approaches for the characterization of dual-phase porous sintered steel microstructure were applied. The first one is based on the identification of individual matrix phases, while the second one estimates the average (homogenized) properties of the metallic matrix. The feasibility of both procedures was tested by the application of estimated material parameters in numerical mesoscale models of realistic microstructure of a ferrite/bainite porous steel.

Thereby, stress–strain characteristics estimated by the numerical models were compared to the experimental curve obtained by the macroscopic uniaxial tension test. In contrast to existing works, here different methods for the extraction of stress–strain curves from microindentation data were used and compared, based on both sharp and spherical tips. From the presented results of this preliminary research, the following conclusions can be drawn:

- Sufficiently accurate estimations of elastic parameters of individual material phases can be obtained by microindentation, which could be used to investigate the influence of porosity on macroscopic elastic behavior of multi-phase sintered steels by numerical mesoscale simulations.
- Microindentation might not be suitable for the identification of plastic parameters of individual material phases in heterogeneous multi-phase porous steels, especially for softer ductile phases like ferrite. Although further extensive statistical analysis is needed to estimate errors, the presented results imply that large deviations from expected values could occur, regardless of the applied identification method, leading to completely erroneous mechanical responses of microstructure in numerical simulations.
- The identification of average properties of metallic matrix by grid indentation may result in an acceptable global elasto-plastic response in numerical mesoscale simulations of porous multi-phase sintered steels. This approach considers porosity, including the shape and distribution of pores, which is often the main mechanism that causes stress concentrations and initiates the plastic flow in the microstructure, but it neglects the heterogeneity of the metallic matrix, including the influence of phase interfaces, which is important for a detailed study of local inelastic processes in microstructures of multi-phase sintered steels. Nevertheless, further research will be undertaken to investigate the potential of the proposed homogenization approach for studying the influence of porosity on global inelastic behavior in porous sintered steels.

The presented results were obtained by using relatively large indentation forces, which may cause significant pile-up effects during indentation. Therefore, the above conclusions should be confirmed by applying smaller indentation forces, especially for the characterization of individual phases. In addition, a more extensive analysis is needed for obtaining statistically reliable data, involving a detailed error analysis

for plastic parameters and performing more indents at various locations in microstructure.

Acknowledgements This work has been fully supported by Croatian Science Foundation under the project "Multiscale Numerical Modelling and Experimental Investigation of Aging Processes in Sintered Structural Components" (MultiSintAge, PZS-1 2019-02-4177).

Author contribution *Zoran Tomić*: Conceptualization, Methodology, Investigation, Experimental investigation, Numerical calculation, Results preparation, Writing – original draft, *Tomislav Jarak*: Conceptualization, Methodology, Investigation, Supervision, Writing – original draft, review & editing, *Benjamin Pavlović*: Investigation, Numerical calculation, Results preparation, *Zdenko Tonković*: Supervision, Resources, Writing – review & editing.

Funding This work has been supported by Croatian Science Foundation under project "Multiscale Numerical Modelling and Experimental Investigation of Aging Processes in Sintered Structural Components" (MultiSintAge, PZS-1 2019-02-4177).

Data Availability Data sharing not applicable.

Declarations

Conflict of Interest All authors declare that they have no known competing financial interests or personal relationships that are relevant to the content of this article.

References

1. Brecher C, Löpenhaus C, Schroers M, Frech T (2017) Scholzen: Optimization of NVH behavior of gears by alternative gear materials. In: International Conference on Gears 2017 2 Bände. VDI Verlag GmbH, Düsseldorf, pp 539–552. https://doi.org/10.51202/9783181022948
2. Dudrova E, Kabátova M (2016) A review of failure of sintered steels: Fractography of static and dynamic crack nucleation, coalescence, growth and propagation. Powder Metall 59:148–167. https://doi.org/10.1080/00325899.2016.1145786
3. Doroszko M, Seweryn A (2021) Numerical modelling of the mesofracture process of sintered 316L steel under tension using microtomography. Eng Fracture Mechanics 255:107965. https://doi.org/10.1016/j.engfracmech.2021.107965
4. Doroszko M, Seweryn A (2020) Pore-scale numerical modelling of large deformation behaviour of sintered porous metals under compression using computed microtomography. Mech Mater 141:103259. https://doi.org/10.1016/j.mechmat.2019.103259
5. Doroszko M, Seweryn A (2015) Modeling of the tension and compression behavior of sintered 316L using micro computed tomography. Acta Mech. Autom 9:70–74. https://doi.org/10.1515/ama-2015-0012
6. Madej L, Legwand A, Mojzeszko M, Chraponski J, Roskosz S, Cwajna J (2018) Experimental and numerical two- and three-dimensional investigation of porosity morphology of the sintered metallic material. Arch Civ Mech Eng 18:1520–1534
7. Scherff F, Gola J, Scholl S et al (2021) Numerical simulation of dual-phase steel based on real and virtual three-dimensional microstructures. Continuum Mech Thermodyn 33:1989–2006. https://doi.org/10.1007/s00161-021-00980-x
8. Tomić Z, Gubeljak N, Jarak T, Polančec T, Tonković Z (2022) (2022) Micro - and macromechanical properties of sintered steel with different porosity. Scr Mater 217:114787. https://doi.org/10.1016/j.scriptamat.2022.114787
9. Tomić Z, Jarak T, Lesičar T, Gubeljak N, Tonković Z (2023) Modelling of Fatigue Microfracture in Porous Sintered Steel Using a Phase-Field Method. Materials 16(11):4174. https://doi.org/10.3390/ma16114174
10. Ishikawa N, Yasuda K, Sueyoshi H, Endo S, Ikeda H, Morikawa T, Higashida K (2015) Microscopic deformation and strain hardening analysis of ferrite–bainite dual-phase steels using micro-grid method. Acta Materialia. 97:257–268. https://doi.org/10.1016/j.actamat.2015.06.037
11. Sun X, Choi KS, Liu WN, Khaleel MA (2009) Predicting failure modes and ductility of dual phase steels using plastic strain localization. Int J Plasticity 25(10):1888–1909. https://doi.org/10.1016/j.ijplas.2008.12.012
12. Qiao G-Y, Zhao Z-T, Shi X-B, Shan Y-Y, Gu Y, Xiao F-R (2021) Effect of Bainite to Ferrite Yield Strength Ratio on the Deformability of Mesostructures for Ferrite/Bainite Dual-Phase Steels. Materials 14(18):5352. https://doi.org/10.3390/ma14185352
13. Zhou J, Gokhale AM, Gurumurthy A, Bhat SP (2015) Realistic microstructural RVE-based simulations of stress–strain behavior of a dual-phase steel having high martensite volume fraction. Materials Sci Eng: A 630:107–115. https://doi.org/10.1016/j.msea.2015.02.017
14. Zhao Z, Wang X, Qiao G, Zhang S, Liao B, Xiao F (2019) Effect of bainite morphology on deformation compatibility of mesostructure in ferrite/bainite dual-phase steel: Mesostructure-based finite element analysis. Mater Des 180:107870. https://doi.org/10.1016/j.matdes.2019.107870
15. Basantia SK, Bhattacharya A, Khutia N et al (2021) Plastic Behavior of Ferrite-Pearlite, Ferrite-Bainite and Ferrite–Martensite Steels: Experiments and Micromechanical Modelling. Met Mater Int 27:1025–1043. https://doi.org/10.1007/s12540-019-00519-5
16. Uchic MD, Shade PA, Dimiduk DM (2009) Plasticity of micrometerscale single crystals in compression. Annu Rev Mater Res 39:361–386
17. Gianola DS, Eberl C (2009) Micro- and nanoscale tensile testing of materials. JOM 3:24–35
18. Magagnosc DJ, Ligda JP, Sano T, Schuster BE (2018) Femtosecond laser machining of micro-tensile specimens for high throughput mechanical testing. In: Starman L, Hay J (eds) Micro and Nanomechanics, vol 5. Conference Proceedings of the Society for Experimental Mechanics Series. Springer, Cham, pp 7–9. https://doi.org/10.1007/978-3-319-63405-0_2
19. Voyiadjis G, Yaghoobi M (2019) Size effects in plasticity: from macro to nano, 1st edn. Academic Press, Elsevier Inc.
20. Durst K, Göken M, Pharr GM (2008) Indentation size effect in spherical and pyramidal indentations. J Phys D Appl Phys 41:74005. https://doi.org/10.1088/0022-3727/41/7/074005
21. Bushby AJ, Dunstan DJ (2004) Plasticity size effects in nanoindentation. J Mater Res 19:13. https://doi.org/10.1557/jmr.2004.19.1.137
22. Oliver WC, Pharr GM (1992) An improved technique for determining hardness and elastic modulus using load and displacement sensing indentation experiments. J Mater Res 7:1564–1583. https://doi.org/10.1557/JMR.1992.1564
23. Giannakopoulos AE, Suresh S (1999) Determination of elastoplastic properties by instrumented sharp indentation. Scr Mater 40:1191–1198
24. Dao M, Chollacoop N, Van Vliet KJ, Venkatesh A, Suresh S (2001) Computational modeling of the forward and reverse problems in instrumented sharp indentation. Acta Mater 49:3899–3918
25. Bucaille JL, Stauss S, Felder E, Michler J (2003) Determination of plastic properties of metals by instrumented indentation using different sharp indenters. Acta Mater 51:1663–1678

26 Pathak S, Kalidindi SR (2015) Spherical nanoindentation stress–strain curves. Mater Sci Eng R Reports 91:1–36. https://doi.org/10.1016/j.mser.2015.02.001

27. Mesarovic D, Fleck NA (1999) Spherical indentation of elastic-plastic solids. Proc R Soc a-Mathematical Phys Eng Sci 455:2707–2728

28. Herbert EG, Pharr GM, Oliver WC, Lucas BN, Hay JL (2001) On the measurement of stress–strain curves by spherical indentation. Thin Solid Films 398–399:331–5. https://doi.org/10.1016/S0040-6090(01)01439-0

29 Herbert EG, Oliver WC, Pharr GM (2006) On the measurement of yield strength by spherical indentation. Philos Mag 86:5521–39. https://doi.org/10.1080/14786430600825103

30. Ruiz-Moreno A, Hähner P, Fumagalli F, Haiblikova V, Conte M, Randall N (2020) Stress−strain curves and derived mechanical parameters of P91 steel from spherical nanoindentation at a range of temperatures. Mater Des 194:108950. https://doi.org/10.1016/j.matdes.2020.108950

31. Pathak S, Shaffer J, Kalidindi SR (2009) Determination of an effective zero-point and extraction of indentation stress-strain curves without the continuous stiffness measurement signal. Scr Mater 60:439–42. https://doi.org/10.1016/j.scriptamat.2008.11.028

32 Donohue BR, Ambrus A, Kalidindi SR (2012) (2012) Critical evaluation of the indentation data analyses methods for the extraction of isotropic uniaxial mechanical properties using finite element models. Acta Mater 60:3943–52. https://doi.org/10.1016/j.actamat.2012.03.034

33. Cuervo-Basurto A, Narvaez-Tovar CA, Rodriguez-Baracaldo R (2022) Assessment of microindentation method in the characterization of DP600 response using phases distribution and a specific shape parameter along RVEs and FEM simulation approaches. J App Res Technol 20:686–702. https://doi.org/10.22201/icat.24486736e.2022.20.6.1121

34. Cheng G, Choi KS, Hu X, Sun X (2016) Determining individual phase properties in a multi-phase Q&P steel using multi-scale indentation tests. Mater Sci Eng A 652:384–95. https://doi.org/10.1016/j.msea.2015.11.072

35 Shen Y-L, Guo YL (2001) Indentation modelling of heterogeneous materials. Model Simul Mater Sci Eng 9:391–8. https://doi.org/10.1088/0965-0393/9/5/304

36. Pöhl F, Huth S, Theisen W (2013) Finite element method-assisted acquisition of the matrix influence on the indentation results of an embedded hard phase. Mater Sci Eng A 559:822–8. https://doi.org/10.1016/j.msea.2012.09.029

37. Heidari M, Karimzadeh A, Ayatollahi MR, Yahya MY (2021) Effects of particle distribution and calculation method on results of nano-indentation technique in heterogeneous nanocomposites-experimental and numerical approaches. Int J Solids Struct. 225:111054. https://doi.org/10.1016/j.ijsolstr.2021.111054

38. Kannan R, Wang Y, Nouri M, Li D, Li L (2018) Materials Science & Engineering A Instrumented indentation study of bainite / martensite duplex microstructure. Mater Sci Eng A 713:1–6

39. Madej L, Legwand A, Setty M et al (2022) Evaluation of capabilities of the nanoindentation test in the determination of flow stress characteristics of the matrix material in porous sinters. Archiv Civ Mech Eng 22:21. https://doi.org/10.1007/s43452-021-00343-y

40. Abaqus Analysis User's Guide (2014) vol 4. Dassault Systems Simulia Corp., Providence, RI, USA

41. Gu W, Yao Z (2011) Evaluation of surface cracking in micron and sub-micron scale scratch tests for optical glass BK7. J Mech Sci Technol 25:1167. https://doi.org/10.1007/s12206-011-0306-2

42. Calcutt V (2001) Introduction to copper: fact sheets. Copper Development Association Inc. https://www.copper.org/publications/newsletters/innovations/2001/08/intro_fac.html. Accessed 13 Oct 2022

43. Copper Alloy 110/C110/C11000 Electrolytic Tough Pitch (ETP) (2022) Basic Copper. https://basiccopper.com/copper-c110-alloy-electrolytic-tough-pitch.html. Accessed 13 Oct 2022

44. Tran HS, Bouffioux C, Dedry O, Rojas-Ulloa C, Duchêne L, Mertens A et al (2022) Identification of a soft matrix-hard inclusion material by indentation. Int J Mech Sci 235:107723. https://doi.org/10.1016/j.ijmecsci.2022.107723

45. Tabor D (1951) The Hardness of Metals, 1st edn. Oxford University Press, Londkon

46. Zhang T, Wang S, Wang W (2019) A comparative study on uniaxial tensile property calculation models in spherical indentation tests (SITs). Int J Mech Sci 155:159–69. https://doi.org/10.1016/j.ijmecsci.2019.02.044

47. Bruns S, Petho L, Minnert C, Michler J, Durst K (2020) Fracture toughness determination of fused silica by cube corner indentation cracking and pillar splitting. Mater Des 186:108311. https://doi.org/10.1016/j.matdes.2019.108311

48. Torres-Torres D, Muñoz-Saldaña J, De Guevara L, Hurtado-Macías A, Swain MV (2010) Geometry and bluntness tip effects on elastic-plastic behaviour during nanoindentation of fused silica: Experimental and FE simulation. Model Simul Mater Sci Eng 18:075006. https://doi.org/10.1088/0965-0393/18/7/075006

49 Shuman DJ, Costa ALM, Andrade MS (2007) Calculating the elastic modulus from nanoindentation and microindentation reload curves. Mater Charact 58:380–9. https://doi.org/10.1016/j.matchar.2006.06.005

50. Ghassemi-Armaki H, Mass R, Baht SP, Sriram S, Greer JR, Kumar RS (2014) Deformation response of ferrite and martensite in a dual-phase steel. Acta Mater 62:197–211

51. Tao P, Gong J, Wang Y, Jiang Y, Li Y, Cen W (2018) Characterization on stress-strain behavior of ferrite and austenite in a 2205 duplex stainless steel based on nanoindentation and finite element method. Results Phys 11:377–84. https://doi.org/10.1016/j.rinp.2018.06.023

52. Ternero F, Rosa LG, Urban P, Montes JM, Cuevas FG (2021) Influence of the Total Porosity on the Properties of Sintered Materials—A Review. Metals 11(5):730. https://doi.org/10.3390/met11050730

53. Manoylov AV, Borodich FM, Evans HP (2013) Modelling of elastic properties of sintered porous materials. Proc R Soc A Math Phys Eng Sci 469:20120689. https://doi.org/10.1098/rspa.2012.0689